UNIVERSITÄT
ZU KÖLN

Precipitation formation in low-level mixed-phase clouds: determining relevant processes and drivers based on cloud radar observations from a high Arctic site

Inaugural-Dissertation zur Erlangung des Doktorgrades der
Mathematisch-Naturwissenschaftlichen Fakultät der Universität zu Köln

vorgelegt von

Giovanni Chellini

aus Florenz, Italien

Köln, 2024

Berichterstatter:
Dr. Stefan Kneifel
Prof. Dr. Ulrich Löhnert

Tag der mündlichen Prüfung:
8. Januar 2024

Abstract

Low-level mixed-phase clouds (LLMPCs) shroud large portions of Earth's surface at high latitudes. They have been shown to dramatically affect the surface energy budget, yet, large uncertainties in their model representation remain, both in climate simulations, and in numerical weather prediction. Both computational limitations and poor understanding of a number of processes taking place in LLMPCs are thought to give rise to such uncertainties. In particular, precipitation formation processes have been relatively understudied in LLMPCs, and reaching a refined understanding is expected to lead to an improvement in model performance, as precipitation determines the cloud's mass sink, and hence lifetime.

In this dissertation, precipitation formation processes are investigated in LLMPCs at the high Arctic site of Ny-Ålesund, based on long-term cloud radar observations. Cloud radars are in fact especially suited for ice microphysical studies, due to the wide spectrum of observational fingerprints of ice microphysical processes that they provide. Doppler radar observations provide information on dynamics, multi-frequency radar observations on ice particle size, and polarimetric radar observations on particle shape and concentration. Radar data are combined with thermodynamic information, which further allows to discriminate between ice microphysical processes, due to their high sensitivity to temperature.

In the first part of the dissertation, the relevance of the aggregation process for LLMPCs at Ny-Ålesund is assessed. Aggregation occurs when ice particles collide to form larger ice particles. A long-term dataset of dual-frequency radar observations, as well as thermodynamic information, is used to statistically assess the relevance of aggregation and its sensitivity to varying cloud thermodynamic conditions. The study finds that larger aggregate snowflakes are predominantly produced in LLMPCs whose mixed-phase layer is at temperatures compatible with the growth and subsequent mechanical entanglement of dendritic crystals. Surprisingly, the second enhanced aggregation zone close to the 0°C isotherm, typically observed in deeper cloud systems, is absent.

In the second part, a novel state-of-the-art long-term dataset developed within this dissertation is presented. It combines dual-frequency and polarimetric Doppler cloud radar observations, together with thermodynamic information, and other auxiliary variables. After detailing the processing and curation approaches, the results on aggregation are confirmed, and expanded upon. Additionally, temperature regimes where columnar ice particles, riming, i.e., the collection of supercooled liquid droplets by ice crystals, and secondary ice production are likely to occur are identified.

In the final part of the dissertation, the developed dataset is used to assess the effect of turbulence on aggregation and riming in LLMPCs at Ny-Ålesund. LLMPCs are in fact inherently turbulent, and maintained by turbulent overturning generated at cloud top. The turbulent kinetic energy dissipation rate (EDR) is retrieved, and the sensitivity of aggregation and riming to varying EDR conditions is investigated. It is shown that higher EDR regimes enhance the aggregation of particles, and are associated with signatures of increased ice particle concentration, possibly caused by fragmentation of ice particles. In temperature regimes more favorable to riming, turbulence dramatically enhances the particles' fall velocities, denoting higher degrees of riming.

Contents

Chapter 1

Introduction

1.1 Motivation

At any time, 70% of the Earth's surface is eclipsed by clouds [King et al., 2013, Stubenrauch et al., 2013]. It is hence no surprise that clouds dramatically affect and shape the characteristics of Earth's atmosphere and surface. They extensively interact with solar and terrestrial radiation, greatly conditioning the energy budget, and are an integral and essential component of the hydrological cycle [e.g., Wallace and Hobbs, 2006]. Still, our ability to represent cloudiness in models across scales, from global to local to microscopic, is lacking in a number of areas. This is attributable to a number of factors, including knowledge gaps in cloud processes, and computational constraints, which lead to the need for the development of parametrizations which dramatically simplify physical processes. Consequently, while vast and extensive improvements in modeling capabilities have been achieved in recent decades, large errors, e.g., in short-term precipitation forecasts and in cloud radiative effects in climate projections, are still widespread [e.g., Zelinka et al., 2017, Korolev et al., 2017, Hyder et al., 2018, Brdar and Seifert, 2018, Morrison et al., 2020].

Mixed-phase clouds (MPCs) are especially challenging to simulate, as they feature, at least in part of their volume, the coexistence of liquid and ice particles [Korolev et al., 2017]. This mixture is generally thought to be thermodynamically unstable, as the saturation vapor pressure of ice is lower than that of liquid. This leads, in absence of further effects maintaining saturation with respect to the liquid phase, to evaporation of the liquid droplets and growth of the ice particles by vapor deposition. This process is a cornerstone of cloud microphysics and known as the Wegener-Bergeron-Findeisen (WBF) process [Wegener, 1911, Bergeron, 1935, Findeisen, 1938]. Despite this, mixed-phase conditions are observed in several cloud types across the whole globe, ranging from cloud tops in the storm tracks [Naud

et al., 2006, Hu et al., 2010], to mid-level stratiform clouds at the mid-latitudes [Fleishauer et al., 2002, Bühl et al., 2016, Barrett et al., 2020], to tropical altocumuli [Ansmann et al., 2009], to orographic clouds [Rauber and Grant, 1986, Ramelli et al., 2021]. Furthermore, a third of precipitation in the extra-tropics originates from MPCs [Mülmenstädt et al., 2015]. It is now established that complex microphysical, dynamic and thermodynamic interactions operating on multiple scales contribute to maintaining mixed-phase conditions [Morrison et al., 2012, Korolev et al., 2017]. As an example, cloud-top overturning, generated either via entrainment, shear, or radiative cooling, has been shown to produce and maintain supercooled water even in the presence of ice crystals [Rauber and Tokay, 1991, Morrison et al., 2012]. This process typically occurs on scales of hundreds of meters or smaller, making it difficult for models to accurately produce supercooled liquid unless high enough resolution, or accurate subgrid-scale parametrizations, are achieved [Furtado et al., 2016, Barrett et al., 2017, Kretzschmar et al., 2020, Vignon et al., 2021]. The full extent of interacting processes is, to a degree, still poorly understood, and anyhow arduous to include in models [e.g., Andronache, 2017].

Model performance is worsened especially by the vastly different characteristics of cloud liquid and ice particles, and the diverse processes that determine their evolution. Cloud liquid and cloud ice particles have vastly different radiative properties [Sun and Shine, 1995]; liquid droplets nucleate more efficiently due to the large availability of cloud condensation nuclei (CCN), while ice particles in MPCs mainly nucleate via liquid-dependent pathways [Ansmann et al., 2009, Westbrook and Illingworth, 2011, Hande and Hoose, 2017]; at the same time, the ice phase removes mass from the cloud layer more efficiently than the liquid phase, as ice particles can reach significantly large sizes while keeping relatively low fall velocities when compared to droplets [Pruppacher and Klett, 2012, Ch. 15-16]. These effects, among others, make model representation of MPCs highly sensitive to the *phase partitioning*, namely the relative distribution, production and sink of ice and liquid phases. Uncertainties in the phase partitioning in fact can in turn cascade into uncertainties in cloud radiative properties, and in precipitation, which determines cloud lifetime [McCoy et al., 2015, Tan et al., 2016, Furtado and Field, 2017, Hyder et al., 2018, Tan and Storelvmo, 2019].

Both cloud lifetime and cloud radiative properties of MPCs are crucial for climate projections. Low-level mixed-phase clouds (LLMPCs) in fact shroud large portions of the Earth's surface throughout most of the year at high latitudes. Here, they often take on the form of low-level stratus or stratocumulus, topped by a liquid layer, where ice nucleates and grows. The liquid layer at cloud top is thought to maintain itself against the continuous mass loss due to precipitation via turbulent overturning driven by cloud-top radiative cooling [Morrison et al., 2012, McFarquhar et al., 2021]. Additionally, over open ocean LLMPCs may further

form and persist via roll or cell convection [Brümmer, 1999, Muhlbauer et al., 2014, Eirund et al., 2019]. LLMPCs have been extensively observed across the Arctic region [Shupe and Intrieri, 2004, Mioche et al., 2015], above the Southern Ocean [Hu et al., 2010, Morrison et al., 2011, Kanitz et al., 2011, Huang et al., 2012], and, to a lesser extent, above Antarctica [Lawson and Gettelman, 2014, Listowski et al., 2019]. LLMPCs at high latitudes have vast implications for the energy budget [Dong and Mace, 2003, Zuidema et al., 2005, Lawson and Gettelman, 2014, McCoy et al., 2015]. During the winter months, when solar radiation is at its minimum, LLMPCs shield the surface and limit the amount of energy that it looses to space via longwave radiative cooling [Curry et al., 1996, Shupe and Intrieri, 2004, Miller et al., 2015]; during the summer months, when insolation reaches its maximum, the longwave warming is counterbalanced by shortwave cooling, as LLMPCs over open ocean or snow-free land dramatically increase the albedo, reflecting solar radiation back to space [Shupe and Intrieri, 2004, Bodas-Salcedo et al., 2016]. In some cases this leads to an overall cooling effect on the surface during the summer months [Matus and L'Ecuyer, 2017, Ebell et al., 2020]. Both terrestrial and solar radiative effects are driven by the liquid phase [Bodas-Salcedo et al., 2016, Ebell et al., 2020], while the overall duration of an LLMPC is driven by the cloud's mass sink, i.e., precipitation, and hence by the ice phase [Harrington and Olsson, 2001, Simpfendoerfer et al., 2019]. Consequently, models need to correctly represent the phase partitioning of LLMPCs, and hence the processes determining the evolution of both the liquid and ice phase, together with their interaction [Cronin and Tziperman, 2015, Tan and Storelvmo, 2019, Proske et al., 2022]. The most dramatic example of the effects of an incorrect phase partitioning is the large bias in solar radiation reflection over the Southern Ocean in a number of climate models [Bodas-Salcedo et al., 2014, Hyder et al., 2018]. Similarly, uncertainties in phase partitioning of LLMPCs have been indicated as one of the causes of the disagreement on the sign of the cloud feedback in the Arctic across several climate models [Storelvmo et al., 2015, Tan et al., 2016, Goosse et al., 2018].

Accurate understanding and model parametrizations of ice precipitation formation processes are still eluding the meteorological community [e.g., Morrison et al., 2020]. Ice crystals can take on a wide spectrum of complex shapes, typically referred to as *habits*, depending with high sensitivity on temperature and humidity [e.g., Bailey and Hallett, 2009]. At temperatures relevant for LLMPCs, most observed habits consist of either columnar or plate-like structures. In mixed-phase conditions, and at specific temperatures, they can grow by vapor deposition into highly complex habits and large sizes, especially needle-like particles, and fractal-like dendritic structures [e.g., Takahashi et al., 1991]. Once sufficiently large sizes are reached, ice particles can further grow by collisions with other ice particles, and, in mixed-phase conditions, with droplets as well. These collisional growth processes are generally

referred to as, respectively, *aggregation* and *riming* [Pruppacher and Klett, 2012, Ch. 16]. The efficiency of both collisional processes is highly sensitive to the shape and size of the ice particles: while dendritic particles are highly efficient at forming ice aggregates by entangling their dendritic branches [Connolly et al., 2012], they efficiently collect droplets only at sizes 10 times larger than those required by columnar particles [Wang and Ji, 2000]. Moreover, both aggregation and riming can lead to the formation of new ice particles, with varying efficiency depending on temperature and habit, via processes collectively referred to as *secondary ice production* (SIP) processes [e.g., Korolev and Leisner, 2020].

The relevance of the mentioned processes for LLMPCs is still unclear, together with their sensitivity to the unique thermodynamic and dynamical features of these clouds [Avramov and Harrington, 2010, Tan and Storelvmo, 2019, Proske et al., 2022]. Inside the liquid layer ice particles can in fact concurrently grow by vapor deposition, aggregation, and riming. In particular, the relative importance of aggregation and riming, together with its dependence on the amount of liquid, and the nucleated ice habits has so far not been quantified in LLMPCs. Furthermore, the role of turbulence on cold precipitation formation has been vastly overlooked in the cloud microphysics community. Theoretical studies have suggested that turbulence might increase the collision rates between hydrometeors [Pumir and Wilkinson, 2016, Sheikh et al., 2022], hence it is likely that turbulence generated by cloud-top radiative cooling in LLMPCs might favor the growth of ice particles by aggregation and riming. Therefore the main research questions of this thesis are as follows:

- Are aggregation and riming relevant ice-growth processes for precipitation formation in LLMPCs?
- How sensitive are they to varying cloud thermodynamic conditions?
- Does cloud-top driven turbulence affect the relevance of either process?

Gaining a deeper understanding of these topics through observations is likely to inform the cloud microphysics community about which areas of model parametrizations should be prioritized to achieve an improved representation of precipitation formation in LLMPCs in weather and climate models.

Knowledge on ice microphysical processes can be gained via a number of observational techniques, including laboratory studies, in-situ approaches, and spaceborne, as well as ground-based, remote sensing. Due to the wide spectrum of spatial and temporal scales involved in cloud processes, different techniques provide insights into different processes, and advances in cloud physics have relied and will continue to rely on a large number of vastly different techniques. Laboratory studies have been invaluable for the determination of the processes affecting individual

particles, and have widely informed model parametrizations [Takahashi et al., 1991, Seifert and Beheng, 2006, Morrison et al., 2020]. Similarly, in-situ approaches provide a wealth of information on particle properties [Bailey and Hallett, 2009, Schwarzenboeck et al., 2009, Waitz et al., 2022], however they lack in spatial and temporal coverage. In contrast, remote sensing techniques have the advantage of being suited for the collection of long-term datasets with high temporal resolution or extensive spatial coverage. Cloud remote sensing instruments are typically classified into active or passive. Active remote sensing instruments, such as radar and lidar, transmit a signal and then measure properties of the radiation that is scattered back to the instrument itself by cloud particles. The characteristics of the received signal can then be linked to hydrometeor properties. Active instruments have the advantage of allowing for the accurate ranging of targets, by measuring the time delay between the transmitted and received signals. Additionally, in the case of instruments with Doppler capabilities, the frequency shift of the received signal generated by the Doppler effect can be used to estimate the velocity of targets. Conversely, passive remote sensing observations, especially in the microwave region, can be used to retrieve column-integrated cloud and thermodynamic properties, as well as profiles of certain thermodynamic quantities. Therefore, active remote sensing observations, complemented with retrievals from passive remote sensing, are especially suited for studies of cloud particle evolution, and its interaction with cloud dynamics and thermodynamics [e.g., Andronache, 2017].

While spaceborne active remote sensing has the advantage of providing information on cloud distribution both vertically and horizontally on a global scale, it still falls behind in terms of resolution and sensitivity, when compared to ground-based remote sensing. Especially the presence of a large blind zone close to the surface, the lack of Doppler capabilities (as of writing this thesis), and the intrinsic impossibility for satellite instruments to resolve the short-term time evolution, limit the suitability of spaceborne observations for process studies of LLMPCs [e.g., Maahn et al., 2014, Schirmacher et al., 2023]. In contrast, ground-based remote sensing provides highly spatially and temporally resolved data, and millimeter-wavelength meteorological radars (hereafter *cloud radars*) in particular have become key instruments for cloud studies in recent decades [Kollias et al., 2007]. Compared to other active remote sensing instruments operating at visible and ultraviolet wavelengths, cloud radars are especially sensitive to ice particles, and, in addition to Doppler capabilities, a number of further techniques have been developed to maximize the amount of information provided. In particular, polarimetric setups provide information on the shape, size, and concentration of asymmetric particles [e.g., Bechini et al., 2013, Schrom et al., 2015, Schrom and Kumjian, 2016], while multiple-wavelength setups allow for the derivation of variables indicative of the size of ice particles [e.g., Hogan et al., 2000, Liao et al., 2005, Kneifel et al.,

2016]. Combined use of multiple-wavelength polarimetric Doppler cloud radar observations and thermodynamic retrievals from passive microwave remote sensing therefore serves as an ideal framework for the study of ice microphysical processes in LLMPCs, together with their interaction with dynamics and thermodynamics.

1.2 Thesis objectives

This dissertation was carried out within the framework of the *"ArctiC Amplification: Climate Relevant Atmospheric and SurfaCe Processes and Feedback Mechanisms (AC)^3"* project. (AC)^3 is a collaborative research project funded by the Deutsche Forschungsgemeinschaft (DFG; German Research Foundation) with the objective of addressing knowledge gaps in understanding and quantifying the processes and feedbacks determining Arctic amplification, namely the observed and projected increased warming of the Arctic region compared to the global average [Wendisch et al., 2019, 2023]. Throughout the three decades 1991-2021 the Arctic region has in fact warmed at a rate that is double the global average, with reference to the period 1951-1980 [Wendisch et al., 2023]. Climate models currently display limitations in their ability to reproduce recent changes in the Arctic region, therefore future projections are highly uncertain [Smith et al., 2019, Cohen et al., 2020]. These limitations have been attributed to an inaccurate model representation of a wide spectrum of processes, including cloud processes, and processes determining LLMPC characteristics in particular [Pithan and Mauritsen, 2014, Tan et al., 2016, Tan and Storelvmo, 2019, Kretzschmar et al., 2020].

It is within (AC)^3 that a number of instruments for the continuous long-term observation of clouds and precipitation was installed at the AWIPEV research base located in Ny-Ålesund, Spitsbergen, Norway. Ny-Ålesund is a coastal site located in the European high Arctic at 79°N, in the region where Arctic amplification is the most intense [Dahlke and Maturilli, 2017]. The instruments installed at the site include a 94-GHz Doppler cloud radar and a 24-GHz Doppler precipitation radar, both first installed in 2016-2017, followed by a 35-GHz polarimetric Doppler cloud radar, and a snowfall imager (the Video In Situ Snowfall Sensor, VISSS; Maahn et al. [2024]), which were installed during the preparation of this dissertation in October 2021. These instruments complemented daily radiosonde launches and a wide suite of instruments managed by the Alfred Wegener Institute (AWI), and already present at the site, including a microwave radiometer, and a ceilometer.

In this dissertation, the long-term datasets collected at AWIPEV are curated and analyzed to address knowledge gaps in precipitation formation processes in LLMPCs. The analysis builds upon the processing routines developed by Küchler et al. [2017] and Gierens [2021] for the 94-GHz cloud radar, by Maahn and Kollias [2012] for the 24-GHz precipitation radar, and by Crewell and Löhnert [2007] and

Nomokonova et al. [2020] for the microwave radiometer. The processing routines for the newly-installed 35-GHz cloud radar, together with the calibration procedure for all radar systems, were developed as part of this dissertation. Additionally, the turbulent kinetic energy dissipation rate (EDR) retrieval developed by Borque et al. [2016] was here adapted to the data and objectives of this dissertation. The processed data were matched with thermodynamic retrievals from the microwave radiometer, and, with the help of the Cloudnet hydrometeor classification product [Illingworth et al., 2007], searched for LLMPC events. Long-term statistics of radar variables recorded during LLMPC events are then performed, and interpreted to gain insights on the relevance of ice-growth processes, and their dependence on cloud parameters, with a focus on temperature, liquid content, and turbulence.

1.3 Thesis overview

This dissertation is structured as follows: Chapter 2 contains a review of topics relevant for the understanding of the studies, the subsequent three chapters include the studies performed within the framework of the dissertation, while results are discussed and conclusions are drawn in Chapter 6. The topics illustrated in Chapter 2 include basic concepts of ice microphysical processes and turbulence, including a summary of the topic of dynamics of heavy particles in turbulence, and finally an overview of the physics behind cloud radar observations, along with an introduction to the main measured quantities.

Chapter 3 includes the first study, **Study 1**, which was published in Chellini et al. [2022]. Here, a 3-year dataset of 94-GHz cloud radar, 24-GHz precipitation radar, as well as temperature profiles, is used to statistically assess the relevance of aggregation in LLMPCs at Ny-Ålesund. The study finds that larger aggregate snowflakes (mass median diameter larger than 1 mm) are predominantly produced in LLMPCs whose mixed-phase layer is at temperatures between -15 and -10°C. This coincides with the temperature regime known for favoring aggregation due to growth and subsequent mechanical entanglement of dendritic crystals. Surprisingly, a lack of a second enhanced aggregation zone close to the 0°C isotherm, typically observed in deeper cloud systems, is found. Moreover, low Doppler velocity values suggest that significant riming of large particles is unlikely at temperatures colder than -5°C.

Chapter 4 includes the second study, **Study 2**, published in Chellini et al. [2023]. The study presents a comprehensive long-term dataset published within the framework of this dissertation, which combines 94-GHz and polarimetric 35-GHz Doppler cloud radar observations, together with temperature profiles, among other variables. The data are accurately calibrated and quality controlled, and novel processing approaches are developed to address artifacts unique to this dataset. All

methods are described in detail in the study, and finally statistics of the temperature dependence of radar variables are presented. The occurrence of processes inferred in **Study 1** is confirmed, and expanded upon, identifying temperature regimes where columnar ice particles, riming, and SIP are likely to take place.

Chapter 5 includes the third study, **Study 3**, which has been submitted to a scientific journal. Here, the dataset presented in **Study 2** is used to assess the effect of turbulence on aggregation and riming in LLMPCs at Ny-Ålesund. 94-GHz Doppler cloud radar observations, together with auxiliary data, are used to retrieve the EDR, and the developed approach is presented. It is shown that higher EDR regimes enhance the aggregation of particles, and are associated with signatures of increased ice particle concentration, possibly caused by fragmentation. In temperature regimes more favorable to riming, turbulence dramatically enhances the particles' fall velocity, denoting higher degrees of riming. An additional analysis to **Study 3** is further presented in Section 5.1, investigating the possible enhancement of ice particle settling velocity by turbulence, although the results are not fully conclusive.

In Chapter 6 results from the three studies are summarized and discussed, conclusions are drawn, and recommendations for future work are presented.

Chapter 2

Theory

This chapter provides an overview of the fundamental concepts needed for a complete understanding of **Study 1**, **Study 2**, and **Study 3**. Section 2.1 introduces cloud microphysical processes, with a focus on ice microphysics, Section 2.2 presents fundamental notions of atmospheric turbulence, and introduces the topic of heavy particle dynamics in turbulence, relevant for **Study 3**. Finally, Section 2.3 illustrates the theoretical basis behind active microwave remote sensing, with a focus on applications to cloud radar observations of frozen hydrometeors.

2.1 Cloud microphysics

The term *cloud microphysics* refers to the branch of cloud physics that studies the processes that determine the formation and evolution of individual cloud condensate particles. Describing the evolution of individual liquid and ice particles involves explaining their growth, decay, interaction, and dynamics. In particular, ice particles may first form either by homogeneous or heterogeneous nucleation (Section 2.1.1), grow by vapor deposition (2.1.2), then gain sufficient mass to sediment (2.1.3). Interactions, and in particular collisions, between particles also play a key role in the evolution of ice particles, as collisions allow for the formation of particles with higher mass, which sediment more efficiently (2.1.4). Ice particles may produce further ice particles via so-called secondary ice production (SIP) processes (2.1.5). A complete description of these processes requires knowledge from a number of physical disciplines, including thermodynamics, kinematics and fluid dynamics.

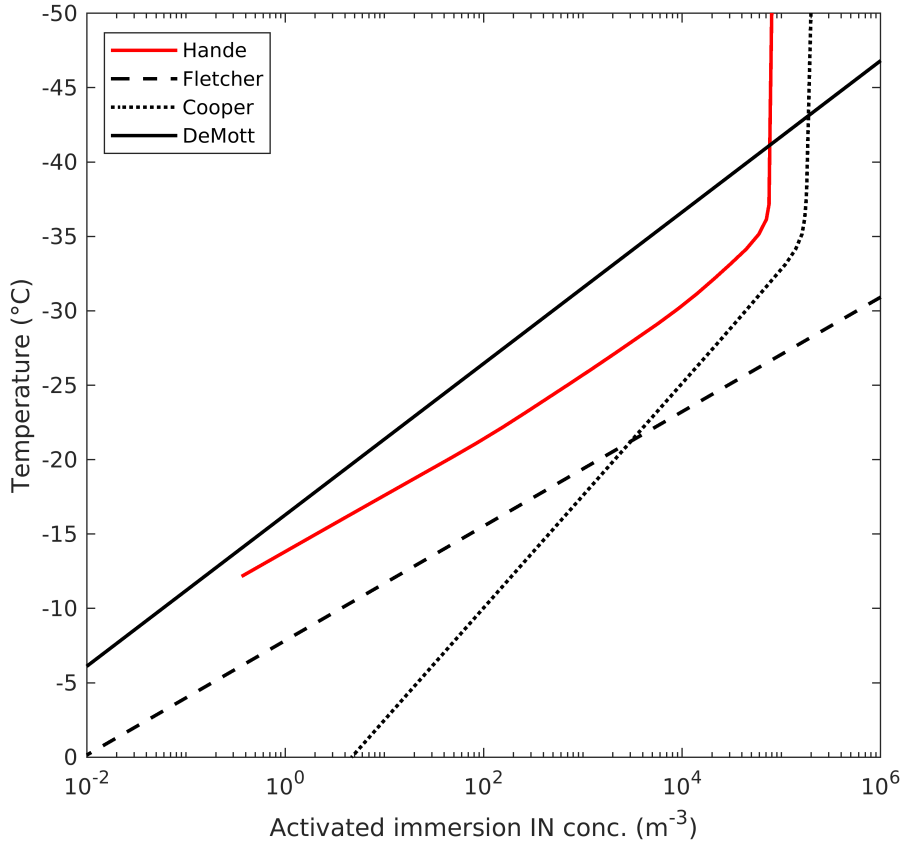

Figure 2.1: Parametrizations for the number concentration of activated immersion ice nuclei (IN) as function of temperature, as proposed by: Hande et al. [2015], Fletcher [1962a], Cooper [1986], and DeMott et al. [2015]. Figure adapted from Hande et al. [2015].

2.1.1 Ice nucleation

Once water vapor saturation with respect to ice has been reached, the initial formation of ice crystals can take place via a number of pathways. They can be classified in first instance based on whether they rely on the presence of aerosol particles (*heterogeneous nucleation*) or not (*homogeneous nucleation*), and based on whether ice is nucleated directly from the vapor phase (*deposition nucleation*), or relies on the freezing of supercooled droplets (*freezing nucleation*) [e.g., Kanji et al., 2017]. Homogeneous deposition nucleation requires extreme temperatures and supersaturations, typically not found in the troposphere, while homogeneous freezing occurs for the most part at temperatures below -38°C [Lohmann et al., 2016, Section 8.1.1]. Therefore at warmer temperatures ice nucleation relies on the presence of aerosol particles which contain either sites or complex molecules which

facilitate the initial formation of the crystalline lattice of ice, and consequently lead either to the freezing of droplets or the deposition of water vapor onto their surface. These particles are typically referred to as *ice nuclei* (IN) or *ice nucleating particles* (INP). A number of particles of varying origin can act as IN, ranging from insoluble solid particles, such as mineral dust, to nanoscale biological fragments, such as marine organic aerosol [Kanji et al., 2017]. INs do not facilitate the nucleation of ice particles at any temperature below 0°C, but become *active* at a specific temperature, which varies with aerosol species, and only allow for the nucleation of ice at temperatures close or colder than the activation temperature. Examples of proposed temperature dependencies of activated IN concentration are shown in Fig. 2.1. It has been shown in recent years that at supercooled temperatures T $\gtrsim$ -25°C ice nucleation takes place for the most part through heterogeneous freezing, and that at these temperatures heterogeneous deposition nucleation is not relevant [Prenni et al., 2009, De Boer et al., 2011, Westbrook and Illingworth, 2011]. Therefore ice nucleation at temperatures warmer than -25°C can, for the most part, only occur in MPCs, and only via liquid-dependent pathways [Westbrook and Illingworth, 2011, Hande and Hoose, 2017]. Heterogeneous freezing can take place via a number of pathways, e.g., due to a supercooled droplet coming into contact with an IN (*contact freezing*), or due to the presence of an inactivated IN in its volume, which is then activated (*immersion freezing*) [e.g., Kanji et al., 2017].

2.1.2 Depositional growth

The initial stages of growth of a newly nucleated ice particle are determined by depositional growth: if saturation with respect to ice is achieved, water molecules in the vapor phase deposit on the ice particle by forming hydrogen bonds and contribute to the growth of the ice crystal lattice. Considering in first instance the simplified scenario of a stationary crystal in stationary air, the rate at which depositional growth takes place is solely determined by molecular diffusion of water molecules in the vapor phase towards the crystal, and transport of the consequently released latent heat away from it. Fick's laws of diffusion [Fick, 1855] can be therefore applied to the diffusion of water vapor and heat in presence of an ice particle to obtain the rate of increase (or decrease in sub-saturated conditions) of the particle's mass [Lamb and Verlinde, 2011, Eq. 8.40]:

$$\frac{dm_p}{dt} = 4\pi C s_i \left[\frac{\overline{R} T_\infty}{M_w D'_v e_i(T_\infty)} + \frac{l_s}{M_w k'_T T_\infty} \left(\frac{l_s}{\overline{R} T_\infty} - 1 \right) \right]^{-1}, \tag{2.1}$$

where C is a particle-specific constant named *capacitance*, s_i is the supersaturation with respect to ice, $\overline{R}$ is the universal gas constant, T_∞ is the air temperature at a large distance from the crystal, l_s is the latent heat of sublimation of water per

unit mass, M_w is the molecular weight of water, D'_v is the diffusivity of water vapor in air, and k'_T is the heat conductivity of air. In Eq. 2.1 the terms in the square bracket are thermodynamic terms, the first related to latent heat release and heat diffusion, and the second related to vapor diffusion. The capacitance C for particles belonging to a given habit can be approximated as [Westbrook et al., 2008]:

$$C = f(\alpha) \cdot a, \tag{2.2}$$

and is therefore only a function of particle size a, defined as half the maximum span across the basal crystal face, and of the aspect ratio α, defined, in the case of an ice crystal, as the ratio between the maximum span across the basal crystal face, and the span of the crystal along the direction perpendicular to the basal face. Westbrook et al. [2008] showed that for ice aggregates C reaches the asymptotic value of 0.25-0.28.

The depositional growth rate in Eq. 2.1 displays a wide range of magnitudes: e.g., Takahashi et al. [1991] have shown in a laboratory study that at liquid water saturation individual crystals grown for 15 minutes at varying temperatures reach masses of $5 \cdot 10^{-7}$ g at -2°C, 10^{-6} g at -8°C and 10^{-5} g at -15°C and decrease back to 10^{-6} g at -20°C. At liquid water saturation a peak in depositional growth is observed between -13 and -15°C [Takahashi, 2014], which is closely linked with the maximum in the difference between liquid and ice saturation vapor pressures observed at -12°C [e.g., Murphy and Koop, 2005]. Depositional growth rate and saturation pressure difference are respectively displayed in Fig. 2.2c and Fig. 2.2a. This is especially relevant in mixed-phase clouds, where saturation with respect to liquid is reached, and will be a central topic of **Study 1**. In addition to growth rate, ice particles grow according to different habits depending on temperature and ice supersaturation: the temperature region between -10 and -20°C is characterized by the growth of plate-like particles, and in particular dendrites, stellar particles and sectored plates at water saturation, while the temperature regime between -10 and -8°C is characterized by isometric particles, and at temperatures warmer than -8°C columnar particles are found, which may grow into needles at high supersaturations [e.g., Bailey and Hallett, 2009]. The dependence of the aspect ratio of ice particles grown at water saturation on temperature is displayed in Fig. 2.2b.

The depositional growth rate in Eq. 2.1 applies under the assumption of a stationary crystal in still air. If the crystal is sedimenting, the transport of vapor towards the crystal and of latent heat away from the crystal is facilitated by the relative motion between air and the crystal itself. This effect is typically quantified via a *ventilation factor* $\overline{f}_v$, which multiplies the right-hand side of Eq. 2.1 [Pruppacher and Klett, 2012, Sec. 13.3.2]. The ventilation factor is typically expressed as function of the particle's Reynolds number Re_p, and typically takes on values between 1 and 2 [e.g., Pitter et al., 1974], with $\overline{f}_v = 1$ in the case of a

stationary crystal in still air, and maximum values reaching up to $\overline{f}_v \sim 4$, in the case of broad-branch and plate crystals at $Re_p \sim 100$ [Ji and Wang, 1999].

2.1.3 Sedimentation

Cloud particles are subject to the gravitational force, and as such tend to sediment towards the ground. Small particles might have negligible sedimentation velocities, such as liquid droplets smaller than 30 µm [Lohmann et al., 2016, Sec. 7.2.3], and might be prevented from sedimenting by updrafts. At the same time, large snow particles may reach sedimentation velocities of 1 to 1.5 m s^{-1}, while graupel particles may reach velocities up to 3 m s^{-1} [e.g., Locatelli and Hobbs, 1974]. In still air, the sedimentation velocity of particles is close to the theoretical terminal velocity, computed by balancing the two forces acting on the particle, gravity and drag. The topic of particles sedimenting in non-still air will be briefly addressed in Section 2.2.3.

A particle sedimenting in still air is subject to the forces of gravity and drag, which, respectively, take on the form:

$$F_{grav} = m_p g, \tag{2.3a}$$

$$F_{drag} = \frac{1}{2}\rho_a \mathcal{A} v_T^2 C_D(Re_p), \tag{2.3b}$$

where the air density ρ_a in turn varies with temperature, pressure, and humidity. In Eq. 2.3a g is the gravitational acceleration, while in Eq. 2.3b $\mathcal{A}$ is the particle's cross-sectional area perpendicular to the direction of gravity, v_T its terminal velocity, C_D is the drag coefficient, which is only function of the particle's Reynolds number Re_p [Pruppacher and Klett, 2012, Sec. 10.2.2.2]. The drag coefficient C_D can be obtained analytically only under very restrictive assumptions, and is typically investigated experimentally or numerically. It is anyways instructive to look at the behaviour of $C_D(Re_p)$ in the limits of small particle Reynolds numbers ($Re_p << 1$, Stokes drag) and large particle Reynolds numbers ($Re_p >> 1$, Newtonian drag), in fact [e.g., Böhm, 1992]:

$$C_D(Re_p << 1) \propto Re_p^{-1}, \tag{2.4a}$$

$$C_D(Re_p >> 1) \propto 1. \tag{2.4b}$$

Following Karrer et al. [2020] the latter dependencies can be combined with the coefficients of mass-size and area-size relations for specific classes of ice particles, as well as Eq. 2.3, to obtain:

$$v_T(Re_p << 1) \propto D_{max}^{b_m - 0.5 - 0.25 \cdot b_A} \overset{dendrite}{\sim} D_{max}^{1.3}, \tag{2.5a}$$

$$v_T(Re_p >> 1) \propto D_{max}^{0.5 \cdot (b_m - 1.5 - 0.25 \cdot b_A)} \overset{dend.aggr.}{\sim} D_{max}^{0.1}, \tag{2.5b}$$

where D_{max} is the maximum dimension of the ice particle, and on the right-hand side the exponents of the mass-size and area-size relations b_m and b_A were replaced with the values reported for dendrites and dendrite aggregates by Karrer et al. [2020]. Eq. 2.5a shows that the increase in terminal velocity with size at small Re_p (i.e., at small D_{max}) is close to linear. As particle size increases, the increase of v_T with size slows down, and in the large Re_p limit further increases of terminal velocity with size are marginal (Eq. 2.5b).

Under the assumption of a rigid spherical particle in a Stokes flow (i.e., $Re_p << 1$), the drag coefficient can be computed analytically, and Eq. 2.3b takes on the form [Pruppacher and Klett, 2012, Eq. 10.40]:

$$F_{drag} = 6\pi a \rho_a \nu v_T, \tag{2.6}$$

where ν is air kinematic viscosity, and a is the particle's radius. For a sphere in a Stokes flow, the terminal velocity can be easily computed by equating the latter equation with the gravitational force in Eq. 2.3a:

$$v_T = \frac{m_p g}{6\pi a \nu \rho_a} = \underbrace{\left(\frac{2}{9}\frac{a^2}{\nu}\frac{\rho_p}{\rho_a}\right)}_{\tau_p} g. \tag{2.7}$$

The content of the parentheses on the right-hand side of Eq. 2.7 is typically referred to as the *relaxation time* of the particle τ_p, and will come in handy when studying the dynamics of particles in a turbulent flow in Section 2.2.3. With the definition of τ_p the terminal velocity can be simply expressed as $v_T = \tau_p g$.

2.1.4 Collisional growth

As depositional growth takes place, particles grow in size and their terminal velocity increases. The development of relative velocities between particles then allows for collisions between hydrometeors, which in turn lead to the formation of larger particles. Collisions between ice particles leading to the formation of larger ice particles are typically referred to as *aggregation*, and collisions between ice particles and supercooled liquid droplets are typically referred to as *riming*. Aggregation leads to the formation of *aggregates*, while riming leads to the formation of *rimed particles*, or, in the case of higher degrees of riming, *graupel*. Aggregation and riming are the dominant processes leading to precipitation formation in cold clouds [Lohmann et al., 2016, Ch. 8].

Ice-ice collisions: aggregation

An ice particle population can be described by a distribution $n(m,t)$: $n(m,t)dm$ represents the number of particles at a given time t with mass in the range m

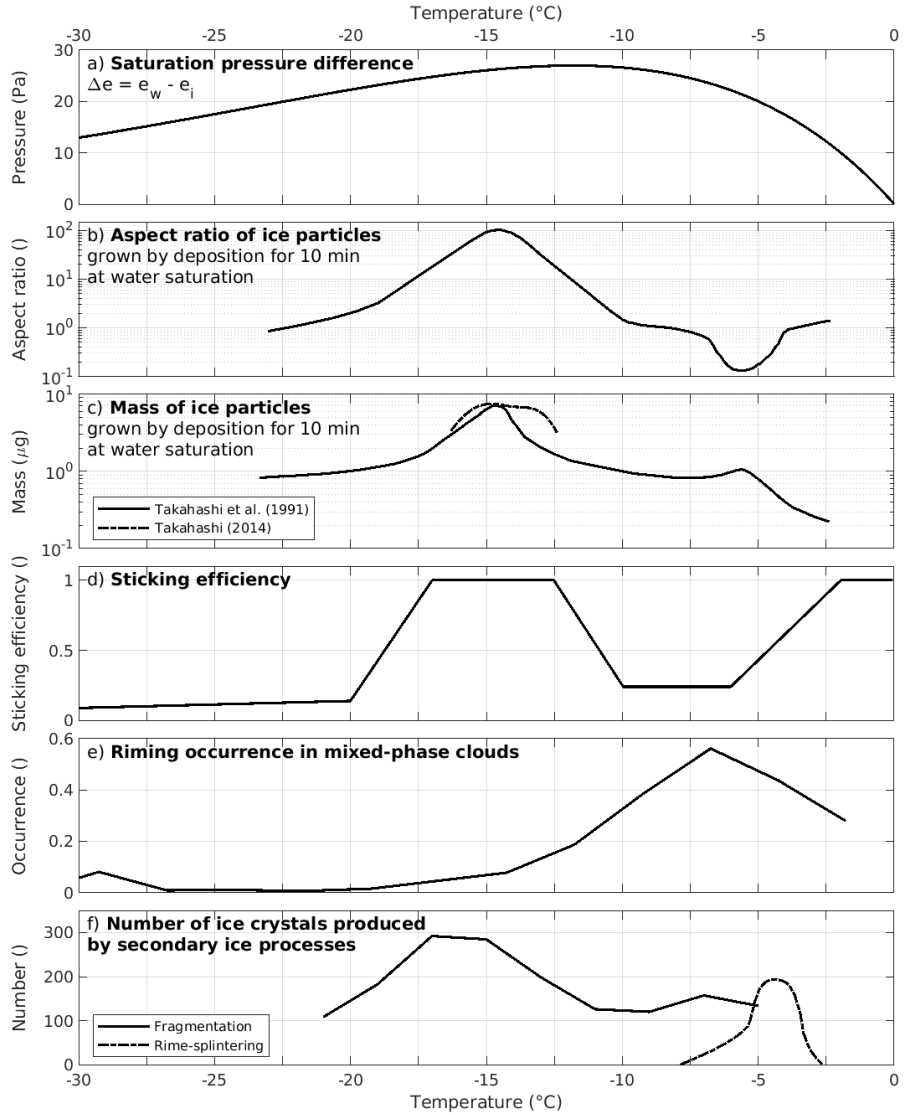

Figure 2.2: Temperature dependence of a number of quantities related to ice microphysics. Panel a displays the difference between water and ice saturation pressures, computed with Eq. 7 and 10 in Murphy and Koop [2005]. Panels b and c display, respectively, the aspect ratio and mass of ice particles grown in a laboratory environment by depositional growth at water saturation for 10 minutes, based on the results by Takahashi et al. [1991] and Takahashi [2014]. Panel d includes the sticking efficiency parametrization proposed by Karrer et al. [2021]. Panel e displays the frequency of occurrence of rimed particles in mixed-phase clouds, based on in-situ airborne observations, adapted from Waitz et al. [2022]. Lastly, panel e reports the number of ice crystals produced by collisional fragmentation and rime-splintering. The collisional fragmentation curve was computed based on the results reported in Takahashi et al. [1995], averaged in 2°C-wide bins. The rime-splintering curve is based on the results by Heymsfield and Mossop [1984], who measured the number of splinters associated with an increase in particle mass of 1 milligram due to riming, in a laboratory study.

to $m + dm$. An aggregation event between two particles of masses m_i and m_j, occurring over a time interval δt will lead to a change in $n(m, t)$:

$$n(m_i + m_j, t + \delta t)dm = n(m_i + m_j, t)dm + 1, \tag{2.8a}$$

$$n(m_i, t + \delta t)dm = n(m_i, t)dm - 1, \tag{2.8b}$$

$$n(m_j, t + \delta t)dm = n(m_j, t)dm - 1. \tag{2.8c}$$

Hence the aggregation process conserves the total mass of the particle population. The same concept can be generalized to the whole particle population by introducing an *aggregation kernel* $K_{agg}(m_i, m_j)$, which represents the probability of particles m_i and m_j to collide and stick to generate an aggregate. $K_{agg}(m_i, m_j)$ needs to be estimated for any particle couple in the particle population, and it can be expressed in the form [Karrer et al., 2021]:

$$K_{agg}(m_i, m_j) = \left(\mathcal{A}(m_i)^{0.5} + \mathcal{A}(m_j)^{0.5}\right)^2 |v(m_i) - v(m_j)|\, E_{coll}(m_i, m_j)\, E_{stick}(T), \tag{2.9}$$

where $\mathcal{A}(m)$ and $v(m)$ are the geometric cross section and velocity of particle m, while $E_{coll}(m_i, m_j)$ and $E_{stick}(T)$ are respectively the *collection efficiency* and the *sticking efficiency*, and both are ≤ 1. The collection and sticking efficiencies reduce the aggregation kernel obtained by purely geometrical considerations (i.e., only the cross section and velocity terms in Eq. 2.9), since small particles might follow the flow's streamlines around large particles (hence $E_{coll}(m_i, m_j) \leq 1$), or particles might collide but not stick to form an aggregate (hence $E_{stick}(T) \leq 1$). The sticking efficiency $E_{stick}(T)$ is for the most part only dependent on temperature.

The introduction of the aggregation kernel allows for the formulation of a general expression for the aggregation process, named the *stochastic collection equation* [e.g., Pruppacher and Klett, 2012, Khain et al., 2015, Karrer et al., 2021]:

$$\begin{aligned}\left.\frac{\partial n(m_i, t)}{\partial t}\right|_{agg} = \frac{1}{2}\int_0^{m_i} K_{agg}(m_i - m_j, m_j)n(m_j, t)n(m_i - m_j, t)dm_j \\ - \int_0^{\infty} K_{agg}(m_i, m_j)n(m_i, t)n(m_j, t)dm_j\end{aligned} \tag{2.10}$$

The first term on the right-hand side of 2.10 is equivalent to 2.8a, as it increases $n(m_i, t)$, while the second term is equivalent to 2.8b and 2.8c.

One of the main terms driving or inhibiting aggregation is the sticking efficiency $E_{stick}(T)$, which, upon collision, determines the probability that the two particles stick together. Two temperature regions that particularly favor aggregation are the dendritic growth zone (DGZ) between -20 and -10°C [Mitchell, 1988, Connolly et al., 2012, Karrer et al., 2021] and the region close to 0°C [Lin et al., 1983, Cotton et al., 1986, Karrer et al., 2021]. In the DGZ the dendrites' ability to

mechanically entangle their branches increases $E_{stick}(T)$, and together with their large cross-sectional area, favors a rapid formation of aggregates [Connolly et al., 2012, Pruppacher and Klett, 2012, Sec. 14.7]. Close to the melting level the presence of a quasi-liquid layer on the ice particles [Fletcher, 1962b, Fabry and Zawadzki, 1995, Slater and Michaelides, 2019] is thought to also lead to an increase in $E_{stick}(T)$ and favor intense aggregation [Fabry and Zawadzki, 1995]. Recently, Karrer et al. [2021] proposed a parametrization of the sticking efficiency which takes into account these two enhanced aggregation regions, and is shown in Fig. 2.2d.

A number of studies have suggested that aggregation between ice crystals might be further facilitated by electrostatic forces [Latham and Saunders, 1970, Saunders and Wahab, 1975, Connolly et al., 2005, Stith et al., 2014, Korolev et al., 2020]. This process has been however poorly studied, and robust evidence of its occurrence, and an accurate theoretical explanation are missing. This is mainly attributable to the current lack of instrumentation capable of systematically observing this process [Morrison et al., 2020].

Ice-liquid collisions: riming

Riming may be described in a similar fashion to the stochastic collection equation introduced for aggregation in Eq. 2.10, by expanding said equation to a system of two equations describing the reduction in the number of liquid droplets $n_{liq}(m,t)$ and the increase in mass of ice particles $n_{ice}(m,t)$. Note that the integral of $n_{ice}(m,t)$ is conserved by riming, as the number of ice particles does not change. Under the realistic assumption of a high number of collisions between a single ice crystal and liquid droplets, a simpler yet equally effective treatment of the problem may be achieved by formulating the *continuous growth equation* [Lohmann et al., 2016, Eq. 8.13]:

$$\frac{dm_i}{dt} = \widetilde{E}_{coll}(m_i)\mathcal{A}(m_i)v(m_i)\,\mathrm{LWC}, \tag{2.11}$$

where it is assumed that the velocity of supercooled droplets is negligible, and droplets are treated as a continuum, with the mass of supercooled liquid per unit volume given via the *liquid water content* (LWC). The collection efficiency $\widetilde{E}_{coll}(m_i)$ associated with the ice particle m_i is averaged across the droplet population [Lohmann et al., 2016, Sec. 8.3.3.2]. Note that the sticking efficiency $\widetilde{E}_{stick}(m_i)$ is not included in Eq. 2.11, as supercooled droplets rapidly freeze upon impact with an ice crystal, effectively rendering $\widetilde{E}_{stick}(m_i) = 1$ [Lamb and Verlinde, 2011, Sec. 9.4].

The collection efficiency $\widetilde{E}_{coll}(m_i)$ displays a dramatic dependence on the ice particle's Reynolds number Re_p, which leads to the introduction of a *riming cutoff*. Ice particles with size below the cutoff have effectively $\widetilde{E}_{coll}(m_i) \sim 0$, as droplets

will follow the flow streamlines around the particle. The riming cutoff depends on particle habit, and has been estimated to be 35 µm for columnar ice crystals, 110 µm for hexagonal plates, and 200 µm for broad-branch crystals (similar to stellar or sectored plates) [Wang and Ji, 2000].

Riming has been reported to occur, for the most part, at temperatures close to or warmer than -10°C, when accounting for all ice cloud types, with a frequency of occurrence increasing with temperature, reaching a maximum of 6 to 13% close to 0°C [Kneifel and Moisseev, 2020]. Recently Waitz et al. [2022] studied the occurrence of riming in mixed-phase clouds, based on in-situ airborne observations, reporting its occurrence at temperatures as cold as -30°C. They reported a frequency of occurrence higher than 10% only at temperatures warmer than -15°C, with a maximum close to 60% found at -7°C (see Fig. 2.2e).

2.1.5 Secondary ice production

In addition to the ice nucleation pathways illustrated in Section 2.1.1, the number concentration of ice particles may be increased by a number of processes collectively referred to as *secondary ice production* (SIP). Under a wide spectrum of conditions the number concentration of ice particles has been in fact reported to be more than an order of magnitude higher than the number concentration of INs [Crawford et al., 2012, Crosier et al., 2011, Henneberger et al., 2013, Heymsfield and Willis, 2014, Lawson et al., 2017]. The recent comprehensive review work by Korolev and Leisner [2020] identified six main SIP processes: ejection of splinters by freezing droplets during riming (typically referred to as *rime-splintering*), droplet shattering during freezing (*droplet shattering*), fragmentation due to ice–ice collision (henceforth simply *collisional fragmentation*), ice particle fragmentation due to thermal shock during riming, fragmentation of sublimating ice, and activation of ice-nucleating particles in transient supersaturation around freezing drops. Only the first three processes will be here illustrated, as their role in cloud microphysics has been demonstrated by a high number of studies [e.g., Rangno, 2008, Lasher-Trapp et al., 2016, Lawson et al., 2017, Phillips et al., 2018, Luke et al., 2021, Georgakaki et al., 2022].

Rime-splintering may occur during the riming process, as droplets collide with ice crystals and freeze. Droplets freeze from the surface towards the inside, and as the inner regions of the droplet freeze, pressure builds up, leading to bursting of the frozen surface and the ejection of splinters [Heymsfield and Mossop, 1984]. Rime-splintering requires specific conditions to take place, in particular temperatures between -3 and -8°C, and the presence of droplets with diameters both smaller than 13 µm, and larger than 24 µm [Hallett and Mossop, 1974, Mossop, 1976, 1978, Choularton et al., 1980]. The number of ice crystals produced by rime-splintering, associated with an increase of particle mass of 1 mg by riming, as reported in

the laboratory study by Heymsfield and Mossop [1984] is displayed in Fig. 2.2f. Rime-splintering is also referred to as *Hallett-Mossop process*, after Hallett and Mossop [1974] who first determined the conditions required for its occurrence, and reproduced it in a laboratory.

In contrast with rime-splintering, droplet shattering has been observed to occur under a wide spectrum of temperatures, ranging from -30 to -5°C [e.g., Lauber et al., 2018]. Droplet shattering involves the freezing of a droplet, and the subsequent ejection of splinters or larger fragments. It has been reported to occur in the case of droplets with diameters larger than 100 µm [Korolev et al., 2004, Lauber et al., 2018, Wildeman et al., 2017]. Freezing typically occurs heterogeneously at temperatures warmer than -38°C, hence at least one IN is required for each droplet shattering event. A number of studies have suggested that droplet shattering may be the dominant SIP process in MPCs [e.g., Rangno, 2008, Lauber et al., 2018].

Collisional fragmentation may occur upon collision between ice particles, as such it is closely linked with aggregation. It has been reported by a number of laboratory and field studies [e.g., Jiusto and Weickmann, 1973, Takahashi, 1993, Takahashi et al., 1995, Schwarzenboeck et al., 2009], and has been suggested to be especially relevant in the collisions of stellar and dendritic particles, due to their fragile structure [Rangno and Hobbs, 2001, Schwarzenboeck et al., 2009, von Terzi et al., 2022, Pasquier et al., 2022]. Moreover, Takahashi et al. [1995] measured the number of fragments produced by graupel-graupel collisions in a laboratory study, and reported a maximum at temperatures between -18 and -14°C, in part compatible with dendritic growth. Their results are displayed in Fig. 2.2f. Grzegorczyk et al. [2023] confirmed and expanded upon the results by Takahashi et al. [1995], investigating the production of fragments in a laboratory study at -15°C. They reported the formation of 150 to 600 fragments for a graupel-graupel collision, with a large portion of fragments with maximum size close to 75 µm, and 70 to 500 fragments for a graupel-dendrite collision, with half of the collisions producing fragments with a bimodal size distribution, with maxima close to 400 µm and 50 µm. Recently Georgakaki et al. [2022] suggested that high rates of collisional fragmentation may be achieved under conditions which favor intense aggregation, and reported that collisional fragmentation can increase the ice number concentration by up to three orders of magnitude.

2.2 Notions of turbulence

Most flows occurring in the atmospheric boundary layer are turbulent, and a number of cloud types, including LLMPCs, are inherently turbulent phenomena [Morrison et al., 2012, Barrett et al., 2020]. Turbulence can be thought of as consisting of irregular swirls of motion, termed *eddies*, superimposed on a mean

wind [Stull, 1988, Sec. 1.3]. As Tennekes and Lumley [1972] state, precisely defining turbulence presents a significant challenge, instead, one can outline the characteristics commonly found in turbulent flows. Among other characteristics, they list: irregularity, or randomness, three dimensional vorticity fluctuations, and dissipation, as turbulent flows always dissipate energy in the form of heat. Irregularity in particular doesn't allow for a deterministic description of turbulence, and statistical methods are the only viable approach [Tennekes and Lumley, 1972, Ch. 1].

2.2.1 Turbulent kinetic energy

Taylor [1938] first proposed that the treatment of turbulence can be simplified by assuming it to be frozen; i.e., that advection doesn't change the statistical characteristics of a turbulent flow. This assumption is nowadays known as *Taylor's frozen turbulence hypothesis*, and is useful in cases when eddies evolve on time scales much longer than the time needed for the flow to advect the eddies past the sensor [Powell and Elderkin, 1974].

Air velocity can be decomposed as the sum of the velocity of a mean flow, and the velocity of the turbulent fluctuations:

$$\mathbf{u} = \begin{pmatrix} u_x \\ u_y \\ u_z \end{pmatrix} = \begin{pmatrix} \overline{u_x} + u'_x \\ \overline{u_y} + u'_y \\ \overline{u_z} + u'_z \end{pmatrix} = \overline{\mathbf{u}} + \mathbf{u}', \tag{2.12}$$

where $\mathbf{u}$ is the air velocity in vector form, and u_x, u_y, and u_z its orthogonal components, with u_z along the vertical direction. $\overline{\mathbf{u}}$ and $\mathbf{u}'$ indicate, respectively, the mean wind and the turbulent fluctuations [Stull, 1988, Sec. 2.2, 2.3, 2.4].

The decomposition presented in Eq. 2.12 further allows to decompose the total kinetic energy (KE) of the flow into a mean kinetic energy (MKE), and a turbulent kinetic energy (TKE) [Stull, 1988, Sec. 2.5]:

$$\overline{\mathrm{KE}} = \frac{1}{2}\overline{\mathbf{u}^2} = \frac{1}{2}\overline{\mathbf{u}}^2 + \frac{1}{2}\overline{\mathbf{u}'^2} = \mathrm{MKE} + \mathrm{TKE}. \tag{2.13}$$

The so-defined TKE is therefore the mean kinetic energy (per unit mass of air) associated with the turbulent fluctuations in the averaging window.

The evolution of the TKE is described by the TKE budget equation [Stull, 1988, Eq. 5.1a]:

$$\underbrace{\frac{\partial \mathrm{TKE}}{\partial t}}_{I} + \underbrace{\overline{u_j}\frac{\partial \mathrm{TKE}}{\partial x_j}}_{II} = \underbrace{-\frac{1}{2}\frac{\partial \overline{u'_j u'^2_i}}{\partial x_j}}_{III} + \underbrace{\frac{g_i}{\overline{\theta_v}}\left(\overline{u'_i \theta'_v}\right)}_{IV} \underbrace{-\overline{u'_i u'_j}\frac{\partial \overline{u_i}}{\partial x_j}}_{V} \underbrace{-\frac{1}{\overline{\rho_a}}\frac{\partial\left(\overline{u'_i p'}\right)}{\partial x_i}}_{VI} - \underbrace{\varepsilon}_{VII}, \tag{2.14}$$

where Einstein's summation notation is adopted, and the fluid is treated following the Eulerian approach. The derivation of Eq. 2.14 can be found in e.g., Stull [1988, Sec. 4.1, 4.3, 5.1]. On the left-hand side of Eq. 2.14, term I is the temporal variation of TKE in the studied Eulerian volume, while term II describes the advection of TKE by the mean wind. Term III quantifies the turbulent transport of TKE, as TKE$= 0.5\overline{u_i'^2}$ under the summation notation. Term IV describes the production or consumption of TKE due to buoyancy: θ_v in fact represents the virtual potential temperature, and g_i is the gravitational acceleration in vector form. This term is the main driver of turbulence production in the LLMPCs here studied. Increasing radiative cooling with height in fact causes this term (and in particular its vertical component) to be positive, contributing to an increase in TKE [Deardorff, 1981]. Term V describes mechanical TKE production or loss due to shear in the mean wind, described by the partial derivatives of the components of $\overline{\mathbf{u}}$. Term VI describes the redistribution of TKE due to pressure perturbations. Finally, term VII, is the so-called *eddy dissipation rate* (EDR), which is a sink term quantifying the dissipation of kinetic energy into heat by viscous forces [Stull, 1988, Sec. 5.1, 5.2].

2.2.2 The energy cascade and eddy dissipation rate

Turbulent flows dissipate kinetic energy by transferring it to eddies of decreasing size, until at the smallest scales of the flow viscosity converts kinetic energy into heat. This concept, named *energy cascade*, was first suggested by Richardson [1922], and then theoretically expanded by Kolmogorov [1941a,b]. Although eddies cannot be precisely defined, they can be conceived as turbulent motions which display at least moderate coherence over a region of size ℓ. In turbulent flows at sufficiently high Reynolds number, eddies are typically classified into two groups based on their size: the energy-containing range, and the universal equilibrium range. Kolmogorov's hypothesis of local isotropy states that small-scale turbulent motions are statistically isotropic: it follows that the demarcation size ℓ_{EI} between the two ranges can be defined in such a way that eddies belonging to the universal equilibrium range are isotropic. Larger anisotropic eddies are named energy-containing, as it can be shown that the bulk of TKE is contained in this size range. The concept of energy cascade frames the energy dissipation as a sequence of processes that pass on kinetic energy to smaller and smaller isotropic eddies. As such the rate at which energy is dissipated, i.e., the EDR, is determined by the first processes in the sequence. These first processes occur at the interface between the energy containing range, and the universal equilibrium range, and determine the magnitude of the EDR [Pope, 2000, Sec. 6.1].

Kolmogorov, via his similarity hypotheses [Kolmogorov, 1941b], suggested that the universal equilibrium range can be further subdivided into two eddy size ranges:

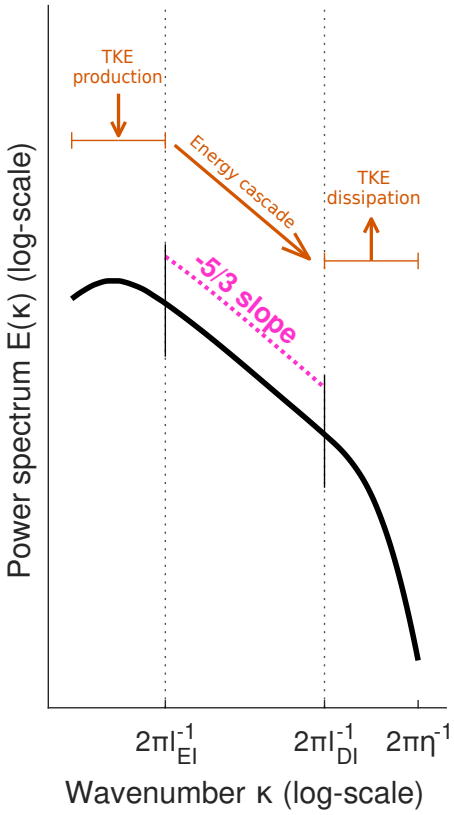

Figure 2.3: Diagram illustrating the main concepts behind the structure of the energy spectrum E(κ), and its subdivision into energy-containing range ($\kappa < 2\pi\ell_{EI}^{-1}$), the inertial subrange ($2\pi\ell_{EI}^{-1} < \kappa < 2\pi\ell_{DI}^{-1}$), and the dissipation range ($2\pi\ell_{DI}^{-1} < \kappa < 2\pi\eta^{-1}$). Figure produced based on figures 6.1, 6.2, 6.11, and 6.12 in Pope [2000].

the inertial subrange, and the dissipation range. In the inertial subrange viscous forces are still negligible, and statistics of motions in this range depend solely on the EDR ε. The dissipation range contains the smallest eddies, and the dissipation of kinetic energy into heat takes place at these scales. Here viscous forces are relevant, and statistics of motions depend on ε and kinematic viscosity ν. Via simple dimensional consideration it can be shown that, in the inertial subrange, the energy spectrum takes on the universal form [Pope, 2000, Sec. 6.1, 6.5]:

$$E(\kappa) = \alpha_K \varepsilon^{2/3} \kappa^{-5/3}, \tag{2.15}$$

where α_K is a universal constant, typically referred to as Kolmogorov constant, with $\alpha_K \sim 0.5$ [e.g., Sreenivasan, 1995], and $\kappa = 2\pi\ell^{-1}$ is the wavenumber. Eq. 2.15 is fundamental to several approaches for the estimation of the EDR from lidar and radar observations [e.g., Rogers and Tripp, 1964, Bouniol et al., 2004, O'Connor

et al., 2005, Borque et al., 2016], including the approach used in this dissertation, and described in Section 2.3.6. The dependence of the energy spectrum in Eq. 2.15 on ε alone in fact allows for a straightforward determination of ε from the variance of a velocity time series. This is not as simple in the energy containing range and in the dissipation range, due to anisotropy in the former, and the additional dependence on viscosity in the latter.

In the dissipation range dimensional analysis allows for the characterization of the characteristic scales of the motion, named Kolmogorov microscales:

$$\eta = \nu^{3/4}\varepsilon^{-1/4}, \tag{2.16a}$$

$$\tau_\eta = \nu^{1/2}\varepsilon^{-1/2}, \tag{2.16b}$$

$$u_\eta = \nu^{1/4}\varepsilon^{1/4}. \tag{2.16c}$$

So-defined η, τ_η, and u_η are, respectively, the Kolmogorov length scale, time scale, and velocity scale. The demarcation ℓ_{DI} between the inertial and dissipation subranges can now be defined, and needs to satisfy $\ell_{DI} >> \eta$ [Pope, 2000, Sec. 6.1]. The concepts illustrated in the current section are summarized in the diagram in Figure 2.3.

2.2.3 Heavy particle dynamics in turbulence

The dynamics of particles suspended in a turbulent flow are significantly altered by the turbulent flow itself. Although this is still a developing field, especially in terms of applications to cloud microphysics, a number of processes that lead turbulent flows to increase collision rates between suspended particles [Pumir and Wilkinson, 2016, Sheikh et al., 2022], and enhance their settling velocity [Maxey, 1987, Wang and Maxey, 1993, Siewert et al., 2014] have been identified.

Turbulence and collision rates

While the traditional theory of hydrometeor collisional growth, as illustrated in Section 2.1.4, relies solely on gravity-induced differential settling velocities, and is hence a one-dimensional process (i.e., can only occur along the vertical direction), turbulence can further produce collisions in the horizontal plane, in addition to enhancing collision rates along the vertical [Pumir and Wilkinson, 2016]. Turbulence enhances the collision rates via different processes depending on the inertia of the particles in relation to the inertia of the fluid. The inertia of a particle can be quantified via its relaxation time τ_p. The particle's relaxation time is the time constant in the exponential decay of the particle velocity due to drag, it hence quantifies the time a particle needs to reach terminal velocity in still air, or to adjust its velocity to changing background air velocity. In the case of a spherical

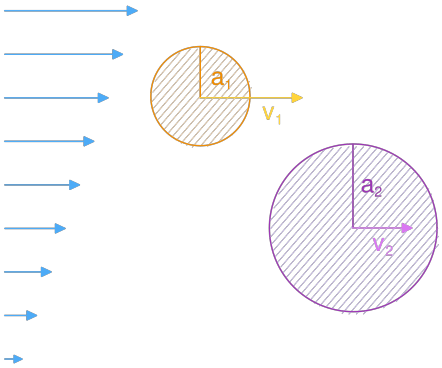

Figure 2.4: Diagram illustrating the Saffman-Turner mechanism under the simplified scenario of a locally sheared flow. Blue arrows indicate air velocity, while a_i and v_i indicate, respectively, the radius and velocity of the i-th particle. Figure produced based on figures 4b and 5 in Pumir and Wilkinson [2016].

particle, with density much larger than air density, and subject to Stokes drag, τ_p takes on the form (see Eq. 2.7; and additionally Maxey and Riley [1983], Pumir and Wilkinson [2016]):

$$\tau_p = \frac{2}{9}\frac{a^2}{\nu}\frac{\rho_p}{\rho_a}, \tag{2.17}$$

where a is the particle's radius, and ρ_p and ρ_a are, respectively, the density of the particle, and of air. For particles smaller than the Kolmogorov length scale η, the inertia of the fluid can be quantified via the Kolmogorov time scale τ_η [Wang and Maxey, 1993, Aliseda et al., 2002]. Therefore, an adimensional quantity relating the two time scales can be defined:

$$St = \frac{\tau_p}{\tau_\eta} = \frac{1}{18}\frac{\rho_p}{\rho_a}\left(\frac{2a}{\eta}\right)^2. \tag{2.18}$$

This is the so-called *Stokes number* [Pumir and Wilkinson, 2016]. The right-hand side of Eq. 2.18 illustrates the dependence of this quantity on the flow and particle characteristics: it scales linearly with particle density ρ_p, quadratically with particle diameter $2a$, it's inversely proportional to air density ρ_a and to the squared size of the smallest eddies η.

Under the condition that $St << 1$, particle inertia is negligible, and particles act as tracers for the air motion [Stout et al., 1995]. When this condition is satisfied collision rates are enhanced via the *Saffman-Turner mechanism*, named after the seminal work by Saffman and Turner [1956]. They derived an analytical expression for the collision rate within a bidisperse particle population in a turbulent flow, under the assumption that both particle types closely follow the flow. Here, collisions are only caused by gradients in the fluid velocity field. A diagram illustrating this

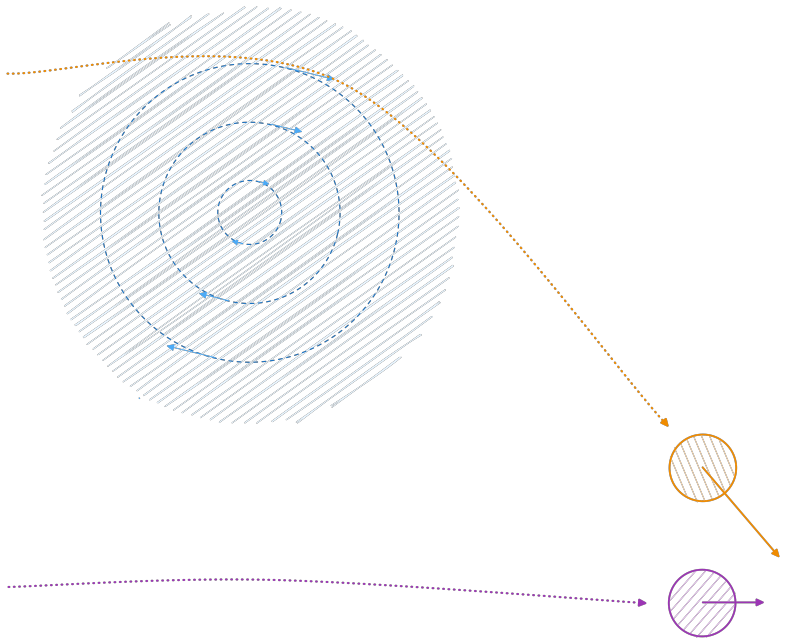

Figure 2.5: Diagram illustrating the sling effect. Arrows indicate air (blue) and particle (purple, orange) velocities, while dotted lines indicate particle trajectories, and dashed lines indicate flow streamlines associated with idealized eddies. Figure produced based on Fig. 1 in Falkovich and Pumir [2007].

mechanism is given in Fig. 2.4. The expression for the number of collisions per unit time and unit volume in presence of the Saffman-Turner mechanism alone, $\mathcal{N}_{S-T}$, takes on the form [Saffman and Turner, 1956]:

$$\mathcal{N}_{S-T} = \left(\frac{8\pi}{15}\right)^{1/2} \frac{n_1' n_2' (a_1 + a_2)^3}{\tau_\eta}, \tag{2.19}$$

where n_i' and a_i indicate the number concentration and radius of the two particle types. Eq. 2.19 indicates that the collision rate is proportional to $\varepsilon^{1/2}$.

When particles grow to large enough sizes that their inertia is no longer negligible, namely $St \gtrsim 0.1$, collision rates are further enhanced by two additional processes: clustering in regions of the flow with low vorticity, henceforth referred to simply as *clustering* [Maxey, 1987, Saw et al., 2008], and favored crossing between particle trajectories, due to them being spun out of eddies by centrifugal forces; this phenomenon is termed *sling effect* [Falkovich et al., 2002], and is illustrated in the diagram in Fig. 2.5. These two processes will be here illustrated following the simplified analytical treatment by Pumir and Wilkinson [2016], who obtained relations for a monodisperse particle population. The same processes have been

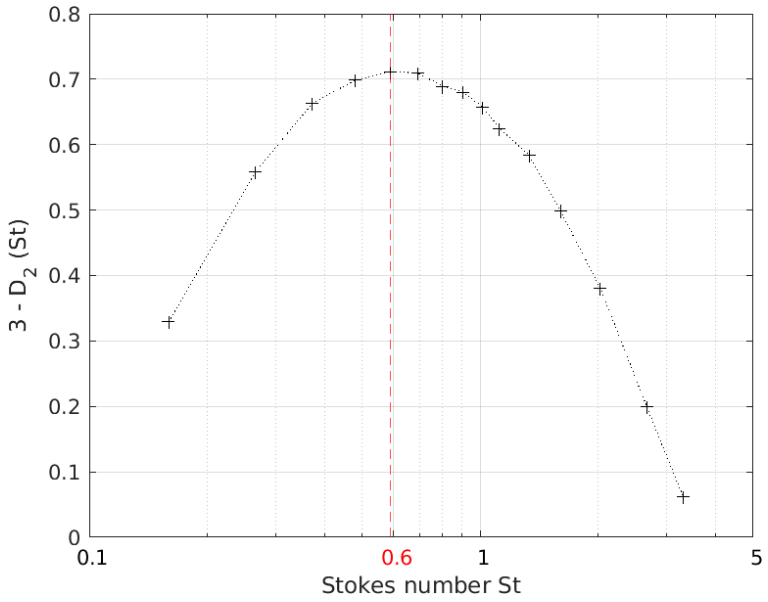

Figure 2.6: Values for the exponent $3 - D_2(St)$ of the power law in Eq. 2.22, as function of the Stokes number St. The red line indicates the maximum. Data from Bec et al. [2007].

shown to be relevant for bidisperse particle populations in direct numerical simulation (DNS) studies, although the relative contributions of clustering and the sling effect in this case, as well as their interaction with gravity, are still open questions [Woittiez et al., 2009, Dhariwal and Bragg, 2018, Momenifar et al., 2019].

Maxey [1987] first suggested that centrifugal forces generated by eddies push particles in regions of the flow with low vorticity, leading to a local increase in number concentration in these regions. This phenomenon was then verified by a number of studies, including experimental studies in liquid clouds and snowfall [e.g., Squires and Eaton, 1991, Lehmann et al., 2007, Saw et al., 2008, Nemes et al., 2017, Petersen et al., 2019, Bertens et al., 2021, Li et al., 2021a]. The increase of collision rates due to clustering can be thought of as attributable to particle couples that follow similar trajectories for a finite amount of time. Such component of the collision rate for a given particle can be expressed as [Pumir and Wilkinson, 2016]:

$$\mathcal{R}_{adv} = \sqrt{\frac{8\pi}{15}} \frac{n'(2a)^3}{\tau_\eta} \mathcal{C}(2a). \tag{2.20}$$

Note that the latter equation expresses the collision rate for one particle, in contrast with Eq. 2.19 which expresses the total number of collisions per unit volume and unit time. In Eq. 2.20 $\mathcal{C}(\Delta r)$ is the so-called *radial distribution function* (RDF), which describes how particle number concentration varies as a function of distance

Δr from a reference particle. In Eq. 2.20 $\mathcal{C}(\Delta r)$ is evaluated at $\Delta r = 2a$ as two particles will only collide if their separation is equal or smaller than the diameter $2a$. If particles are distributed homogeneously in space $\mathcal{C}(\Delta r) = 1$ for any value of Δr, and therefore Eq. 2.20 is reduced to the Saffman-Turner scenario described by Eq. 2.19:

$$\mathcal{R}_{S-T} = \sqrt{\frac{8\pi}{15}} \frac{n'(2a)^3}{\tau_\eta}. \tag{2.21}$$

It can be shown that the radial distribution function $\mathcal{C}(\Delta r)$ takes on the approximate power-law form [Pumir and Wilkinson, 2016]:

$$\mathcal{C}(\Delta r) \sim \left(\frac{\Delta r}{\eta}\right)^{D_2(St)-3}, \tag{2.22}$$

where the exponent $D_2(St) - 3$ is a function of the Stokes number, and needs to be investigated numerically. As an example, the values computed by Bec et al. [2007] are displayed in Fig. 2.6. Bec et al. [2007] found the maximum in $3 - D_2(St)$ at $St \sim 0.6$, with $3 - D_2(0.6) \sim 0.7$. The term then rapidly goes to 0 as St both decreases and increases. Therefore clustering is limited to particles with inertia on the same order of that of the fluid, and $\mathcal{C}(\Delta r) \sim 1$ otherwise.

Collision rates are further enhanced by the sling effect, which facilitates the intersection of particle trajectories by introducing large relative velocities between particles. Such large velocities are produced by centrifugal forces that particles are subject to when traversing eddies. The relevance of the sling effect has been demonstrated by a number of studies, for the most part based on DNS, with a low number of laboratory studies [e.g., Bewley et al., 2013, Saw et al., 2014, Voßkuhle et al., 2014, Ravichandran and Govindarajan, 2015, Sheikh et al., 2022]. In contrast with clustering, which increases concentration locally because particle subsets may follow similar trajectories, the sling effect produces an increase in concentration locally because particles follow vastly different trajectories. The sling effect in fact locally increases concentration where (and when) particle trajectories cross. For this reason, Pumir and Wilkinson [2016] argue that the contributions to collision rate from clustering and the sling effect are essentially independent and additive. They report an analytical expression of the form:

$$\mathcal{R}_{sling} = K_0 \frac{n' a^2 \eta}{\tau_\eta} \sqrt{St}\, e^{-S_0/St}, \tag{2.23}$$

where K_0 and S_0 are constants to be determined numerically. K_0 determines the asymptotic collision rate under the limit $St \to \infty$, and S_0 determines the St cutoff value where the sling effect becomes relevant [Pumir and Wilkinson, 2016]. While clustering has a maximum at $St \sim 0.6$, Eq. 2.23 shows that the sling effect is

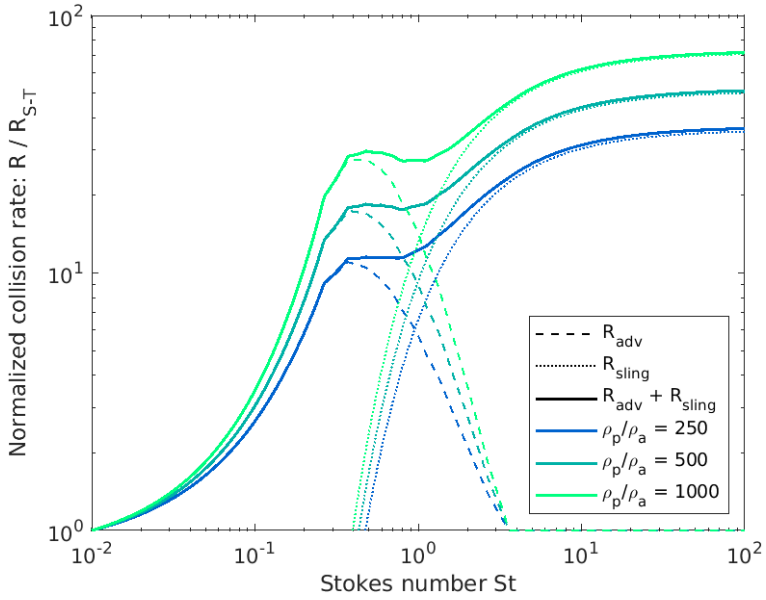

Figure 2.7: Example of the dependence of the normalized collision rate $\mathcal{R} \cdot \mathcal{R}_{S-T}^{-1}$ given in Eq. 2.24 on the Stokes number St and the ratio of the densities of the particle and the fluid ρ_p/ρ_a. The total collision rate $\mathcal{R}$ is decomposed into its advective component $\mathcal{R}_{adv}$, which accounts for the Saffman-Turner mechanism and clustering, and its component accounting for the sling effect $\mathcal{R}_{sling}$. In Eq. 2.24 the values for $D_2(St)$ are taken from Bec et al. [2007], K_0 is set to 50, following Voßkuhle et al. [2015], and S_0 is set to 1.7, following Falkovich and Pumir [2007].

relevant at any St above the cutoff value, and that for large St ($St >> S_0$) the collision rate is proportional to $\sqrt{St}$. Voßkuhle et al. [2015] showed that $K_0 \sim 50$, while Falkovich and Pumir [2007] showed that, for particles with characteristics similar to cloud droplets $S_0 \sim 2$.

Fig. 2.7 displays example of the dependence of the total turbulence-induced collision rate $\mathcal{R}$ on St, and the ratio between the density of the particles and that of air ρ_p/ρ_a. The collision rate is calculated by summing the advective component $\mathcal{R}_{adv}$ introduced in Eq. 2.20, which accounts for the Saffman-Turner mechanism and clustering, together with the sling-effect component $\mathcal{R}_{sling}$ in Eq. 2.23. For simplicity $\mathcal{R}$ is normalized by the value obtained in the Saffman-Turner limit $\mathcal{R}_{S-T}$, given in Eq. 2.21:

$$\mathcal{R} \cdot \mathcal{R}_{S-T}^{-1} = (\mathcal{R}_{adv} + \mathcal{R}_{sling}) \cdot \mathcal{R}_{S-T}^{-1} = \left(18St\frac{\rho_p}{\rho_a}\right)^{(D_2(St)-3)/2} + \frac{\sqrt{5}K_0}{16\sqrt{3\pi}}\sqrt{\frac{\rho_p}{\rho_a}}\, e^{-S_0/St}. \tag{2.24}$$

Such normalization allows for a simplified estimation of the collision rate, without any assumptions on particle size or concentration, the only two required parameters

being St and ρ_p/ρ_a. Fig. 2.7 displays the dependence of the normalized collision rate on these two parameters. In Eq. 2.24 the values for $D_2(St)$ are taken from Bec et al. [2007], K_0 is set to 50, following Voßkuhle et al. [2015], and S_0 is set to 1.7, following Falkovich and Pumir [2007]. The figure elucidates the relevance of inertial processes for the enhancement of collision rates. Clustering is relevant at $0.1 \lesssim St \lesssim 2$, and reaches its maximum at $St \sim 0.6$, and the term tends to the Saffman-Turner limit on both sides of this interval. In contrast, contributions due to the sling effect increase monotonically with St: the sling effect becomes non-negligible at $St \gtrsim 0.5$, and reaches the same magnitude as clustering at $St \sim 1$. At $St > 2$ the collision rate is dominated by the sling effect, and the normalized collision rate then tends to an asymptotic value as St further increases. While St is the main driver of the collision rate, the density ratio ρ_p/ρ_a further modulates the collision rate, increasing it the denser the particles are with respect to the fluid. Note that, even in absence of the normalization factor, the Saffman-Turner contribution to the collision rate is independent of the density ratio, as particles are assumed to be tracers.

Turbulence and settling: preferential sweeping

Maxey [1987] first suggested that the velocity of particles settling in a turbulent flow is increased, due to particles being preferentially swept to regions of the eddies with velocity aligned with the velocity of the particles (see sketch in Fig. 2.8). The process can be easily understood by stating the equation of motion [Maxey and Riley, 1983, Tom and Bragg, 2019]:

$$\ddot{\mathbf{x}}^p(t) = \frac{1}{\tau_p}(\mathbf{u}(\mathbf{x}^p(t), t) - \dot{\mathbf{x}}^p(t)) + \mathbf{g}, \tag{2.25}$$

where $\mathbf{x}^p(t)$, $\dot{\mathbf{x}}^p(t)$, $\ddot{\mathbf{x}}^p(t)$, respectively indicate a particle's position, velocity. and acceleration at time t, and the fluid velocity $\mathbf{u}(\mathbf{x}^p(t), t)$ is calculated at the position of the particle. By assuming identical particles, and performing an ensemble average (indicated with angle brackets), i.e., an average across all particles, and taking only the vertical component one obtains [Tom and Bragg, 2019]:

$$\langle v_z(t)\rangle = \langle \dot{x}_z^p(t)\rangle = \langle u_z(\mathbf{x}^p(t), t)\rangle + \tau_p g. \tag{2.26}$$

In Eq. 2.26 the term $\tau_p g$ is simply the terminal velocity determined by drag and gravity alone, as derived in Eq. 2.7. The average vertical velocity of particles equals $\tau_p g$ when the average fluid velocity at the particle positions $\langle u_z(\mathbf{x}^p(t), t)\rangle$ is 0. The simplest scenario that leads to $\langle u_z(\mathbf{x}^p(t), t)\rangle = 0$ is when the fluid is still, as treated in Section 2.1.3. Alternatively $\langle u_z(\mathbf{x}^p(t), t)\rangle = 0$ is achieved when the particles are distributed uniformly throughout the fluid, and sample descending and ascending

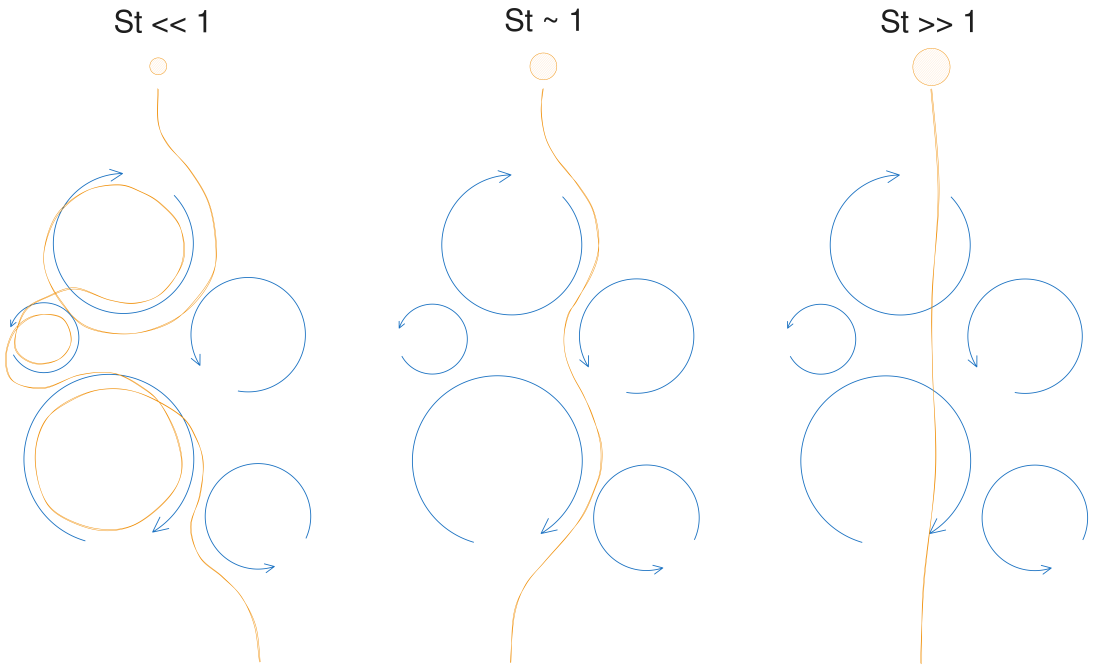

Figure 2.8: Diagram illustrating the three regimes of motion of particles settling in turbulence, including preferential sweeping (middle). If the particle's Stokes number St is much smaller than unity, the particle is suspended and follows the flow. When St is close to unity, the particle is preferentially swept to the downward regions of the flow. If St is much larger than unity the particle's motion is only marginally modified by the flow. Figure produced based on Fig. 1 in Stout et al. [1995].

regions equally. Inertial particles in turbulence are however preferentially swept to descending regions of the flow: as illustrated in Fig. 2.8, as a particle settles through an eddy, it is pushed towards the descending region of the eddy itself [Maxey, 1987, Stout et al., 1995]. Therefore more particles sample descending regions of the flow than ascending ones, and $\langle u_z(\mathbf{x}^p(t), t)\rangle > 0$, leading to $\langle v_z(t)\rangle > \tau_p g$.

The magnitude of the settling velocity enhancement is still under debate, as a number of factors have been shown to determine it. Aliseda et al. [2002], Monchaux and Dejoan [2017], and Huck et al. [2018] have shown in laboratory and DNS studies that, in addition to St, the magnitude of preferential sweeping is increased both by particle volume fraction and number concentration: both contribute to the formation of particle clusters in the descending regions of the flow, which in turn drag the fluid downwards, which further enhances settling speeds. Tom and Bragg [2019] further suggested that the magnitude of the velocity enhancement depends dramatically on the *Taylor-microscale Reynolds number* Re_λ (see e.g., Section 3.2

in Tennekes and Lumley [1972] for a formal definition), which quantifies the range of scales present in a turbulent flow. Tom and Bragg [2019] found that, as St increases, particles are preferentially swept by an increasingly wider range of eddy sizes, e.g., spanning close to 5 orders of magnitude at $St \sim 1$. The applicability of results available in the literature to real cloud microphysical scenarios is therefore highly uncertain, as laboratory and DNS studies reached at most values of Re_λ on the order of 10^2 [e.g., Tom and Bragg, 2019], while in typical cloud conditions Re_λ can reach values on the order of 10^4 [Onishi and Seifert, 2016]. For this reason most results on preferential sweeping available in the literature will not be reported here.

Li et al. [2021a] and Li et al. [2021c] recently investigated preferential sweeping in snowfall, and reported particle dynamics and distribution compatible with the presence of the process. Both studies investigated preferential sweeping via particle image velocimetry, which consists in the illumination of snowflakes close to the ground with a vertically-aligned light sheet, and the capture of high-frequency images with a camera. Li et al. [2021a] reported the presence of particle clusters: they observed dramatically higher settling velocities compared to the average velocity, up to 90% faster during an event characterized by $\varepsilon = 0.031$ m^2 s^{-3}, with the velocity enhancement increasing with cluster size. Li et al. [2021c] reported, during an event with $\varepsilon = 0.035$ m^2 s^{-3}, 18% higher particle concentration on the downward size of eddies, and 52% higher fall velocities when comparing particles in the downward and upward sides of eddies. They further observed particle accelerations of 0.16 to 0.33 m s^{-2} on the downward sides of eddies, and -0.0065 to -0.12 m s^{-2} on the upward sides.

2.3 Active microwave remote sensing

Active microwave remote sensing provides an invaluable tool to detect, characterize and improve our understanding of precipitation and clouds. In particular Doppler radars, with their ability to measure the power backscattered by targets, and resolve the distance and velocity of targets along the radar beam, allow for the characterization of the distribution and dynamics of precipitation and cloud particles. Since the 1950s, centimeter-wavelength radars have in fact been used to detect precipitation, and are now used operationally by weather services for monitoring and short-term forecasting of precipitation. Starting in the 1990s, technical advances have allowed for the developments of radars operating at millimeter wavelength, which provide high sensitivity to cloud particles, as well as fine range, time, and velocity resolution [e.g., Kollias et al., 2007].

2.3.1 Basic principles of operation and the radar equation

The simplest radar observable is the so-called *equivalent radar reflectivity factor* Z_e (henceforth referred to simply as reflectivity). It quantifies the power of the signal that targets scatter back to the radar. It depends on a number of factors, first and foremost on the scatterers present in the radar sampling volume, typically hydrometeors, but also on the instrument's characteristics. One of the many definitions of Z_e is [Fabry, 2015, Ch. 2-3]:

$$Z_e = \frac{\lambda^4}{\pi^5} |K_W|^{-2} \int_0^\infty N(\sigma_{b,\lambda})\, \sigma_{b,\lambda}\, d\sigma_{b,\lambda}, \tag{2.27}$$

where λ is the radar wavelength, and $\sigma_{b,\lambda}$ is the backscattering cross section of the targets in the radar sampling volume. The $|K_W|^2$ term in Eq. 2.27 is typically referred to, in the weather and cloud radar communities, as *dielectric constant of liquid water* [e.g., Fabry, 2015, Sec. 3.2]; confusingly, this quantity does not coincide with the ϵ_W quantity typically referred to as dielectric constant, or relative permittivity in electromagnetism (see e.g., Jackson [1975], Section 4.3, for a definition). In the following, $|K_W|^2$ will be referred to as dielectric constant, while ϵ_W will be referred to as complex relative permittivity. $|K_W|^2$ is computed as [Fabry, 2015, sections 3.1, 3.2]:

$$|K_W|^2 = \left| \frac{n_W^2 - 1}{n_W^2 + 2} \right|^2 = \left| \frac{\epsilon_W - 1}{\epsilon_W + 2} \right|^2, \tag{2.28}$$

where $n_W = \epsilon_W^{0.5}$ is the complex index of refraction of liquid water. The latter equation is based on the Clausius-Mossotti relation [Mossotti, 1846, Clausius, 1879], and $|K_W|$ is proportional to the induced electric dipole moment of a liquid water sphere, whose size is much smaller than the radar wavelength [Doviak and Zrnić, 1984, Sec. 3.2.1]. The backscattering cross section $\sigma_{b,\lambda}$ quantifies the fraction of incident energy that a target scatters back in the direction of the incident wave. Drawing a parallel with the concept of geometrical cross section, in qualitative terms $\sigma_{b,\lambda}$ can be thought of as the electric size of the scatterer. In Eq. 2.27 the integral is performed across all scatterers in the radar sampling volume, and $N(\sigma_{b,\lambda})\, d\sigma_{b,\lambda}$ represents the number of scatterers with backscattering cross section between $\sigma_{b,\lambda}$ and $\sigma_{b,\lambda} + d\sigma_{b,\lambda}$. For simplicity, due to the extremely low values of Z_e, it is typically expressed in the non-SI units of $\mathrm{mm}^6\ \mathrm{m}^{-3}$. Due to the wide range of orders of magnitude spanned by this variable, it is also expressed in logarithmic scale, in the $\mathrm{dBZ_e}$ units. Reflectivities expressed in linear and logarithmic units are related by the formula:

$$Z_e\,[\mathrm{dBZ_e}] = 10 \log_{10} \left(\frac{Z_e\,[\mathrm{mm^6\,m^{-3}}]}{1\,\mathrm{mm^6\,m^{-3}}} \right). \tag{2.29}$$

For simplicity $\mathrm{dBZ_e}$ will be hereafter indicated simply as dBZ.

While the expression for $\sigma_{b,\lambda}$ for an arbitrary particle is highly complex, under the assumption of a spherical target with diameter D much smaller than the radar wavelength, it reduces to [Bohren and Huffman, 1998, Eq. 5.9]:

$$\sigma_{b,\lambda} = \frac{\pi^5 D^6}{\lambda^4} \left| \frac{n_t^2 - 1}{n_t^2 + 2} \right|^2 , \tag{2.30}$$

where n_t is the target's complex index of refraction. Note that the rightmost term in Eq. 2.30 is equivalent to the dielectric constant in Eq. 2.28. The take-away message from Eq. 2.30 is that, under the mentioned assumptions, the backscattering cross section is proportional to $D^6\lambda^{-4}$. By plugging the latter equation in the definition of reflectivity in Eq. 2.27, the dependence on λ is lost. If the target is an ice particle with maximum dimension D_{max} much smaller than the radar wavelength, its backscattering cross section can be expressed with Eq. 2.30, with D equal to the diameter of a sphere with the same volume as the ice particle, and n_t equal to the complex index of refraction of ice [e.g., Westbrook et al., 2006, Lu et al., 2013].

The equivalent radar reflectivity factor $\mathrm{Z_e}$, as introduced in Eq. 2.27, can be used to state the so-called *radar equation for distributed targets*, which relates the backscattered power measured by the radar to instrument, path, and scatterer characteristics. Many variants of this equation exist, and here the one derived in Fabry [2015] for radars with parabolic antennas will be illustrated. The received power due to scatterers located at a range r can be calculated as [Fabry, 2015, Eq. 3.4]:

$$P_r = \underbrace{\frac{1.22^2 0.55^2 10^{-18} \pi^7 c}{1024 \ln(2)}}_{\text{constants}} \underbrace{\frac{P_t \vartheta D_a^2}{\lambda^4}}_{\text{instrument}} \underbrace{\frac{T(0,r)^2}{r^2}}_{\text{path}} \underbrace{|K_W|^2 \mathrm{Z_e}}_{\text{targets}}, \tag{2.31}$$

where the second term on the right-hand side contains instrument-specific parameters, the third term includes properties associated with the path between the instrument and the targets, and the last term includes the scatterer characteristics, via $\mathrm{Z_e}$. The instrument-specific parameters included in the equations are the transmitted power P_t, the duration of the transmitted pulse ϑ, and the antenna diameter D_a.

The $T(0,r)$ term in Eq. 2.31 is the transmittance of the atmosphere evaluated along the path between the instrument and the targets, located at range r. If the atmosphere is fully transparent to the radar signal, it follows that $T(0,r) = 1$, and hence $\mathrm{Z_e}$ can be easily estimated from Eq. 2.31 from the received power based on instrument characteristics and range r alone. If this is not the case, the radar signal is subject to *attenuation*, and the transmittance of the atmosphere along the beam needs to be estimated. Typically, the process of estimating attenuation is highly complex, as, especially at millimeter wavelengths, the radar signal can be

attenuated both by atmospheric gases, in particular water vapor and molecular oxygen, and by hydrometeors, both liquid and frozen. The topic is further discussed in Section 4.8 of **Study 2**.

The estimate of reflectivity in Eq. 2.31 based on the received power P_r might be further impaired by miscalibration in the measurement of P_r by the radar. The received power might be in fact underestimated by the instrument, which then leads to an underestimation of Z_e. Approaches used to mitigate instrument miscalibrations are discussed in Section 3.2.1 of **Study 1** and Section 4.7 of **Study 2**.

2.3.2 Scattering regimes

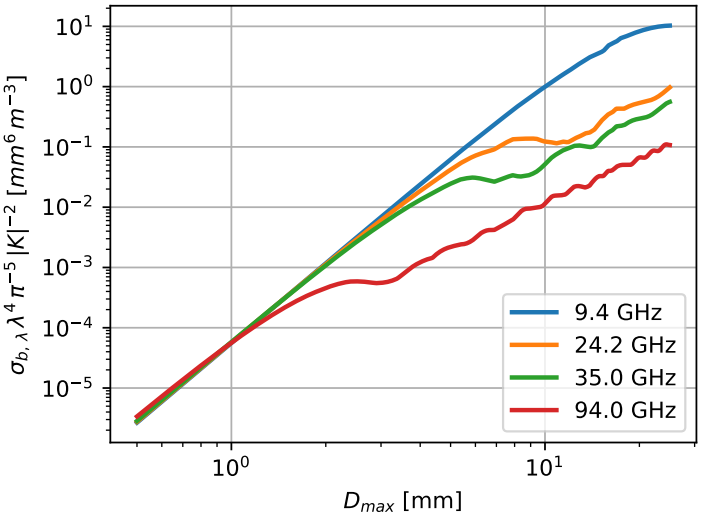

Figure 2.9: Normalized backscattering cross section of a single aggregate of dendrites, as function of aggregate size and displayed at multiple radar frequencies. Data taken from the snowScatt snowflake scattering database [Ori et al., 2021].

When commenting Eq. 2.30 it was highlighted that, under the assumption of scatterers characterized by a size much smaller than the radar wavelength λ, the backscattering cross section $\sigma_{b,\lambda}$ is proportional to $D^6\lambda^{-4}$. When scatterers have a size much smaller than λ it is said that they scatter according to the *Rayleigh regime*. As scatterers reach sizes comparable to the radar wavelength they transition into *non-Rayleigh scattering*, also referred to as *Mie scattering* if the scatterers are spherical and characterized by uniform density. Under Rayleigh scattering it can be assumed that each point of the scatterer is subject to the same electric field; as such, the dipoles induced by the incident wave oscillate in phase

throughout the whole volume of the scatterer. As scatterer size increases, entering the non-Rayleigh regime, different regions of the scatterer are subject to varying electric field magnitudes, and induced dipoles oscillate out of phase, leading to a smaller backscattering cross section $\sigma_{b,\lambda}$ compared to the theoretical value under Rayleigh scattering [Bohren and Huffman, 1998, Fabry, 2015].

Fig. 2.9 illustrates the dependence of backscattering cross section on scatterer size and radar frequency. A single aggregate of dendrites is here taken as scatterer, and $\sigma_{b,\lambda}$ is displayed for a number of radar frequencies; the specific particle type and radar frequencies here chosen will be relevant for **Study 1**, **Study 2**, and **Study 3**. The displayed values are taken from the scattering database by Ori et al. [2021], who estimated scattering properties of snow particles using the *self-similar Rayleigh-Gans approximation* [see e.g., Hogan and Westbrook, 2014]. The figure illustrates how the normalized backscattering cross section (proportional to Z_e in linear units) varies with scatterer size: at sizes $D_{max} \lesssim 1$ mm all curves overlap, the dendrite aggregate produces similar backscatter at all frequencies, and the normalized backscattering cross section is a power law of size. Hence, Rayleigh scattering is achieved at all displayed frequencies. As size increases, the backscattering cross section deviates from the Rayleigh-regime power law, first at higher frequencies. Such differential scattering at different frequencies under non-Rayleigh scattering can be used to infer the characteristic size of the ice particle population in the radar volume [e.g., Hogan et al., 2000, Liao et al., 2005, Kneifel et al., 2015]. A commonly used variable for this purpose is the *dual-wavelength ratio* (DWR), defined as the ratio between reflectivities measured at two separate frequencies. Given two reflectivity measurements Z_{e,λ_1} and Z_{e,λ_2} at two separate wavelengths $\lambda_1 > \lambda_2$, the DWR can be defined as (in linear units):

$$\mathrm{DWR}_{\lambda_1,\lambda_2} = Z_{e,\lambda_1} \cdot {Z_{e,\lambda_2}}^{-1}. \tag{2.32}$$

Since $Z_{e,\lambda_1} \geq Z_{e,\lambda_2}$, it follows that $\mathrm{DWR}_{\lambda_1,\lambda_2} \geq 1$ in linear units, or $\mathrm{DWR}_{\lambda_1,\lambda_2} \geq 0$ dB in decibels. In first instance, the DWR is mainly determined by the characteristic size of the particle population. This means that the DWR is invariant under multiplication of the particle size distribution (PSD) by a constant factor, as such a factor would cancel out in the division in Eq. 2.32. However, the DWRs of two particle populations with the same characteristic size, but different particle shapes and PSD widths may be different [Battaglia et al., 2020]. The DWR variable is further explained in Section 2 of **Study 1**, and examples of its dependence on ice particle population characteristics are given in Appendix A of **Study 1**.

2.3.3 Radar polarimetry

Radars transmitting and receiving at different polarization directions can further provide information on shape, size, and concentration of asymmetrical particles.

Dual-polarization radars in fact leverage the non-spherical shape of targets on the plane orthogonal to the beam direction. Upon impinging on a target, the wave transmitted by the radar undergoes three main interactions: the forward-propagating wave is partially attenuated, it is delayed, leading to an increase in phase, due to the higher index of refraction of the target compared to air, and it is partially scattered, with a possible change in phase of the scattered wave. If the target is asymmetric, the magnitude of these interactions along the two polarization directions will differ, leading to differences in amplitude and phase between the two signals received along the two polarization directions. A number of variables can be defined, based on these amplitude and phase differences, to express the effect of differential backscattering and differential propagation on the received signal [Fabry, 2015, Sec. 6.1]. In this section the most common polarimetric variables are introduced in qualitative terms; their formal definitions are given in Section 3 of **Study 2**.

The simplest dual-polarization observable is the so-called *differential reflectivity* $\mathrm{Z_{DR}}$, which quantifies the difference in amplitude between the received signals at horizontal and vertical polarization caused by differential backscattering. When operating at low elevation, dual-polarization radars typically transmit and receive at vertically and horizontally aligned polarization. As such, they measure a reflectivity at horizontal polarization $\mathrm{Z_{e\,H}}$ and a reflectivity at vertical polarization $\mathrm{Z_{e\,V}}$. $\mathrm{Z_{DR}}$ can be defined as:

$$\mathrm{Z_{DR}} = \mathrm{Z_{e\,H}} \cdot \mathrm{Z_{e\,V}}^{-1}, \tag{2.33}$$

where both reflectivities are expressed in linear units. $\mathrm{Z_{DR}}$ is often expressed in decibels, and in the case of an asymmetrical target with larger horizontal dimension, $\mathrm{Z_{e\,H}} > \mathrm{Z_{e\,V}}$, and hence $\mathrm{Z_{DR}} > 0$ dB. Large positive $\mathrm{Z_{DR}}$ values (in logarithmic scale) are observed in presence of large raindrops or plate-like ice crystals, while negative $\mathrm{Z_{DR}}$ values (in logarithmic scale) are rarer, and typically observed in presence of conical graupel [Fabry, 2015, Sec. 6.2.1]. Similarly to DWR, $\mathrm{Z_{DR}}$ is invariant under multiplication of the PSD by a constant factor.

Other polarimetric variables typically used in a low-elevation dual-polarization instrument setup include the *differential phase shift* Φ_{DP} between the received signals at horizontal and vertical polarization, together with its range derivative, the *specific differential phase shift* $\mathrm{K_{DP}}$. The phase difference Φ_{DP} can receive contributions from both differential backscattering and differential propagation. For instance, if the radar beam travels through an asymmetrical particle population with the major dimensions preferentially aligned horizontally, the signal at horizontal polarization will be delayed more than that at vertical polarization. This scenario would lead to $\Phi_{\mathrm{DP}} = \phi_{HH} - \phi_{VV} > 0°$, where ϕ_{HH} and ϕ_{VV} are the phases of the received signals at horizontal and vertical polarization. Another source of differential phase is non-Rayleigh scattering, as targets scattering in this regime might introduce a

phase difference δ between ϕ_{HH} and ϕ_{VV} [Fabry, 2015, Ch. 6]. It has however been shown that at cloud radar wavelengths δ produced by dry ice particles is negligible [Lu et al., 2015, von Terzi et al., 2022]. In absence of contributions from δ, Φ_{DP} is only determined by propagational effects, and, in presence of asymmetrical particles with their major dimensions preferentially aligned horizontally, it increases monotonically with range [Fabry, 2015, Sec. 6.2.3]. Under these conditions, $\mathrm{K_{DP}}$, the half range derivative of Φ_{DP}, can be related, in cold clouds, to the number concentration of small asymmetric ice particles [Bechini et al., 2013, Schrom et al., 2015]. $\mathrm{K_{DP}}$, being the range derivative of a phase quantity, is typically expressed in the units of $^\circ$ km^{-1}. Φ_{DP} and $\mathrm{K_{DP}}$ have the advantage of not being affected by attenuation [Fabry, 2015, Sec. 6.2.3].

A further variable derived from low-elevation dual-polarization observations is the *copolar correlation coefficient* (or simply *correlation coefficient*) ρ_{HV}, related to the diversity in shape and orientation of the particles in the radar volume. If the radar volume contains identical Rayleigh targets, not necessarily spherical, each target will equally contribute to the total measured difference in amplitude and in phase between the received signals at horizontal and vertical polarization, leading to identical signals at the two polarization directions, except for a constant amplitude factor and a constant phase shift. In these conditions, the two signals are perfectly correlated, and $\rho_{\mathrm{HV}} = 1$. If the targets are not identical, they will introduce varying amplitude and phase differences between the two polarizations leading to the received signals at the two polarization directions having non-constant amplitude and phase differences, and hence $\rho_{\mathrm{HV}} < 1$. In the presence of non-Rayleigh targets, the additional backscattering differential phase shifts (whose total contribution is quantified by δ) will further lower ρ_{HV} [Fabry, 2015, Sec. 6.2.4].

Polarimetric configurations bring additional information on scatterers also when operating at zenith, via the *linear depolarization ratio* (LDR). This variable is typically measured in zenith by transmitting along one polarization direction, and receiving at both directions. LDR is the ratio between the reflectivities measured orthogonal and parallel to the transmit direction. It is hence sensitive to particles which backscatter a portion of the polarized transmitted signal as unpolarized (i.e., they *depolarize* the signal). LDR is typically sensitive to prolate particles, such as columns and needles [Oue et al., 2015, Li et al., 2021b].

2.3.4 Doppler observations, spectra, and moments

The received signal carries information on the scatterers' velocities via the Doppler effect. If a scatterer has non-zero velocity along the radar beam direction, it will backscatter the transmitted wave at a different frequency, higher if it's moving towards the radar, and lower if moving away from the radar. Associated with a change in frequency is a change in phase of the received signal. Phase of the signal

backscattered by a target at range r can be in fact expressed as [e.g., Fabry, 2015, Eq. 5.1]:

$$\phi = -\frac{4\pi f n_{air}}{c} r, \tag{2.34}$$

which can be differentiated with respect to time to obtain:

$$\frac{d\phi}{dt} = -\frac{4\pi f n_{air}}{c}\frac{dr}{dt} = -\frac{4\pi f n_{air}}{c} v_D, \tag{2.35}$$

where n_{air} is the refractive index of air. Hence, measuring the change in phase ϕ allows for an estimate of the along-beam component of the scatterer's velocity v_D. This quantity is typically referred to as *Doppler velocity*. In practice, the received signal contains a spectrum of Doppler frequency shifts, as hydrometeors in the radar volume typically display a wide range of velocities. When processing observations, the time series of the received signal typically undergoes Fourier analysis, to obtain the so-called *Doppler spectrum*. The Doppler spectrum separates the contributions to reflectivity from particles characterized by varying Doppler velocities [Kumjian, 2018, Sec. 6].

Information contained in Doppler spectra is typically condensed by calculating a number of spectral moments M_n. The zeroth moment is the sum of all spectral lines, and is hence simply reflectivity $\mathrm{Z_e}$. Moment 1 is computed as:

$$M_1 = {M_0}^{-1} \int_{v_{D\,min}}^{v_{D\,max}} v_D \cdot s(v_D) dv_D, \tag{2.36}$$

where $s(v)$ is spectral reflectivity, normalized with respect to Doppler-bin width, and expressed in $\mathrm{mm^6\ m^{-3}\ (m\ s^{-1})^{-1}}$. It follows from the definition in Eq. 2.36 that M_1 is the reflectivity-weighted mean velocity of targets, and is therefore typically referred to as *mean Doppler velocity* (MDV). The second moment is typically computed as:

$$M_2 = \left[{M_0}^{-1} \int_{v_{D\,min}}^{v_{D\,max}} (v_D - M_1)^2 \cdot s(v_D) dv_D \right]^{0.5}. \tag{2.37}$$

M_2 can be interpreted as a reflectivity-weighted standard deviation of velocities, and quantifies the spread of target velocity around the MDV. It is therefore usually referred to as *Doppler spectrum width*, and is driven by broadening in the hydrometeor fall velocity distribution (and hence broadening of the PSD), wind shear within the radar beam, and turbulence, among other factors [Doviak and Zrnić, 1984]. Lastly, the third moment is typically computed as:

$$M_3 = M_0^{-1} M_2^{-3} \int_{v_{D\,min}}^{v_{D\,max}} (v_D - M_1)^3 \cdot s(v_D) dv, \tag{2.38}$$

it quantifies the degree of symmetry of $s(v)$ with respect to a Gaussian distribution with zeroth, first and second moments matching those of $s(v)$. It is typically referred to as *Doppler spectrum skewness*, or simply *skewness*. It has applications in the study of multimodal particle populations, such as for the detection of drizzle formation [Kollias et al., 2011, Luke and Kollias, 2013, Acquistapace et al., 2019], or the onset of ice formation from supercooled liquid [Gierens, 2021]. Higher moments have limited applications, and will not be here introduced.

2.3.5 Bringing everything together: observational fingerprints

The previous sections illustrated the physical mechanisms that link scatterer properties with radar observables. However, none of the introduced radar variables can be directly translated into the microphysical variables used in Section 2.1 to characterize particle populations and how they evolve. Nonetheless, the many observables here introduced provide valuable clues that, together with knowledge of the microphysical processes, can be used to infer characteristics of the observed particle populations. Hence the term *observational fingerprints*: similarly to a detective at a crime scene, radar data can be searched for specific signatures which signal the presence of specific hydrometeors and cue the way they evolve. This approach will be key in inferring the results of **Study 1**, **Study 2**, and **Study 3**.

2.3.6 Retrieving the eddy dissipation rate

In addition to hydrometeor dynamics, Doppler velocity observations allow for the retrieval of a number of variables characterizing the atmospheric flow. These include in particular wind speed along the radar beam [e.g., Kollias et al., 2002, Shupe et al., 2008b], as well as the EDR. In this section the approaches typically used to retrieve the EDR are introduced, as they are relevant for **Study 3**. Most approaches rely on the seminal work by Rogers and Tripp [1964]. They proposed that, under the assumption that all scatterers in the radar beam act as tracers for air motion, the TKE averaged over a time interval Δt can be derived from the variance of a time series of MDV and the mean of a time series of spectrum width, with both time series recorded during the same time interval Δt. Note that, for the purpose of this section, Δt will be referred to as averaging time, not to be confused with the instrument's integration time, or time resolution, δt. The averaging time needs to be selected in such a manner that the MDV and spectrum width time series contain a sufficient number of samples, namely $\Delta t >> \delta t$. With this premise, according to Rogers and Tripp [1964], the TKE can be decomposed

into two components:

$$2 \cdot \mathrm{TKE} = \overline{(v_{mD}^2 - \overline{v_{mD}}^2)} + \overline{\sigma_D^2} = \sigma_{\overline{v}}^2 + \overline{\sigma_D^2}, \tag{2.39}$$

where v_{mD} is the MDV, σ_D is the Doppler spectrum width, and the averaging is performed over Δt. The first term on the right-hand side of Eq. 2.39, $\sigma_{\overline{v}}^2$, is the variance of the MDV time series, while the second term is the average of the squared Doppler spectrum width time series.

The two variances $\sigma_{\overline{v}}^2$ and $\overline{\sigma_D^2}$ are determined by disjoint sets of eddies: these two sets are separated by a length scale ℓ_1, which is the length scale of the largest eddies being advected through the radar volume during the integration time δt. Therefore only eddies with length scale $\ell > \ell_1$ contribute to $\sigma_{\overline{v}}^2$, while only eddies with length scale $\ell \leq \ell_1$ contribute to $\overline{\sigma_D^2}$. Two additional length scales ℓ_0 and ℓ_2 can be defined, in such a way that: ℓ_0 represents the length scale of the largest eddies that contribute to $\sigma_{\overline{v}}^2$, ℓ_1 is at the interface between the eddies contributing to $\sigma_{\overline{v}}^2$, and those contributing to $\overline{\sigma_D^2}$, and ℓ_2 represents the length scale of the smallest eddies contributing to $\overline{\sigma_D^2}$. Similarly to ℓ_1, ℓ_0 is the length scale of the largest eddies traveling through the radar volume during the averaging time Δt [Bouniol et al., 2004, O'Connor et al., 2005]. Therefore, ℓ_0 and ℓ_1 depend on the mean horizontal wind speed V_h, which determines the sizes of the eddies being advected through the radar volume during Δt or δt. The two length scales ℓ_0 and ℓ_1 can be expressed as [O'Connor et al., 2005]:

$$\ell_0 = \Delta t \cdot V_h + 2r \sin(\theta/2), \tag{2.40a}$$

$$\ell_1 = \delta t \cdot V_h + 2r \sin(\theta/2), \tag{2.40b}$$

where θ is the half-power beamwidth, and r is range. Lastly, ℓ_2 is simply the smallest scale that can be probed by the Doppler radar, namely half the radar wavelength $\lambda/2$ [Kollias et al., 2001].

The two variances $\sigma_{\overline{v}}^2$ and $\overline{\sigma_D^2}$ can hence be written in terms of the turbulent energy spectrum $E(\kappa)$, using $k_{0,1,2} = 2\pi\ell_{0,1,2}^{-1}$ as integration extremes [Bouniol et al., 2004]:

$$\sigma_{\overline{v}}^2 = \int_{k_0}^{k_1} E(\kappa) d\kappa, \tag{2.41a}$$

$$\overline{\sigma_D}^2 = \int_{k_1}^{k_2} E(\kappa) d\kappa. \tag{2.41b}$$

Under the assumption that the wavenumber interval $[k_0, k_1]$ falls within the inertial subrange, Eq. 2.41a can be combined with the expression for the energy spectrum in the inertial subrange in Eq. 2.15 to obtain:

$$\varepsilon = \left(\frac{2}{3}\alpha_K\right)^{-\frac{3}{2}} \sigma_{\overline{v}}^3 \left(k_0^{-\frac{2}{3}} - k_1^{-\frac{2}{3}}\right)^{-\frac{3}{2}} \overset{k_0 << k_1}{\approx} \left(\frac{2}{3}\alpha_K\right)^{-\frac{3}{2}} \sigma_{\overline{v}}^3 k_0. \tag{2.42}$$

The formula in Eq. 2.42 has been used by a number of studies to retrieve the EDR, including Bouniol et al. [2004], O'Connor et al. [2005], and Shupe et al. [2008a].

While a similar relation could in theory be derived to relate ε and σ_D based on Eq. 2.41b, such relation is more nuanced, as it requires taking into account the antenna illumination pattern. The contribution to σ_D by motions on scales both small and large compared to the beam dimensions is in fact reduced [Srivastava and Atlas, 1974]. Analytic expressions to obtain the EDR, as function of σ_D and antenna parameters were derived by Frisch and Clifford [1974], and later on improved by Labitt [1981]. Such relations are not included in this dissertation; the reader can find them e.g., in Chapman and Browning [2001, Eq. 6-7]. The Frisch-Clifford-Labitt relations have been used by a number of studies to derive the EDR, including Chapman and Browning [2001], Fang et al. [2014], and Borque et al. [2016]. The spectrum-width-based approach has the significant disadvantage that it can only be applied in cases where the microphysical contribution to spectrum width is negligible when compared to the turbulence-induced broadening of the Doppler spectrum [Rogers and Tripp, 1964, O'Connor et al., 2005], and is hence not suited for applications to precipitating clouds.

The velocity-variance approach as derived in Eq. 2.42 relies on the assumption that the wavenumber interval $[k_0, k_1]$ falls completely within the inertial subrange. While the lower bound k_0 can be tuned to match known values compatible with the inertial subrange, the higher bound k_1 is fixed and determined by the radar measurement setup, and horizontal wind. Recently Borque et al. [2016] proposed some improvements to this approach, only selecting wavenumber intervals compatible with the inertial subrange. This solves the issues of arbitrary choices of k_0, and of the possible inclusion of the low wavenumber portion of the dissipation range, when k_1 falls within this range. The approach by Borque et al. [2016] in fact involves performing a fast Fourier transform (FFT) of the velocity time series (hereafter indicated as $S(\kappa)$), and only calculating the variance associated with the portion of the spectrum that fits the inertial subrange -5/3 power law. This is done by performing a linear fit to the FFT output (brought to log-log scale), attempting it in several wavenumber intervals $[k_{low}, k_{high}]$; the EDR is then computed for all intervals whose fit has a slope within -5/3 $\pm$ 1/3. Following this approach, the EDR can be easily computed by integrating Eq. 2.15 between k_{low} and k_{high} [Borque et al., 2016]:

$$\varepsilon = \left(\frac{2}{3\alpha_K} \int_{k_{low}}^{k_{high}} S(\kappa) d\kappa \right)^{3/2} \left(k_{low}^{-2/3} - k_{high}^{-2/3} \right)^{-3/2}; \tag{2.43}$$

or alternatively in terms of frequency f:

$$\varepsilon = \frac{2\pi}{V_h} \left(\frac{2}{3\alpha_K} \int_{f_{low}}^{f_{high}} S(f) df \right)^{3/2} \left(f_{low}^{-2/3} - f_{high}^{-2/3} \right)^{-3/2}. \tag{2.44}$$

Borque et al. [2016] then compute the final EDR value as the mean value across all valid frequency intervals, and estimate the associated uncertainty as its standard deviation.

Chapter 3

Study 1: Assessing the relevance of ice aggregation

Chellini, G., R. Gierens, and S. Kneifel (2022). **Ice aggregation in low-level mixed-phase clouds at a high Arctic site: Enhanced by dendritic growth and absent close to the melting level**. *Journal of Geophysical Research: Atmospheres*, 127, e2022JD036860, https://doi.org/10.1029/2022JD036860.

The content of this chapter has been published under the Creative Commons Attribution 4.0 International Public License.

Author contributions: GC and SK planned and structured the article. RG processed the 94-GHz radar data, and GC calibrated all radar systems. GC further combined and analyzed data from all sources, and prepared the visualization of the results. All authors contributed to the interpretation of the results. GC drafted the manuscript and reviewed it iteratively with RG and SK.

Check for updates

JGR Atmospheres

RESEARCH ARTICLE
10.1029/2022JD036860

Ice Aggregation in Low-Level Mixed-Phase Clouds at a High Arctic Site: Enhanced by Dendritic Growth and Absent Close to the Melting Level

Giovanni Chellini[1], Rosa Gierens[1], and Stefan Kneifel[1,2]

[1]Institute for Geophysics and Meteorology, University of Cologne, Cologne, Germany, [2]Meteorological Institute, Ludwig-Maximilians-University Munich, Munich, Germany

Key Points:

- Low-level mixed-phase clouds (MPCs) at Ny-Ålesund produce large aggregates predominantly at dendritic-growth temperatures
- Enhanced aggregation due to dendritic growth occurs intermittently in limited regions of the MPC
- The typically observed enhanced aggregation zone close to 0°C is absent in low-level MPCs at the site

Correspondence to:
G. Chellini,
g.chellini@uni-koeln.de

Citation:
Chellini, G., Gierens, R., & Kneifel, S. (2022). Ice aggregation in low-level mixed-phase clouds at a high Arctic site: Enhanced by dendritic growth and absent close to the melting level. *Journal of Geophysical Research: Atmospheres*, *127*, e2022JD036860. https://doi.org/10.1029/2022JD036860

Received 1 APR 2022
Accepted 30 JUL 2022

Abstract Low-level mixed-phase clouds (MPCs) occur extensively in the Arctic, and are known to play a key role for the energy budget. While their characteristic structure is nowadays well understood, the significance of different precipitation-formation processes, such as aggregation and riming, is still unclear. Using a 3-year data set of vertically pointing W-band cloud radar and K-band Micro Rain Radar (MRR) observations from Ny-Ålesund, Svalbard, we statistically assess the relevance of aggregation in Arctic low-level MPCs. Combining radar observations with thermodynamic profiling, we find that larger snowflakes (mass median diameter larger than 1 mm) are predominantly produced in low-level MPCs whose mixed-phase layer is at temperatures between −15 and −10°C. This coincides with the temperature regime known for favoring aggregation due to growth and subsequent mechanical entanglement of dendritic crystals. Doppler velocity information confirms that these signatures are likely due to enhanced ice particle growth by aggregation. Signatures indicative of enhanced aggregation are however not distributed uniformly across the cloud deck, and only observed in limited regions, suggesting a link with dynamical effects. Low Doppler velocity values further indicate that significant riming of large particles is unlikely at temperatures colder than −5°C. Surprisingly, we find no evidence of enhanced aggregation at temperatures warmer than −5°C, as is typically observed in deeper cloud systems. Possible reasons are discussed, likely connected to the ice habits that form at temperatures warmer than −10°C, increased riming, and lack of particle populations characterized by broader size distributions precipitating from higher altitudes.

Plain Language Summary Low-level mixed-phase clouds (MPCs), that is, shallow clouds containing both liquid droplets and ice crystals, form frequently in the Arctic region. Their characteristic structure—consisting of one or multiple liquid layers at sub-zero temperatures, from which ice crystals form and precipitate—is nowadays well understood. However, the processes that lead to the growth of ice crystals into snow have been overlooked. Using a 3-year data set of radar observations from Ny-Ålesund, in Svalbard, Norway, we are able to identify situations when the ice particle growth is dominated by aggregation of several individual crystals. Combining radar observations with temperature information, we find that larger snowflakes are only produced in MPCs if their liquid portion is at temperatures between −15 and −10°C. This coincides with the temperature regime known for favoring aggregation due to growth and subsequent entanglement of branched crystals. Surprisingly, we find no evidence of enhanced ice aggregation at temperatures warmer than −5°C, as is typically observed in deeper cloud systems. Possible reasons are discussed, likely connected to the ice crystal shapes that develop at temperatures warmer than −10°C, increased liquid droplet production, and lack of particles precipitating from higher altitudes.

1. Introduction

Low-level mixed-phase clouds (MPCs) are ubiquitous in the Arctic. They have been shown to occur widely and frequently (e.g., Mioche et al., 2015; Morrison et al., 2012) and to persist typically for several hours (de Boer et al., 2009; Shupe, 2011), with some recorded cases lasting up to several days (e.g., Zuidema et al., 2005). They are further known to introduce, on average, a strong positive surface radiative forcing (Shupe & Intrieri, 2004; Serreze & Barry, 2011; Matus & L'Ecuyer, 2017; Tan & Storelvmo, 2019). Arctic low-level MPCs display a characteristic structure with one or multiple shallow liquid layers close to cloud top, from which ice particles form and precipitate (Shupe et al., 2006). Their persistence is due to a complex interplay of several processes (Morrison et al., 2012), and they have been found to occur under a variety of conditions, including both stable and unstable

© 2022. The Authors.
This is an open access article under the terms of the Creative Commons Attribution License, which permits use, distribution and reproduction in any medium, provided the original work is properly cited.

stratification, and under a wide spectrum of aerosol concentrations (Gierens et al., 2020; Jackson et al., 2012; Kalesse, de Boer, et al., 2016; Sotiropoulou et al., 2014; Young et al., 2016). Intense cloud-top radiative cooling caused by the supercooled liquid close to cloud top drives buoyant production of turbulence in the cloud layer, which, in turn, drives condensation and maintains the liquid layer (Shupe et al., 2008; Solomon et al., 2011).

Precipitation has been shown to strongly influence many properties of Arctic low-level MPCs. Precipitation, especially when deposited to the surface, withdraws moisture and ice nuclei from the MPC (Morrison et al., 2012; Solomon et al., 2014, 2015). Lower cloud fractions and faster dissipation have been in fact suggested for Arctic stratocumuli that develop precipitation (Harrington & Olsson, 2001; Simpfendoerfer et al., 2019). The modeling experiments by Eirund et al. (2019) have shown that ice precipitation induces thinning and break-up of the organization in Arctic stratocumuli, by generating cold pools at the surface. This effect has been observed to play a role in the transition from mixed-phase stratocumuli to open-cellular convection in cold-air outbreaks (Abel et al., 2017). Avramov and Harrington (2010) further suggested, based on a model sensitivity experiment, that the phase partitioning of Arctic low-level MPCs is strongly sensitive to the assumptions on mass-size, and size-fall speed relations of ice particles, and thus on the ice habits included in the model. It can then be expected that in addition to cloud lifetime, phase-partitioning, and organization, precipitation further affects the radiative characteristics of the MPC (Avramov & Harrington, 2010; Eirund et al., 2019; Harrington & Olsson, 2001; Proske et al., 2021; Solomon et al., 2015; Tan & Storelvmo, 2019). Tan and Storelvmo (2019) have shown that in the Community Earth System Model (CESM) larger ice particles in Arctic MPCs lead to a stronger cloud-phase feedback, that in turn increases the magnitude of Arctic amplification. Gaining process-level understanding of precipitation formation in Arctic low-level MPCs is thus necessary for an accurate model representation of these clouds, including their radiative effects in climate models.

The role of individual ice-growth processes, such as aggregation and riming, in the formation of precipitation in Arctic low-level MPCs is still unclear. In-situ observations of ice particles in Arctic low-level MPCs reported in the literature vary largely: pristine ice crystals, aggregates, and rimed particles have all been observed (Avramov et al., 2011; McFarquhar et al., 2007; Mioche et al., 2017; Wendisch et al., 2019). McFarquhar et al. (2007) reported observing mostly irregular and rimed branched crystals at cloud base, from in-situ aircraft observations at Utqiaġvik, Alaska. At the same site, Avramov et al. (2011) observed dendrites and large aggregates. Mioche et al. (2017) compiled in-situ observations from several aircraft campaigns above the Greenland and Norwegian seas, reporting large fractions of rimed or irregular ice particles. Fitch and Garrett (2022) reported, based on long-term ground-based in-situ observations, that, at Oliktok Point, Alaska, 65% of all frozen precipitation displays some degree of riming, even with observed liquid water path (LWP) of less than 50 g/m^2.

Doppler radar observations at multiple wavelengths can constrain the microphysical processes that determine the formation of precipitation, by providing information on particle fall speed and size. Observations taken at multiple wavelengths can be combined to derive the mean particle size of the hydrometeor population based on their differential scattering properties (Battaglia et al., 2020). The dual-wavelength ratio (DWR), that is, the ratio of equivalent radar reflectivity factors at two separate frequencies, increases when particles grow in size and transition from the Rayleigh scattering regime into the non-Rayleigh scattering regime (e.g., Hogan et al., 2000; Liao et al., 2005). When combined with in-cloud temperature and filtering for intense riming using vertical Doppler velocity information, DWR information has been used to derive the typical temperature regions favoring aggregation for midlatitude clouds by, for example, Dias Neto et al. (2019) and Barrett et al. (2019). These authors observed a first noticeable increase in DWR at Ka-band and W-band to occur in the temperature interval from −15 to −10°C, consistently with early cloud chamber studies (e.g., Kobayashi, 1957). Said temperature region is part of the often-called dendritic-growth zone (DGZ), where several plate-like particle habits are preferentially growing, including dendrites. The DGZ extends from −20 to −10°C, with enhanced depositional growth between −18 and −12°C (Takahashi, 2014; Takahashi et al., 1991). The dendrites' large cross-sectional area and ability to mechanically entangle their branches favor a rapid formation of aggregates (Connolly et al., 2012; Pruppacher & Klett, 2012, Section 14.7). A second enhanced aggregation zone close to 0°C is often observed as well, revealed by a further increase in DWR at several frequency combinations (W-band, Ka-band, Ku-band, and X-band) (Chase et al., 2018; Dias Neto et al., 2019; Tridon et al., 2019). Close to the melting level the presence of a quasi-liquid layer on the ice particles (Fletcher, 1962; Slater & Michaelides, 2019) is thought to favor intense aggregation (Fabry & Zawadzki, 1995).

In this study, we investigate the significance of different ice-growth processes, with a focus on aggregation, for precipitation formation in low-level MPCs at the high Arctic site of Ny-Ålesund, Svalbard, Norway. We obtain a 3-year statistics of DWR in Arctic low-level MPCs, by combining radar observations from a W-band cloud radar and a K-band precipitation radar, and searching the data set for observational fingerprints of ice-growth processes. We combine radar observations with thermodynamic retrievals from a co-located microwave radiometer, to further constrain the thermodynamic conditions that produce said fingerprints. This publication is thus structured as follows: essential theoretical aspects of dual-wavelength radar observations are explained in Section 2, the instruments and further techniques used are described in Section 3, results are shown and discussed in Section 4, and finally the main conclusions and questions raised by this study are summarized in Section 5.

2. Background: Dual-Wavelength Radar Approach

The equivalent radar reflectivity factor Z_e (hereafter called reflectivity) for an ensemble of scatterers in the measurement volume is defined as:

$$Z_e = \frac{\lambda^4}{\pi^5} \|K_W(\lambda)\|^{-2} \int_0^\infty N(\sigma_{b,\lambda})\, \sigma_{b,\lambda} d\sigma_{b,\lambda}, \tag{1}$$

where λ is the transmitted signal wavelength, $\|K_W(\lambda)\|^2$ is the dielectric constant of liquid water, $\sigma_{b,\lambda}$ is the wavelength-dependent backscattering cross-section of the individual scatterers, and $N(\sigma_{b,\lambda})$ its number distribution across the scatterer population (Fabry, 2018, chs. 2 and 3). Therefore, at a given wavelength, Z_e depends on both size (through $\sigma_{b,\lambda}$) and concentration of particles (through $N(\sigma_{b,\lambda})$), in addition to habit, phase, and orientation, and does not provide unequivocal information on particle size. Following the definition of Z_e, values measured at two wavelengths are equal if scattering from all particles and at both wavelengths can be approximated by Rayleigh scattering. If the particles increase in size, they first start to deviate from Rayleigh scattering at the shorter wavelength: this leads to a smaller Z_e at the shorter wavelength compared to the longer one, where more particles are still in the Rayleigh scattering regime (Battaglia et al., 2020). As a result, quantities combining Z_e values at both wavelengths can be related to the characteristic size of the underlying particle size distribution (PSD; Hogan et al., 2000; Kneifel et al., 2016; Liao et al., 2005; Matrosov et al., 2005; Szyrmer & Zawadzki, 2014; Tridon & Battaglia, 2015).

The most commonly used variable to quantify differential scattering of the radar beams at two separate wavelengths is the dual-wavelength ratio (DWR; sometimes named dual-frequency ratio, DFR), defined as:

$$DWR_{\lambda_1,\lambda_2} = \frac{Z_{e,\lambda_1}}{Z_{e,\lambda_2}}, \tag{2}$$

where Z_{e,λ_i} are the equivalent reflectivity factors in linear units and λ_1 is commonly chosen to be larger than λ_2. With this convention DWR = 0 dB if particles scatter according to the Rayleigh regime at both wavelengths and if their $\|K_W(\lambda)\|^2$ (Equation 1) are identical or have been corrected for. DWR values increase as particles transition into non-Rayleigh scattering at the shorter wavelength, then reach a saturation value as non-Rayleigh scattering is reached at both wavelengths. As a result, the DWR can be used as a proxy for the mean size of the sampled particle population (Hogan et al., 2000; Kneifel et al., 2016; Liao et al., 2005). The relation between DWR and particle size is, however, not univocal, and further depends on the particle shape and density (e.g., Matrosov et al., 2019) as well as on the PSD shape (Mason et al., 2019). Using the scattering database of Ori et al. (2021) and dendrite aggregates as well as a simple inverse exponential PSD, we find for example, a DWR_{K-W} of 3 (6, 9) dB to correspond to a mass median diameter of 1.5 (2.4, 3.7) mm, respectively. The maximum DWR value for such modeled dendrite aggregates is 11.4 dB, obtained for a mass median diameter of 8.1 mm, while the saturation DWR value is 9.4 dB. The full dependency of DWR on mass median diameter for different particle types is shown in Appendix A.

Table 1
Selected Technical Specifications of the Three Radar Systems Used in This Study: Two Cloud Radars, JOYRAD-94 and MiRAC-A, and A Precipitation Radar, MRR-2

	JOYRAD-94	MiRAC-A	MRR-2
Central frequency	94.0 GHz	94.0 GHz	24.23 GHz
Time res.	2–3 s	2–3 s	60 s
Integration time	0.5–0.6 s	0.5–0.6 s	60 s
Range res.	3.2–7.5 m	3.2–7.5 m	30 m
Min. range	100 m	100 m	30 m
Max. range	12 km	12 km	960 m
Sensitivity at 100 m	−62 dBZ	−64 dBZ	−13 dBZ
Sensitivity at 900 m	−50 dBZ	−50 dBZ	−6 dBZ
Beam width (half power)	0.5°	0.85°	1.5°

Note. Further information on the instruments can be found, respectively, in Küchler et al. (2017), Mech et al. (2019), and Klugmann et al. (1996).

3. Data Sets and Methods

3.1. Measurement Site

The observations analyzed in this study were obtained at the observatory of the Arctic research base AWIPEV in Ny-Ålesund, Svalbard. Ny-Ålesund is located at 79°N, in the region where Arctic amplification is the most intense (e.g., Dahlke & Maturilli, 2017). The site is located 13 m above sea level close to the coast of the Kongsfjorden, a fjord with surrounding mountains with altitudes of 500–1,000 m. Similar to other locations in the Arctic, the lower troposphere above Ny-Ålesund is often stably stratified. Temperature and humidity inversions have been found in respectively 75% and 84% of the daily radiosondes launched between 1993 and 2014 (Maturilli & Kayser, 2017). Mean monthly values of surface air temperature have been observed to range between 5.8°C in July and −12.0°C in March (Maturilli et al., 2013) and average yearly precipitation has been measured to be 564 mm/year with a large standard deviation of 444 mm/year, in the 2012–2019 period (Mori et al., 2021). Furthermore, remote sensing observations of clouds at this location have already been analyzed in depth by previous studies, such as Nomokonova, Ebell, et al. (2019), Vassel et al. (2019), Nomokonova et al. (2020), Gierens et al. (2020), and Ebell et al. (2020).

The characteristics of low-level MPCs at Ny-Ålesund have been reported by previous studies, in particular by Nomokonova, Ebell, et al. (2019) and Gierens et al. (2020). Their statistics display similar low-level MPC characteristics, compared to what has been observed at other Arctic sites, such as during the Surface Heat Budget of the Arctic Ocean (SHEBA) campaign (Shupe et al., 2006), at Utqiaġvik, Alaska (de Boer et al., 2009; Zhao & Wang, 2010), and at Eureka, Nunavut, Canada (de Boer et al., 2009). Nomokonova, Ebell, et al. (2019) observed a frequency of occurrence of 20.6% for single-layer MPCs (with no restriction on cloud depth or cloud-top height). They report an average LWP of 66 g/m^2, and average ice water path (IWP) of 164 g/m^2 for this cloud type. Gierens et al. (2020) estimated the occurrence of low-level MPCs lasting more than 1 hr to be 23%, with average LWP and IWP values of 35 and 12 g/m^2, respectively. The height of the liquid base of low-level MPCs ranges typically from 0.54 to 1.0 km, which is at or above the height of the surrounding mountaintops (Gierens et al., 2020).

3.2. Radar Systems

In this study, we calculate DWRs (K-band and W-band) of MPCs based on continuous zenith-pointing radar observations available from September 2017 to October 2018, and from June 2019 to February 2021. The W-band observations are obtained with 94-GHz frequency-modulated continuous wave (FMCW) Doppler cloud radars (RPG-FMCW-94-SP, manufactured by Radiometer Physics GmbH [RPG]; Küchler et al., 2017). Observations from two slightly different RPG-FMCW-94-SP radar systems have been combined: during the first time period, observations were collected with the MiRAC-A (Mech et al., 2019) which has a slightly larger beamwidth than the JOYRAD-94 (Küchler et al., 2017), used from June 2019 onwards. Both systems collected data with a temporal resolution of 2–3 s and vertical resolutions between 3 and 8 m depending on the range region (for technical details of the radars see Table 1, Küchler et al. (2017), and Gierens (2021)). The measurements were set up with a minimum and maximum range of 100 m and 12 km, respectively.

The W-band observations are complemented by observations from a K-band (24 GHz), zenith-pointing, FMCW Doppler Micro Rain Radar (MRR-2; Metek GmbH; Klugmann et al., 1996). Due to its economic and light-weight design, it has been frequently used to study snowfall in mountainous (Cha et al., 2009; Kneifel et al., 2011) and polar regions (Durán-Alarcón et al., 2019; Grazioli et al., 2017), evaluate satellite products (Maahn et al., 2014; Souverijns et al., 2018) and model performance (Scarchilli et al., 2020). We use the processing method developed by Maahn and Kollias (2012), which is fine-tuned for observations of frozen hydrometeors. The resolution in time (60 s) and range (30 m) is much coarser than the W-band cloud radars. Its average sensitivity for this measurement setup ranges between −13 and −6 dBZ, depending on range. Said sensitivity was calculated as the mean average

noise level times 1.2, as that is the lowest threshold for spectral reflectivity values to be considered as signal in the processing routine by Maahn and Kollias (2012).

To calculate DWRs, we averaged the W-band data to the MRR resolution. The reflectivity from the W-band cloud radars was averaged in linear scale, then converted to decibel. Note that during the study period, the MRR was set up to measure with a maximum range of 960 m. Calculated DWRs are therefore only available from the lowest W-band range gate (100 m) up to this height. DWR was not corrected for liquid attenuation, due to the typically low amounts of liquid observed in low-level MPCs in the Arctic. Only 24.2% of the MPC events detected by the MRR in fact displayed LWP higher than 150 g m^{-2} (see Section 4.1), which leads to a total two-way attenuation of approximately 1.2 dB at W-band, according to Tridon et al. (2020). Furthermore, in most of the analysis, we focus on the DWR value at the base of the liquid layer of the MPC, where the radar signal has undergone negligible attenuation. Mean Doppler velocity (MDV) was taken from the W-band cloud radars, and was also averaged to the same time and range resolution as the MRR. To analyze DWR and MDV in a consistent manner, MDV values above the maximum range of the MRR were ignored.

3.2.1. Radar Calibration Evaluation

Since the aim of our analysis is gaining information on particle size based on DWR calculated from Z_e at K-band and W-band, evaluating the calibration (especially in a relative sense) of all radar systems involved is necessary. The radar calibration constant might change, for example, due to drifts, which can lead to biases in the measured Z_e. In our analysis, we obtained calibration offsets for the MRR following a disdrometer-based approach (e.g., Dias Neto et al., 2019; Myagkov et al., 2020). The W-band radars were instead calibrated using a DWR-based approach, requiring that the DWR distribution for observations of Rayleigh targets only has its mode at 0 dB. All the derived offsets are reported in Table B1 in Appendix B.

At the AWIPEV site, a Parsivel disdrometer (Löffler-Mang & Joss, 2000) is installed, and data are available for the whole study period. Parsivel measures volume-equivalent sizes and fall speeds of particles that fall through its laser beam. It thus provides PSDs, and fall speed distributions of the particle population. A critical assessment of its performance can be found in Battaglia et al. (2010). The disdrometer-based calibration method consists in forward simulating Z_e values from drop size distribution (DSD) observed by Parsivel during rain events. The simulated reflectivities were then compared with the observed ones, taken from the range gate between 120 and 150 m. We selected the rain events based on the following criteria:

1. The disdrometer detects liquid precipitation. If frozen precipitation is detected all liquid within 10 min is ignored.
2. Only data from June through September are used, and only when surface temperature (from nearby weather station) is greater than 5°C, to exclude misclassified frozen or partially melted precipitation.
3. Disdrometer data are only used if rain rate ≥0.1 mm/hr following the approach by Williams et al. (2005). Additionally, only measurements containing at least 25 samples per minute are used. Both criteria are required in order for the disdrometer measurements to be representative of the drop population.
4. DSDs from Parsivel must contain particles larger than 1 mm. This criterion was determined following Myagkov et al. (2020), so that evaporation of the drops between the chosen range gate and the ground does not affect the forward simulated Z_e values.
5. Events are required to last at least 1 hr, with gaps allowed for a total of one sixth of the duration of the event.

Reflectivity values were based on the observed DSDs, and forward simulated with the T-matrix method (Leinonen, 2014; Waterman, 1965), using a drop shape model from Thurai et al. (2007). Following Huang et al. (2008), the drops were assumed to have Gaussian distributed canting angles, with 0° mean value and a 10° standard deviation. Attenuation coefficients were calculated using the same approach, and were multiplied by twice the height of the used range gates. The path-integrated attenuation was then subtracted from the forward simulated reflectivity values. All Z_e values below −10 dBZ and above 25 dBZ were excluded. It should be noted that we did not compare time series of observed and simulated Z_e but rather compared the Z_e distributions of the total rainfall event. This mitigates the issue of time delays between Z_e observed at the lowest radar range gate and the surface observations. A single median reflectivity value was then obtained for all events in each June-through-September period, for both the observations and the forward simulation. In each period, the Z_e offset was obtained by subtracting the two median values. In the periods from October to May, monthly Z_e offset values were calculated by linearly interpolating the obtained values.

We attempted to apply the same disdrometer-based approach to the calibration of the W-band radars, but we observed a strong dependence of the calculated offset values on the accumulated precipitation during the events (not shown). We hypothesize that this is due to deterioration of the coating of the radomes, leading to the radomes taking in some rain water, thus causing increasing attenuation of the signal. Although this phenomenon is not an issue for snowfall observations, it hampers the applicability of the disdrometer-based method to the W-band radars. For the MRR, we did not observe any attenuating effect due to wet antenna. Unlike the W-band radars, the MRR is not covered by a radome. Due to this reason, we used the calibrated MRR as our reference and estimated the offsets of the W-band radars using a DWR-based approach in light snowfall. This approach using light snowfall is overall similar to relative calibration methods applied to cloud radar observations of low-reflectivity Rayleigh-scattering hydrometeors by Hogan et al. (2000), Dias Neto et al. (2019), and Tridon et al. (2020). The relative offset estimated with this approach uses the fact that, for observations of Rayleigh-scattering frozen hydrometeors only, the DWR is approximately 0 dB. Rayleigh-scattering hydrometeors are typically selected by requiring that the radar reflectivity at the longer wavelength is below a certain threshold: for example, Dias Neto et al. (2019) used a threshold of −10 dBZ in Ka-band reflectivity when calibrating a W-band radar. In our case, due to the low sensitivity of the MRR such a low threshold could not be used. Therefore, selecting MRR echoes of solely Rayleigh targets was not possible. Nonetheless, Matrosov et al. (2019) reported scattering calculations, as well as observations from the Arctic site of Oliktok point, Alaska, of DWR of frozen hydrometeors at Ka-band and W-band, showing that for Ka-band reflectivities between −5 and 0 dBZ, the DWR distribution has its peak close to 0 dB, and is thus associated with Rayleigh scattering. Therefore, the radar measurements used in the calibration were selected with the following criteria:

1. Signal corresponds to ice-only clouds, based on the Cloudnet target classification (see Section 3.3).
2. Z_e from MRR is between −5 and 0 dBZ.
3. If Parsivel detects liquid precipitation, all echoes within 10 min are ignored.

Monthly DWR distributions for observations satisfying these conditions were then obtained, and the mode of the distribution was taken as monthly Z_e offset. Following the results by Matrosov et al. (2019), this calibration approach rests on the assumption that the monthly DWR distributions are characterized by a peak associated with Rayleigh scattering, and a tail on the right side of the peak, associated with non-Rayleigh scattering. The mode of the distribution was chosen as offset, so that, after applying the offset, the peak of the distribution is centered around a DWR value of 0 dB. The bins used to calculate the distributions are 0.5 dB wide. We estimated the uncertainty associated with this calibration approach by taking the left standard deviation of the monthly DWR distributions with respect to the mode. The root mean square value of such monthly uncertainties is 2.1 dB. An example further illustrating the DWR calibration and uncertainty calculation procedure is given in Appendix B.

3.3. Temperature Soundings and Hydrometeor Classification

Many microphysical processes are known to be strongly dependent on temperature (e.g., Pruppacher & Klett, 2012, chs. 9, 13, and 14), we thus investigate the dependence of DWR statistics on in-cloud temperature, as well as cloud-top and cloud-base temperature. Additional information on cloud phase is also needed, to properly identify MPC events. For these reasons, we use temperature profiles retrieved from a HATPRO (Humidity And Temperature PROfiler; Rose et al., 2005) microwave radiometer, and the Cloudnet target classification product (Hogan & O'Connor, 2004; Illingworth et al., 2007). The HATPRO is operated by the Alfred Wegener Institute (AWI) and measures on the same platform as the radar systems. In addition to temperature soundings, HATPRO observations are also used to retrieve LWP. To increase the accuracy of temperature profiles especially in the lowest 1 km, the observations at seven channels along the 60 GHz oxygen absorption band are obtained at various elevation angles (Crewell & Lohnert, 2007). Elevation scans are regularly performed every 15–20 min. The profiles are linearly interpolated in time to the same resolution as the MRR (60 s). Gierens et al. (2020) assessed the uncertainty of these temperature retrievals in low-level MPCs against radiosondes (see their fig. 3c), and found an RMSE of 0.7K at the surface, that increases to 1.6K (2.0K) at the liquid base of the MPC (cloud top).

Observations from the W-band cloud radar, HATPRO, and a ceilometer (model Vaisala CL51; Maturilli and Ebell (2018)), together with output from the ICOsahedral Nonhydrostatic weather model (ICON; Zängl et al. (2015)), in its global numerical weather prediction mode (ICON-IGLO), are operationally combined into the Cloudnet product (Hogan & O'Connor, 2004; Illingworth et al., 2007). In particular, we use the target classification product which classifies hydrometeors into: cloud droplets, supercooled cloud droplets, and cloud ice,

as well as drizzle or rain. The presence of liquid at sub-zero temperatures is mainly based on ceilometer observations. The ceilometer signal undergoes far greater attenuation when traversing a cloud layer containing cloud droplets, compared to an ice layer, because of the droplets' far higher number concentration. This leads to limitations of the Cloudnet product if more than one liquid layer is present, as often the pulse is unable to penetrate the lowest liquid layer. We will henceforth use the term *liquid base* to refer to the base of the lowest liquid layer detected by the ceilometer. We will further refer to the portion of the MPC above the liquid base as *mixed-phase layer* (MPL). In this study, we use the Cloudnet target classification product to derive the height of the liquid base, and cloud-top height.

3.4. Selection of Mixed-Phase Cloud Events

Low-level MPC events were identified following an approach similar to that employed by Gierens et al. (2020). The events were detected using the following criteria:

1. Cloud top is at or below 2,500 m.
2. If multiple cloud layers are present below 2,500 m, they are considered as one if separated by 60 m or less, otherwise only the lowest layer is included in the analysis, and the remaining ones are excluded.
3. Cloudnet indicates the presence of both liquid and ice in the cloud layer.
4. Liquid and ice are present for at least 60 min, with gaps allowed for a total of one sixth the total duration of the event.

During intense precipitation events, snow might accumulate on the ceilometer aperture, thus leading to ceilometer data not being available, and liquid layers not being identified in the Cloudnet target classification. Under these conditions, criterion three is not satisfied even though a low-level MPC is present. When the ceilometer signal is not available, the presence of liquid was evaluated using the LWP retrievals from HATPRO: an LWP threshold of 10 g/m^2 was used.

Using this approach, we identified a total of 1,605 low-level MPC cases, adding up to a total duration of 7,592 hr. Out of these, 1,042 cases, or 6,022 hr, were detected by the MRR. Out of all cases (cases detected by the MRR), 23.6% (25.6%) were detected in winter, 15.4% (18.0%) in spring, 30.2% (23.0%) in summer, and 30.8% (33.4%) in autumn. We would like to highlight that different subsets of all detected events were used in different parts of the analysis. In Sections 4.3 and 4.4, the value of DWR at liquid base, and its maximum value below the liquid base are evaluated in each sample. When evaluating these quantities, only the subset of data where the ceilometer signal is available and the liquid base is within the MRR range was used. In Section 4.4, we only focus on MPC events detected by the MRR, and with surface temperature colder than 0°C: 508 cases satisfy these conditions.

4. Results and Discussion

A typical low-level MPC event observed from February 4 to 6, 2021 is displayed in Figure 1. The four panels depict Z_e and MDV from the W-band cloud radar, DWR, and LWP. The figure also shows the height of the liquid base and temperature contours, derived from the ceilometer and HATPRO, respectively. The event depicted in the figure produced precipitation characterized by a wide range of DWR values. In particular, the MPC produced high DWR showers intermittently throughout its duration, highlighting the presence of large ice particles. These high DWR showers are alternating with regions characterized by lower DWR values, and even periods when the reflectivity was below the sensitivity of the MRR, and thus DWR values were not available. Figure 1 shows that most high DWR showers originate from within the mixed-phase layer. Interestingly, high DWR values are not necessarily linked to high reflectivity values, and vice versa.

4.1. Impact of MRR Sensitivity and Limited Maximum Range on Detected Cloud Characteristics

In the following analysis, we will focus only on MPC events detected by the MRR. The two limitations of the MRR are its maximum range (960 m), and lower sensitivity compared to the W-band cloud radars. To evaluate the effect of these limitations on the data sampled for the analysis, characteristics of MPCs detected by the MRR, and MPCs detected only by the W-band cloud radars are shown and compared in Figure 2. Overall, MPCs detected by the MRR tend to last longer (median 4.0 hr) and display higher LWP values (median 69.1 g/m^2) compared to events not detected by the MRR (2.0 hr and 23.0 g/m^2, respectively). Figure 2f further shows that

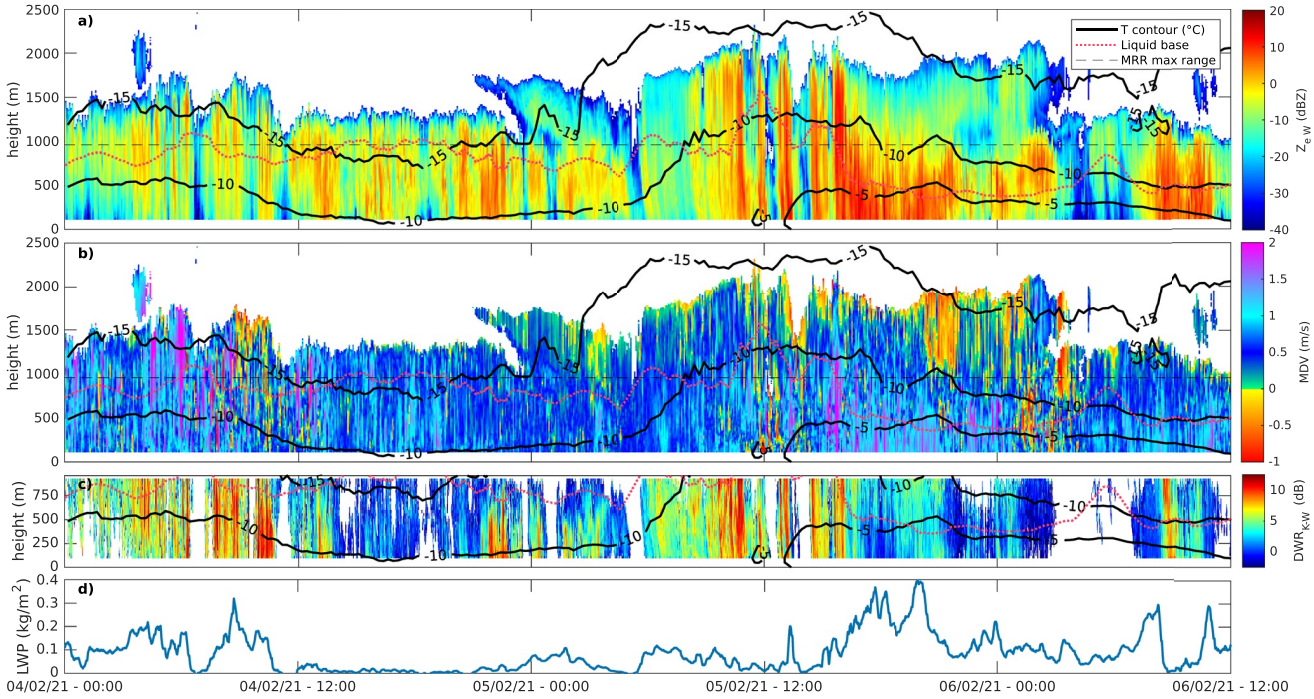

Figure 1. Example of low-level mixed-phase cloud event observed in Ny-Ålesund on February 4–6, 2021. Panels (a) and (b) display the reflectivity and mean Doppler velocity measured by the W-band cloud radar, respectively. Panel (c) depicts the dual-wavelength ratio obtained from Micro Rain Radar (MRR) and cloud radar observations. Panel (d) displays the liquid water path, retrieved from HATPRO microwave radiometer observations. In panels (a–c), contour lines indicate temperature (black) based on retrievals from HATPRO, and the liquid base height (pink dotted) from the Cloudnet target classification product. The horizontal dashed line in panels (a) and (b) indicates the maximum range of the MRR. Times indicated are in UTC.

MPC events detected by the MRR tend to have colder cloud-top temperature (CTT; median −9.8°C), compared to the events only detected by the W-band cloud radars (−8.2°C). Out of all events with CTT between −20 and −10°C, the MRR detects 84.8% of them, while it detects 75.6% of all events with CTT warmer than −10°C. Moreover, the number of MPC events with CTT colder than −20°C identified during the study period is very low (93), and 81.5% of these clouds are detected by the MRR. While 66.2% of MPCs detected by the MRR have their liquid base within the instrument's maximum range, only 12.4% have their top within it (as shown in Figures 2c and 2d). For this reason, the analysis reported in the following sections focuses on precipitation observed at, and below, the liquid base of MPCs. The limited range of the MRR does not appear to introduce a significant bias in the cloud-top height of the detected cases, as the median values for MPC events detected by the MRR is 1,431 m, while that for events not detected by the MRR is 1,341 m. This does not hold true for liquid-base height, as the median value for MPC events detected by the MRR is 791 m, while that for events not detected by the MRR is 1,001 m. The mixed-phase layer depth distributions in Figure 2e, calculated as the difference between cloud-top height and liquid-base height, suggest that this discrepancy in liquid-base height can be mainly attributed to shallower MPCs not being detected by the MRR. The median MPL depth for events detected by the MRR is in fact 480 m, while that for events not detected by the MRR is 280 m.

In summary, the lower sensitivity of the MRR leads to the detection of events that produce higher reflectivities: these events appear to be characterized by a longer duration, higher LWP values, deeper MPLs, and colder CTTs. The limited range of the MRR seems to introduce a bias toward events with lower liquid-base height. Interestingly, a similar bias is not observed in cloud-top height, suggesting that the MPCs causing said bias in liquid-base height are rather shallow, and likely characterized by a low reflectivity as well.

4.2. Characteristic Sizes and Fall Speeds of Precipitating Ice Particles in the Lowest 1 km

In Figure 3, we show long-term statistics of DWR and MDV (taken from W-band cloud radar) as function of temperature, in the detected low-level MPC events. This approach is similar to what has been applied to

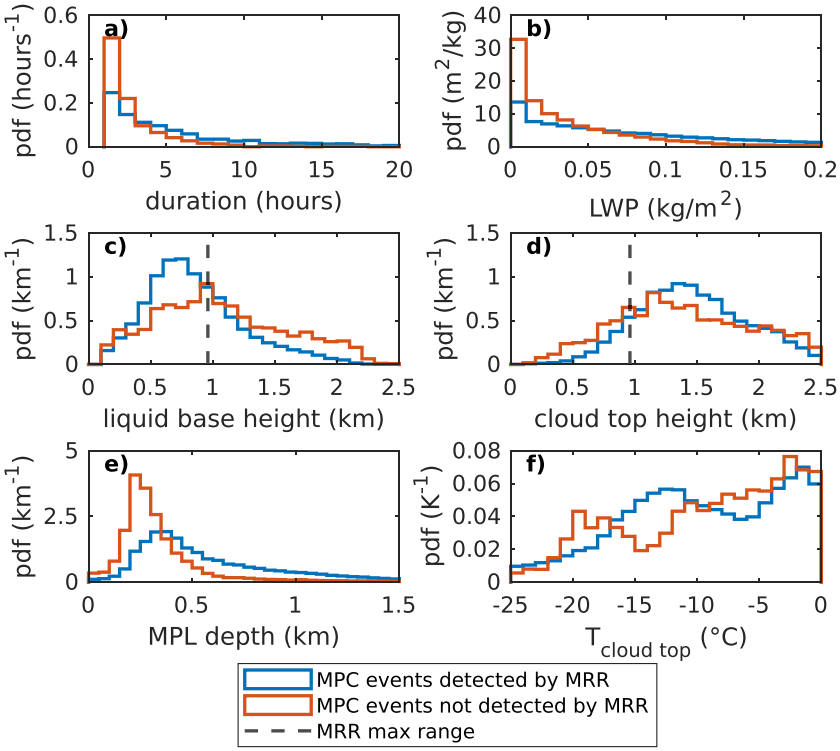

Figure 2. Statistics of mixed-phase cloud characteristics in Ny-Ålesund. Probability density functions (PDFs) are shown for events detected by the Micro Rain Radar (MRR), and for events that were not detected by the MRR, and thus were only detected by the W-band cloud radar. The parameters shown are MPC event duration (a), liquid water path (LWP; b), liquid-base height (c), cloud-top height (d), mixed-phase layer depth (e), and cloud-top temperature (f). The dashed lines in panels c and d indicate the maximum range of the MRR. Bin sizes are respectively: 1 hr, 10 g m^{-2}, 100 m, 100 m, 50 m, 1°C.

triple-wavelength observations in midlatitude clouds by Dias Neto et al. (2019) and Ori et al. (2020). The main difference in our study is that we focus on low-level MPCs and are restricted to the lowest 960 m, as well as clouds that produce large enough Z_e signals to be detected by the MRR. The DWR and MDV statistics in Figure 3 are displayed as contoured frequency by temperature diagrams (CFTDs; Yuter & Houze, 1995). Here, DWR and MDV values are matched with temperature (T) retrieved at the same height, and the figure displays joint histograms of DWR and T (panel a), and MDV and T (panel b). These histograms are normalized to one at each chosen T level. Note that, unlike many other studies where CFTDs are employed, panels (a) and (b) in Figure 3 should not be interpreted as continuous profiles. Because of the limited depth of low-level MPCs, and the limited range of the MRR, each available profile only spans a portion of the displayed temperature range. The mean temperature difference between the lowest W-band cloud radar range gate (100 m), and the highest MRR range gate (960 m) is 5.2°C, with 1.8°C standard deviation. The total number of samples (Figure 3c) reveals that 90% (95%) of observations occur at temperatures higher than −12.7°C (−15.1°C), with maxima at −10 and 0°C.

Figure 3 displays that at temperatures colder than −15°C median DWR values are close to 1 dB, corresponding to median sizes smaller than 1 mm. Median DWR then rapidly increases to 4.1 dB between −15 and −12°C. These enhanced DWR signals can be found at temperatures as high as −6°C, with a distinct maximum between −12 and −8°C (5.6 dB). At temperatures close to 0°C, the median DWR decreases back to lower values, with a median of 2.7 dB between −5 and 0°C. Similarly, median MDV in Figure 3b has a relatively constant value of 0.6 m/s between −20 and −12°C, typical for small ice crystals (Barthazy & Schefold, 2006; Heymsfield & Westbrook, 2010; Kajikawa, 1972; Mitchell, 1996), grown most likely by vapor deposition. At the −13°C level where the DWRs increase, we also find the MDVs to increase. Interestingly, while the DWRs seem to remain almost constant between −12 and −8°C, the MDVs steadily increase, reaching values close to 1 m/s, which is a typical terminal velocity of larger aggregates (Brandes et al., 2008; Heymsfield et al., 2007; Karrer et al., 2020; Locatelli & Hobbs, 1974). A similar behavior in terms of both DWR and MDV can be noticed in the case study in Figure 1 as well. Combining DWR and MDV information, together with previous knowledge from

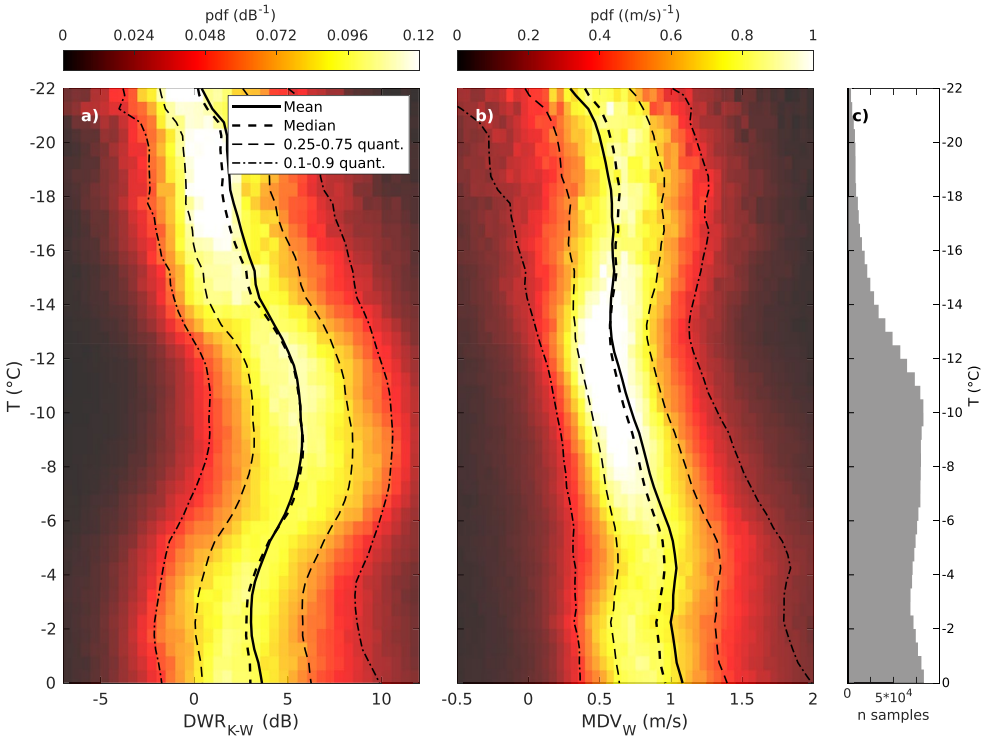

Figure 3. Contoured frequency by temperature diagram (CFTD) of dual-wavelength ratio (DWR; panel a) and mean Doppler velocity (MDV; panel b) in the detected mixed-phase cloud events. Panel (c) displays the number of samples available at each temperature level. MDV values are only included if Micro Rain Radar (MRR) echoes are available. Bin sizes are: 1 dB, 0.05 m/s, and 0.5°C.

midlatitude clouds, we thus hypothesize that aggregation might play an important role in the formation of the high DWR hydrometeors we observe between −15 and −5°C. The region of increasing DWR starting at −15°C is likely associated with rapid depositional growth of branched dendritic particles in the DGZ, which subsequently aggregate. An increase in DWR associated with enhanced aggregation in the DGZ has been previously observed in midlatitude clouds (Barrett et al., 2019; Dias Neto et al., 2019; Lamer et al., 2021; Ori et al., 2020; Oue et al., 2021). The presence of high DWR particles at temperatures warmer than −10°C in Figure 3a could be simply a result of particles that mainly aggregated in the DGZ and then sedimented to warmer temperatures, while continuing to aggregate.

The low fall velocities observed in Figure 3b at temperatures colder than −5°C are not indicative of severe riming that could explain the observed DWRs. However, we cannot rule out the possibility of light riming of the larger aggregates, as well as smaller rimed particles, as their terminal fall velocities could overlap with the fall velocity of larger, unrimed aggregates. Riming has in fact been observed to occur frequently in Arctic MPCs (Fitch & Garrett, 2022; McFarquhar et al., 2007; Mioche et al., 2017). However, the MDVs from 72.3% (82.7, 91.6%) of the observed echoes are slower than 1.0 m/s (1.2, 1.5 m/s) between −15 and −5°C, which corresponds to a rime mass fraction of 0.31 (0.47, 0.65) according to Kneifel and Moisseev (2020). It further appears unlikely that the DWR increase at −15°C is mainly driven by riming: first, we are not aware of any evidence that riming preferentially occurs at −15°C. Second, in this temperature regime, the Wegener-Bergeron-Findeisen process has its maximum (Korolev & Mazin, 2003) and has been shown to hamper the formation and survival of liquid droplets (Silber et al., 2021).

Although the DWRs at temperatures warmer than −5°C decrease back to lower values (median of 2.7 dB between −5 and 0°C), the MDVs remain almost constant, close to 1 m/s (median of 1.1 m/s between −5 and 0°C). One potential explanation for this signature could be the higher terminal fall velocity of needle particles, which, together with columns, preferentially grow at temperatures higher than −10°C by vapor deposition (e.g., Bailey & Hallett, 2009). They can reach terminal velocities close to 1 m/s at smaller sizes compared to plate-like particles

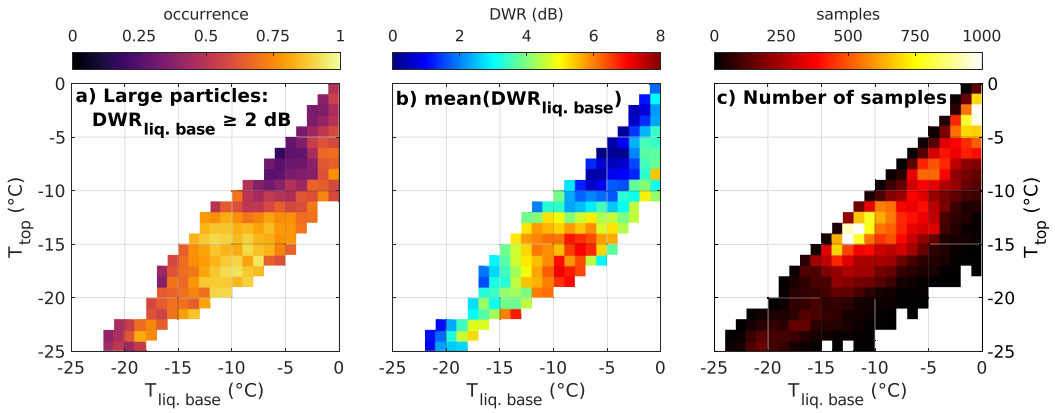

Figure 4. Frequency of occurrence of dual-wavelength ratio (DWR) above 2 dB at liquid base (a), mean DWR at liquid base (b), and number of samples at liquid base (c) as function of cloud-top and liquid-base temperature. In panels (a) and (b), bins with less than 60 total samples are ignored. Bins are 1°C wide.

(Kajikawa, 1972; Mitchell, 1996). Also, the presence of supercooled drizzle and potential enhanced riming of smaller ice particles with low DWR could explain the observed behavior. The likelihood for the formation of drizzle and intensified riming has been found to strongly increase at temperatures closer to the melting level (Cortinas Jr et al., 2004; Kneifel & Moisseev, 2020; Zhang et al., 2017). Overall, the DWR-MDV behavior found for MPCs at temperatures close to 0°C is significantly different from what is observed at the midlatitudes. Several studies observed a second and even stronger DWR increase from −5°C toward the melting level (Chase et al., 2018; Dias Neto et al., 2019; Ori et al., 2020; Tridon et al., 2019). Interestingly, we are able to find a similar behavior also in Ny-Ålesund in cloud systems that are deeper than 2.5 km, as shown in Appendix C. The lack of aggregation close to the melting level in the detected low-level MPC events is further explored in the next section.

4.3. Precipitation Formation in the Mixed-Phase Layer

In the previous section, we analyzed DWR values with respect to temperature retrieved at the same height. We can assume that in low-level MPCs, the main nucleation and initial depositional growth takes place in the mixed-phase layer (MPL), where on average saturation with respect to liquid water is reached. Therefore, we investigate how much the particles already aggregate in the MPL and how relevant the temperature of the MPL is for the occurrence of larger aggregates in the entire profile.

We analyze the DWRs observed at the liquid-base height, and relate it to the cloud-top and liquid-base temperatures in Figure 4. For a simpler interpretation, in panel a, we group the profiles into small particles (DWR at liquid base lower than 2 dB, corresponding to a mass median diameter of approximately 1.3 mm; see Figure A1 in Appendix A) and larger particles (DWR at liquid base equal or higher than 2 dB), that are most likely a result of aggregation and/or riming. The threshold of 2 dB was also chosen because of the estimated uncertainty on DWR of 2.1 dB. DWR values higher than 2 dB can thus confidently be attributed to non-Rayleigh scattering by hydrometeors. We also tested slightly different DWR thresholds but did not find a substantial impact on the results (not shown). Figure 4a thus shows the frequency of occurrence of DWRs at liquid base higher than 2 dB. Panels (b) and (c) in the figure display the mean DWR value at liquid base, and number of available samples, respectively, both as function of liquid-base temperature and CTT.

Figure 4a illustrates that large particles appear to mainly originate from mixed-phase layers with liquid-base temperature higher than −15°C and CTT lower than −10°C. In this temperature regime, 76.8% of the samples in fact display DWRs at liquid base of 2 dB or larger. The mean DWR value at liquid base (Figure 4b) also illustrates that even very thin MPLs on average generate particles with DWRs of 5 dB or higher, if they contain temperatures of −13 to −14°C. Interestingly, this overlaps with the −15.5 to −13.3°C interval, where the laboratory study by Takahashi (2014) observed the maximum growth rate of plate-like crystals. As expected, if the MPL is thicker (larger difference between cloud-top and liquid-base temperature), also the mean DWRs increase, because of the longer time particles can grow by deposition and subsequent aggregation.

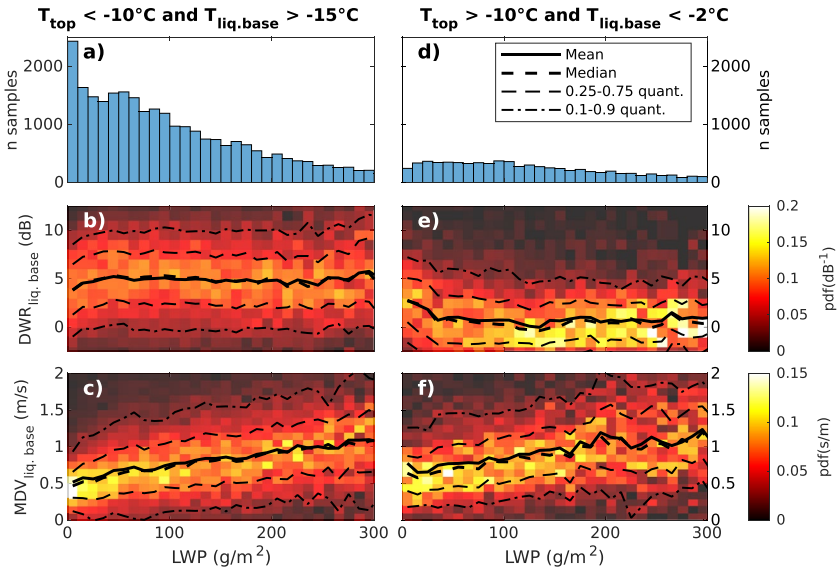

Figure 5. Liquid water path (LWP) distribution (a, d), and joint LWP-DWR (b, e), and LWP-MDV (c, f) distributions for mixed-phase cloud (MPC) events in two distinct regimes. Panels (a–c) include MPC events whose mixed-phase layer is at least partly in the temperature interval between −15 and −10°C. Panels (d– f) include MPC events whose mixed-phase layer temperature does not exceed −2°C and does not succeed −10°C. The joint distributions in panels (b, c, e, and f) are normalized to one in each LWP bin. Bin widths are: 5 g/m^2, 0.5 dB, and 0.05 m/s.

Figure 4b shows that enhanced DWR values can also be found in MPLs at temperatures colder than −15°C (i.e., liquid-base temperature colder than −15°C in the figure), namely temperatures belonging to the colder portion of the DGZ, or colder than the DGZ completely. However, the mean DWR and overall frequency of occurrence are generally much lower than what we observe when temperatures between −15 and −10°C are observed in the MPL: this is clearly indicated by the low number of samples in Figure 4c for cases with liquid-base temperature colder than −15°C. Interestingly, for the events with liquid-base temperature colder than −15°C, the MPL also needs to be deeper (i.e., larger temperature difference between cloud top and liquid base) to produce enhanced DWRs.

The dependence of DWR and MDV at liquid base on LWP is shown in Figure 5, for two separate temperature regimes. Enhanced aggregation in the −10 to −15°C temperature region appears to occur already at relatively small LWP values. No substantial change in DWR is found for increasing LWP. This independence can be interpreted as a proof that the observed DWR signature is mainly caused by aggregation rather than riming as the latter would be expected to increase with LWP. However, Figure 5c shows that the MDV observed at the liquid base continuously increases with larger LWP. We suspect that, while riming is not the main mechanism that increases DWR, it is still contributing to the observed increasing particle fall speeds by increasing ice particle density.

4.3.1. Discussion: Rapid Depositional Growth and Subsequent Aggregation in the DGZ

The preferential growth of dendrites in the DGZ is thought to lead to a more efficient aggregation, compared to other temperature regions (Pruppacher & Klett, 2012, Section 14.7), although many details of these processes are still not thoroughly understood. We believe that the signatures found in this study are particularly valuable to better constrain the process of dendritic growth and subsequent aggregation. Unlike in deeper clouds, no particles from above enter the DGZ in the low-level MPCs that are the focus of this study. Instead, we can assume that all ice particles are nucleated and grown within the relatively narrow region of the mixed-phase layer. We can further assume that the majority of particles in the MPL grow in conditions that are close to liquid water saturation. This allows to compare and relate our results directly to recent laboratory experiments investigating depositional growth (Takahashi, 2014) or aggregation (Connolly et al., 2012) in the temperature regime of the DGZ.

A number of factors are known to be mainly responsible for the rapid formation of aggregates in the DGZ. Here, the maximum difference between liquid and ice saturation pressures is found (Pruppacher & Klett, 2012), and a maximum of the Wegener-Bergeron-Findeisen (WBF) process is observed (Korolev, 2007). At these

temperatures, if high enough ice supersaturations are reached, ice particles grow into dendritic shape (Bailey & Hallett, 2009; Pruppacher & Klett, 2012, Section 13.3), which is connected to enhanced capacitance (Westbrook et al., 2008; Pruppacher & Klett, 2012, Section 13.3) and ventilation coefficients (Takahashi et al., 1991). All these effects together lead to a maximum in the water vapor depositional growth on ice particles in this temperature region (Takahashi, 2014; Takahashi et al., 1991). As already mentioned, Takahashi (2014) found that the depositional growth rate is maximized between −15.5 and −13.3°C (see their Figure 6). After a growth time of 10 min, they observed particles reaching maximum sizes of 1.5–1.8 mm with preferentially stellar, dendritic or fern-like habits. This temperature region coincides with the MPL temperatures where we observed the largest DWRs in Figure 4b.

In addition to the very favorable depositional growth conditions, the slower terminal fall velocities of dendrites compared to other shapes with similar mass (e.g., Kajikawa, 1972; Mitchell, 1996) allow them to stay in the supersaturated layer of the cloud for a longer time compared to other ice habits. For example, a 1 mm dendrite falls at 0.3 m/s while the same sized column, which grows for example, at temperatures higher than −10°C, has a terminal velocity of 0.8 m/s (Mitchell, 1996). The rapid depositional growth will eventually lead to a sufficiently large diversity of terminal velocities and particles sizes needed for collisions. Moreover, turbulent motions frequently observed in the MPL (e.g., Morrison et al., 2012) can be expected to further enhance the likelihood for particle collisions. Their unique shape allows them to stick to each other by mechanical entanglement of their branches (Connolly et al., 2012; Pruppacher & Klett, 2012, Section 14.7).

4.3.2. Discussion: On the Absence of Aggregation Close to the Melting Level

The question remains, why do we not observe major DWR increases due to particle aggregation close to the melting level in low-level MPCs? Figure 4 highlights that increases in DWR are indeed observed at the liquid base, when its temperature is between −2 and 0°C. Considering the 1.6–2.0K uncertainty of the temperature retrievals in the MPL, we cannot exclude that this signature is caused by melting particles. Even if melting particles are not responsible for the enhanced DWRs, the DWRs found close to 0°C in Figures 3 and 4 are still significantly smaller than those observed in previous studies in midlatitude clouds (Chase et al., 2018; Dias Neto et al., 2019; Ori et al., 2020; Tridon et al., 2019), and in deeper cloud systems in Ny-Ålesund as well (Appendix C).

In general, enhanced aggregation close to the melting level is thought to be caused by the thickening of a quasi-liquid layer on the snowflake surface (Fabry & Zawadzki, 1995; Fletcher, 1962; Slater & Michaelides, 2019). This quasi-liquid layer forms on any ice particle, whether being a single crystal, aggregate, or rimed particle, and it increases its aggregation efficiency by enhancing its sticking efficiency. In extreme scenarios, this can lead to the formation of snowflakes several centimeters in size (Lawson et al., 1998). The absence of this second enhanced aggregation zone could be related to lower ice number concentrations in low-level MPCs at temperatures warmer than −10°C, compared to MPCs at dendritic-growth temperatures. However, the studies by Rangno and Hobbs (2001) and Mioche et al. (2017) have shown otherwise. They reported, based on airborne in-situ observations, that MPC events with CTT between −10 and 0°C, and MPC events with CTT between −20 and −10°C display similar ice number concentrations. Furthermore, signatures of secondary ice processes have been observed in Arctic MPCs close to the melting level (Luke et al., 2021).

Although we cannot provide a conclusive answer to this question with our remote sensing observations alone, we discuss possible processes that could lead to the observed lack of aggregation. First, the depositional growth rate at temperatures higher than −10°C is at least 1 order of magnitude smaller than at −15°C (see e.g., fig. 4 in Takahashi et al. (1991)). Due to the higher terminal fall velocities of columns, needles, and isometric particles, which are often observed in this temperature regime, the time for the particles to grow by deposition is also much shorter than in the DGZ. Due to this effect, particle populations that are fully nucleated at temperatures warmer than the DGZ might not develop broad enough size distributions to aggregate as efficiently as particles nucleated in or above the DGZ, despite the increase in sticking efficiency at temperatures higher than −5°C. Although we are not aware of evidence in literature to fully support this claim, Field et al. (2005) did report on average broader ice PSDs in the −5 to −15°C range, compared to the +5 to −5°C temperature interval, in midlatitude stratiform clouds, based on in-situ airborne observations. We thus hypothesize, that particle populations nucleated at temperatures compatible with dendritic-growth, or colder, are needed to trigger the typically observed enhanced aggregation close to the melting level. This is not the case in the low-level MPCs that are the focus of this study, as their limited depth often leads to CTT being warmer than −10°C when temperatures higher than −5°C are observed in the MPL.

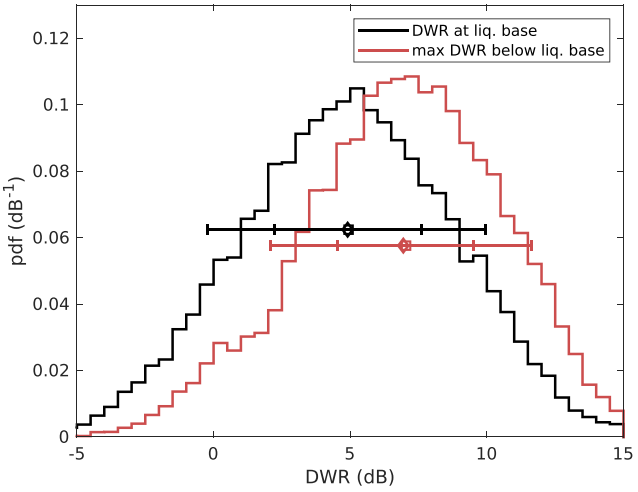

Figure 6. Probability density functions (PDFs) for dual-wavelength ratio (DWR) values at and below the liquid base in low-level mixed-phase clouds (MPCs). The black line is relative to values observed at liquid base, while the red line is relative to the maximum DWR value observed in each column below the liquid base. Error bars display 0.1, 0.25, 0.75, and 0.9 quantiles of the two distributions, with diamonds representing the mean values, and squares representing the median values. The data used are only for MPC events with liquid base temperature higher than −15°C and cloud-top temperature lower than −10°C. Samples with surface temperature warmer than 0°C are excluded. Bins are 0.5 dB wide.

A more frequent occurrence of riming, which was found in Kneifel and Moisseev (2020) to rapidly increase from −12°C toward 0°C, could further enhance the particles' terminal velocities and limit their residence time in the MPL. A suppression of aggregation by riming has been in fact suggested by Li et al. (2020), who observed lower DWRs (at X-band and Ka-band) in rimed snow, compared to unrimed snow, close to the melting level of stratiform precipitation events at Hyytiälä, Finland. Increased riming is likely in warmer MPC events at Ny-Ålesund, as remote sensing observations of single-layer MPCs at the site have shown a liquid fraction above 0.9 in more than 90% (80%) of the cases, when CTT is higher than −5°C (between −10 and −5°C) (Nomokonova, Ebell, et al., 2019). In contrast, liquid fractions for single-layer MPCs with CTTs between −15 and −10°C are below 0.8 in approximately 50% of the cases (Nomokonova, Ebell, et al., 2019). The dependence of DWR and MDV on LWP for MPCs in this temperature regime displayed in Figures 5e and 5f is also compatible with increased riming. DWR values are in fact close to 0 dB for LWP values larger than 15 g/m^2, and MDV values tend to increase with increasing LWP.

4.4. Further Aggregation Below the Mixed-Phase Layer

While the growth of dendritic branches from ice particles is likely to mostly take place in the mixed-phase layer of the MPC, as it requires high supersaturations with respect to ice (Pruppacher & Klett, 2012, Section 2.2), aggregation of ice particles can be expected to continue below it. Further increases in DWR below the MPL are in fact observed in the case study shown in Figure 1, for example, on February 4, 2021 between 7 and 11 UTC or between 22 and 24 UTC on the same day. In this section, we evaluate the further DWR increase below the MPL and how strong this increase is in relation to the aggregation signal at the liquid base. We restrict the analysis to profiles where the liquid-base temperatures are higher than −15°C and the CTTs are lower than −10°C as this is the region where we find the majority of large DWR signatures at liquid base. Connecting processes at different heights in one vertical profile is challenging, as the particles are advected by changing horizontal winds often causing complex fall streaks in the radar time-height display (Kalesse, Szyrmer, et al., 2016; Pfitzenmaier et al., 2017, 2018). To avoid these difficulties, we do not directly compare DWR values measured at different heights in the same column. Instead in Figure 6, we analyze the distributions of DWR values observed at the liquid base, and of the maximum DWR values observed below the liquid base in each column. Note that in a given column, these two values can be the same, if the maximum DWR is at liquid base: this is observed in 15.3% of the available samples. In order to avoid high DWR signals originating from melting particles, samples measured when surface temperature was warmer than 0°C are ignored in this analysis.

From Figure 6, it is clear that aggregation continues to increase mean aggregate size despite the likely sub-saturated air below liquid base (e.g., Shupe et al., 2008). The median (mean) of the largest DWRs observed below the MPL is 7.0 dB (6.9 dB), and is 43% (41%) larger than the median (mean) DWR of 4.9 dB (4.9 dB) at liquid base. Below the liquid base, we can attribute most of the DWR increase to aggregation, as riming cannot occur because of the absence of liquid water. The narrower distribution of the maximum DWR below liquid base is due to the fact that the DWRs approach the saturation value, as the particle sizes grow. DWR saturation values for unrimed and lightly rimed aggregates have been estimated in Appendix A to be 10–11 dB for the 24 and 94 GHz combination.

4.5. Persistence of High DWR Signals

Several previous studies demonstrated that Arctic MPCs display a complex horizontal structure, and high spatial variability in terms of dynamics and hydrometeors (Eirund et al., 2019; Ruiz-Donoso et al., 2020; Schäfer et al., 2018; Shupe et al., 2008). It appears therefore interesting to investigate whether the observed high DWR signatures are restricted to limited regions of the MPC, as observed in Figure 1, or whether enhanced aggregation tends to occur uniformly across the cloud field.

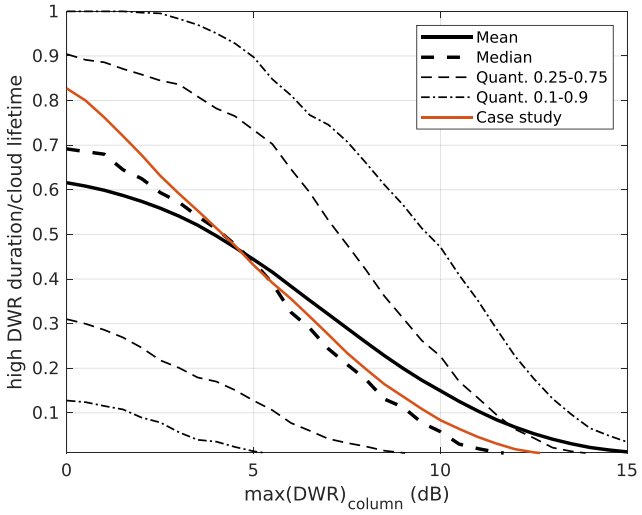

Figure 7. Distributions of the ratio between the duration of high dual-wavelength ratio (DWR) signals and the total duration of the mixed-phase cloud (MPC) event. The duration of high DWR signals is calculated as the total time during an MPC event that the maximum DWR in each column exceeds the value indicated on the *x*-axis. The curves indicate the mean, median, and quantiles of the duration ratio. Only MPC events with the mixed-phase layer at least partly at temperatures between −15 and −10°C are included. The red curve represents the case study observed on February 4–6, 2021, illustrated in Figure 1. Note that the quantity indicated on the *y*-axis, being a ratio between time intervals, is unitless.

The vertically pointing radars used in this study do not resolve the complete horizontal structure of the cloud field but rather observe the variability of clouds that are advected over the measurement site. The observed variability is thus usually a combination of temporal and spatial variability, and spatial variability is only resolved along the wind direction (e.g., Shupe et al., 2008). We estimated the duration of DWR signals exceeding certain thresholds and related them to the total duration of the MPC event (detected by the more sensitive W-band cloud radar, see Section 3). The full distribution of this quantity, together with its values for the case study in Figure 1, is shown in Figure 7. Note that, unlike the statistics presented in Sections 4.2–4.4, all available samples during MPC events were analyzed, including those with no signal in the MRR data. We would like to also highlight that the statistics shown in Figure 7 are sensitive to the definition of MPC event, as this in turn affects the event duration.

For interpreting Figure 7, it might help to consider first the red curve which represents the distribution of DWR in relation to the event duration from the case study shown in Figure 1. We see that cloud regions where the maximum DWR in each column exceeds 5 dB appear for 43.1% of the total MPC duration. Higher DWR values, for example, exceeding 8 dB, are only observed for 19.8% of the total duration of the event. The tendency of finding larger DWR values in shorter time periods of the cloud can also be observed when looking at the temporal DWR evolution shown in Figure 1c. High DWRs in the case study do not display a straightforward relation with features in the MDV (e.g., upward motions) or the reflectivity field.

Similarly to the case study, 50% of all MPC cases (median line) display DWR values larger than 5 dB for at least 43.8% of the event duration. For larger DWR thresholds, the quantile curves bend relatively quickly to decreasing duration ratios. Again, this result highlights that high DWR particles appear to form in limited regions of the cloud layer and for a limited amount of time, when compared to the cloud overall extent and duration. In summary, Figure 7 reveals that 50% of the observed MPCs display DWR values equal or higher than 2 (5, 8) dB for at least 62.5% (43.8%, 17.5%) of the total cloud duration. At the same time, 25% of the observed MPCs display DWR values equal or higher than 2 (5, 8) dB for at least 84.5% (70.2%, 36.1%) of the total cloud duration.

The analysis shown in the previous sections strongly suggests that temperatures compatible with the DGZ are essential in order for MPCs to produce large aggregates. However, their occurrence in limited regions of the MPC indicates that temperature might not be the only driver. Previous studies have shown that dynamical processes are essential in producing ice precipitation in Arctic MPCs, and that precipitation is in turn intertwined with the organization of the stratocumulus deck (Eirund et al., 2019; Shupe et al., 2008). At the same time, aerosol concentrations, surface conditions, and surface coupling significantly affect the phase partitioning (Gierens et al., 2020; Griesche et al., 2021; Kalesse, de Boer, et al., 2016; Norgren et al., 2018; Solomon et al., 2018). While we highlighted the relevance of the DGZ for the formation of large aggregates in low-level MPCs at Ny-Ålesund, investigating the role of individual processes for the formation of said aggregates is out of the scope of this study.

5. Conclusions and Open Questions

Using a combination of remote sensing instruments, in particular, a 24-GHz precipitation radar and a 94-GHz cloud radar, we evaluated the significance of different ice-growth processes, with a focus on aggregation, for the formation of precipitation in low-level MPCs at the high Arctic site of Ny-Ålesund. The combination of equivalent reflectivity factors measured at two radar frequencies into the DWR was used to obtain information on the characteristic size of the particle population. The 3-year statistics of DWR, matched with MDV, thermodynamic retrievals from a microwave radiometer, and phase information from the Cloudnet target classification, provided robust observational constraints for the microphysical processes leading to the formation of precipitation in low-level MPCs at the site.

This study revealed the unique role of the DGZ in the formation of precipitable ice particles in low-level MPCs at Ny-Ålesund, together with the absence of enhanced aggregation typically observed close to the melting level in deeper cloud systems. The main findings of this study are as follows:

1. Enhanced DWR signatures occurred predominantly in low-level MPCs whose mixed-phase layer was, at least partly, at temperatures between −15 and −10°C. This feature is compatible with similar signatures observed at the midlatitudes (Barrett et al., 2019; Dias Neto et al., 2019). This signature is typically attributed to enhanced aggregation due to mechanical entanglement of ice particles with dendritic branches, which preferentially grow in this temperature region (Pruppacher & Klett, 2012, Sections 2.2 and 14.7). In particular, the highest DWR values at the liquid base of the MPC were observed in conjunction with temperatures of −13 to −14°C, in agreement with laboratory studies that reported the highest depositional-growth rates at these temperatures (Takahashi, 2014; Takahashi et al., 1991). While riming likely also plays a role, as confirmed by increasing MDV with LWP, we argue that the growth of the larger ice particles is to be mainly attributed to rapid depositional growth of plate-like particles, and subsequent aggregation. Moreover, the relevance of aggregation in low-level MPCs in this temperature region is further confirmed by the additional increase in DWR observed below the liquid base, where riming cannot take place.
2. While our results demonstrate that mixed-phase layer temperatures compatible with dendritic growth are essential for the formation of large aggregates, these larger hydrometeors are only observed in limited regions of the cloud field. This suggests that dynamical processes might be at play in the formation of these larger aggregates. We reckon that further investigation is needed to understand the link between the growth of dendritic particles and their subsequent aggregation, and dynamics in low-level MPCs throughout the Arctic region.
3. Typically a second enhanced aggregation zone close to 0°C is observed in midlatitude clouds (Dias Neto et al., 2019; Fabry & Zawadzki, 1995), and in deeper cloud systems in Ny-Ålesund as well. This is usually attributed to the increased sticking efficiency of melting ice particles. The lack of high DWR signals close to the melting level (−5 to 0°C) in low-level MPCs in Ny-Ålesund suggests that this process is absent in these clouds. Since low-level MPCs span a limited temperature range, particles sedimenting from colder temperatures, characterized by a broader size distribution, might be necessary to trigger the enhanced aggregation typically observed. As such, further investigating this temperature regime bears the potential to substantially improve our understanding of aggregation in general, not only limited to low-level MPCs. While we cannot provide a conclusive answer from the remote-sensing perspective, we speculate that specific ice habits and increased riming might contribute to the suppression of aggregation. Ice habits that grow at temperatures higher than −10°C typically have faster fall velocities and smaller cross sections than dendrites (Kajikawa, 1972; Mitchell, 1996; Pruppacher & Klett, 2012, Sections 2.2, 10.5). Additionally, lower depositional growth rates have been reported at temperatures warmer than −10°C, compared to dendritic-growth temperatures (Takahashi et al., 1991). MDV information, together with evidence of increased drizzle production and riming reported in previous studies (Cortinas Jr et al., 2004; Kneifel & Moisseev, 2020; Nomokonova, Ebell, et al., 2019; Zhang et al., 2017), indicates that riming might also be relevant at these temperatures, and might suppress aggregation.

While it is reasonable to assume that similar microphysical processes occur in low-level MPCs throughout the whole Arctic region, because of the homogeneous characteristics that they display across different sites (de Boer et al., 2009; Gierens et al., 2020; Morrison et al., 2012; Nomokonova, Ebell, et al., 2019; Shupe, 2011; Shupe et al., 2006; Zhao & Wang, 2010), this hypothesis should be tested by looking for similar observational fingerprints at other Arctic observatories. The multi-frequency and Doppler radar observations presented in this study provided strong observational constraints for the microphysical processes taking place in low-level MPCs at Ny-Ålesund, nevertheless the range of observational fingerprints can be substantially extended with polarimetric observations. The recent extension of the AWIPEV site with a polarimetric Ka-band radar will allow us to better constrain ice particle concentration and shape in the future. It will further enable us to obtain DWR profiles reaching cloud top, as well as overcome the sensitivity limitations of the MRR. In this regard, dual-frequency cloud radar observations provide the unique opportunity to test and improve the representation of ice-growth processes in numerical models (Karrer et al., 2021; Ori et al., 2020), and this possibility will be in the future explored with the ICOsahedral Non-hydrostatic (ICON) modeling framework (Zängl et al., 2015), in its Large Eddy Model (LEM) version.

Appendix A: Examples of DWR Dependence on Particle Size

Figure A1 illustrates examples of DWR dependence on ice particle shape and size. DWR values were computed using the scattering database developed by Ori et al. (2021). PSDs are assumed to be inverse exponential, and the figure shows the dependency of DWR on the mass median diameter $D0$. The chosen particle types are: unrimed dendrite aggregates, unrimed column and dendrite aggregates, and rimed column and dendrite aggregates. Three values for the degree of riming have been chosen, indicated by the effective LWP (ELWP): 0.1, 0.2, and 0.5 kg/m^2. ELWP is defined as the LWP that produces the simulated amount of riming, assuming a riming efficiency of 100% (Leinonen et al., 2018; Leinonen & Szyrmer, 2015). The figure shows that DWR is 0 dB when $D0$ is 1 mm for all particle types, it then rapidly increases as $D0$ increases. It then reaches a saturation value between 10 and 11 dB for unrimed and lightly rimed (ELWP = 0.1, 0.2 kg/m^2) aggregates, when $D0$ is above 10 mm. The saturation value is higher for higher degrees of riming.

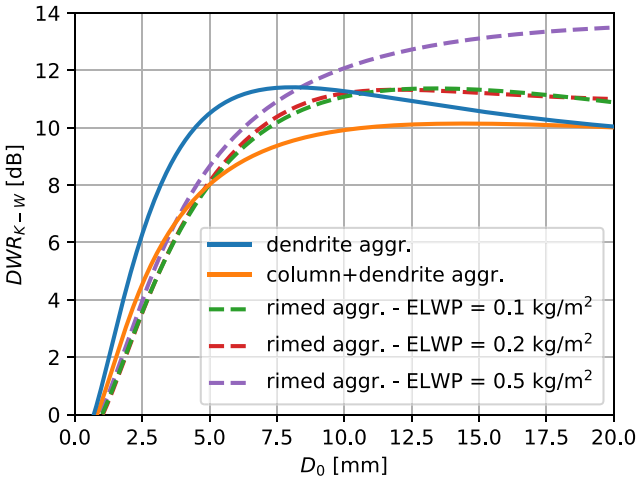

Figure A1. Calculation of dual-wavelength ratio (DWR) at K-band (24.2 GHz) and W-band (94.0 GHz) for different ice particle types, as function of the mass median diameter $D0$, obtained with the scattering database by Ori et al. (2021). The ice particles included are: unrimed dendrite aggregates, unrimed dendrite and column aggregates, and rimed dendrite and column aggregates. The degree of riming for the rimed aggregates is indicated by the effective liquid water path (ELWP, see text for definition).

Appendix B: Example of the Calibration Procedure and List of Derived Calibration Offsets

Figure B1 shows an example of the calibration procedure described in Section 3.2.1. The figure depicts a monthly histogram of DWR for the month of December 2020, before (a) and after (b) applying the calibration procedure. Only data observed during calibration events (see Section 3.2.1) are included. The calibration procedure consists in determining the mode of the uncalibrated DWR histogram (vertical line in panel a), which is then used as monthly offset for the W-band reflectivities. This approach thus relies on the assumption that the peak of the distribution is associated with Rayleigh scattering, and the tail on the right side of the peak is associated with non-Rayleigh scattering. The offset is then added to all W-band reflectivities, leading to the whole histogram being shifted so that its mode is now at 0 dB (panel b, dashed vertical line). The uncertainty on DWR is calculated by assuming that all DWR values on the left side of the peak are associated with Rayleigh scattering. The left-side standard deviation (i.e., only for calibrated DWR values lower than 0 dB) with respect to the mode is thus taken as uncertainty (dash-dotted line in panel b).

All derived monthly offsets for all radar systems are displayed in Table B1.

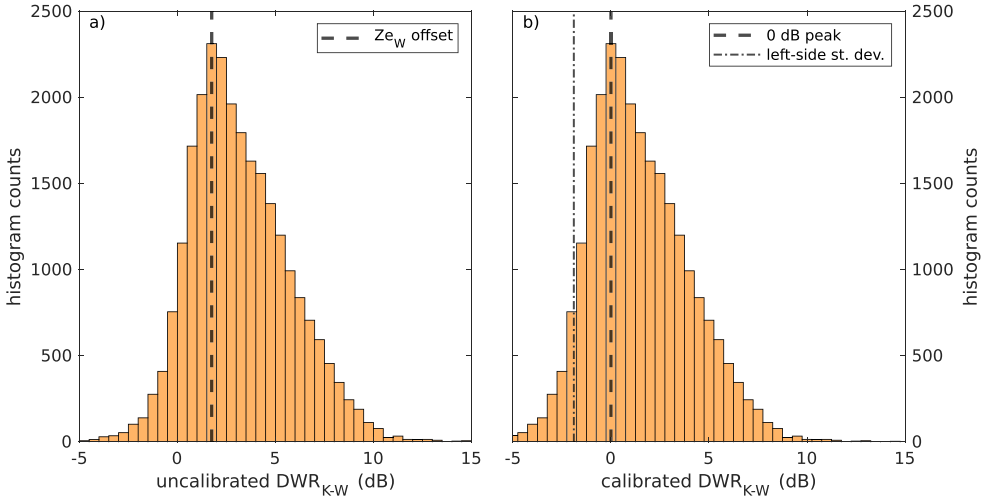

Figure B1. Monthly dual-wavelength ratio (DWR) histograms for the month of December 2020 before (panel a) and after (panel b) applying the calibration procedure. Only DWR values observed during calibration events are included in the histogram. The dashed vertical lines in panels (a) and (b) indicate the mode of the distribution, while the dash-dotted vertical line in panel (b) indicates the left-side standard deviation with respect to the mode. See text for more details. Bins in both histograms are 0.5 dB wide.

Table B1
Monthly Calibration Offsets Obtained for the Three Radar Systems Used in the Study, Expressed in dB

Month	09/2017	10/2017	11/2017	12/2017	01/2018	02/2018	03/2018	04/2018	05/2018	06/2018	07/2018	08/2018	09/2018	10/2018
MRR-2	−0.81	(−0.87)	(−0.92)	(−0.98)	(−1.04)	(−1.10)	(−1.15)	(−1.21)	(−1.27)	−1.33	−1.33	−1.33	−1.33	(−1.35)
MiRAC-A	−0.75	2.75	3.25	3.75	2.25	4.75	2.25	2.75	2.75	1.25	0.75	0.75	1.25	2.75
Month	06/2019	07/2019	08/2019	09/2019	10/2019	11/2019	12/2019	01/2020	02/2020	03/2020	04/2020	05/2020	06/2020	07/2020
MRR-2	−1.57	−1.57	−1.57	−1.57	(−1.61)	(−1.64)	(−1.68)	(−1.71)	(−1.74)	(−1.78)	(−1.81)	(−1.85)	−1.88	−1.88
JOYRAD-94	1.75	−0.25	−0.25	−0.25	0.75	1.25	2.25	2.25	1.75	0.75	0.75	5.25	0.25	−0.25
Month	08/2020	09/2020	10/2020	11/2020	12/2020	01/2021	02/2021	–	06–09/2021					
MRR-2	−1.88	−1.88	(−1.88)	(−1.89)	(−1.89)	(−1.89)	(−1.90)	–	−1.91					
JOYRAD-94	−0.25	1.25	−0.25	3.25	1.75	1.25	1.25	–	–					

Note. Values indicated in parentheses were obtained by linear interpolation.

Appendix C: DWR Signatures in Deep Cloud Systems in Ny-Ålesund

Similarly to Figure 3, Figure C1 displays CFTDs of DWR and MDV. All cloud systems with cloud-top height higher than 2.5 km detected during the study period were included in this figure, adding up to a total duration of 2,941 hr. DWR and MDV values are matched with temperature (T) retrieved at the same height, and the figure displays joint histograms of DWR and T (panel a), and MDV and T (panel b).

In addition to the typical increase in DWR corresponding to the DGZ (Barrett et al., 2019; Dias Neto et al., 2019; Lamer et al., 2021; Ori et al., 2020; Oue et al., 2021), the figure displays a further increase in DWR close to the melting level, which is typically observed at the midlatitudes (Chase et al., 2018; Dias Neto et al., 2019; Ori et al., 2020; Tridon et al., 2019).

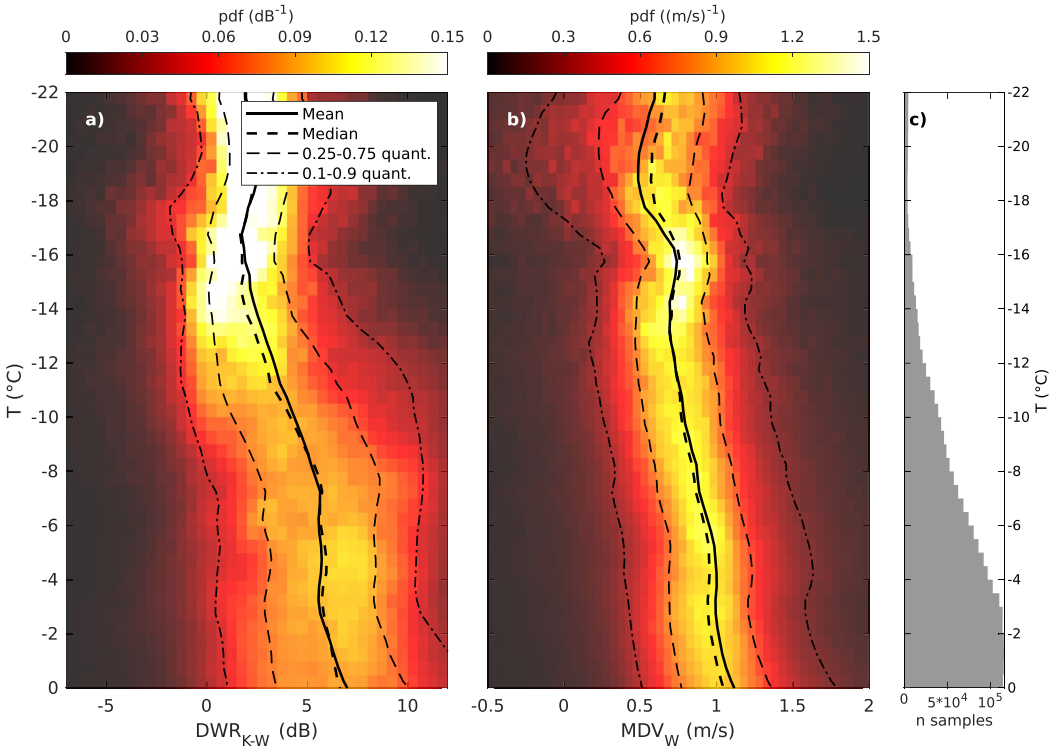

Figure C1. Contoured frequency by temperature diagram (CFTD) of dual-wavelength ratio (DWR) and mean Doppler velocity (MDV) in clouds with cloud-top height above 2.5 km. All clouds with cloud-top height above 2.5 km that are detected by the Micro Rain Radar (MRR) during the study period at sub-zero temperatures are included. Panel (c) displays the number of samples available at each temperature level. Since MDV is obtained from the W-band cloud radar, MDV values are only included if MRR echoes are available. Bin sizes are: 1 dB, 0.05 m/s, 0.5°C.

Data Availability Statement

Microwave radiometer retrievals are available in Nomokonova, Ritter, and Ebell (2019) (for the 2017–2018 period), and in Ebell and Ritter (2022) (for the 2019–2021 period). The Cloudnet target classification product can be downloaded from https://cloudnet.fmi.fi/. The processed DWR and MDV data are available in Chellini et al. (2022). Although not necessary to reproduce the results reported in this study, the MRR and 94-GHz cloud radar original data will be published in the near future on the PANGAEA archive (https://pangaea.de).

Acknowledgments
The authors gratefully acknowledge the funding by the Deutsche Forschungsgemeinschaft (DFG, German Research Foundation)—Project no. 268020496—TRR 172, within the Transregional Collaborative Research Center "ArctiC Amplification: Climate Relevant Atmospheric and SurfaCe Processes, and Feedback Mechanisms (AC)^3." Contributions by Stefan Kneifel were funded by the DFG under grant KN 1112/2-1 and KN 1112/2-2 as part of the Emmy-Noether Group "Optimal combination of Polarimetric and Triple Frequency radar techniques for Improving Microphysical process understanding of cold clouds" (OPTIMice). This study would not have been possible without Kerstin Ebell and Pavel Krobot, who managed the data, including the application of the Cloudnet algorithm. In this regard, the authors would also like to thank the Alfred Wegener Institute (AWI) for sharing their HATPRO and ceilometer data. The authors wish to thank Lukas Pfitzenmaier, whose assistance was invaluable when evaluating the calibration of the radar systems, and Davide Ori, for producing the scattering tables used in the disdrometer-based calibration. The authors would like to further acknowledge the discussions with Ulrich Löhnert and Maximilian Maahn, which helped improve the manuscript. Last but not least, the authors wish to thank the AWIPEV staff for operating the instruments. The authors would like to express their gratitude to the three anonymous reviewers, whose constructive criticism helped significantly improve the quality of the manuscript. GC also acknowledges the support from the Graduate School of Geosciences (GSGS) of the University of Cologne, as well as the Integrated Research Training Group (IRTG) of the (AC)^3 consortium. Open Access funding enabled and organized by Projekt DEAL.

References

Abel, S. J., Boutle, I. A., Waite, K., Fox, S., Brown, P. R., Cotton, R., et al. (2017). The role of precipitation in controlling the transition from stratocumulus to cumulus clouds in a Northern Hemisphere cold-air outbreak. *Journal of the Atmospheric Sciences*, *74*(7), 2293–2314. https://doi.org/10.1175/JAS-D-16-0362.1

Avramov, A., Ackerman, A. S., Fridlind, A. M., van Diedenhoven, B., Botta, G., Aydin, K., et al. (2011). Toward ice formation closure in Arctic mixed-phase boundary layer clouds during ISDAC. *Journal of Geophysical Research: Atmospheres*, *116*(D1), D00T08. https://doi.org/10.1029/2011JD015910

Avramov, A., & Harrington, J. Y. (2010). Influence of parameterized ice habit on simulated mixed phase Arctic clouds. *Journal of Geophysical Research: Atmospheres*, *115*(D3), D03205. https://doi.org/10.1029/2009JD012108

Bailey, M. P., & Hallett, J. (2009). A comprehensive habit diagram for atmospheric ice crystals: Confirmation from the laboratory, AIRS II, and other field studies. *Journal of the Atmospheric Sciences*, *66*(9), 2888–2899. https://doi.org/10.1175/2009JAS2883.1

Barrett, A. I., Westbrook, C. D., Nicol, J. C., & Stein, T. H. M. (2019). Rapid ice aggregation process revealed through triple-wavelength Doppler spectrum radar analysis. *Atmospheric Chemistry and Physics*, *19*(8), 5753–5769. https://doi.org/10.5194/acp-19-5753-2019

Barthazy, E., & Schefold, R. (2006). Fall velocity of snowflakes of different riming degree and crystal types. *Atmospheric Research*, *82*(1–2), 391–398. https://doi.org/10.1016/j.atmosres.2005.12.009

Battaglia, A., Rustemeier, E., Tokay, A., Blahak, U., & Simmer, C. (2010). PARSIVEL snow observations: A critical assessment. *Journal of Atmospheric and Oceanic Technology*, *27*(2), 333–344. https://doi.org/10.1175/2009JTECHA1332.1

Battaglia, A., Tanelli, S., Tridon, F., Kneifel, S., Leinonen, J., & Kollias, P. (2020). Triple-frequency radar retrievals. In V. Levizzani, C. Kidd, D. B. Kirschbaum, C. D. Kummerow, K. Nakamura, & F. J. Turk (Eds.), *Satellite precipitation measurement* (Vol. 1, pp. 211–229). Springer International Publishing. https://doi.org/10.1007/978-3-030-24568-9_13

Brandes, E. A., Ikeda, K., Thompson, G., & Schönhuber, M. (2008). Aggregate terminal velocity/temperature relations. *Journal of Applied Meteorology and Climatology*, *47*(10), 2729–2736. https://doi.org/10.1175/2008JAMC1869.1

Cha, J.-W., Chang, K.-H., Yum, S. S., & Choi, Y.-J. (2009). Comparison of the bright band characteristics measured by Micro Rain Radar (MRR) at a mountain and a coastal site in South Korea. *Advances in Atmospheric Sciences*, *26*(2), 211–221. https://doi.org/10.1007/s00376-009-0211-0

Chase, R. J., Finlon, J. A., Borque, P., McFarquhar, G. M., Nesbitt, S. W., Tanelli, S., et al. (2018). Evaluation of triple-frequency radar retrieval of snowfall properties using coincident airborne in situ observations during OLYMPEX. *Geophysical Research Letters*, *45*(11), 5752–5760. https://doi.org/10.1029/2018GL077997

Chellini, G., Gierens, R., & Kneifel, S. (2022). Dual-wavelength radar observations of precipitation at Ny-Ålesund (1 Sep. 2017 - 9 Oct. 2018, 14 June 2019 - 28 Feb. 2021). [Dataset]. PANGAEA. https://doi.pangaea.de/10.1594/PANGAEA.943550

Connolly, P., Emersic, C., & Field, P. (2012). A laboratory investigation into the aggregation efficiency of small ice crystals. *Atmospheric Chemistry and Physics*, *12*(4), 2055–2076. https://doi.org/10.5194/acp-12-2055-2012

Cortinas, J. V., Jr., Bernstein, B. C., Robbins, C. C., & Walter Strapp, J. (2004). An analysis of freezing rain, freezing drizzle, and ice pellets across the United States and Canada: 1976–90. *Weather and Forecasting*, *19*(2), 377–390. https://doi.org/10.1175/1520-0434(2004)019<0377:aaofrf>2.0.co;2

Crewell, S., & Lohnert, U. (2007). Accuracy of boundary layer temperature profiles retrieved with multifrequency multiangle microwave radiometry. *IEEE Transactions on Geoscience and Remote Sensing*, *45*(7), 2195–2201. https://doi.org/10.1109/TGRS.2006.888434

Dahlke, S., & Maturilli, M. (2017). Contribution of atmospheric advection to the amplified winter warming in the Arctic North Atlantic region. *Advances in Meteorology*, *2017*, 4928620. https://doi.org/10.1155/2017/4928620

de Boer, G., Eloranta, E. W., & Shupe, M. D. (2009). Arctic mixed-phase stratiform cloud properties from multiple years of surface-based measurements at two high-latitude locations. *Journal of the Atmospheric Sciences*, *66*(9), 2874–2887. https://doi.org/10.1175/2009JAS3029.1

Dias Neto, J., Kneifel, S., Ori, D., Trömel, S., Handwerker, J., Bohn, B., et al. (2019). The TRIple-frequency and Polarimetric radar Experiment for improving process observations of winter precipitation. *Earth System Science Data*, *11*(2), 845–863. https://doi.org/10.5194/essd-11-845-2019

Durán-Alarcón, C., Boudevillain, B., Genthon, C., Grazioli, J., Souverijns, N., van Lipzig, N. P., et al. (2019). The vertical structure of precipitation at two stations in East Antarctica derived from micro rain radars. *The Cryosphere*, *13*(1), 247–264. https://doi.org/10.5194/tc-13-247-2019

Ebell, K., Nomokonova, T., Maturilli, M., & Ritter, C. (2020). Radiative effect of clouds at Ny-Ålesund, Svalbard, as inferred from ground-based remote sensing observations. *Journal of Applied Meteorology and Climatology*, *59*(1), 3–22. https://doi.org/10.1175/JAMC-D-19-0080.1

Ebell, K., & Ritter, C. (2022). HATPRO microwave radiometer measurements at AWIPEV, Ny-Ålesund (2019-2021). [Dataset]. PANGAEA. https://doi.pangaea.de/10.1594/PANGAEA.943004

Eirund, G. K., Lohmann, U., & Possner, A. (2019). Cloud ice processes enhance spatial scales of organization in Arctic stratocumulus. *Geophysical Research Letters*, *46*(23), 14109–14117. https://doi.org/10.1029/2019GL084959

Fabry, F. (2018). *Radar meteorology: Principles and practice*. Cambridge University Press. https://doi.org/10.1017/CBO9781107707405

Fabry, F., & Zawadzki, I. (1995). Long-term radar observations of the melting layer of precipitation and their interpretation. *Journal of the Atmospheric Sciences*, *52*(7), 838–851. https://doi.org/10.1175/1520-0469(1995)052<0838:ltroot>2.0.co;2

Field, P., Hogan, R., Brown, P., Illingworth, A., Choularton, T., & Cotton, R. (2005). Parametrization of ice-particle size distributions for mid-latitude stratiform cloud. *Quarterly Journal of the Royal Meteorological Society: A Journal of the Atmospheric Sciences, Applied Meteorology and Physical Oceanography*, *131*(609), 1997–2017. https://doi.org/10.1256/qj.04.134

Fitch, K. E., & Garrett, T. J. (2022). Graupel precipitating from thin arctic clouds with liquid water paths less than 50 g m^{-2}. *Geophysical Research Letters*, *49*(1), e2021GL094075. https://doi.org/10.1029/2021GL094075

Fletcher, N. H. (1962). Surface structure of water and ice. *Philosophical Magazine*, *7*(74), 255–269. https://doi.org/10.1080/14786436208211860

Gierens, R. (2021). Observations of Arctic low-level mixed-phase clouds at Ny-Ålesund: Characterization and insights gained by high-resolution Doppler radar. (Doctoral dissertation, Universität zu Köln, Köln). Retrieved from https://kups.ub.uni-koeln.de/53900/

Gierens, R., Kneifel, S., Shupe, M. D., Ebell, K., Maturilli, M., & Löhnert, U. (2020). Low-level mixed-phase clouds in a complex Arctic environment. *Atmospheric Chemistry and Physics*, *20*(6), 3459–3481. https://doi.org/10.5194/acp-20-3459-2020

Grazioli, J., Madeleine, J.-B., Gallée, H., Forbes, R. M., Genthon, C., Krinner, G., & Berne, A. (2017). Katabatic winds diminish precipitation contribution to the Antarctic ice mass balance. *Proceedings of the National Academy of Sciences of the United States of America*, *114*(41), 10858–10863. https://doi.org/10.1073/pnas.1707633114

Griesche, H. J., Ohneiser, K., Seifert, P., Radenz, M., Engelmann, R., & Ansmann, A. (2021). Contrasting ice formation in arctic clouds: Surface-coupled vs. surface-decoupled clouds. *Atmospheric Chemistry and Physics*, *21*(13), 10357–10374. https://doi.org/10.5194/acp-21-10357-2021

Harrington, J. Y., & Olsson, P. Q. (2001). On the potential influence of ice nuclei on surface-forced marine stratocumulus cloud dynamics. *Journal of Geophysical Research: Atmospheres*, *106*(D21), 27473–27484. https://doi.org/10.1029/2000JD000236

Heymsfield, A. J., Van Zadelhoff, G.-J., Donovan, D. P., Fabry, F., Hogan, R. J., & Illingworth, A. J. (2007). Refinements to ice particle mass dimensional and terminal velocity relationships for ice clouds. Part II: Evaluation and parameterizations of ensemble ice particle sedimentation velocities. *Journal of the Atmospheric Sciences*, *64*(4), 1068–1088. https://doi.org/10.1175/JAS3900.1

Heymsfield, A. J., & Westbrook, C. (2010). Advances in the estimation of ice particle fall speeds using laboratory and field measurements. *Journal of the Atmospheric Sciences*, *67*(8), 2469–2482. https://doi.org/10.1175/2010JAS3379.1

Hogan, R. J., Illingworth, A. J., & Sauvageot, H. (2000). Measuring crystal size in cirrus using 35-and 94-GHz radars. *Journal of Atmospheric and Oceanic Technology*, *17*(1), 27–37. https://doi.org/10.1175/1520-0426(2000)017<0027:mcsicu>2.0.co;2

Hogan, R. J., & O'Connor, E. J. (2004). Facilitating cloud radar and lidar algorithms: The cloudnet instrument synergy/target categorization product. Cloudnet documentation, 14.

Huang, G.-J., Bringi, V. N., & Thurai, M. (2008). Orientation angle distributions of drops after an 80-m fall using a 2D video disdrometer. *Journal of Atmospheric and Oceanic Technology*, *25*(9), 1717–1723. https://doi.org/10.1175/2008JTECHA1075.1

Illingworth, A., Hogan, R., O'connor, E., Bouniol, D., Brooks, M., Delanoë, J., et al. (2007). CLOUDNET: Continuous evaluation of cloud profiles in seven operational models using ground-based observations. *Bulletin of the American Meteorological Society*, *88*(6), 883–898. https://doi.org/10.1175/bams-88-6-883

Jackson, R. C., McFarquhar, G. M., Korolev, A. V., Earle, M. E., Liu, P. S., Lawson, R. P., et al. (2012). The dependence of ice microphysics on aerosol concentration in arctic mixed-phase stratus clouds during ISDAC and M-PACE. *Journal of Geophysical Research: Atmospheres*, *117*(D15), D15207. https://doi.org/10.1029/2012JD017668

Kajikawa, M. (1972). Measurement of falling velocity of individual snow crystals. *Journal of the Meteorological Society of Japan Ser. II*, *50*(6), 577–584. https://doi.org/10.2151/jmsj1965.50.6_577

Kalesse, H., de Boer, G., Solomon, A., Oue, M., Ahlgrimm, M., Zhang, D., et al. (2016). Understanding rapid changes in phase partitioning between cloud liquid and ice in stratiform mixed-phase clouds: An arctic case study. *Monthly Weather Review*, *144*(12), 4805–4826. https://doi.org/10.1175/MWR-D-16-0155.1

Kalesse, H., Szyrmer, W., Kneifel, S., Kollias, P., & Luke, E. (2016). Fingerprints of a riming event on cloud radar Doppler spectra: Observations and modeling. *Atmospheric Chemistry and Physics*, *16*(5), 2997–3012. https://doi.org/10.5194/acp-16-2997-2016

Karrer, M., Seifert, A., Ori, D., & Kneifel, S. (2021). Improving the representation of aggregation in a two-moment microphysical scheme with statistics of multi-frequency Doppler radar observations. *Atmospheric Chemistry and Physics*, *21*(22), 17133–17166. https://doi.org/10.5194/acp-21-17133-2021

Karrer, M., Seifert, A., Siewert, C., Ori, D., von Lerber, A., & Kneifel, S. (2020). Ice particle properties inferred from aggregation modelling. *Journal of Advances in Modeling Earth Systems*, *12*(8), e2020MS002066. https://doi.org/10.1029/2020MS002066

Klugmann, D., Heinsohn, K., & Kirtzel, H. J. (1996). A low cost 24 GHz FM-CW Doppler radar rain profiler. *Contributions to Atmospheric Physics*, *69*.

Kneifel, S., Kollias, P., Battaglia, A., Leinonen, J., Maahn, M., Kalesse, H., & Tridon, F. (2016). First observations of triple-frequency radar Doppler spectra in snowfall: Interpretation and applications. *Geophysical Research Letters*, *43*(5), 2225–2233. https://doi.org/10.1002/2015GL067618

Kneifel, S., Maahn, M., Peters, G., & Simmer, C. (2011). Observation of snowfall with a low-power FM-CW K-band radar (Micro Rain Radar). *Meteorology and Atmospheric Physics*, *113*(1), 75–87. https://doi.org/10.1007/s00703-011-0142-z

Kneifel, S., & Moisseev, D. (2020). Long-term statistics of riming in nonconvective clouds derived from ground-based Doppler cloud radar observations. *Journal of the Atmospheric Sciences*, *77*(10), 3495–3508. https://doi.org/10.1175/JAS-D-20-0007.1

Kobayashi, T. (1957). Experimental researches en the snow crystal habit and growth by means of a diffusion cloud chamber. *Journal of the Meteorological Society of Japan Ser. II*, *35*, 38–47. https://doi.org/10.2151/jmsj1923.35A.0_38

Korolev, A. (2007). Limitations of the Wegener–Bergeron–Findeisen mechanism in the evolution of mixed-phase clouds. *Journal of the Atmospheric Sciences*, *64*(9), 3372–3375. https://doi.org/10.1175/JAS4035.1

Korolev, A., & Mazin, I. P. (2003). Supersaturation of water vapor in clouds. *Journal of the Atmospheric Sciences*, *60*(24), 2957–2974. https://doi.org/10.1175/1520-0469(2003)060<2957:sowvic>2.0.co;2

Küchler, N., Kneifel, S., Löhnert, U., Kollias, P., Czekala, H., & Rose, T. (2017). A W-band radar–radiometer system for accurate and continuous monitoring of clouds and precipitation. *Journal of Atmospheric and Oceanic Technology*, *34*(11), 2375–2392. https://doi.org/10.1175/JTECH-D-17-0019.1

Lamer, K., Oue, M., Battaglia, A., Roy, R. J., Cooper, K. B., Dhillon, R., & Kollias, P. (2021). Multifrequency radar observations of clouds and precipitation including the G-band. *Atmospheric Measurement Techniques*, *14*(5), 3615–3629. https://doi.org/10.5194/amt-14-3615-2021

Lawson, R. P., Stewart, R. E., & Angus, L. J. (1998). Observations and numerical simulations of the origin and development of very large snowflakes. *Journal of the Atmospheric Sciences*, *55*(21), 3209–3229. https://doi.org/10.1175/1520-0469(1998)055<3209:oansot>2.0.co;2

Leinonen, J. (2014). High-level interface to T-matrix scattering calculations: Architecture, capabilities and limitations. *Optics Express*, *22*(2), 1655–1660. https://doi.org/10.1364/OE.22.001655

Leinonen, J., Kneifel, S., & Hogan, R. J. (2018). Evaluation of the Rayleigh–Gans approximation for microwave scattering by rimed snowflakes. *Quarterly Journal of the Royal Meteorological Society*, *144*(S1), 77–88. https://doi.org/10.1002/qj.3093

Leinonen, J., & Szyrmer, W. (2015). Radar signatures of snowflake riming: A modeling study. *Earth and Space Science*, *2*(8), 346–358. https://doi.org/10.1002/2015EA000102

Li, H., Tiira, J., von Lerber, A., & Moisseev, D. (2020). Towards the connection between snow microphysics and melting layer: Insights from multifrequency and dual-polarization radar observations during BAECC. *Atmospheric Chemistry and Physics*, *20*(15), 9547–9562. https://doi.org/10.5194/acp-20-9547-2020

Liao, L., Meneghini, R., Iguchi, T., & Detwiler, A. (2005). Use of dual-wavelength radar for snow parameter estimates. *Journal of Atmospheric and Oceanic Technology*, *22*(10), 1494–1506. https://doi.org/10.1175/JTECH1808.1

Locatelli, J. D., & Hobbs, P. V. (1974). Fall speeds and masses of solid precipitation particles. *Journal of Geophysical Research*, *79*(15), 2185–2197. https://doi.org/10.1029/JC079i015p02185

Löffler-Mang, M., & Joss, J. (2000). An optical disdrometer for measuring size and velocity of hydrometeors. *Journal of Atmospheric and Oceanic Technology*, *17*(2), 130–139. https://doi.org/10.1175/1520-0426(2000)017⟨0130:AODFMS⟩2.0.CO;2

Luke, E. P., Yang, F., Kollias, P., Vogelmann, A. M., & Maahn, M. (2021). New insights into ice multiplication using remote-sensing observations of slightly supercooled mixed-phase clouds in the Arctic. *Proceedings of the National Academy of Sciences of the United States of America*, *118*(13), e2021387118. https://doi.org/10.1073/pnas.2021387118

Maahn, M., Burgard, C., Crewell, S., Gorodetskaya, I. V., Kneifel, S., Lhermitte, S., et al. (2014). How does the spaceborne radar blind zone affect derived surface snowfall statistics in polar regions? *Journal of Geophysical Research: Atmospheres*, *119*(24), 13–604. https://doi.org/10.1002/2014JD022079

Maahn, M., & Kollias, P. (2012). Improved Micro Rain Radar snow measurements using Doppler spectra post-processing. *Atmospheric Measurement Techniques*, *5*(11), 2661–2673. https://doi.org/10.5194/amt-5-2661-2012

Mason, S. L., Hogan, R. J., Westbrook, C. D., Kneifel, S., Moisseev, D., & von Terzi, L. (2019). The importance of particle size distribution and internal structure for triple-frequency radar retrievals of the morphology of snow. *Atmospheric Measurement Techniques*, *12*(9), 4993–5018. https://doi.org/10.5194/amt-12-4993-2019

Matrosov, S. Y., Heymsfield, A., & Wang, Z. (2005). Dual-frequency radar ratio of nonspherical atmospheric hydrometeors. *Geophysical Research Letters*, *32*(13), L13816. https://doi.org/10.1029/2005GL023210

Matrosov, S. Y., Maahn, M., & De Boer, G. (2019). Observational and modeling study of ice hydrometeor radar dual-wavelength ratios. *Journal of Applied Meteorology and Climatology*, *58*(9), 2005–2017. https://doi.org/10.1175/JAMC-D-19-0018.1

Maturilli, M., & Ebell, K. (2018). Twenty-five years of cloud base height measurements by ceilometer in Ny-Ålesund, Svalbard. *Earth System Science Data*, *10*(3), 1451–1456. https://doi.org/10.5194/essd-10-1451-2018

Maturilli, M., Herber, A., & König-Langlo, G. (2013). Climatology and time series of surface meteorology in Ny-Ålesund, Svalbard. *Earth System Science Data*, *5*(1), 155–163. https://doi.org/10.5194/essd-5-155-2013

Maturilli, M., & Kayser, M. (2017). Arctic warming, moisture increase and circulation changes observed in the Ny-Ålesund homogenized radiosonde record. *Theoretical and Applied Climatology*, *130*(1), 1–17. https://doi.org/10.1007/s00704-016-1864-0

Matus, A. V., & L'Ecuyer, T. S. (2017). The role of cloud phase in Earth's radiation budget. *Journal of Geophysical Research: Atmospheres*, *122*(5), 2559–2578. https://doi.org/10.1002/2016JD025951

McFarquhar, G. M., Zhang, G., Poellot, M. R., Kok, G. L., McCoy, R., Tooman, T., et al. (2007). Ice properties of single-layer stratocumulus during the Mixed-Phase Arctic Cloud Experiment: 1. Observations. *Journal of Geophysical Research: Atmospheres*, *112*(D24), D24201. https://doi.org/10.1029/2007JD008633

Mech, M., Kliesch, L.-L., Anhäuser, A., Rose, T., Kollias, P., & Crewell, S. (2019). Microwave Radar/radiometer for Arctic Clouds (MiRAC): First insights from the ACLOUD campaign. *Atmospheric Measurement Techniques*, *12*(9), 5019–5037. https://doi.org/10.5194/amt-12-5019-2019

Mioche, G., Jourdan, O., Ceccaldi, M., & Delanoë, J. (2015). Variability of mixed-phase clouds in the Arctic with a focus on the Svalbard region: A study based on spaceborne active remote sensing. *Atmospheric Chemistry and Physics*, *15*(5), 2445–2461. https://doi.org/10.5194/acp-15-2445-2015

Mioche, G., Jourdan, O., Delanoë, J., Gourbeyre, C., Febvre, G., Dupuy, R., et al. (2017). Vertical distribution of microphysical properties of Arctic springtime low-level mixed-phase clouds over the Greenland and Norwegian seas. *Atmospheric Chemistry and Physics*, *17*(20), 12845–12869. https://doi.org/10.5194/acp-17-12845-2017

Mitchell, D. L. (1996). Use of mass-and area-dimensional power laws for determining precipitation particle terminal velocities. *Journal of the Atmospheric Sciences*, *53*(12), 1710–1723. https://doi.org/10.1175/1520-0469(1996)053<1710:uomaad>2.0.co;2

Mori, T., Kondo, Y., Ohata, S., Goto-Azuma, K., Fukuda, K., Ogawa-Tsukagawa, Y., et al. (2021). Seasonal variation of wet deposition of black carbon at Ny-Ålesund, Svalbard. *Journal of Geophysical Research: Atmospheres*, *126*, e2020JD034110. https://doi.org/10.1029/2020JD034110

Morrison, H., de Boer, G., Feingold, G., Harrington, J., Shupe, M. D., & Sulia, K. (2012). Resilience of persistent Arctic mixed-phase clouds. *Nature Geoscience*, *5*(1), 11–17. https://doi.org/10.1038/ngeo1332

Myagkov, A., Kneifel, S., & Rose, T. (2020). Evaluation of the reflectivity calibration of W-band radars based on observations in rain. *Atmospheric Measurement Techniques*, *13*(11), 5799–5825. https://doi.org/10.5194/amt-13-5799-2020

Nomokonova, T., Ebell, K., Löhnert, U., Maturilli, M., & Ritter, C. (2020). The influence of water vapor anomalies on clouds and their radiative effect at Ny-Ålesund. *Atmospheric Chemistry and Physics*, *20*(8), 5157–5173. https://doi.org/10.5194/acp-20-5157-2020

Nomokonova, T., Ebell, K., Löhnert, U., Maturilli, M., Ritter, C., & O'Connor, E. (2019). Statistics on clouds and their relation to thermodynamic conditions at Ny-Ålesund using ground-based sensor synergy. *Atmospheric Chemistry and Physics*, *19*(6), 4105–4126. https://doi.org/10.5194/acp-19-4105-2019

Nomokonova, T., Ritter, C., & Ebell, K. (2019). HATPRO microwave radiometer measurements at AWIPEV, Ny-Ålesund (2016-2018). [Dataset]. PANGAEA. https://doi.pangaea.de/10.1594/PANGAEA.902183

Norgren, M. S., Boer, G. D., & Shupe, M. D. (2018). Observed aerosol suppression of cloud ice in low-level Arctic mixed-phase clouds. *Atmospheric Chemistry and Physics*, *18*(18), 13345–13361. https://doi.org/10.5194/acp-18-13345-2018

Ori, D., Schemann, V., Karrer, M., Dias Neto, J., von Terzi, L., Seifert, A., & Kneifel, S. (2020). Evaluation of ice particle growth in ICON using statistics of multi-frequency Doppler cloud radar observations. *Quarterly Journal of the Royal Meteorological Society*, *146*(733), 3830–3849. https://doi.org/10.1002/qj.3875

Ori, D., von Terzi, L., Karrer, M., & Kneifel, S. (2021). snowScatt 1.0: Consistent model of microphysical and scattering properties of rimed and unrimed snowflakes based on the self-similar Rayleigh-Gans Approximation. *Geoscientific Model Development*, *14*(3), 1511–1531. https://doi.org/10.5194/gmd-14-1511-2021

Oue, M., Kollias, P., Matrosov, S. Y., Battaglia, A., & Ryzhkov, A. V. (2021). Analysis of the microphysical properties of snowfall using scanning polarimetric and vertically pointing multi-frequency Doppler radars. *Atmospheric Measurement Techniques*, *14*(7), 4893–4913. Retrieved from https://amt.copernicus.org/articles/14/4893/2021/

Pfitzenmaier, L., Dufournet, Y., Unal, C. M., & Russchenberg, H. W. (2017). Retrieving fall streaks within cloud systems using Doppler radar. *Journal of Atmospheric and Oceanic Technology*, *34*(4), 905–920. https://doi.org/10.1175/JTECH-D-16-0117.1

Pfitzenmaier, L., Unal, C. M., Dufournet, Y., & Russchenberg, H. W. (2018). Observing ice particle growth along fall streaks in mixed-phase clouds using spectral polarimetric radar data. *Atmospheric Chemistry and Physics*, *18*(11), 7843–7862. https://doi.org/10.5194/acp-18-7843-2018

Proske, U., Ferrachat, S., Neubauer, D., Staab, M., & Lohmann, U. (2021). Assessing the potential for simplification in global climate model cloud microphysics. *Atmospheric Chemistry and Physics Discussions*, *22*, 4737–4762. https://doi.org/10.5194/acp-2021-801

Pruppacher, H. R., & Klett, J. D. (2012). *Microphysics of clouds and precipitation: Reprinted 1980*. Springer. https://doi.org/10.1007/978-94-009-9905-3

Rangno, A. L., & Hobbs, P. V. (2001). Ice particles in stratiform clouds in the Arctic and possible mechanisms for the production of high ice concentrations. *Journal of Geophysical Research: Atmospheres*, *106*(D14), 15065–15075. https://doi.org/10.1029/2000JD900286

Rose, T., Crewell, S., Löhnert, U., & Simmer, C. (2005). A network suitable microwave radiometer for operational monitoring of the cloudy atmosphere. *Atmospheric Research*, *75*(3), 183–200. https://doi.org/10.1016/j.atmosres.2004.12.005

Ruiz-Donoso, E., Ehrlich, A., Schäfer, M., Jäkel, E., Schemann, V., Crewell, S., et al. (2020). Small-scale structure of thermodynamic phase in Arctic mixed-phase clouds observed by airborne remote sensing during a cold air outbreak and a warm air advection event. *Atmospheric Chemistry and Physics*, *20*(9), 5487–5511. https://doi.org/10.5194/acp-20-5487-2020

Scarchilli, C., Ciardini, V., Grigioni, P., Iaccarino, A., De Silvestri, L., Proposito, M., et al. (2020). Characterization of snowfall estimated by in situ and ground-based remote-sensing observations at Terra Nova Bay, Victoria Land, Antarctica. *Journal of Glaciology*, *66*(260), 1006–1023. https://doi.org/10.1017/jog.2020.70

Schäfer, M., Loewe, K., Ehrlich, A., Hoose, C., & Wendisch, M. (2018). Simulated and observed horizontal inhomogeneities of optical thickness of Arctic stratus. *Atmospheric Chemistry and Physics*, *18*(17), 13115–13133. https://doi.org/10.5194/acp-18-13115-2018

Serreze, M. C., & Barry, R. G. (2011). Processes and impacts of arctic amplification: A research synthesis. *Global and Planetary Change*, *77*(1–2), 85–96. https://doi.org/10.1016/j.gloplacha.2011.03.004

Shupe, M. D. (2011). Clouds at Arctic atmospheric observatories. Part II: Thermodynamic phase characteristics. *Journal of Applied Meteorology and Climatology*, *50*(3), 645–661. https://doi.org/10.1175/2010jamc2468.1

Shupe, M. D., & Intrieri, J. M. (2004). Cloud radiative forcing of the Arctic surface: The influence of cloud properties, surface albedo, and solar zenith angle. *Journal of Climate*, *17*(3), 616–628. https://doi.org/10.1175/1520-0442(2004)017<0616:crfota>2.0.co;2

Shupe, M. D., Kollias, P., Persson, P. O. G., & McFarquhar, G. M. (2008). Vertical motions in Arctic mixed-phase stratiform clouds. *Journal of the Atmospheric Sciences*, *65*(4), 1304–1322. https://doi.org/10.1175/2007JAS2479.1

Shupe, M. D., Matrosov, S. Y., & Uttal, T. (2006). Arctic mixed-phase cloud properties derived from surface-based sensors at SHEBA. *Journal of the Atmospheric Sciences*, *63*(2), 697–711. https://doi.org/10.1175/JAS3659.1

Silber, I., McGlynn, P. S., Harrington, J. Y., & Verlinde, J. (2021). Habit-dependent vapor growth modulates Arctic supercooled water occurrence. *Geophysical Research Letters*, *48*(10), e2021GL092767. https://doi.org/10.1029/2021GL092767

Simpfendoerfer, L. F., Verlinde, J., Harrington, J. Y., Shupe, M. D., Chen, Y.-S., Clothiaux, E. E., & Golaz, J.-C. (2019). Formation of Arctic stratocumuli through atmospheric radiative cooling. *Journal of Geophysical Research: Atmospheres*, *124*(16), 9644–9664. https://doi.org/10.1029/2018JD030189

Slater, B., & Michaelides, A. (2019). Surface premelting of water ice. *Nature Reviews Chemistry*, *3*(3), 172–188. https://doi.org/10.1038/s41570-019-0080-8

Solomon, A., Boer, G. d., Creamean, J. M., McComiskey, A., Shupe, M. D., Maahn, M., & Cox, C. (2018). The relative impact of cloud condensation nuclei and ice nucleating particle concentrations on phase partitioning in Arctic mixed-phase stratocumulus clouds. *Atmospheric Chemistry and Physics*, *18*(23), 17047–17059. https://doi.org/10.5194/acp-18-17047-2018

Solomon, A., Feingold, G., & Shupe, M. D. (2015). The role of ice nuclei recycling in the maintenance of cloud ice in Arctic mixed-phase stratocumulus. *Atmospheric Chemistry and Physics*, *15*(18), 10631–10643. Retrieved from https://acp.copernicus.org/articles/15/10631/2015/

Solomon, A., Shupe, M. D., Persson, O., Morrison, H., Yamaguchi, T., Caldwell, P. M., & de Boer, G. (2014). The sensitivity of springtime Arctic mixed-phase stratocumulus clouds to surface-layer and cloud-top inversion-layer moisture sources. *Journal of the Atmospheric Sciences*, *71*(2), 574–595. https://doi.org/10.1175/jas-d-13-0179.1

Solomon, A., Shupe, M. D., Persson, P. O. G., & Morrison, H. (2011). Moisture and dynamical interactions maintaining decoupled Arctic mixed-phase stratocumulus in the presence of a humidity inversion. *Atmospheric Chemistry and Physics*, *11*(19), 10127–10148. https://doi.org/10.5194/acp-11-10127-2011

Sotiropoulou, G., Sedlar, J., Tjernström, M., Shupe, M. D., Brooks, I. M., & Persson, P. O. G. (2014). The thermodynamic structure of summer Arctic stratocumulus and the dynamic coupling to the surface. *Atmospheric Chemistry and Physics*, *14*(22), 12573–12592. https://doi.org/10.5194/acp-14-12573-2014

Souverijns, N., Gossart, A., Lhermitte, S., Gorodetskaya, I. V., Grazioli, J., Berne, A., et al. (2018). Evaluation of the CloudSat surface snowfall product over Antarctica using ground-based precipitation radars. *The Cryosphere*, *12*(12), 3775–3789. https://doi.org/10.5194/tc-12-3775-2018

Szyrmer, W., & Zawadzki, I. (2014). Snow studies. Part IV: Ensemble retrieval of snow microphysics from dual-wavelength vertically pointing radars. *Journal of the Atmospheric Sciences*, *71*(3), 1171–1186. https://doi.org/10.1175/JAS-D-12-0286.1

Takahashi, T. (2014). Influence of liquid water content and temperature on the form and growth of branched planar snow crystals in a cloud. *Journal of the Atmospheric Sciences*, *71*(11), 4127–4142. https://doi.org/10.1175/JAS-D-14-0043.1

Takahashi, T., Endoh, T., Wakahama, G., & Fukuta, N. (1991). Vapor diffusional growth of free-falling snow crystals between −3 and −23°C. *Journal of the Meteorological Society of Japan Series II*, *69*(1), 15–30. https://doi.org/10.2151/jmsj1965.69.1_15

Tan, I., & Storelvmo, T. (2019). Evidence of strong contributions from mixed-phase clouds to Arctic climate change. *Geophysical Research Letters*, *46*(5), 2894–2902. https://doi.org/10.1029/2018GL081871

Thurai, M., Huang, G. J., Bringi, V. N., Randeu, W. L., & Schönhuber, M. (2007). Drop shapes, model comparisons, and calculations of polarimetric radar parameters in rain. *Journal of Atmospheric and Oceanic Technology*, *24*(6), 1019–1032. https://doi.org/10.1175/JTECH2051.1

Tridon, F., & Battaglia, A. (2015). Dual-frequency radar Doppler spectral retrieval of rain drop size distributions and entangled dynamics variables. *Journal of Geophysical Research: Atmospheres*, *120*(11), 5585–5601. https://doi.org/10.1002/2014JD023023

Tridon, F., Battaglia, A., Chase, R. J., Turk, F. J., Leinonen, J., Kneifel, S., et al. (2019). The microphysics of stratiform precipitation during OLYMPEX: Compatibility between triple-frequency radar and airborne in situ observations. *Journal of Geophysical Research: Atmospheres*, *124*(15), 8764–8792. https://doi.org/10.1029/2018JD029858

Tridon, F., Battaglia, A., & Kneifel, S. (2020). Estimating total attenuation using Rayleigh targets at cloud top: Applications in multilayer and mixed-phase clouds observed by ground-based multifrequency radars. *Atmospheric Measurement Techniques*, *13*(9), 5065–5085. https://doi.org/10.5194/amt-13-5065-2020

Vassel, M., Ickes, L., Maturilli, M., & Hoose, C. (2019). Classification of Arctic multilayer clouds using radiosonde and radar data in Svalbard. *Atmospheric Chemistry and Physics*, *19*(7), 5111–5126. https://doi.org/10.5194/acp-19-5111-2019

Waterman, P. (1965). Matrix formulation of electromagnetic scattering. *Proceedings of the IEEE*, *53*(8), 805–812. https://doi.org/10.1109/PROC.1965.4058

Wendisch, M., Macke, A., Ehrlich, A., Lüpkes, C., Mech, M., Chechin, D., et al. (2019). The Arctic cloud puzzle: Using ACLOUD/PASCAL multiplatform observations to unravel the role of clouds and aerosol particles in arctic amplification. *Bulletin of the American Meteorological Society*, *100*(5), 841–871. https://doi.org/10.1175/BAMS-D-18-0072.1

Westbrook, C. D., Hogan, R. J., & Illingworth, A. J. (2008). The capacitance of pristine ice crystals and aggregate snowflakes. *Journal of the Atmospheric Sciences*, *65*(1), 206–219. https://doi.org/10.1175/2007jas2315.1

Williams, C. R., Gage, K. S., Clark, W., & Kucera, P. (2005). Monitoring the reflectivity calibration of a scanning radar using a profiling radar and a disdrometer. *Journal of Atmospheric and Oceanic Technology*, *22*(7), 1004–1018. https://doi.org/10.1175/JTECH1759.1

Young, G., Jones, H. M., Choularton, T. W., Crosier, J., Bower, K. N., Gallagher, M. W., et al. (2016). Observed microphysical changes in Arctic mixed-phase clouds when transitioning from sea ice to open ocean. *Atmospheric Chemistry and Physics*, *16*(21), 13945–13967. https://doi.org/10.5194/acp-16-13945-2016

Yuter, S. E., & Houze, R. A., Jr. (1995). Three-dimensional kinematic and microphysical evolution of Florida cumulonimbus. Part II: Frequency distributions of vertical velocity, reflectivity, and differential reflectivity. *Monthly Weather Review*, *123*(7), 1941–1963. https://doi.org/10.1175/1520-0493(1995)123<1941:tdkame>2.0.co;2

Zängl, G., Reinert, D., Rípodas, P., & Baldauf, M. (2015). The ICON (ICOsahedral Non-hydrostatic) modelling framework of DWD and MPI-M: Description of the non-hydrostatic dynamical core. *Quarterly Journal of the Royal Meteorological Society*, *141*(687), 563–579. https://doi.org/10.1002/qj.2378

Zhang, D., Wang, Z., Luo, T., Yin, Y., & Flynn, C. (2017). The occurrence of ice production in slightly supercooled Arctic stratiform clouds as observed by ground-based remote sensors at the ARM NSA site. *Journal of Geophysical Research: Atmospheres*, *122*(5), 2867–2877. https://doi.org/10.1002/2016JD026226

Zhao, M., & Wang, Z. (2010). Comparison of arctic clouds between European Center for Medium-Range Weather Forecasts Simulations and Atmospheric Radiation Measurement Climate Research Facility long-term observations at the North Slope of Alaska Barrow site. *Journal of Geophysical Research: Atmospheres*, *115*(D23), D23202. https://doi.org/10.1029/2010JD014285

Zuidema, P., Baker, B., Han, Y., Intrieri, J., Key, J., Lawson, P., et al. (2005). An Arctic springtime mixed-phase cloudy boundary layer observed during SHEBA. *Journal of the Atmospheric Sciences*, *62*(1), 160–176. https://doi.org/10.1175/JAS-3368.1

Chapter 4

Study 2: Development and first analysis of a long-term dataset of dual-frequency polarimetric Doppler cloud radar observations

Chellini, G., R. Gierens, K. Ebell, T. Kiszler, P. Krobot, A. Myagkov, V. Schemann, and S. Kneifel (2023). **Low-level mixed-phase clouds at the high Arctic site of Ny-Ålesund: A comprehensive long-term dataset of remote sensing observations**. *Earth System Science Data Discussions [preprint]*, https://doi.org/10.5194/essd-2023-157, in review.

The content of this chapter has been published under the Creative Commons Attribution 4.0 International Public License.

The final peer-reviewed article has been published under the Creative Commons Attribution 4.0 International Public License, and can be found at:

Chellini, G., R. Gierens, K. Ebell, T. Kiszler, P. Krobot, A. Myagkov, V. Schemann, and S. Kneifel (2023). **Low-level mixed-phase clouds at the high Arctic site of Ny-Ålesund: A comprehensive long-term dataset of remote sensing observations**. *Earth System Science Data*, 15, 5427–5448, https://doi.org/10.5194/essd-15-5427-2023.

Author contributions: GC processed the Ka-band radar data, including the developing of the range folding and ground clutter corrections, performed the calibration and attenuation correction of all radar systems, matched the data from

all instruments and compiled the final files, all with the supervision of SK. RG processed the W-band data, and KE processed the HATPRO data and applied the Cloudnet target classification. TK ran the ICON-LEM simulations, with the supervision of VS. GC, RG and PK operated the cloud radars, with support from AM. PK handled the data transfer and storage. AM provided guidance on radar operation and data processing. SK and GC designed the dataset, and GC wrote the manuscript and performed the analysis, with feedback from all authors.

https://doi.org/10.5194/essd-2023-157
Preprint. Discussion started: 6 June 2023
© Author(s) 2023. CC BY 4.0 License.

Open Access Earth System Science Data Discussions

Low-level mixed-phase clouds at the high Arctic site of Ny-Ålesund: A comprehensive long-term dataset of remote sensing observations

Giovanni Chellini[1], Rosa Gierens[1], Kerstin Ebell[1], Theresa Kiszler[1], Pavel Krobot[1], Alexander Myagkov[2], Vera Schemann[1], and Stefan Kneifel[1, 3]

[1]Institute for Geophysics and Meteorology, University of Cologne, Cologne, Germany
[2]Radiometer Physics GmbH, Meckenheim, Germany
[3]Meteorological Institute, Ludwig-Maximilians-University Munich, Munich, Germany

Correspondence: Giovanni Chellini (g.chellini@uni-koeln.de)

Abstract. We present a comprehensive quality-controlled 15-month dataset of remote sensing observations of low-level mixed-phase clouds (LLMPCs) taken at the high Arctic site of Ny-Ålesund, Svalbard, Norway. LLMPCs occur frequently in the Arctic region, and extensively affect the energy budget. However, our understanding of the ice microphysical processes taking place in these clouds is incomplete. The dual-wavelength and polarimetric Doppler cloud radar observations, which are the cornerstones of the dataset, provide valuable fingerprints of ice microphysical processes, and the high number of cases included allows for the compiling of robust statistics for process studies. The radar data are complemented with thermodynamic retrievals from a microwave radiometer, liquid base height from a ceilometer and wind fields from large-eddy simulations. All data are quality controlled, especially the cloud radar data, which are accurately calibrated, matched, and corrected for gas and liquid-hydrometeor attenuation, ground clutter and range folding. We finally present an analysis of the temperature dependence of Doppler, dual-wavelength, and polarimetric radar variables, to illustrate how the dataset can be used for cloud microphysical studies. The dataset has been published in Chellini et al. (2023) and is freely available at: www.doi.org/10.5281/zenodo.7803064.

1 Introduction

Clouds are an essential component of the Earth system, considerably impacting the energy budget and driving the hydrological cycle (Wallace and Hobbs, 2006). As such, they are thought to play a role in the enhanced warming observed in the Arctic region in the past decades, termed Arctic Amplification (Shupe and Intrieri, 2004; Serreze and Barry, 2011; Matus and L'Ecuyer, 2017; Tan and Storelvmo, 2019). Clouds in the Arctic display features unique to this region, in particular the widespread and frequent occurrence of low-level mixed-phase clouds (LLMPCs) (Morrison et al., 2012; Mioche et al., 2015; de Boer et al., 2009; Shupe, 2011). Arctic LLMPCs are typically characterized by a shallow liquid layer at cloud top, where ice crystals form and grow into precipitation (Shupe et al., 2006; Morrison et al., 2012; Chellini et al., 2022). The liquid layer sustains itself from the continuous mass loss due to precipitation via turbulence-driven condensation; turbulence and updrafts being in turn produced buoyantly by cloud-top radiative cooling (Solomon et al., 2011; Morrison et al., 2012).

https://doi.org/10.5194/essd-2023-157
Preprint. Discussion started: 6 June 2023
© Author(s) 2023. CC BY 4.0 License.

Open Access Earth System Science Data Discussions

A variety of questions on the macro- and microphysical processes determining the radiative and thermodynamic characteristics, as well as the organization, phase-partitioning, and precipitation intensity of Arctic LLMPCs remains unanswered (Shupe et al., 2022; Wendisch et al., 2023) In particular, ice microphysical processes and their interaction with the liquid phase and turbulence are expected to affect precipitation, and therefore to determine the mass sink of the cloud layer (Morrison et al., 2012; Solomon et al., 2014, 2015). Harrington and Olsson (2001) and Simpfendoerfer et al. (2019) have in fact suggested lower cloud fractions and faster dissipation for Arctic mixed-phase stratocumuli that develop precipitation. It is speculated that precipitation-induced cold pools at the surface lead to thinning and break-up of the organization in Arctic stratocumuli (Abel et al., 2017; Eirund et al., 2019). Moreover, model sensitivity experiments have shown that the phase partitioning of Arctic LLMPCs is strongly sensitive to the assumptions on the habits of the ice particles, via mass-size, and size-fall speed relations (Avramov and Harrington, 2010). Sotiropoulou et al. (2022) recently showed that a more realistic representation of secondary ice production and ice aggregation processes in the NorESM2 climate model leads to an improvement in the degree of agreement with observations, especially ice water content (IWC) retrievals. Furthermore, the magnitude of Arctic Amplification itself in the Community Earth System Model (CESM) has been showed to be sensitive to the size of ice particles in Arctic LLMPCs; owing to a stronger cloud-phase feedback the larger the ice particles (Tan and Storelvmo, 2019). Achieving a complete understanding of ice microphysical processes in Arctic LLMPCs is therefore necessary in order to reach a correct representation of these unique clouds, together with their radiative effect, in climate models.

Millimeter-wavelength radars can effectively provide robust observational fingerprints to constrain cloud microphysical processes (e.g., Kollias et al., 2007; von Terzi et al., 2022). Cloud radars with Doppler capabilities have been widely used to gain insights into macrophysical characteristics (Shupe et al., 2006; Nomokonova et al., 2019), precipitation characteristics (Zhao and Garrett, 2008; Schoger et al., 2021), phase partitioning (De Boer et al., 2011; Kalesse et al., 2016; Griesche et al., 2020; Gierens, 2021), and dynamics and turbulence (Shupe et al., 2008; Mages et al., 2023) in Arctic clouds. The addition of polarimetric and multi-frequency capabilities can further expand the spectrum of obtainable fingerprints. Linear depolarization and dual polarization observations can in fact provide strong constrains for the shape and concentration of ice particles (Oue et al., 2015; von Terzi et al., 2022). At the same time, millimeter-radar observations at multiple wavelengths provide robust constraints for the size of ice particles: the ratio of the radar reflectivities measured at two separate wavelengths, named the dual-wavelength ratio (DWR), can be related to the characteristic size of the ice particle population (Hogan et al., 2000; Dias Neto et al., 2019). Furthermore, ice microphysical processes are highly sensitive to temperature (Pruppacher and Klett, 2012), hence matching radar observations with accurate thermodynamic information can further constrain the microphysical processes generating the radar fingerprints (Barrett et al., 2019; von Terzi et al., 2022).

Here, we present a quality-controlled dataset including dual-wavelength, polarimetric, Doppler cloud radar observations of LLMPC events taken at the high Arctic site of Ny-Ålesund, Svalbard, Norway, from 10 October 2021 until 31 December 2022. Observations from a zenith-pointing 94 GHz cloud radar, and a 35 GHz dual-polarization scanning cloud radar are complemented with thermodynamic retrievals from a microwave radiometer, cloud base height from a ceilometer and wind fields from large-eddy simulations. The objective is to provide a quality-controlled, ready-to-use, comprehensive dataset for microphysical studies of LLMPCs, taken at a site where such observations were not available until now. To our knowledge,

https://doi.org/10.5194/essd-2023-157
Preprint. Discussion started: 6 June 2023
© Author(s) 2023. CC BY 4.0 License.


similar datasets featuring multi-frequency polarimetric Doppler cloud radar observations in the Arctic, coupled with thermodynamic information, are only available at the site of Utqiaġvik (Verlinde et al., 2016), in the American high Arctic, and for the MOSAiC expedition (Shupe et al., 2022), which took place in the central Arctic. We thus believe that this dataset will be a valuable addition to the already publicly available datasets, providing a tool for microphysical studies of Arctic LLMPCs in the European high Arctic, where Arctic Amplification has been shown to be the most intense (Dahlke and Maturilli, 2017). The dataset was published in Chellini et al. (2023) and is freely available at www.doi.org/10.5281/zenodo.7803064.

2 Measurement site and instruments

Observations were carried out at the observatory of the Arctic research station AWIPEV in Ny-Ålesund (Fig. 1), located at 79°N along the coast of the Kongsfjorden, a fjord on the west side of Spitzbergen, the main island of the Svalbard archipelago. The area features a mountainous terrain, with peaks reaching 700 m. The observatory is located at 11 meters above sea level, within 500 meters from the sea and 2 km from the Zeppelin mountain (556 meters high). The Kongsfjorden is surrounded by several glaciers, and the surface is of the tundra type. During the observational period the sea surface inside the fjord remained for the most part ice-free.

The orography often channels surface wind along the fjord axis, at 120° (southeasterly) (Beine et al., 2001; Esau and Repina, 2012; Graßl et al., 2022) . The surface wind layer thickness has been estimated to be comparable to the height of the surrounding mountains, with a yearly cycle of 500 m in summer and 1000 m in winter (Esau and Repina, 2012). The free troposphere above generally displays a westerly flow (Maturilli and Kayser, 2017).

Mean monthly surface air temperature peaks in July, at 5.8°C, and has its minimum in March at -12.0°C (Maturilli et al., 2013). Median monthly values of integrated water vapor (IWV) display a similar yearly cycle, with a March minimum of 3 kg m^{-2} and a July maximum of 13 kg m^{-2} (Nomokonova et al., 2020). Temperature and moisture inversions are a frequent feature of the lower troposphere at Ny-Ålesund, observed respectively in 75 and 84% of the daily radiosondes launched between 1993 and 2014 (Maturilli and Kayser, 2017).

Cloud characteristics at the site have been reported by a number of studies, including Nomokonova et al. (2019), Vassel et al. (2019), Koike et al. (2019), Nomokonova et al. (2020), Gierens et al. (2020), Ebell et al. (2020) and Chellini et al. (2022). Nomokonova et al. (2019) reported a frequency of occurrence of 20.6% for single-layer MPCs, with no restriction on height, while Gierens et al. (2020) estimated the occurrence of single-layer LLMPCs lasting more than 1 hour to be 23%. Chellini et al. (2022) observed an occurrence of LLMPCs lasting more than 1 hour, with no restriction on the number of liquid layers, of 30.7%.

2.1 Cloud radars

Three cloud radar systems were used to collect the data included in the dataset. All systems are frequency-modulated continuous-wave (FMCW) radars, manufactured by Radiometer Physics GmbH (RPG): JOYRAD-94 and MiRAC-A, which are 94 GHz

https://doi.org/10.5194/essd-2023-157
Preprint. Discussion started: 6 June 2023
© Author(s) 2023. CC BY 4.0 License.

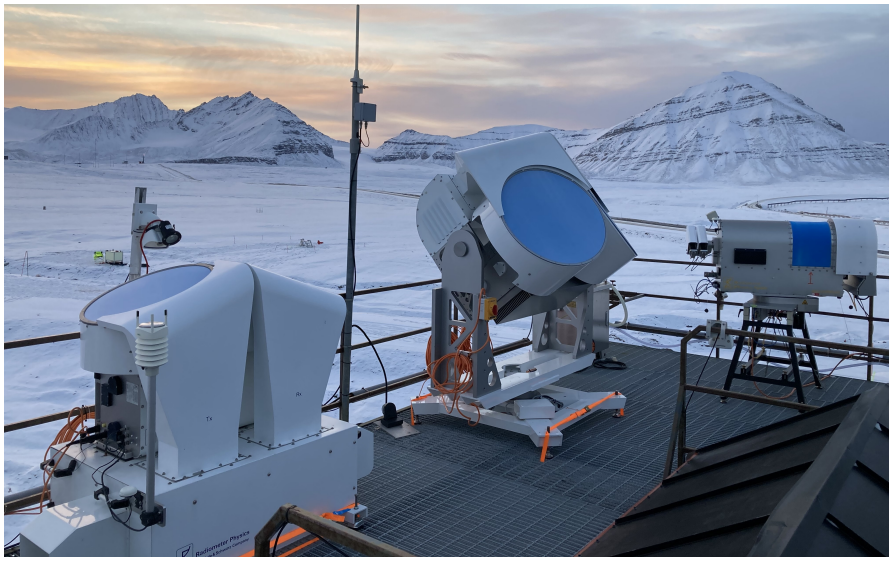

Figure 1. Measurement set-up at the AWIPEV observatory in Ny-Ålesund. From left to right: JOYRAD-94, NyRAD-35, HATPRO.

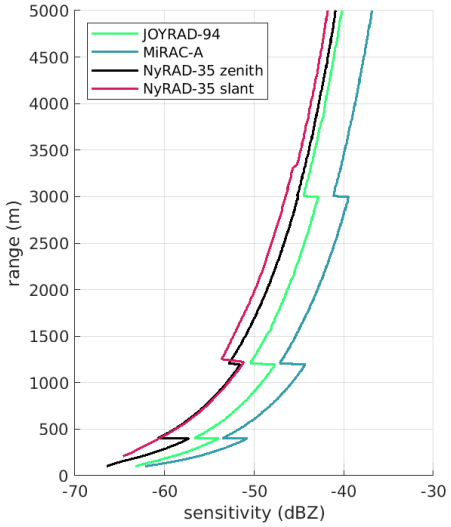

Figure 2. Median profiles of the sensitivity limit of all radar systems and chirp programs used in the study.

https://doi.org/10.5194/essd-2023-157
Preprint. Discussion started: 6 June 2023
© Author(s) 2023. CC BY 4.0 License.

single-polarization zenith-pointing radars (model RPG-FMCW-94-SP, hereafter referred to as W-band), and NyRAD-35, a 35 GHz dual-polarization scanning radar (model RPG-FMCW-35-DP, hereafter referred to as Ka-band).

Contrary to the more commonly used pulsed radars, FMCW radars transmit a continuous wave, which is modulated in frequency around the central frequency (i.e. 35 or 94 GHz for the radars employed in this study). The signal is modulated in a saw-tooth pattern, with each individual ramp step typically referred to as chirp. Multiple chirps are combined into a chirp sequence, and target ranging is performed by determining the frequency difference between the transmitted and the received chirp sequence, named intermediate frequency (IF). In practice, due to a limited IF bandwidth, a number of chirp sequences is required in order to sample the whole troposphere. The radar transmits the chirp sequences in succession, with the total time resolution being determined by the sum of the sampling time needed for each chirp sequence. We refer to a group of chirp sequences as chirp program, and the timestamp indicated in the files refers to the end of each execution of a chirp program. The exact chirp program settings can be defined by the user, and the values used to collect the data are reported in Table 2. The sensitivity profiles associated with the different chirp programs and instruments are displayed in Fig. 2.

The Ka-band was operated throughout the whole dataset period, while JOYRAD-94 was operated until 22 June 2022, when it was replaced by MiRAC-A. The technical characteristics of JOYRAD-94 are described in Küchler et al. (2017), while MiRAC-A is described in Mech et al. (2019). The details regarding the processing of data from both W-band radars, in particular the noise removal and Doppler aliasing correction, are presented in Küchler et al. (2017). The two W-band systems are similar in most aspects, the major differences being the larger beam width of MiRAC-A (0.85°) compared to JOYRAD-94 (0.5°), and the longer time resolution of JOYRAD-94, which despite using the same chirp program settings as MiRAC-A during the study period, needs an extra 0.4 seconds to reinitialize the measurements before the first chirp sequence of each chirp program. Nonetheless, the effective integration time is the same for both instruments in a given chirp sequence, and ranges between 0.27 and 0.37 s. Data from both W-band radars have already been used in a number of studies, including Dias Neto et al. (2019), Wendisch et al. (2019), Gierens et al. (2020), and Schween et al. (2022).

Data from NyRAD-35, the Ka-band radar, are instead first used in this dataset, and more details on the instrument, as well as the data processing will be given. NyRAD-35 is a dual-polarization simultaneous transmission simultaneous reception (STSR) radar, with elevation-scanning capabilities. The scanner can perform full 180° scans in elevation, and is operated at a constant azimuth of approximately 27°, i.e. along the north-north-east to south-south-west direction. STSR radars receive at horizontal and vertical polarization, but transmit a signal that is linearly polarized along the 45° direction between vertical and horizontal directions. This allows both for linear depolarization ratio (LDR) observations in zenith and typical dual-polarization variable observations at low elevations. The radar was set up to perform a scan cycle that includes zenith observations and lower elevation observations (30°-40° elevation). For optimal matching with the W-band radars, the chirp program during zenith observations was set up with the same range resolution as the W-band radars. Matching Ka- and W-band observations in zenith allows for the calculation of the DWR, in order to obtain information on the characteristics size of the ice particle population. The slanted observations are instead used to obtain dual-polarization variables, such as differential reflectivity (Z_{DR}) or specific differential phase (K_{DP}). A different chirp program is used for low elevation observations, with a constant range resolution of 29.8 m. Similarly to the W-band radars, the noise level is determined with the widely-used approach by Hildebrand and Sekhon

https://doi.org/10.5194/essd-2023-157
Preprint. Discussion started: 6 June 2023
© Author(s) 2023. CC BY 4.0 License.

	JOYRAD-94	MiRAC-A	NyRAD-35
Central frequency	94.0 GHz	94.0 GHz	35.0 GHz
Time res.	2.4 s	2.0 s	6.0/4.0 s
Beam width (half power)	0.5°	0.85°	1.0°
Polarimetry	single pol.	single pol.	dual pol. (STSR)
Orientation	zenith only	zenith only	scanning
Data availability	10.10.21-22.06.22	23.06.22-31.12.22	10.10.21-31.12.22
Variables	Doppler moments	Doppler moments	Doppler moments, LDR (zenith), polarimetry (low elevation)
Aliasing corrected	yes	yes	no

Table 1. Selected specifications of the three radar systems used in this study: two W-band cloud radars, JOYRAD-94 and MiRAC-A, and a Ka-band cloud radar, NyRAD-35.

(1974). Aliasing is instead not corrected, since the Nyquist range is large enough not to produce aliasing in zenith observations in most conditions (see Table 2), while velocity information is not of interest at lower elevations, since a radial component of the horizontal wind is present in the observed Doppler velocity. At low elevation Ka-band observations are affected by ground clutter, namely artefacts caused by backscattering of the signal by the ground surface, and range folding, i.e. the incorrect ranging of targets located beyond the maximum unambiguous range of the measurements. The correction of such artefacts is described in detail in sections 4.3 and 4.4.

2.2 Microwave radiometer

Radar observations are complemented with thermodynamic information from a Humidity and Temperature Profiler (HATPRO; generation 2) microwave radiometer (Rose et al., 2005). HATPRO records brightness temperatures (BTs) in 14 channels, 6 located in the K-band close to the 22-GHz water vapour absorption line, one located in the Ka-band in the atmospheric window at 31.4 GHz, and the remaining 7 in the V-band close to the 60-GHz oxygen absorption line. Liquid water path (LWP), integrated water vapour (IWV) and temperature profiles are retrieved from BT observations using the multivariable linear regression approach described in Nomokonova et al. (2019). Temperature in particular is retrieved using the approach by Crewell and Löhnert (2007), which exploits BTs observed at multiple elevations, so called boundary-layer scans, to improve the accuracy of the retrieval, especially in the lowest 1 km. The accuracy of this technique was assessed by Gierens et al. (2020) in single-layer LLMPCs at Ny-Ålesund against radiosondes, and they reported an RMSE of 0.7 K at the surface, that increases to 1.6 K (2.0 K) at the base of the liquid layer (cloud top) of the LLMPC. HATPRO performs a 30-minute scan cycle, starting every hour at :00 and :30 past; it is composed of a full 360° azimuth scan at 30° elevation lasting 2-3 minutes, followed by a boundary layer scan for the temperature retrieval, and zenith observations for the remaining part of the scan cycle (ca. 23 minutes). During the zenith observations a second boundary layer scan is performed, approximately 15 minutes after the previous one. The LWP and IWV values included in the dataset are recorded during the azimuth scans and the zenith

https://doi.org/10.5194/essd-2023-157
Preprint. Discussion started: 6 June 2023
© Author(s) 2023. CC BY 4.0 License.

Open Access Earth System Science Data Discussions

	W-band	Ka-band zenith	Ka-band off-zenith
Chirp Seq. 1:			
Min range [m]	100	100	200
Max range [m]	400	400	1243
Range res. [m]	3.2	3.2	29.8
Nyquist range [m s^{-1}]	5.1	23.3	28.4
Doppler res. [m s^{-1}]	0.020	0.045	0.055
Integration time [s]	0.37	1.47	0.37
Tot. sampling time [s]	0.64	1.51	1.24
Chirp Seq. 2:			
Min range [m]	400	400	1243
Max range [m]	1200	1200	3329
Range res. [m]	7.5	7.5	29.8
Nyquist range [m s^{-1}]	5.1	22.0	19.1
Doppler res. [m s^{-1}]	0.020	0.043	0.075
Integration time [s]	0.27	1.47	0.78
Tot. sampling time [s]	0.48	1.60	0.98
Chirp Seq. 3:			
Min range [m]	1200	1200	3329
Max range [m]	3000	3000	6309
Range res. [m]	9.7	9.7	29.8
Nyquist range [m s^{-1}]	3.2	10.8	9.7
Doppler res. [m s^{-1}]	0.013	0.042	0.076
Integration time [s]	0.37	1.74	0.69
Tot. sampling time [s]	0.50	1.94	0.85
Chirp Seq. 4:			
Min range [m]	3000	3000	6309
Max range [m]	13000	13000	14000
Range res. [m]	23.8	23.8	29.8
Nyquist range [m s^{-1}]	3.2	8.1	4.7
Doppler res. [m s^{-1}]	0.025	0.063	0.037
Integration time [s]	0.27	0.64	0.73
Tot. sampling time [s]	0.38	0.95	0.92

Table 2. Chirp program settings for the radar observations reported in this study: the chirp program reported for W-band was used both for JOYRAD-94 and MiRAC-A. Two separate chirp programs were used for NyRAD-35 (Ka-band) depending on elevation.

https://doi.org/10.5194/essd-2023-157
Preprint. Discussion started: 6 June 2023
© Author(s) 2023. CC BY 4.0 License.


observations: off-zenith values are multiplied by the sine of the elevation angle to obtain the corresponding vertical value. The temperature profiles included in the dataset are only taken from the boundary layer scans, and interpolated to a finer time resolution.

Retrievals from HATPRO are quality controlled via two separate approaches: by eliminating data points were rain was recorded by the instrument's weather station, and by using a spectral consistency check. The first approach consists in eliminating all data points when the weather station detected precipitation and temperature above 0°C, as rain depositing on the instrument's radome might invalidate the BT observations. A further sanity check is performed by retrieving the BT for each channel individually based on BTs observed by all other channels: if the simulated and observed BTs do not match within a certain tolerance, the data point is assumed invalid and removed form the dataset. The exact criteria used to remove unreliable data points were determined empirically, and are as follows:

- at K- and Ka-band the sum of the absolute differences between channels 2 through 7 is larger than 3 K,
- at V-band the sum of the absolute differences between all channels is larger than 10 K,
- at V-band 4 or more channels have absolute differences larger than 2 K.

Data are removed if any of the listed criteria is satisfied. This approach is especially useful after periods of rain, when precipitation has stopped, but the radome is still wet, thus effectively rendering the BTs unreliable.

2.3 Cloudnet target classification product

In order to obtain cloud phase information, used to determine whether a certain cloud event is a LLMPC, and information on the height of the liquid base of LLMPCs we use the Cloudnet target classification product (Hogan and O'Connor, 2004; Illingworth et al., 2007). The product combines data from the W-band cloud radars, microwave radiometer, and a ceilometer (model Vaisala CL51; Maturilli and Ebell (2018)), together with output from the ICOsahedral Nonhydrostatic weather model (ICON; Zängl et al. (2015)), in its global numerical weather prediction mode (ICON-NWP), to classify the phase associated with radar and ceilometer echoes. It distinguishes between: cloud droplets, supercooled cloud droplets, and cloud ice, as well as drizzle or rain. The algorithm determines the presence of liquid at sub-zero temperatures based on ceilometer echoes, as layers composed of liquid droplets produce intense backscattering of the ceilometer signal. We employ the phase information in the Cloudnet product to determine the presence of LLMPCs, as described in section 4.2. Additionally, we extract from the Cloudnet product the height of the base of the lowest liquid layer in LLMPCs, and include it in the dataset.

2.4 ICON-LEM setup

Additional meteorological variables not obtainable via our observations were needed in the dataset, especially humidity and pressure profiles, necessary to correct the radar data for attenuation. For these purposes we extract background thermodynamic profiles, as well as wind fields, from the output of the ICON model, ran in its large-eddy version (ICON-LEM; Dipankar et al., 2015; Schemann et al., 2020). ICON-LEM uses a 3D Smagorinsky turbulence scheme, and is ran in a circular domain with

https://doi.org/10.5194/essd-2023-157
Preprint. Discussion started: 6 June 2023
© Author(s) 2023. CC BY 4.0 License.

Open Access Earth System Science Data Discussions

110 km diameter centered around Ny-Ålesund, 600 m horizontal resolution and 100 vertical levels. The domain of the LEM is nested in a larger domain, where ICON is run in the numerical weather prediction (ICON-NWP) mode, which is used as forcing. The full details on the model set-up can be found in Schemann and Ebell (2020) and Kiszler et al. (2023). Compared to their set-up a slight modification in the microphysical scheme was applied, which does not significantly impact the variables used in this dataset. Kiszler et al. (2023) in particular validated the model output against radiosondes and HATPRO retrievals and found strikingly good agreement between simulated and observed wind and humidity fields. Wind fields from ICON-LEM are interpolated to the same range and time resolution as the radar data, and included in the dataset. The wind data from the first three hours after the start of each simulation (daily at midnight) are not included, as they might not be reliable.

3 Derivation of polarimetric variables from STSR-mode cloud radars

STSR cloud radars are still not largely used, and the derivation of certain polarimetric variables, especially the correlation coefficient between the received signals at horizontal and vertical polarization ρ_{HV} and the linear depolarization ratio (LDR), can be approached with a variety of methods. Hence, in this section we provide a brief summary of how we derive typical polarimetric variables from STSR radar observations. Cloud radars operating at STSR mode (also called hybrid mode) measure the so-called coherency matrix $\mathbf{B}$. The calculation of the coherency matrix follows Eq. 3.146 in Bringi and Chandrasekar (2001), given for the processing of a pulse train in weather radars. In contrast, cloud radars compute the coherency matrix for each spectral line of a Doppler spectrum. For a spectral line at a given range the coherency matrix $\mathbf{B}$ can be expressed as function of the received electric field:

$$\mathbf{B} = \langle \mathbf{E}\mathbf{E}^{\dagger} \rangle = \begin{pmatrix} \langle E_h E_h^* \rangle & \langle E_h E_v^* \rangle \\ \langle E_v E_h^* \rangle & \langle E_v E_v^* \rangle \end{pmatrix}, \tag{1}$$

where $\mathbf{E}$ is a column vector that indicates the complex amplitude of the received electric field, and E_h and E_v respectively its horizontal and vertical components. The complex conjugate is indicated with *, the conjugate transpose with $\dagger$, and the $\langle\cdot\rangle$ brackets indicate averaging across multiple samples. The elements of the spectral coherency matrix can then be expressed as:

$$\mathbf{B} = \begin{pmatrix} B_{hh} & \dot{B}_{hv} \\ \dot{B}_{hv}^* & B_{vv} \end{pmatrix}, \tag{2}$$

where B_{hh} and B_{vv} are real numbers proportional to the power received at horizontal and vertical polarization, respectively; $\dot{B}_{hv}$ is instead the complex covariance between the two received components. Here all components of $\mathbf{B}$ are rescaled to have the typical units of the equivalent radar reflectivity factor in linear scale, i.e. $\mathrm{mm}^6\ \mathrm{m}^{-3}$.

Before radar variables are calculated, spectral lines containing signal have to be detected. For the detection we use the approach described in (Görsdorf et al., 2015, see Sec. 3.3. therein). For the threshold we used 6 standard deviations of noise above the mean spectral noise level. In this dataset the mean spectral noise level determination is performed with the algorithm by Hildebrand and Sekhon (1974). In the following $\widetilde{B}_{hh}$ and $\widetilde{B}_{vv}$ indicate a spectral line exceeding the threshold and having the mean spectral noise level subtracted in the horizontal and vertical channel, respectively. Reflectivity at horizontal and vertical

https://doi.org/10.5194/essd-2023-157
Preprint. Discussion started: 6 June 2023
© Author(s) 2023. CC BY 4.0 License.

polarization directions can be expressed as:

$$\mathrm{Z_{eH}} = \sum \widetilde{B}_{hh},\ \mathrm{Z_{eV}} = \sum \widetilde{B}_{vv}, \tag{3}$$

where $\sum$ indicates summation over all spectral lines detected in a Doppler spectrum. Differential reflectivity can be expressed as:

$$\mathrm{Z_{DR}} = \frac{\sum \widetilde{B}_{hh}}{\sum \widetilde{B}_{vv}} = \frac{\mathrm{Z_{eH}}}{\mathrm{Z_{eV}}}. \tag{4}$$

Following von Terzi et al. (2022) we include in the dataset the maximum spectral $\mathrm{Z_{DR}}$ as well:

$$\mathrm{sZ_{DR\,max}} = \max(\mathrm{sZ_{DR}}) = \max\left(\frac{\widetilde{B}_{hh}}{\widetilde{B}_{vv}}\right), \tag{5}$$

where the maximum is calculated across all Doppler spectral lines with $\widetilde{B}_{hh,vv} > 0$. Similarly to von Terzi et al. (2022), in order to reduce the noise-induced variance of the variable we calculate the maximum in eq. 5 only across spectral lines with spectral signal-to-noise ratio (sSNR) higher than 10 dB in both polarimetric channels. Here sSNR is defined as the ratio of $\widetilde{B}_{hh,vv}$ over the corresponding mean spectral noise level, i.e. the total noise power divided by the number of Doppler bins. Furthermore, in order to achieve higher consistency between different chirp sequences $\mathrm{sZ_{DR}} = \widetilde{B}_{hh}/\widetilde{B}_{vv}$ is linearly interpolated (in log-scale) on a common Doppler resolution of 0.1 m $\mathrm{s^{-1}}$ before calculating the maximum.

The phase shift between the horizontal and vertical components of the received electric fields can be expressed as:

$$\Phi_{\mathrm{DP}} = \mathrm{phase}\left(\sum \dot{B}^*_{hv}\right) \doteq \arctan\left(\frac{\mathrm{Im}(\sum \dot{B}^*_{hv})}{\mathrm{Re}(\sum \dot{B}^*_{hv})}\right), \tag{6}$$

where $\mathrm{Re}(z)$ and $\mathrm{Im}(z)$ indicate the real and imaginary parts of the complex number z. Note that here the summation is performed only over spectral lines where the signal is detected at both polarizations. By calculating the half range derivative of Φ_{DP} one obtains the specific differential phase $\mathrm{K_{DP}}$. $\mathrm{K_{DP}}$ typically displays large noise-induced fluctuations (e.g. Trömel et al., 2013), hence additional processing needs to be performed in order to reduce its variance. Here we calculate Φ_{DP} by including a sSNR threshold of 10 dB in the summation in eq. 6, and $\mathrm{K_{DP}}$ is further smoothed by applying a moving average in range (10 range gates, or 298 m) and time (5 minutes), similarly to von Terzi et al. (2022).

3.1 Correlation coefficient calculation

The correlation coefficient between the horizontal and vertical components of the received electric field ρ_{HV} is typically computed with the formula (Bringi and Chandrasekar, 2001, eq. 6.110a):

$$\rho_{\mathrm{HV}} = \frac{|\sum \dot{B}_{hv}|}{\sqrt{(\sum B_{hh}) \cdot (\sum B_{vv})}}. \tag{7}$$

Note that here the summation is performed only over spectral lines where the signal is detected at both polarizations. According to Bringi and Chandrasekar (2001, Eq. 6.122 therein) ρ_{HV} calculated this way is prone to a bias due to the signal-to-noise ratio

https://doi.org/10.5194/essd-2023-157
Preprint. Discussion started: 6 June 2023
© Author(s) 2023. CC BY 4.0 License.

(SNR). This often leads to apparent signatures in ρ_{HV} which are not caused by cloud microphysics but rather by a low SNR. One possible solution to this problem is to subtract the corresponding mean noise level from the power estimates in the denominator of Eq. 7:

$$\rho_{\mathrm{HV}} = \frac{|\sum \dot{B}_{hv}|}{\sqrt{(\sum \widetilde{B}_{hh}) \cdot (\sum \widetilde{B}_{vv})}}. \tag{8}$$

Myagkov and Ori (2022) noted however that this approach often leads to inaccurate ρ_{HV} values, due to the removed noise level being an estimate which might not exactly correspond with the true noise power. In some occasions ρ_{HV} values computed with eq. 8 might in fact exceed 1. Here we propose a modification to eq. 8 that has the potential to circumvent the effects of an incorrect noise level estimation on ρ_{HV}. We use eq. 7 instead of eq. 8, and only perform the summation on spectral lines where ρ_{HV} is not strongly affected by noise contributions. We approach this by searching for spectral lines where the contributions from non-coherent antenna coupling (Myagkov et al., 2015) as well as particle depolarization exceed contributions from noise. We decompose the coherency matrix $\mathbf{B}$ into non-coherent and fully coherent components following Born and Wolf (1975, Sec. 10.8 therein):

$$\mathbf{B} = 0.5A\mathbf{I} + \mathbf{C}, \text{ with } \det(\mathbf{C}) = 0, \tag{9}$$

where A is the non-coherent power, $\mathbf{I}$ is a 2×2 unity matrix, $\mathbf{C}$ is the coherency matrix of the fully coherent component, and det is the matrix determinant.

Following Myagkov and Ori (2022, Sec. 3.1 therein) we represent the measurements in the basis in which the coherency matrix is diagonal, i.e. the orthogonal linear components of the received signal are not correlated:

$$\mathbf{D} = \begin{pmatrix} D_{cc} & 0 \\ 0 & D_{xx} \end{pmatrix} = 0.5A\mathbf{I} + \mathrm{tr}(\mathbf{C}) \begin{pmatrix} 1 & 0 \\ 0 & 0 \end{pmatrix}, \tag{10}$$

where tr is the matrix trace. The elements D_{cc} and D_{xx} can be computed as the eigenvalues of the coherency matrix $\mathbf{B}$. As can be seen from Eq. 10, the element D_{xx} contains only the non-coherent component. The non-coherent component in general includes contributions by noise, by depolarization by cloud particles, and by the presence of non-coherent antenna coupling. By determining the spectral lines with signal in D_{xx} (same procedure as for B_{hh} and B_{vv}), we identify spectral lines with considerable contribution from non-coherent antenna coupling and depolarization by cloud particles. The correlation coefficient is then calculated as in Eq. 7 with the summations performed only over spectral lines where D_{xx} exceeds the threshold over the noise level.

We calculate the linear depolarization ratio (LDR) in zenith from ρ_{HV} following the approach given in Galletti and Zrnic (2011) and Galletti et al. (2011). Assuming the reflection symmetry (Nghiem et al., 1992) and that $\mathrm{Z_{DR}}$ is equal to 1 (in linear units), which is typically the case at vertical elevation, LDR can be computed by combining Eq. 12 in Galletti and Zrnic (2011) with Eq. 10 in Galletti et al. (2011), to obtain:

$$\mathrm{LDR} = \frac{1 - \rho_{\mathrm{HV}}}{1 + \rho_{\mathrm{HV}}}. \tag{11}$$

https://doi.org/10.5194/essd-2023-157
Preprint. Discussion started: 6 June 2023
© Author(s) 2023. CC BY 4.0 License.

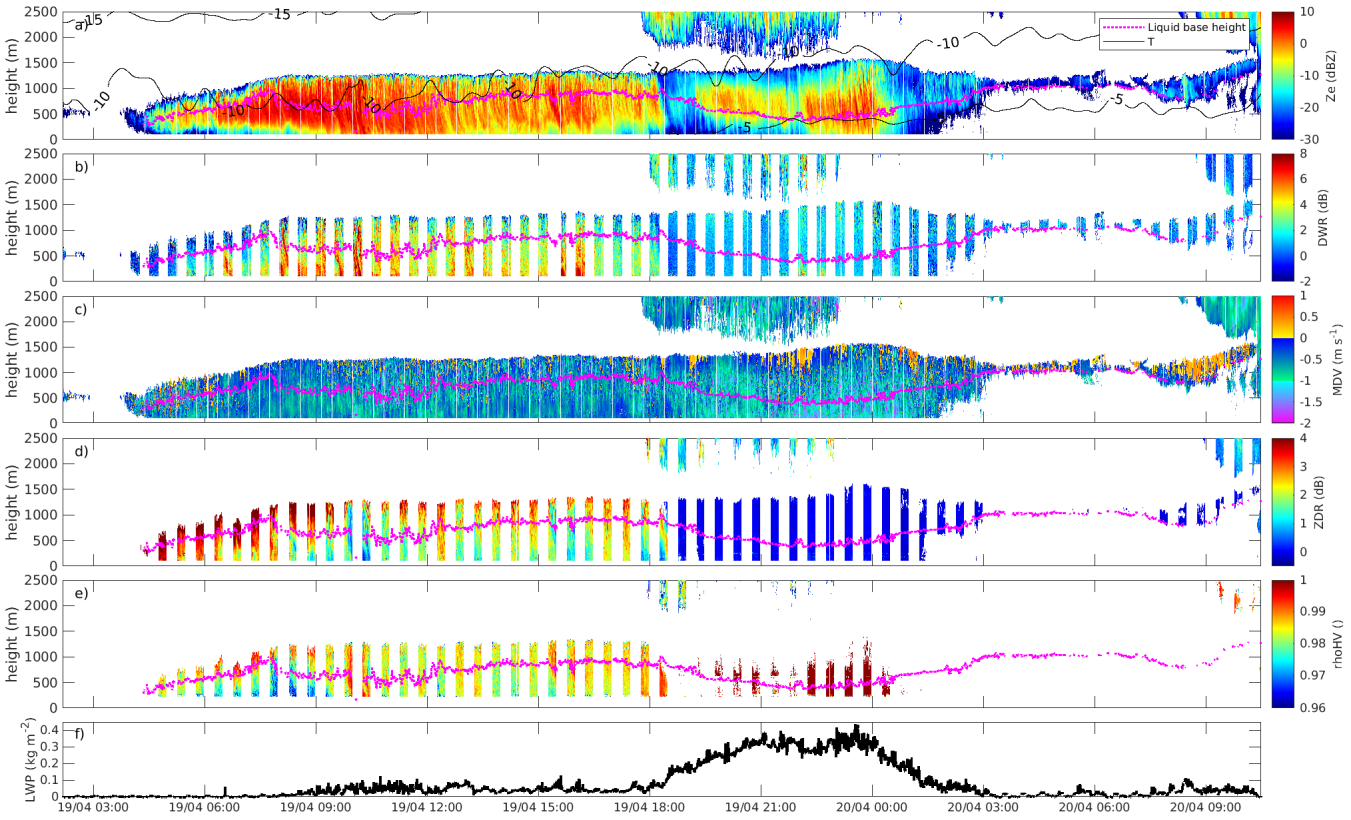

Figure 3. LLMPC event detected on 19-20 April 2022. Panels respectively display: reflectivity from W-band radar with temperature contours overlayed (a), dual-wavelength ratio (b), mean Doppler velocity from W-band radar (c), differential reflectivity (d), correlation coefficient (e), liquid water path (f). All radar variables were recorded at zenith elevation, except for differential reflectivity and correlation coefficient that were recorded at 30° elevation. The dotted magenta line on panels a through e indicates the base height of the lowest liquid layer.

We found that Eq. 11 at times produces LDR values below the integrated cross-polarization ratio (ICPR) of the instrument, which is the minimum LDR value that the radar can measure (Chandrasekar and Keeler, 1993; Myagkov et al., 2015). The radar manufacturer in fact declares that the ICPR is between -30 and -35 dB, and eq. 11 at times produces values below -35 dB, which is likely attributable to the uncertainty in the approximation given by Eq. 11. This uncertainty is caused by the signal variability due to non-coherent scattering. This effect is however is not an issue, since it is widely accepted in the cloud and weather radar community that high quality LDR observations are obtained when the ICPR is close to or lower than -30 dB. Therefore we set all LDR values below -30 dB obtained from eq. 11 to -30 dB.

https://doi.org/10.5194/essd-2023-157
Preprint. Discussion started: 6 June 2023
© Author(s) 2023. CC BY 4.0 License.

4 Data processing

4.1 Dataset structure

The dataset is structured in the following way: each individual file contains data from all sources for one or multiple LLMPC event; multiple LLMPC events are included in the same file if they are less than 4 hours apart. The criteria used to detect LLMPC events are described in the next section. The variables include Doppler moments from W-band and Ka-band in zenith, LDR in zenith from Ka-band, polarimetric variables from Ka-band at low elevation (30-40°), corrections applied to the radar data (calibration, liquid and gas attenuation), LWP, IWV and temperature profiles retrieved from HATPRO, liquid base height from the ceilometer, and horizontal wind information from ICON-LEM. All variables except low-elevation observations of the Ka-band radar are brought to the same time and range resolution of Ka-band zenith observations, for easier matching of data from different instruments. All corrections have already been applied to the data, and are included in case the user is interested in reconstructing the original uncorrected data. An example of an LLMPC event is given in Fig. 3, which displays a subset of the variables included in the dataset; the signatures displayed in the case study are further commented in section 5.

4.2 LLMPC event detection

LLMPC events were identified following the approach by Chellini et al. (2022), which is here summarized. A set of criteria are applied to the data to determine whether a given cloud event is a LLMPC:

1. Cloud top is at or below 2500 m. If multiple cloud layers are detected, at least one needs to have its top at or below 2500 m.
2. Cloudnet indicates presence of both liquid and ice in the cloud layer(s) with top below 2500 m.
3. Liquid and ice are detected by Cloudnet for at least 60 minutes with gaps allowed. The total duration of gaps in either ice or liquid phase needs to be lower than one sixth of the total duration of the LLMPC event.

During intense precipitation events ceilometer data is not always available. This is due to snow accumulating on the ceilometer aperture and leading to complete attenuation of the signal. Under these conditions Cloudnet only detects ice clouds, and criterion 2 is not satisfied even though a LLMPC might be present. These conditions are detected via the quality flags associated with ceilometer observations in the Cloudnet product. Under these circumstances LWP retrievals from HATPRO are instead used to determine the presence of the liquid phase, requiring that LWP is larger than 10 g m^{-2}.

All data corresponding to a given LLMPC event are collected in the same file, together with the previous and following two hours, in order to provide information on the conditions leading to the onset and cessation of events. Two events are included in the same file if the two hours following a given event overlap with the two hours preceding the next event.

https://doi.org/10.5194/essd-2023-157
Preprint. Discussion started: 6 June 2023
© Author(s) 2023. CC BY 4.0 License.

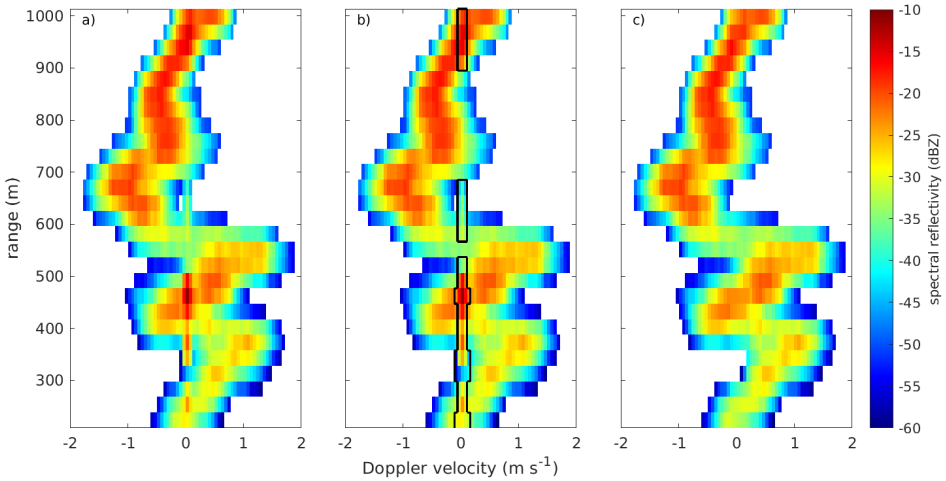

Figure 4. Example of the ground clutter mitigation procedure applied to Doppler spectra recorded at 30° elevation on 15 October 2022 at 21:23:38 UTC. Panel a depicts the original Doppler spectrum, while in panel b the contour indicates the Doppler bins detected as affected by ground clutter. Panel c displays the final spectrum after clutter removal.

4.3 Ka-band: ground clutter mitigation

We found the low elevation observations of the Ka-band radar to be contaminated with ground clutter, namely the presence of artefacts caused by backscattering of the radar signal by the ground. We correct the data using an approach similar to that developed by Williams et al. (2018). Thanks to the lack of moving clutter-generating targets, all clutter signal is only found either in the 0 m s^{-1} Doppler velocity spectral line, or in nearby lines. An example of a Doppler spectrum affected by ground clutter is shown in Fig. 4 panel a, while panel c displays the same spectrum after clutter removal. Indicating the spectral reflectivity in dBZ of the spectral line at 0 m s^{-1} as $\mathrm{sZ_e}(i_0)$, the presence of clutter is determined when the two following criteria are satisfied:

1. $\mathrm{sZ_e}(i_0) - \frac{1}{4}[\mathrm{sZ_e}(i_0-2) + \mathrm{sZ_e}(i_0-1) + \mathrm{sZ_e}(i_0+1) + \mathrm{sZ_e}(i_0+2)] > 2$ dB;
2. $\mathrm{sZ_e}(i_0) < -15$ dBZ.

The second criterion was determined empirically, since we never observed ground clutter characterized by a spectral reflectivity higher than -15 dBZ. If ground clutter is identified, the three spectral lines i_0-1, i_0, and i_0+1 are removed, and replaced with linearly interpolated values between $\mathrm{sZ_e}(i_0-2)$ and $\mathrm{sZ_e}(i_0+2)$. This procedure is applied independently to $\widetilde{B}_{hh}$, $\widetilde{B}_{vv}$, and the modulus of the off-diagonal component $|\dot{B}_{hv}|$. If clutter is identified in $|\dot{B}_{hv}|$, the corresponding spectral lines in phase$(\dot{B}_{hv})$ are also removed, and replaced with the median value of phase$(\dot{B}_{hv})$ across all spectral lines without clutter, and above the noise level. In the lowest 20 range gates (i.e. from 200 to 796 m range) we found, at times, the criteria listed above not to be sufficient, because in some cases ground clutter might also be present in the spectral lines i_0-2 and i_0+2, and might display

https://doi.org/10.5194/essd-2023-157
Preprint. Discussion started: 6 June 2023
© Author(s) 2023. CC BY 4.0 License.

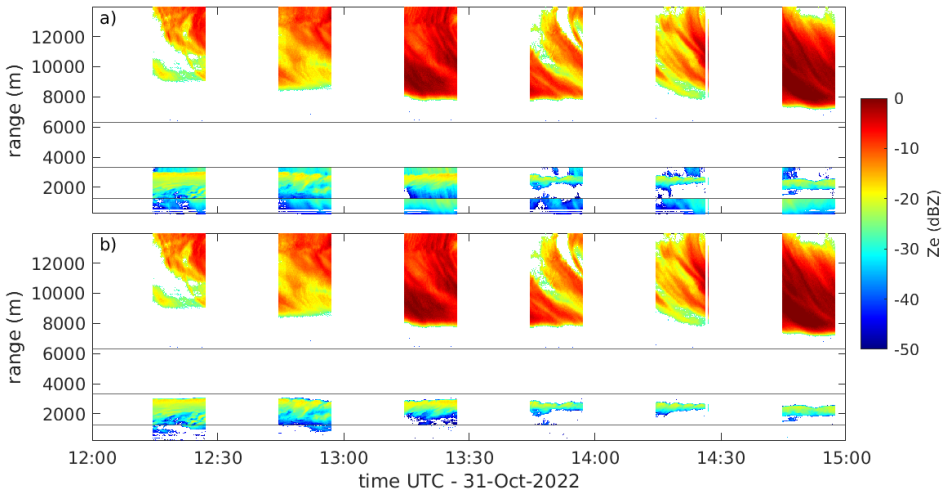

Figure 5. Reflectivity time-height display recorded at 30° elevation on 31 October 2022. Horizontal lines indicate boundaries between chirp sequences. Panel a depicts the original reflectivity values, affected by range folding (in the two lowest chirp sequences), while panel b displays reflectivity after the removal of range folding.

spectral reflectivity in the 0 m s^{-1} spectral line higher than -15 dBZ. After applying the criteria listed above, a second set of criteria is applied in the lowest 20 range gates, to detect possible residual clutter:

1. $\mathrm{sZ_e}(i_0) - \frac{1}{4}[\mathrm{sZ_e}(i_0-3) + \mathrm{sZ_e}(i_0-2) + \mathrm{sZ_e}(i_0+2) + \mathrm{sZ_e}(i_0+3)] > 2$ dB.
2. $\mathrm{sZ_e}(i_0) < 5$ dBZ.

For range gates satisfying these criteria the interpolation is also extended to $i_0 - 3$, $i_0 + 3$.

4.4 Ka-band: range folding correction

At low elevation angles, range folding was sometimes observed in the Ka-band data in the two lowest chirp sequences. Range folding is the incorrect ranging of targets located at ranges larger than the maximum unambiguous range of the radar measurements. The maximum unambiguous range for the two lowest chirp sequences is in fact 10000 m, which at 30° elevation corresponds to a height of 5000 m, above which it is likely to observe clouds. In RPG FMCW radars the apparent range r of a target affected by range folding is:

1. $r = R_{unamb} - (R - R_{max})$, when the actual range R is $R_{unamb} < R < R_{unamb} + R_{max} - R_{min}$,
2. $r = R - (R_{unamb} + R_{max})$, when the actual range R is $R_{unamb} + R_{max} + R_{min} < R < R_{unamb} + 2 \cdot R_{max}$,

where R_{max} and R_{min} are the maximum and minimum ranges of the chirp sequence, as indicated in table 2, and R_{unamb} is the maximum unambiguous range. We found that in the first folding scenario phase($\dot{B}_{hv}$) assumes unrealistic values, and events displaying folding of this type are easily corrected by including a sanity check $|\mathrm{phase}(\dot{B}_{hv})| < 50°$. Folding scenarios of

https://doi.org/10.5194/essd-2023-157
Preprint. Discussion started: 6 June 2023
© Author(s) 2023. CC BY 4.0 License.

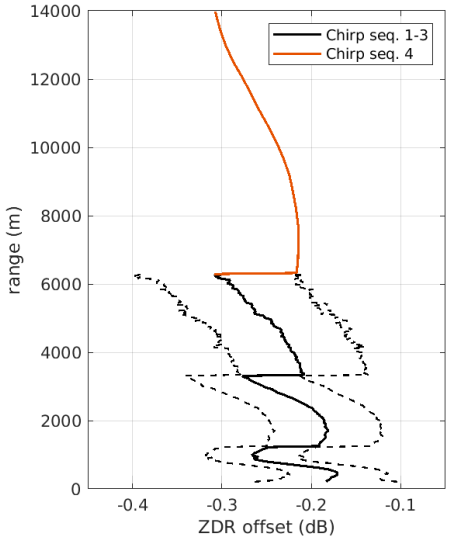

Figure 6. Differential reflectivity (Z_{DR}) offset profile. Black lines indicate values obtained for chirp sequences number 1 to 3, while the orange curve was extrapolated for chirp sequence 4. Dashed lines indicate the median value plus and minus one standard deviation.

the second type are more challenging to correct. We only observed folding of this type to occur in the first chirp sequence, and echoes affected by range folding in the first sequence are captured without range folding in the fourth chirp sequence. Therefore we developed the following procedure to remove range folding from the first chirp sequence when echoes are present in the fourth sequence:

1. Spectra from the first chirp sequences are interpolated to the same Doppler resolution as the fourth chirp sequence.
2. The interpolated spectra are then artificially brought to the same Nyquist range as the fourth chirp sequence by artificially velocity-folding them, as the Nyquist velocity of the fourth chirp sequence is lower than that of the first chirp sequence.
3. Spectral reflectivity from the fourth chirp sequence is rescaled by $r^2 \cdot R^{-2}$ to match the reflectivity of the range folded signal.
4. Spectra from the two chirp sequences are subtracted.
5. The resulting spectra are interpolated back to the original Doppler resolution.
6. Possible residual values below sensitivity and isolated spectral lines are removed.

An example of an event with folding is shown in Fig. 5, before and after the correction.

4.5 Ka-band: Z_{DR} and Φ_{DP} calibration

Radar systems receiving at two polarization directions might display slight offsets in Z_{DR} and Φ_{DP}, due e.g. to differences in antenna gain along the two polarimetric directions, or in the waveguides and feedhorns of the two polarimetric channels. In

https://doi.org/10.5194/essd-2023-157
Preprint. Discussion started: 6 June 2023
© Author(s) 2023. CC BY 4.0 License.

FMCW systems such offsets might further display a dependency on range, as they might depend on the IF, as well as range resolution. Here we evaluate such offsets by exploiting Z_{DR} and Φ_{DP} observations in zenith, as we can expect them to be close to 0 dB and 0° respectively. Since such offsets can be dependent on the chirp program used, we evaluate them using the same chirp program that is used for low-elevation observations. When switching elevation positions the Ka-band radar in fact performs RHI scans (not included in this dataset), that use the same chirp program. In order to derive the offsets, we compile Z_{DR} and Φ_{DP} profiles recorded at elevations between 85 and 95°, and calculate median profiles. The Z_{DR} offset obtained with this approach is displayed in Fig. 6 in black: the values range between -0.31 and -0.17 dB, with a standard deviation of 0.06 dB, that is constant with range. Due to the low number of observations in zenith at range above 6 km, the offset profile for chirp sequence number 4 could not be obtained. We instead used the Z_{DR} offset profile from chirp sequence number 1, expressed it as function of IF, and then mapped it to chirp sequence number 4 by matching the IF to the range gates of chirp sequence number 4. The result of this procedure is shown in red in Fig. 6. The complete offset profile was then subtracted from all Z_{DR} and $sZ_{DR\,max}$ data.

Contrary to Z_{DR}, the offset for Φ_{DP} was found not to vary with range, except for the lowest 8 range gates, and to vary with season, reaching values close to -4.0° in winter, and close to -1.5° in the summer. The latter dependency is likely attributable to thermal expansion and contraction of components of the radar hardware. Due to the variability of the offset we decide not to correct for it, as the absolute value of Φ_{DP} is anyhow not of interest, but rather its change with range, expressed by K_{DP}. Nevertheless, we choose to remove ρ_{HV} and Φ_{DP} (and hence K_{DP}) data from the 8 lowest range gates, as it might contain spurious signals.

4.6 Ka- and W-band: temporal matching

In order to obtain reliable DWRs, accurate matching and calibration of the Ka- and W-band data needs to be performed. The chirp programs of the W-band and the zenith observations of the Ka-band were set up to have the same vertical grid. Temporal matching was performed by bringing the higher temporally-resolved W-band data to the same temporal resolution as the Ka-band observations. The central time of each sample was calculated for each Ka- and W-band chirp sequence, and each Ka-band sample was matched with the nearest available W-band sample, up to a maximum time difference equal to the time resolution of the W-band measurements. By performing this temporal matching we found indications of inconsistencies between the timestamps of the two radars. We attributed them to slightly incorrect timestamps of the Ka-band radar due to errors in the recording of the timestamps by the instrument software. Daily time offsets were determined by shifting the Ka-band data in time, and selecting the time shift that minimized the variance in DWR. The attempted time shifts ranged from -120 seconds to +60 seconds, in steps of 0.25 seconds.

4.7 Ka- and W-band data: calibration

Biases in observed reflectivity might arise due to changes in the calibration constant of the instruments. Hence we evaluated the calibration of all radar systems. While the Ka-band radar was recently calibrated by the manufacturer in August 2021 using the technique from Myagkov et al. (2020, Sec. 4 therein), the W-band radars have not undergone any calibration in the recent

https://doi.org/10.5194/essd-2023-157
Preprint. Discussion started: 6 June 2023
© Author(s) 2023. CC BY 4.0 License.


years. We evaluated the calibration of the Ka-band radar with a widely adopted disdrometer-based approach (e.g., Williams et al., 2005; Myagkov et al., 2020), while the W-band radars were cross-calibrated against the Ka-band radar using a DWR-based approach (Dias Neto et al., 2019; Chellini et al., 2022). Reflectivity from Ka-band zenith observations were compared with forward-simulated reflectivities obtained from drop size distributions (DSDs) measured during rain events by a Parsivel disdrometer (Löffler-Mang and Joss, 2000), which is located on the same platform as the radars, approximately 6 meters away from them. The rain events used for calibration were selected in July, August and September 2022 based on the following criteria:

- Surface temperature (from nearby weather station) is higher than 5°C, and Parsivel detects liquid precipitation.
- In order for the disdrometer measurements to be representative of the drop population, rain rate ≥ 0.1 mm h^{-1} (following Williams et al. (2005)), and measurements contain at least 25 samples per minute.
- DSDs contain particles larger than 1 mm. Such criterion was included so that possible evaporation of the drops between the chosen radar range gate and the disdrometer doesn't affect the forward simulated reflectivities (following Myagkov et al. (2020)).
- Rain events satisfying the previous criteria need to last at least 1 hour, with gaps allowed for a total of one sixth of the duration of the event.

Reflectivities were forward simulated from the DSDs with the T-matrix method (Waterman, 1965; Leinonen, 2014), using a drop shape model from Thurai et al. (2007), with Gaussian distributed canting angles (with 0° mean value and a 10° standard deviation), following Huang et al. (2008). Attenuation due to liquid was simulated as well, and was subtracted from the forward simulated reflectivity values. The forward-simulated reflectivities were compared with observed reflectivities from the range gates between 120 and 150 m. The comparison was performed by calculating the median observed and simulated reflectivity across all calibration events. The calibration offset for the Ka-band radar was found to be -0.14 dB; since this value is well within the uncertainty associated with reflectivity measurements, we do not apply any corrections to Ka-band reflectivity, and consider it already well-calibrated.

The W-band radars are instead cross-calibrated using the Ka-band as reference. The approach consists in exploiting observations of low-reflectivity ice clouds or light snowfall, to ensure the presence of mostly Rayleigh scatterers, which produce similar reflectivities at Ka- and W-band (e.g., Dias Neto et al., 2019; Tridon et al., 2020). The data used in the cross-calibration were selected using the following criteria:

- Cloudnet indicates the presence of ice only clouds.
- LWP retrievals from HATPRO are lower than 10 g m^{-2}.
- Reflectivity from the Ka-band is between -30 dBZ and -10 dBZ, to ensure the presence of mostly Rayleigh scatterers (following Dias Neto et al. (2019)).

https://doi.org/10.5194/essd-2023-157
Preprint. Discussion started: 6 June 2023
© Author(s) 2023. CC BY 4.0 License.

Date	12-Oct-2021	28-Oct-2021	14-Nov-2021	11-Dec-2021	07-Jan-2022	03-Feb-2022
Offset [dB]	0.7 ± 1.1	1.3 ± 1.2	0.5 ± 1.1	0.5 ± 1.0	0.4 ± 1.1	0.5 ± 1.1
Date	02-Mar-2022	29-Mar-2022	26-Apr-2022	20-May-2022	23-Jun-2022	21-Jul-2022
Offset [dB]	0.6 ± 1.3	0.5 ± 1.2	0.2 ± 1.0	0.7 ± 1.1	3.0 ± 1.1	3.3 ± 1.1
Date	19-Aug-2022	15-Sep-2022	12-Oct-2022	10-Nov-2022	05-Dec-2022	01-Jan-2023
Offset [dB]	2.7 ± 1.0	2.9 ± 1.1	2.4 ± 1.0	2.7 ± 1.1	1.9 ± 0.9	-

Table 3. Calibration offsets, and associated uncertainties, obtained for the W-band cloud radars. Positive values indicate an underestimation of reflectivity by the radar. Each offset was computed for the period starting on the date indicated, and ending on the day before the date indicated for the following offset. Values before 22 June 2022 refer to JOYRAD-94, while the remaining values refer to MiRAC-A.

DWR distributions for data points satisfying these criteria are compiled for a number of periods lasting approximately one month, and the mode of each distribution is taken as W-band reflectivity offset for the corresponding period. All offsets, together with the associated uncertainties, are indicated in Table 3. The uncertainty is calculated by taking the left-side standard deviation of the distribution with respect to the mode, as the right side might be affected by non-Rayleigh effects.

4.8 Ka- and W-band: gas and liquid attenuation correction

Millimeter-wavelength radar signal undergoes non-negligible attenuation due to atmospheric gases, especially molecular oxygen and water vapour, and to hydrometeors. Typical path-integrated attenuation for ice and snow at W-band has been estimated as 0.9 dB km^{-1} for ice water path (IWP) values of 1 kg m^{-2} (Nemarich et al., 1988): due to the typically far lower values of IWP observed in LLMPCs at Ny-Ålesund, in 75% of cases below 60 g m^{-2} (Gierens et al., 2020), we deem attenuation due to frozen hydrometeors negligible and do not correct for it. On the other hand attenuation due to liquid hydrometeors is highly relevant at millimeter wavelengths, especially at W-band (e.g., Tridon et al., 2020). Hence we estimate the liquid water content (LWC) and correct the data for liquid attenuation.

Here we correct for gas attenuation using thermodynamic profiles from the ICON-LEM simulations, and simulating the associated attenuation with the Passive and Active Microwave Transfer model (PAMTRA; Mech et al., 2020). PAMTRA computes 2-way path-integrated attenuation profiles due to molecular nitrogen, molecular oxygen, and water vapour, taking temperature, humidity and pressure profiles as input.

Attenuation due to liquid hydrometeors is estimated using a combination of observational and model data. We derive a theoretical scaled adiabatic LWC profile based on liquid base height and cloud top height from Cloudnet, LWP from the microwave radiometer and thermodynamic profiles from the ICON-LEM output. LWC profiles close to scaled adiabatic have been in fact reported in LLMPCs across the Greenland and Norwegian seas by Mioche et al. (2017). The procedure consists in calculating an adiabatic LWC profile starting at the liquid base, until cloud top, using the thermodynamic profiles from ICON-LEM. The obtained adiabatic LWC profile is then rescaled by a vertically-constant factor to match the retrieved LWP. Liquid attenuation is then simulated using the water dielectric constant model by Rosenkranz (2014) and assuming that liquid droplets absorb in the Rayleigh regime, using eq. 5.18 in Bohren and Huffman (2008). This approach relies on the assumption

https://doi.org/10.5194/essd-2023-157
Preprint. Discussion started: 6 June 2023
© Author(s) 2023. CC BY 4.0 License.

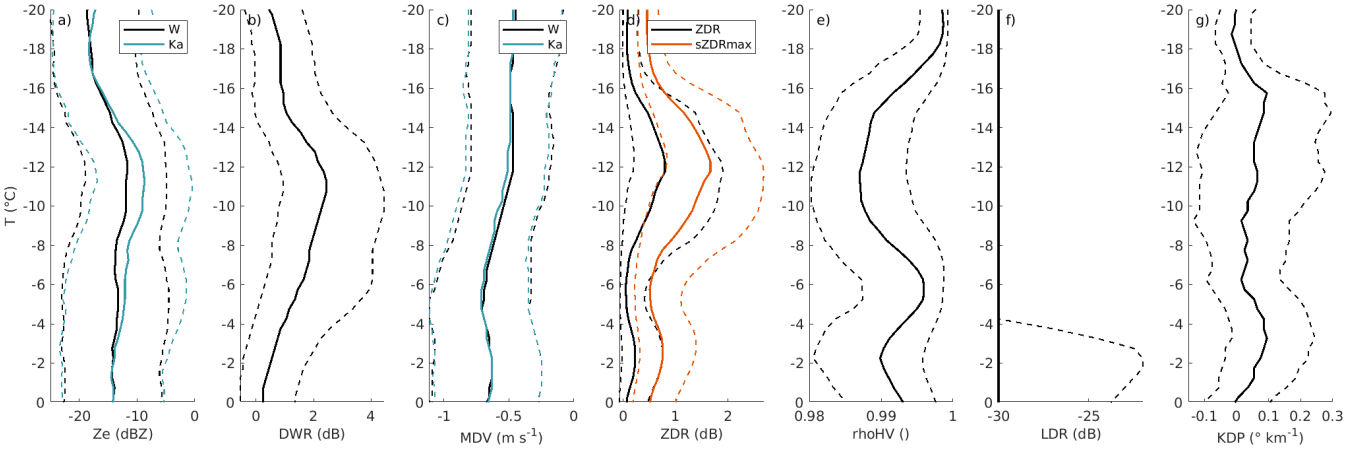

Figure 7. Contoured Frequency by Temperature Diagrams of radar variables in low-level MPCs detected at Ny-Ålesund during the study period. Solid lines indicate the median value in each temperature bin, while dashed lines indicate the 0.25 and 0.75 quantiles. The variables included are: radar reflectivity at W- and Ka-band (a), dual-wavelength ratio (b), mean Doppler velocity at W- and Ka-band (c), differential reflectivity and maximum spectral differential reflectivity (d), correlation coefficient (e), linear depolarization ratio (f), and specific differential phase (g). Temperature is obtained from HATPRO retrievals, temperature bins are 0.5°C wide.

that one continuous liquid layer is present between the liquid base indicated by the ceilometer and cloud top. This might not always be the case. Nonetheless, we deem this approach to be most sound possible with the information that we have available, since the ceilometer only provides the base height of the lowest liquid layer. Additionally the correction is set to 0 dB if LWP is below 20 g m^{-2}. It needs to be highlighted that no liquid correction is applied if either the liquid base information or LWP information are not available. Flags that indicate whether the liquid attenuation correction is available and has been applied have been included in the files. We recommend that the user makes full use of these flags to exclude from quantitative analyses reflectivity values that have not been corrected for liquid attenuation. This is especially relevant when calculating the DWR.

5 Characterization of ice particle formation and growth in LLMPCs at Ny-Ålesund

In this section we present and discuss the case study shown in Fig. 3, as well as a statistical analysis of the temperature dependence of observational fingerprints of microphysical processes obtained from radar measurements. Fig. 3 displays a number of variables recorded during a LLMPC event observed on 19-20 April 2022. The panels of the Figure display radar reflectivity from the W-band radar (a), dual wavelength ratio (b) calculated by subtracting the W-band reflectivity from the Ka-band reflectivity (both in log-scale), mean Doppler velocity from the W-band radar (c), differential reflectivity (d) and correlation coefficient (e) from 30°-elevation Ka-band observations, and LWP (f) retrieved from HATPRO observations. Liquid base height from the ceilometer is overlayed on all panels, while temperature contours are overlayed on panel a. From the onset of the event until 17:30 on 19 April Z_{DR} displays high values, above 2 dB, indicative of the presence of oblate ice particles. The temperature of the liquid layer, slightly colder than -10°C, is compatible with the growth of plate-like particles (e.g.,

https://doi.org/10.5194/essd-2023-157
Preprint. Discussion started: 6 June 2023
© Author(s) 2023. CC BY 4.0 License.

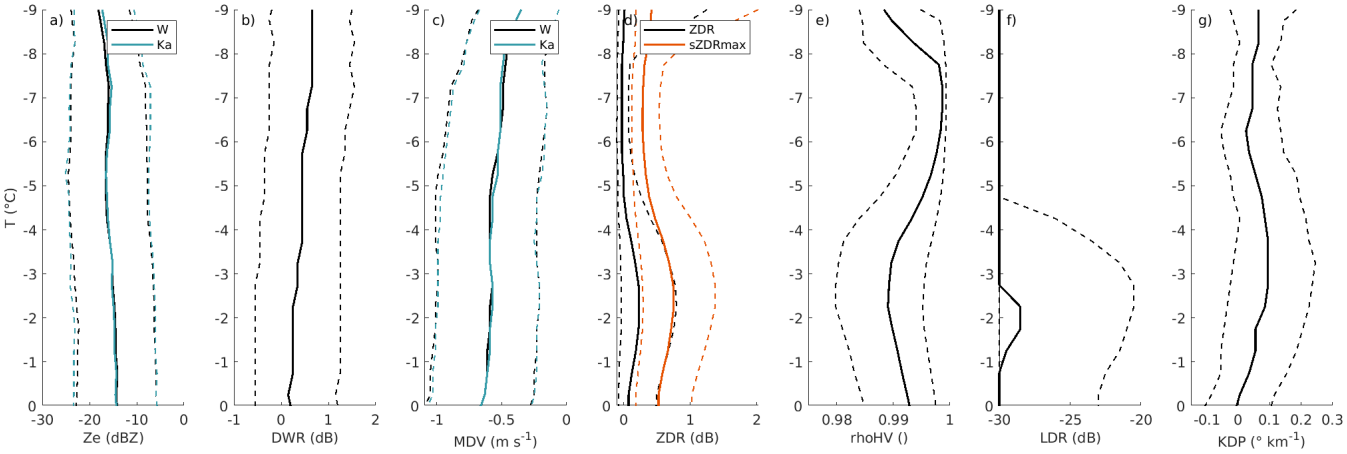

Figure 8. Same as in Fig. 7, but limited to only LLMPC events with cloud-top temperature warmer than -10°C.

Bailey and Hallett, 2009). Ice particles in fact nucleate in the liquid layer, hence their habit is strongly dependent on liquid layer temperature (Myagkov et al., 2016; Chellini et al., 2022). Z_{DR} decreases as particles sediment, and DWR increases, indicating the onset of aggregation, which increases the size of the ice particles (which in turn enhances DWR), and renders the particles more spherical (which in turn lowers Z_{DR}). In this first period MDV displays values close to 1 m s^{-1}, which are compatible with the presence of aggregates of plate-like particles (Locatelli and Hobbs, 1974; Heymsfield and Westbrook, 2010; Karrer et al., 2020). As already reported by Chellini et al. (2022) aggregation already onsets within the liquid layer of the LLMPC. After 17:30 the characteristics of the LLMCP change dramatically: LWP increases from values lower than 100 g m^{-2} to values close to 400 g m^{-2}, and precipitation is mostly composed of small, fast-falling, symmetrical particles. This is indicated respectively by MDV reaching values close to 2 m s^{-1}, ρ_{HV} close to 1, and Z_{DR} close to 0 dB. These factors together suggest the presence of rimed particles and/or drizzle. Interestingly this sudden change in precipitation regime is accompanied by cloud-top temperatures (CTT) rising to values slightly warmer than -10°C, and a higher cloud with base at 1500 to 2000 m. Temperatures between -10 and -8°C in particular have been associated with the growth of isometric particles with higher riming efficiency (Fukuta and Takahashi, 1999; Myagkov et al., 2016), that might explain the dramatic change in radar signatures at 17:30. After 23:00 on April 19th, LWP decreases again and the LLMPC reduces to a thin layer a few hundred meters deep (after 01:00 on April 20th), which does not produce any precipitation, as indicated by the liquid base from the ceilometer being close to the lowest range gates where radar reflectivity is displayed. The layer is likely composed mostly by liquid droplets, as reflectivity is below -20 dBZ.

5.1 Statistical analysis: temperature dependence of radar signatures

Ice microphysics is greatly dependent on temperature (Pruppacher and Klett, 2012), as such we can expect that observational fingerprints of microphysical processes display characteristic temperature dependencies. In order to illustrate these dependencies, in Fig. 7 we show contoured-frequency by temperature diagrams (CFTD; Yuter and Houze Jr, 1995) of most radar

https://doi.org/10.5194/essd-2023-157
Preprint. Discussion started: 6 June 2023
© Author(s) 2023. CC BY 4.0 License.

Open Access Earth System Science Data Discussions

variables introduced in the previous sections. Such diagrams illustrate how distributions of observed variables vary as temperature changes. In the Figure, radar variables for the whole study period are matched with temperature from HATPRO retrievals, and median and quantiles of each variable are then calculated in 0.5°C-wide temperature bins. In order to avoid contamination by other cloud types, only timestamps flagged as containing a LLMPC, and only range gates below the cloud top of the LLMPC are included. The latter selection is performed by determining the lowest radar range gate without signal above the liquid base in each column; all range gates above are ignored, so that higher clouds do not contribute to the statistics. Only data points where the liquid attenuation correction is available are included in the reflectivity and DWR CFTDs.

As already noted by Myagkov et al. (2016) and Chellini et al. (2022), and highlighted when commenting the case study in Fig. 3, in LLMPCs the habit of the ice particles produced is fully determined by the temperature of the liquid layer, where the ice particles nucleate and grow by depositional growth. This is in contrast to deeper cloud systems, where ice habits are less predictable due to particles growing in a number of temperature regimes as they sediment. The first temperature regime that we would like to highlight in Fig. 7 is the so-called dendritic-growth zone, namely the region between -20 and -10°C where plate-like particles grow (e.g., Bailey and Hallett, 2009; Bechini et al., 2013; von Terzi et al., 2022): inside this regime stellar or fern-like dendritic particles are observed under liquid saturation conditions, and especially between -16 and -12°C (Takahashi, 2014). Rapid growth and aggregation of dendritic particles in this temperature regime has been widely reported (Takahashi, 2014; Barrett et al., 2019; Dias Neto et al., 2019). Dendritic particles in fact aggregate efficiently due mechanical entanglement of their dendritic branches (Connolly et al., 2012). Fingerprints of dendritic growth and subsequent aggregation can be especially inferred by examining the dual-wavelength, Doppler, and polarimetric radar variables in Fig. 7: DWR displays a steady increase starting at -15°C and peaking at -11°C, while MDV slightly increases in the same temperature region, displaying median values close to -0.6 m s^{-1}; Z_{DR} and $sZ_{DR\,max}$ both start increasing and reach their maxima at a slightly colder temperature than DWR (-16 and -12°C respectively), while K_{DP}, especially its 0.75 quantile, starts increasing at colder temperatures (-18°C), reaches its maximum at -15°C, then steadily decreases as particles fall towards warmer temperatures. In agreement with Chellini et al. (2022), the observed DWR and MDV values are compatible with low-density dendrite aggregates (Locatelli and Hobbs, 1974; Heymsfield and Westbrook, 2010; Kneifel et al., 2015). Bands of enhanced K_{DP} and Z_{DR} at dendritic-growth temperatures have been widely reported in mid-latitude deep precipitating systems (Bechini et al., 2013; Schrom et al., 2015; Griffin et al., 2018; von Terzi et al., 2022). The maximum in K_{DP} at -15°C can be in fact related to the increase in number concentration of small asymmetric ice particles, and as such, a K_{DP} increase has been suggested to be a prerequisite for the onset of aggregation (Moisseev et al., 2015). The enhancement of Z_{DR} is instead typically interpreted as originating from rapid growth of plate-like particles (Schrom and Kumjian, 2016; Griffin et al., 2018; von Terzi et al., 2022). Interestingly, in typical mid-latitude systems the maximum in Z_{DR} is observed above the maxima of K_{DP} and DWR, and K_{DP} is found to increase steadily from the top of the dendritic-growth zone until its base (von Terzi et al., 2022), while Fig. 7 paints a different picture. In the Figure the peak in K_{DP}, and therefore ice number concentration, at -15°C, is followed by increases in DWR and Z_{DR} at slightly warmer temperatures. These discrepancies might be connected to the limited depths associated with Arctic LLMPCs, compared to mid-latitude deep precipitating systems. Moreover, fragmentation of dendritic and stellar crystals has been widely suggested in literature (e.g., Rangno and Hobbs, 2001; Schwarzenboeck et al., 2009; von Terzi et al.,

https://doi.org/10.5194/essd-2023-157
Preprint. Discussion started: 6 June 2023
© Author(s) 2023. CC BY 4.0 License.

2022; Pasquier et al., 2022), and it might be associated with the increase in ice number concentration suggested by the sharp enhancement in K_{DP} at -15°C.

At CTT warmer than -10°C, LLMPCs at Ny-Ålesund typically produce smaller particles, characterized by DWR close to 0 dB (Chellini et al., 2022). This is confirmed by Fig. 8, which displays CFTDs of the same radar variables included in Fig. 7, but restricted to events with CTT warmer than -10°C. The Figure displays median DWRs lower than 1 dB, compatible with particles with sizes close to or smaller than 1 mm (e.g., Ori et al., 2020), fall velocities that steadily increase from -0.4 m s^{-1} at -10°C to -0.7 m s^{-1} at 0°C, typical for small ice crystals with low degree of riming. Prolate particles, such as columns and needles, typically grow in this temperature regime (e.g., Bailey and Hallett, 2009; Myagkov et al., 2016), and can be easily detected via their enhanced LDR (Oue et al., 2015; Bühl et al., 2016; Li et al., 2021): panel f in Fig. 8 displays that LDR values higher than -20 dB occurred less than 25% of the cases at temperatures between -4 and 0°C, with frequency dramatically decreasing at colder temperatures. They do not seem to produce large aggregates, as DWR remains low. The increase in K_{DP} between -6 and 0°C is compatible with the hypothesis of formation of needle particles in a portion of the cases, as it signals an increase in number concentration of asymmetric particles. Interestingly we can draw a parallel between the increase in Z_{DR} at dendritic growth temperatures, which is preceded by an increase in K_{DP}, and the increase in LDR at column growth temperatures, also preceded by an increase in K_{DP}. This might be due to the time needed for small K_{DP}-producing ice particles to grow either into larger Z_{DR}-producing plates or larger LDR-producing columns. At the same time, this second K_{DP} enhancement region could be an indication of secondary ice production, as it has been reported in Arctic LLMPCs at these temperatures (e.g., Luke et al., 2021; Pasquier et al., 2022). This second K_{DP} enhancement zone has in fact been observed in mid-latitude systems only in a limited fraction of cases by von Terzi et al. (2022), and to a far lesser extent, which supports the hypothesis that the observed enhancement might be attributable to mixed-phase-related secondary ice production, such as droplet shattering or rime splintering. The high fall velocities associated with the higher quartile in MDV could be indicative of riming (e.g., Kneifel and Moisseev, 2020), which is also compatible with low Z_{DR}, as well as high ρ_{HV}, especially observed between -8 and -5°C.

6 Conclusions

We present a comprehensive long-term dataset of remote sensing observations of low-level mixed-phase clouds (LLMPCs), taken at the high Arctic site of Ny-Ålesund, Svalbard, Norway. The dataset in particular features dual-wavelength and polarimetric Doppler cloud radars observations, which are especially suited for ice microphysical studies. Cloud radar observations are complemented by thermodynamic retrievals from a microwave radiometer (temperature, liquid water path, and integrated water vapor), liquid base height from a ceilometer, and wind fields from large-eddy simulations. LLMPCs were detected using criteria based on the persistence of ice and liquid phases, and only periods when LLMPCs were detected were included in the dataset. All variables have undergone extensive quality control, especially the cloud radar observations, that were calibrated, as well as corrected for attenuation, ground clutter, and range folding. Unreliable data from microwave radiometer retrievals

https://doi.org/10.5194/essd-2023-157
Preprint. Discussion started: 6 June 2023
© Author(s) 2023. CC BY 4.0 License.


was also removed using precipitation information and a spectral consistency approach. All variables are brought to the same time and range grids, for easier matching of data originating from different instruments.

The large number of radar variables, coupled with thermodynamic, liquid base height and wind field data, included in the dataset allows for a comprehensive characterization of microphysical, as well as macrophysical, properties of LLMPCs. Microphysical studies will especially benefit from the combination of this dataset with data from the Video In-Situ Snowfall Sensor (VISSS; Maahn et al., 2023), which was operated at Ny-Ålesund during the same period. Additionally, the large number of events included in the dataset (more than 600) enables to compile robust statistics, especially for studies of ice microphysical processes. We demonstrate this by performing a brief statistical analysis of the temperature dependence of Doppler, dual-wavelength and polarimetric radar variables. Expanding upon results from previous studies, we show that LLMPCs at temperatures between -18 and -10°C display dual-wavelength and polarimetric signatures compatible with the rapid increase in number concentration, growth and subsequent aggregation of plate-like particles. We further show fingerprints suggesting the formation of precipitating prolate particles at temperatures warmer than -5°C. The analysis highlighted that LLMPCs are especially suited for process studies, as the ice habits involved can be easily inferred based on temperature, due to the limited depth of such clouds. This makes the dataset an ideal testing environment for lagrangian particle models and microphysical schemes.

7 Data availability

The full dataset has been published in Chellini et al. (2023), and is available at: www.doi.org/10.5281/zenodo.7803064.

Author contributions. GC processed the Ka-band radar data, including the developing of the range folding and ground clutter corrections, performed the calibration and attenuation correction of all radar systems, matched the data from all instruments and compiled the final files, all with the supervision of SK. RG processed the W-band data, and KE processed the HATPRO data and applied the Cloudnet target classification. TK ran the ICON-LEM simulations, with the supervision of VS. GC, RG and PK operated the cloud radars, with support from AM. PK handled the data transfer and storage. AM provided guidance on radar operation and data processing. SK and GC designed the dataset, and GC wrote the manuscript and performed the analysis, with feedback from all authors.

Competing interests. The authors declare that they have no competing interests.

Acknowledgements. GC, RG, KE, TK, PK and VS gratefully acknowledge the funding by the Deutsche Forschungsgemeinschaft (DFG, German Research Foundation)—Project no. 268020496—TRR 172, within the Transregional Collaborative Research Center "ArctiC Amplification: Climate Relevant Atmospheric and SurfaCe Processes, and Feedback Mechanisms (AC)^3." Contributions by SK were partly funded

https://doi.org/10.5194/essd-2023-157
Preprint. Discussion started: 6 June 2023
© Author(s) 2023. CC BY 4.0 License.

by the DFG under grant KN 1112/2-1 and KN 1112/2-2 as part of the Emmy-Noether Group “Optimal combination of Polarimetric and Triple Frequency radar techniques for Improving Microphysical process understanding of cold clouds” (OPTIMice).

The authors would like to express their gratitude to the Alfred Wegener Institute (AWI), and in particular Marion Maturilli and Christoph Ritter, for sharing their HATPRO and ceilometer data. The authors further wish to thank the AWIPEV staff for assisting with the operation of the instruments. The authors wish to thank Bernhard Pospichal, for sharing and applying his spectral consistency method to evaluate the reliability of microwave radiometer retrievals, and Davide Ori, for producing the scattering tables used in the disdrometer-based calibration, and providing assistance when setting up the PAMTRA forward simulations. The authors would like to further acknowledge the discussions with Leonie von Terzi, which helped improve the processing of polarimetric radar data. GC and TK also acknowledge the support from the Graduate School of Geosciences (GSGS) of the University of Cologne, as well as the Integrated Research Training Group (IRTG) of the $(AC)^3$ consortium.

https://doi.org/10.5194/essd-2023-157
Preprint. Discussion started: 6 June 2023
© Author(s) 2023. CC BY 4.0 License.

References

Abel, S. J., Boutle, I. A., Waite, K., Fox, S., Brown, P. R., Cotton, R., Lloyd, G., Choularton, T. W., and Bower, K. N.: The role of precipitation in controlling the transition from stratocumulus to cumulus clouds in a Northern Hemisphere cold-air outbreak, Journal of the Atmospheric Sciences, 74, 2293–2314, https://doi.org/10.1175/JAS-D-16-0362.1, 2017.

Avramov, A. and Harrington, J. Y.: Influence of parameterized ice habit on simulated mixed phase Arctic clouds, Journal of Geophysical Research: Atmospheres, 115, https://doi.org/10.1029/2009JD012108, 2010.

Bailey, M. P. and Hallett, J.: A comprehensive habit diagram for atmospheric ice crystals: Confirmation from the laboratory, AIRS II, and other field studies, Journal of the Atmospheric Sciences, 66, 2888–2899, https://doi.org/10.1175/2009JAS2883.1, 2009.

Barrett, A. I., Westbrook, C. D., Nicol, J. C., and Stein, T. H. M.: Rapid Ice Aggregation Process Revealed through Triple-Wavelength Doppler Spectrum Radar Analysis, Atmospheric Chemistry and Physics, 19, 5753–5769, https://doi.org/10.5194/acp-19-5753-2019, 2019.

Bechini, R., Baldini, L., and Chandrasekar, V.: Polarimetric radar observations in the ice region of precipitating clouds at C-band and X-band radar frequencies, Journal of applied meteorology and climatology, 52, 1147–1169, https://doi.org/doi.org/10.1175/JAMC-D-12-055.1, 2013.

Beine, H., Argentini, S., Maurizi, A., Mastrantonio, G., and Viola, A.: The local wind field at Ny-Ålesund and the Zeppelin mountain at Svalbard, Meteorology and Atmospheric Physics, 78, 107–113, https://doi.org/10.1007/s007030170009, 2001.

Bohren, C. F. and Huffman, D. R.: Absorption and scattering of light by small particles, John Wiley & Sons, 2008.

Born, M. and Wolf, E.: Principles of optics: Electromagnetic theory of propagation, interference and diffraction of light, Pergamon Press, 1975.

Bringi, V. N. and Chandrasekar, V.: Polarimetric Doppler weather radar: principles and applications, Cambridge university press, 2001.

Bühl, J., Seifert, P., Myagkov, A., and Ansmann, A.: Measuring ice-and liquid-water properties in mixed-phase cloud layers at the Leipzig Cloudnet station, Atmospheric Chemistry and Physics, 16, 10 609–10 620, https://doi.org/10.5194/acp-16-10609-2016, 2016.

Chandrasekar, V. and Keeler, R. J.: Antenna pattern analysis and measurements for multiparameter radars, Journal of Atmospheric and Oceanic Technology, 10, 674–683, https://doi.org/10.1175/1520-0426(1993)010<0674:APAAMF>2.0.CO;2, 1993.

Chellini, G., Gierens, R., and Kneifel, S.: Ice Aggregation in Low-Level Mixed-Phase Clouds at a High Arctic Site: Enhanced by Dendritic Growth and Absent Close to the Melting Level, Journal of Geophysical Research: Atmospheres, 127, e2022JD036 860, https://doi.org/10.1029/2022JD036860, 2022.

Chellini, G., Gierens, R., Ebell, K., Kiszler, T., and Kneifel, S.: Low-level mixed-phase clouds at the high Arctic site of Ny-Ålesund: A comprehensive long-term dataset of remote sensing observations, https://doi.org/10.5281/zenodo.7803064, 2023.

Connolly, P., Emersic, C., and Field, P.: A laboratory investigation into the aggregation efficiency of small ice crystals, Atmospheric Chemistry and Physics, 12, 2055–2076, https://doi.org/10.5194/acp-12-2055-2012, 2012.

Crewell, S. and Löhnert, U.: Accuracy of boundary layer temperature profiles retrieved with multifrequency multiangle microwave radiometry, IEEE Transactions on Geoscience and Remote Sensing, 45, 2195–2201, https://doi.org/10.1109/TGRS.2006.888434, 2007.

Dahlke, S. and Maturilli, M.: Contribution of Atmospheric Advection to the Amplified Winter Warming in the Arctic North Atlantic Region, Advances in Meteorology, https://doi.org/10.1155/2017/4928620, 2017.

de Boer, G., Eloranta, E. W., and Shupe, M. D.: Arctic mixed-phase stratiform cloud properties from multiple years of surface-based measurements at two high-latitude locations, Journal of Atmospheric Sciences, 66, 2874–2887, https://doi.org/10.1175/2009JAS3029.1, 2009.

https://doi.org/10.5194/essd-2023-157
Preprint. Discussion started: 6 June 2023
© Author(s) 2023. CC BY 4.0 License.

De Boer, G., Morrison, H., Shupe, M., and Hildner, R.: Evidence of liquid dependent ice nucleation in high-latitude stratiform clouds from surface remote sensors, Geophysical Research Letters, 38, https://doi.org/10.1029/2010GL046016, 2011.

Dias Neto, J., Kneifel, S., Ori, D., Trömel, S., Handwerker, J., Bohn, B., Hermes, N., Mühlbauer, K., Lenefer, M., and Simmer, C.: The TRIple-Frequency and Polarimetric Radar Experiment for Improving Process Observations of Winter Precipitation, Earth System Science Data, 11, 845–863, https://doi.org/10.5194/essd-11-845-2019, 2019.

Dipankar, A., Stevens, B., Heinze, R., Moseley, C., Zängl, G., Giorgetta, M., and Brdar, S.: Large eddy simulation using the general circulation model ICON, Journal of Advances in Modeling Earth Systems, 7, 963–986, https://doi.org/10.1002/2015MS000431, 2015.

Ebell, K., Nomokonova, T., Maturilli, M., and Ritter, C.: Radiative Effect of Clouds at Ny-Ålesund, Svalbard, as Inferred from Ground-Based Remote Sensing Observations, Journal of Applied Meteorology and Climatology, 59, 3–22, https://doi.org/10.1175/JAMC-D-19-0080.1, 2020.

Eirund, G. K., Lohmann, U., and Possner, A.: Cloud ice processes enhance spatial scales of organization in Arctic stratocumulus, Geophysical Research Letters, 46, 14 109–14 117, https://doi.org/10.1029/2019GL084959, 2019.

Esau, I. and Repina, I.: Wind climate in Kongsfjorden, Svalbard, and attribution of leading wind driving mechanisms through turbulence-resolving simulations, Advances in Meteorology, 2012, https://doi.org/10.1155/2012/568454, 2012.

Fukuta, N. and Takahashi, T.: The growth of atmospheric ice crystals: A summary of findings in vertical supercooled cloud tunnel studies, Journal of the atmospheric sciences, 56, 1963–1979, https://doi.org/10.1175/1520-0469(1999)056<1963:TGOAIC>2.0.CO;2, 1999.

Galletti, M. and Zrnic, D. S.: Degree of polarization at simultaneous transmit: theoretical aspects, IEEE Geoscience and Remote Sensing Letters, 9, 383–387, https://doi.org/10.1109/LGRS.2011.2170150, 2011.

Galletti, M., Zrnic, D. S., Melnikov, V. M., and Doviak, R. J.: Degree of polarization: Theory and applications for weather radar at LDR mode, in: 2011 IEEE RadarCon (RADAR), pp. 039–044, IEEE, https://doi.org/10.1109/RADAR.2011.5960495, 2011.

Gierens, R.: Observations of Arctic low-level mixed-phase clouds at Ny-Ålesund: Characterization and insights gained by high-resolution Doppler radar, Ph.D. thesis, Universität zu Köln, Köln, https://kups.ub.uni-koeln.de/53900/, 2021.

Gierens, R., Kneifel, S., Shupe, M. D., Ebell, K., Maturilli, M., and Löhnert, U.: Low-Level Mixed-Phase Clouds in a Complex Arctic Environment, Atmospheric Chemistry and Physics, 20, 3459–3481, https://doi.org/10.5194/acp-20-3459-2020, 2020.

Görsdorf, U., Lehmann, V., Bauer-Pfundstein, M., Peters, G., Vavriv, D., Vinogradov, V., and Volkov, V.: A 35-GHz polarimetric Doppler radar for long-term observations of cloud parameters—Description of system and data processing, Journal of Atmospheric and Oceanic Technology, 32, 675–690, https://doi.org/10.1175/JTECH-D-14-00066.1, 2015.

Graßl, S., Ritter, C., and Schulz, A.: The Nature of the Ny-Ålesund Wind Field Analysed by High-Resolution Windlidar Data, Remote Sensing, 14, 3771, https://doi.org/10.3390/rs14153771, 2022.

Griesche, H. J., Seifert, P., Ansmann, A., Baars, H., Barrientos Velasco, C., Bühl, J., Engelmann, R., Radenz, M., Zhenping, Y., and Macke, A.: Application of the shipborne remote sensing supersite OCEANET for profiling of Arctic aerosols and clouds during Polarstern cruise PS106, Atmospheric Measurement Techniques, 13, 5335–5358, https://doi.org/10.5194/amt-13-5335-2020, 2020.

Griffin, E. M., Schuur, T. J., and Ryzhkov, A. V.: A polarimetric analysis of ice microphysical processes in snow, using quasi-vertical profiles, Journal of Applied Meteorology and Climatology, 57, 31–50, https://doi.org/10.1175/JAMC-D-17-0033.1, 2018.

Harrington, J. Y. and Olsson, P. Q.: On the potential influence of ice nuclei on surface-forced marine stratocumulus cloud dynamics, Journal of Geophysical Research: Atmospheres, 106, 27 473–27 484, https://doi.org/10.1029/2000JD000236, 2001.

Heymsfield, A. J. and Westbrook, C.: Advances in the estimation of ice particle fall speeds using laboratory and field measurements, Journal of the Atmospheric Sciences, 67, 2469–2482, https://doi.org/10.1175/2010JAS3379.1, 2010.

https://doi.org/10.5194/essd-2023-157
Preprint. Discussion started: 6 June 2023
© Author(s) 2023. CC BY 4.0 License.

Hildebrand, P. H. and Sekhon, R.: Objective Determination of the Noise Level in Doppler Spectra, Journal of Applied Meteorology and Climatology, 13, 808–811, https://doi.org/10.1175/1520-0450(1974)013<0808:ODOTNL>2.0.CO;2, 1974.

Hogan, R. J. and O'Connor, E. J.: Facilitating cloud radar and lidar algorithms: the Cloudnet Instrument Synergy/Target Categorization product, Cloudnet documentation, 14, 2004.

Hogan, R. J., Illingworth, A. J., and Sauvageot, H.: Measuring crystal size in cirrus using 35-and 94-GHz radars, Journal of Atmospheric and Oceanic Technology, 17, 27–37, https://doi.org/10.1175/1520-0426(2000)017<0027:MCSICU>2.0.CO;2, 2000.

Huang, G.-J., Bringi, V. N., and Thurai, M.: Orientation Angle Distributions of Drops after an 80-m Fall Using a 2D Video Disdrometer, Journal of Atmospheric and Oceanic Technology, 25, 1717–1723, https://doi.org/10.1175/2008JTECHA1075.1, 2008.

Illingworth, A., Hogan, R., O'connor, E., Bouniol, D., Brooks, M., Delanoë, J., Donovan, D., Eastment, J., Gaussiat, N., Goddard, J., et al.: Cloudnet: Continuous evaluation of cloud profiles in seven operational models using ground-based observations, Bulletin of the American Meteorological Society, 88, 883–898, 2007.

Kalesse, H., de Boer, G., Solomon, A., Oue, M., Ahlgrimm, M., Zhang, D., Shupe, M. D., Luke, E., and Protat, A.: Understanding Rapid Changes in Phase Partitioning between Cloud Liquid and Ice in Stratiform Mixed-Phase Clouds: An Arctic Case Study, Monthly Weather Review, 144, 4805–4826, https://doi.org/10.1175/MWR-D-16-0155.1, 2016.

Karrer, M., Seifert, A., Siewert, C., Ori, D., von Lerber, A., and Kneifel, S.: Ice Particle Properties Inferred From Aggregation Modelling, Journal of Advances in Modeling Earth Systems, 12, e2020MS002 066, https://doi.org/10.1029/2020MS002066, 2020.

Kiszler, T., Ebell, K., and Schemann, V.: A performance baseline for the representation of clouds and humidity in cloud-resolving ICON-LEM simulations in the Arctic, accepted in Journal of Advances in Modeling Earth Systems, https://doi.org/10.1029/2022MS003299, 2023.

Kneifel, S. and Moisseev, D.: Long-Term Statistics of Riming in Nonconvective Clouds Derived from Ground-Based Doppler Cloud Radar Observations, Journal of the Atmospheric Sciences, 77, 3495–3508, https://doi.org/10.1175/JAS-D-20-0007.1, 2020.

Kneifel, S., Lerber, A., Tiira, J., Moisseev, D., Kollias, P., and Leinonen, J.: Observed Relations between Snowfall Microphysics and Triple-frequency Radar Measurements, Journal of Geophysical Research: Atmospheres, 120, 6034–6055, https://doi.org/10.1002/2015JD023156, 2015.

Koike, M., Ukita, J., Ström, J., Tunved, P., Shiobara, M., Vitale, V., Lupi, A., Baumgardner, D., Ritter, C., Hermansen, O., et al.: Year-round in situ measurements of Arctic low-level clouds: Microphysical properties and their relationships with aerosols, Journal of Geophysical Research: Atmospheres, 124, 1798–1822, https://doi.org/10.1029/2018JD029802, 2019.

Kollias, P., Clothiaux, E., Miller, M., Albrecht, B., Stephens, G., and Ackerman, T.: Millimeter-wavelength radars: New frontier in atmospheric cloud and precipitation research, Bulletin of the American Meteorological Society, 88, 1608–1624, https://doi.org/10.1175/BAMS-88-10-1608, 2007.

Küchler, N., Kneifel, S., Löhnert, U., Kollias, P., Czekala, H., and Rose, T.: A W-Band Radar–Radiometer System for Accurate and Continuous Monitoring of Clouds and Precipitation, Journal of Atmospheric and Oceanic Technology, 34, 2375–2392, https://doi.org/10.1175/JTECH-D-17-0019.1, 2017.

Leinonen, J.: High-Level Interface to T-Matrix Scattering Calculations: Architecture, Capabilities and Limitations, Optics Express, 22, 1655–1660, https://doi.org/10.1364/OE.22.001655, 2014.

Li, H., Möhler, O., Petäjä, T., and Moisseev, D.: Two-year statistics of columnar-ice production in stratiform clouds over Hyytiälä, Finland: environmental conditions and the relevance to secondary ice production, Atmospheric Chemistry and Physics, 21, 14 671–14 686, https://doi.org/10.5194/acp-21-14671-2021, 2021.

https://doi.org/10.5194/essd-2023-157
Preprint. Discussion started: 6 June 2023
© Author(s) 2023. CC BY 4.0 License.

Locatelli, J. D. and Hobbs, P. V.: Fall speeds and masses of solid precipitation particles, Journal of Geophysical Research, 79, 2185–2197, https://doi.org/10.1029/JC079i015p02185, 1974.

Löffler-Mang, M. and Joss, J.: An Optical Disdrometer for Measuring Size and Velocity of Hydrometeors, Journal of Atmospheric and Oceanic Technology, 17, 130–139, https://doi.org/10.1175/1520-0426(2000)017<0130:AODFMS>2.0.CO;2, 2000.

Luke, E. P., Yang, F., Kollias, P., Vogelmann, A. M., and Maahn, M.: New insights into ice multiplication using remote-sensing observations of slightly supercooled mixed-phase clouds in the Arctic, Proceedings of the National Academy of Sciences, 118, https://doi.org/10.1073/pnas.2021387118, 2021.

Maahn, M., Moisseev, D., Steinke, I., Maherndl, N., and Shupe, M. D.: Introducing the Video In Situ Snowfall Sensor (VISSS), submitted to Atmospheric Measurement Techniques, 2023.

Mages, Z., Kollias, P., Zhu, Z., and Luke, E. P.: Surface-based observations of cold-air outbreak clouds during the COMBLE field campaign, Atmospheric Chemistry and Physics, 23, 3561–3574, https://doi.org/10.5194/acp-23-3561-2023, 2023.

Maturilli, M. and Ebell, K.: Twenty-Five Years of Cloud Base Height Measurements by Ceilometer in Ny-Ålesund, Svalbard, Earth System Science Data, 10, 1451–1456, https://doi.org/10.5194/essd-10-1451-2018, 2018.

Maturilli, M. and Kayser, M.: Arctic warming, moisture increase and circulation changes observed in the Ny-Ålesund homogenized radiosonde record, Theoretical and Applied Climatology, 130, 1–17, https://doi.org/10.1007/s00704-016-1864-0, 2017.

Maturilli, M., Herber, A., and König-Langlo, G.: Climatology and time series of surface meteorology in Ny-Ålesund, Svalbard, Earth System Science Data, 5, 155–163, https://doi.org/10.5194/essd-5-155-2013, 2013.

Matus, A. V. and L'Ecuyer, T. S.: The role of cloud phase in Earth's radiation budget, Journal of Geophysical Research: Atmospheres, 122, 2559–2578, https://doi.org/10.1002/2016JD025951, 2017.

Mech, M., Kliesch, L.-L., Anhäuser, A., Rose, T., Kollias, P., and Crewell, S.: Microwave Radar/Radiometer for Arctic Clouds (MiRAC): First Insights from the ACLOUD Campaign, Atmospheric Measurement Techniques, 12, 5019–5037, https://doi.org/10.5194/amt-12-5019-2019, 2019.

Mech, M., Maahn, M., Kneifel, S., Ori, D., Orlandi, E., Kollias, P., Schemann, V., and Crewell, S.: PAMTRA 1.0: the Passive and Active Microwave radiative TRAnsfer tool for simulating radiometer and radar measurements of the cloudy atmosphere, Geoscientific Model Development, 13, 4229–4251, https://doi.org/10.5194/gmd-13-4229-2020, 2020.

Mioche, G., Jourdan, O., Ceccaldi, M., and Delanoë, J.: Variability of mixed-phase clouds in the Arctic with a focus on the Svalbard region: a study based on spaceborne active remote sensing, Atmospheric Chemistry and Physics, 15, 2445–2461, https://doi.org/10.5194/acp-15-2445-2015, 2015.

Mioche, G., Jourdan, O., Delanoë, J., Gourbeyre, C., Febvre, G., Dupuy, R., Monier, M., Szczap, F., Schwarzenboeck, A., and Gayet, J.-F.: Vertical distribution of microphysical properties of Arctic springtime low-level mixed-phase clouds over the Greenland and Norwegian seas, Atmospheric Chemistry and Physics, 17, 12 845–12 869, https://doi.org/10.5194/acp-17-12845-2017, 2017.

Moisseev, D. N., Lautaportti, S., Tyynela, J., and Lim, S.: Dual-polarization radar signatures in snowstorms: Role of snowflake aggregation, Journal of Geophysical Research: Atmospheres, 120, 12 644–12 655, https://doi.org/10.1002/2015JD023884, 2015.

Morrison, H., de Boer, G., Feingold, G., Harrington, J., Shupe, M. D., and Sulia, K.: Resilience of Persistent Arctic Mixed-Phase Clouds, Nature Geoscience, 5, 11–17, https://doi.org/10.1038/ngeo1332, 2012.

Myagkov, A. and Ori, D.: Analytic characterization of random errors in spectral dual-polarized cloud radar observations, Atmospheric Measurement Techniques, 15, 1333–1354, https://doi.org/10.5194/amt-15-1333-2022, 2022.

https://doi.org/10.5194/essd-2023-157
Preprint. Discussion started: 6 June 2023
© Author(s) 2023. CC BY 4.0 License.

Myagkov, A., Seifert, P., Wandinger, U., Bauer-Pfundstein, M., and Matrosov, S. Y.: Effects of antenna patterns on cloud radar polarimetric measurements, Journal of Atmospheric and Oceanic Technology, 32, 1813–1828, https://doi.org/10.1175/JTECH-D-15-0045.1, 2015.

Myagkov, A., Seifert, P., Wandinger, U., Bühl, J., and Engelmann, R.: Relationship between temperature and apparent shape of pristine ice crystals derived from polarimetric cloud radar observations during the ACCEPT campaign, Atmospheric Measurement Techniques, 9, 3739–3754, https://doi.org/10.5194/amt-9-3739-2016, 2016.

Myagkov, A., Kneifel, S., and Rose, T.: Evaluation of the Reflectivity Calibration of W-Band Radars Based on Observations in Rain, Atmospheric Measurement Techniques, 13, 5799–5825, https://doi.org/10.5194/amt-13-5799-2020, 2020.

Nemarich, J., Wellman, R. J., and Lacombe, J.: Backscatter and attenuation by falling snow and rain at 96, 140, and 225 GHz, IEEE Transactions on Geoscience and Remote Sensing, 26, 319–329, https://doi.org/10.1109/36.3034, 1988.

Nghiem, S. V., Yueh, S. H., Kwok, R., and Li, F. K.: Symmetry properties in polarimetric remote sensing, Radio Science, 27, 693–711, https://doi.org/10.1029/92RS01230, 1992.

Nomokonova, T., Ebell, K., Löhnert, U., Maturilli, M., Ritter, C., and O'Connor, E.: Statistics on Clouds and Their Relation to Thermodynamic Conditions at Ny-Ålesund Using Ground-Based Sensor Synergy, Atmospheric Chemistry and Physics, 19, 4105–4126, https://doi.org/10.5194/acp-19-4105-2019, 2019.

Nomokonova, T., Ebell, K., Löhnert, U., Maturilli, M., and Ritter, C.: The Influence of Water Vapor Anomalies on Clouds and Their Radiative Effect at Ny-Ålesund, Atmospheric Chemistry and Physics, 20, 5157–5173, https://doi.org/10.5194/acp-20-5157-2020, 2020.

Ori, D., Schemann, V., Karrer, M., Dias Neto, J., von Terzi, L., Seifert, A., and Kneifel, S.: Evaluation of ice particle growth in ICON using statistics of multi-frequency Doppler cloud radar observations, Quarterly Journal of the Royal Meteorological Society, 146, 3830–3849, https://doi.org/10.1002/qj.3875, 2020.

Oue, M., Kumjian, M. R., Lu, Y., Verlinde, J., Aydin, K., and Clothiaux, E. E.: Linear Depolarization Ratios of Columnar Ice Crystals in a Deep Precipitating System over the Arctic Observed by Zenith-Pointing Ka-Band Doppler Radar, Journal of Applied Meteorology and Climatology, 54, 1060–1068, https://doi.org/10.1175/JAMC-D-15-0012.1, 2015.

Pasquier, J. T., Henneberger, J., Ramelli, F., Lauber, A., David, R. O., Wieder, J., Carlsen, T., Gierens, R., Maturilli, M., and Lohmann, U.: Conditions favorable for secondary ice production in Arctic mixed-phase clouds, Atmospheric Chemistry and Physics, 22, 15 579–15 601, https://doi.org/10.5194/acp-22-15579-2022, 2022.

Pruppacher, H. R. and Klett, J. D.: Microphysics of Clouds and Precipitation: Reprinted 1980, Springer, Dordrecht, https://doi.org/10.1007/978-94-009-9905-3, 2012.

Rangno, A. L. and Hobbs, P. V.: Ice Particles in Stratiform Clouds in the Arctic and Possible Mechanisms for the Production of High Ice Concentrations, Journal of Geophysical Research: Atmospheres, 106, 15 065–15 075, https://doi.org/10.1029/2000JD900286, 2001.

Rose, T., Crewell, S., Löhnert, U., and Simmer, C.: A Network Suitable Microwave Radiometer for Operational Monitoring of the Cloudy Atmosphere, Atmospheric Research, 75, 183–200, https://doi.org/10.1016/j.atmosres.2004.12.005, 2005.

Rosenkranz, P. W.: A model for the complex dielectric constant of supercooled liquid water at microwave frequencies, IEEE Transactions on Geoscience and Remote Sensing, 53, 1387–1393, https://doi.org/10.1109/TGRS.2014.2339015, 2014.

Schemann, V. and Ebell, K.: Simulation of mixed-phase clouds with the ICON large-eddy model in the complex Arctic environment around Ny-Ålesund, Atmospheric Chemistry and Physics, 20, 475–485, https://doi.org/10.5194/acp-20-475-2020, 2020.

Schemann, V., Ebell, K., Pospichal, B., Neggers, R., Moseley, C., and Stevens, B.: Linking large-eddy simulations to local cloud observations, Journal of Advances in Modeling Earth Systems, 12, e2020MS002 209, https://doi.org/10.1029/2020MS002209, 2020.

https://doi.org/10.5194/essd-2023-157
Preprint. Discussion started: 6 June 2023
© Author(s) 2023. CC BY 4.0 License.

Schoger, S. Y., Moisseev, D., von Lerber, A., Crewell, S., and Ebell, K.: Snowfall-Rate Retrieval for K- and W-Band Radar Measurements Designed in Hyytiälä, Finland, and Tested at Ny-Ålesund, Svalbard, Norway, Journal of Applied Meteorology and Climatology, 60, 273–289, https://doi.org/10.1175/JAMC-D-20-0095.1, 2021.

Schrom, R. S. and Kumjian, M. R.: Connecting microphysical processes in Colorado winter storms with vertical profiles of radar observations, Journal of Applied Meteorology and Climatology, 55, 1771–1787, https://doi.org/10.1175/JAMC-D-15-0338.1, 2016.

Schrom, R. S., Kumjian, M. R., and Lu, Y.: Polarimetric radar signatures of dendritic growth zones within Colorado winter storms, Journal of Applied Meteorology and Climatology, 54, 2365–2388, https://doi.org/doi.org/10.1175/JAMC-D-15-0004.1, 2015.

Schwarzenboeck, A., Shcherbakov, V., Lefevre, R., Gayet, J. F., Pointin, Y., and Duroure, C.: Indications for Stellar-Crystal Fragmentation in Arctic Clouds, Atmospheric Research, 92, 220–228, https://doi.org/10.1016/j.atmosres.2008.10.002, 2009.

Schween, J. H., del Rio, C., García, J.-L., Osses, P., Westbrook, S., and Löhnert, U.: Life cycle of stratocumulus clouds over 1 year at the coast of the Atacama Desert, Atmospheric Chemistry and Physics, 22, 12 241–12 267, https://doi.org/10.5194/acp-22-12241-2022, 2022.

Serreze, M. C. and Barry, R. G.: Processes and impacts of Arctic amplification: A research synthesis, Global and planetary change, 77, 85–96, https://doi.org/10.1016/j.gloplacha.2011.03.004, 2011.

Shupe, M. D.: Clouds at Arctic atmospheric observatories. Part II: Thermodynamic phase characteristics, Journal of Applied Meteorology and Climatology, 50, 645–661, https://doi.org/10.1175/2010JAMC2468.1, 2011.

Shupe, M. D. and Intrieri, J. M.: Cloud radiative forcing of the Arctic surface: The influence of cloud properties, surface albedo, and solar zenith angle, Journal of Climate, 17, 616–628, https://doi.org/10.1175/1520-0442(2004)017<0616:CRFOTA>2.0.CO;2, 2004.

Shupe, M. D., Matrosov, S. Y., and Uttal, T.: Arctic Mixed-Phase Cloud Properties Derived from Surface-Based Sensors at SHEBA, Journal of the Atmospheric Sciences, 63, 697–711, https://doi.org/10.1175/JAS3659.1, 2006.

Shupe, M. D., Kollias, P., Persson, P. O. G., and McFarquhar, G. M.: Vertical motions in Arctic mixed-phase stratiform clouds, Journal of Atmospheric Sciences, 65, 1304–1322, https://doi.org/10.1175/2007JAS2479.1, 2008.

Shupe, M. D., Rex, M., Blomquist, B., Persson, P. O. G., Schmale, J., Uttal, T., Althausen, D., Angot, H., Archer, S., Bariteau, L., et al.: Overview of the MOSAiC expedition: Atmosphere, Elementa: Science of the Anthropocene, 10, 00 060, https://doi.org/10.1525/elementa.2021.00060, 2022.

Simpfendoerfer, L. F., Verlinde, J., Harrington, J. Y., Shupe, M. D., Chen, Y.-S., Clothiaux, E. E., and Golaz, J.-C.: Formation of Arctic stratocumuli through atmospheric radiative cooling, Journal of Geophysical Research: Atmospheres, 124, 9644–9664, https://doi.org/10.1029/2018JD030189, 2019.

Solomon, A., Shupe, M. D., Persson, P. O. G., and Morrison, H.: Moisture and Dynamical Interactions Maintaining Decoupled Arctic Mixed-Phase Stratocumulus in the Presence of a Humidity Inversion, Atmospheric Chemistry and Physics, 11, 10 127–10 148, https://doi.org/10.5194/acp-11-10127-2011, 2011.

Solomon, A., Shupe, M. D., Persson, O., Morrison, H., Yamaguchi, T., Caldwell, P. M., and de Boer, G.: The sensitivity of springtime Arctic mixed-phase stratocumulus clouds to surface-layer and cloud-top inversion-layer moisture sources, Journal of Atmospheric Sciences, 71, 574–595, 2014.

Solomon, A., Feingold, G., and Shupe, M. D.: The role of ice nuclei recycling in the maintenance of cloud ice in Arctic mixed-phase stratocumulus, Atmospheric Chemistry and Physics, 15, 10 631–10 643, https://doi.org/10.5194/acp-15-10631-2015, 2015.

Sotiropoulou, G., Lewinschal, A., Georgakaki, P., Phillips, V., Patade, S., Ekman, A. M., and Nenes, A.: Sensitivity of Arctic clouds to ice microphysical processes in the NorESM2 climate model, Authorea Preprints, https://doi.org/1002/essoar.10512081.1, 2022.

https://doi.org/10.5194/essd-2023-157
Preprint. Discussion started: 6 June 2023
© Author(s) 2023. CC BY 4.0 License.

Takahashi, T.: Influence of liquid water content and temperature on the form and growth of branched planar snow crystals in a cloud, Journal of the Atmospheric Sciences, 71, 4127–4142, https://doi.org/10.1175/JAS-D-14-0043.1, 2014.

Tan, I. and Storelvmo, T.: Evidence of strong contributions from mixed-phase clouds to Arctic climate change, Geophysical Research Letters, 46, 2894–2902, https://doi.org/10.1029/2018GL081871, 2019.

Thurai, M., Huang, G. J., Bringi, V. N., Randeu, W. L., and Schönhuber, M.: Drop Shapes, Model Comparisons, and Calculations of Polarimetric Radar Parameters in Rain, Journal of Atmospheric and Oceanic Technology, 24, 1019–1032, https://doi.org/10.1175/JTECH2051.1, 2007.

Tridon, F., Battaglia, A., and Kneifel, S.: Estimating total attenuation using Rayleigh targets at cloud top: applications in multilayer and mixed-phase clouds observed by ground-based multifrequency radars, Atmospheric Measurement Techniques, 13, 5065–5085, https://doi.org/10.5194/amt-13-5065-2020, 2020.

Trömel, S., Kumjian, M. R., Ryzhkov, A. V., Simmer, C., and Diederich, M.: Backscatter differential phase—Estimation and variability, Journal of applied meteorology and climatology, 52, 2529–2548, https://doi.org/10.1175/JAMC-D-13-0124.1, 2013.

Vassel, M., Ickes, L., Maturilli, M., and Hoose, C.: Classification of Arctic multilayer clouds using radiosonde and radar data in Svalbard, Atmospheric Chemistry and Physics, 19, 5111–5126, https://doi.org/10.5194/acp-19-5111-2019, 2019.

Verlinde, J., Zak, B., Shupe, M., Ivey, M., and Stamnes, K.: The ARM North Slope of Alaska (NSA) sites, Meteorological Monographs, 57, 8–1, https://doi.org/10.1175/AMSMONOGRAPHS-D-15-0023.1, 2016.

von Terzi, L., Dias Neto, J., Ori, D., Myagkov, A., and Kneifel, S.: Ice microphysical processes in the dendritic growth layer: A statistical analysis combining multi-frequency and polarimetric Doppler cloud radar observations, Atmospheric Chemistry and Physics, 22, 11 795–11 821, https://doi.org/10.5194/acp-22-11795-2022, 2022.

Wallace, J. M. and Hobbs, P. V.: Atmospheric Science (Second Edition), Academic Press, San Diego, second edn., 2006.

Waterman, P.: Matrix formulation of electromagnetic scattering, Proceedings of the IEEE, 53, 805–812, https://doi.org/10.1109/PROC.1965.4058, 1965.

Wendisch, M., Macke, A., Ehrlich, A., Lüpkes, C., Mech, M., Chechin, D., Dethloff, K., Velasco, C. B., Bozem, H., Brückner, M., Clemen, H.-C., Crewell, S., Donth, T., Dupuy, R., Ebell, K., Egerer, U., Engelmann, R., Engler, C., Eppers, O., Gehrmann, M., Gong, X., Gottschalk, M., Gourbeyre, C., Griesche, H., Hartmann, J., Hartmann, M., Heinold, B., Herber, A., Herrmann, H., Heygster, G., Hoor, P., Jafariserajehlou, S., Jäkel, E., Järvinen, E., Jourdan, O., Kästner, U., Kecorius, S., Knudsen, E. M., Köllner, F., Kretzschmar, J., Lelli, L., Leroy, D., Maturilli, M., Mei, L., Mertes, S., Mioche, G., Neuber, R., Nicolaus, M., Nomokonova, T., Notholt, J., Palm, M., van Pinxteren, M., Quaas, J., Richter, P., Ruiz-Donoso, E., Schäfer, M., Schmieder, K., Schnaiter, M., Schneider, J., Schwarzenböck, A., Seifert, P., Shupe, M. D., Siebert, H., Spreen, G., Stapf, J., Stratmann, F., Vogl, T., Welti, A., Wex, H., Wiedensohler, A., Zanatta, M., and Zeppenfeld, S.: The Arctic Cloud Puzzle: Using ACLOUD/PASCAL Multiplatform Observations to Unravel the Role of Clouds and Aerosol Particles in Arctic Amplification, Bulletin of the American Meteorological Society, 100, 841–871, https://doi.org/10.1175/BAMS-D-18-0072.1, 2019.

Wendisch, M., Brückner, M., Crewell, S., Ehrlich, A., Notholt, J., Lüpkes, C., Macke, A., Burrows, J. P., Rinke, A., Quaas, J., Maturilli, M., Schemann, V., Shupe, M. D., Akansu, E. F., Barrientos-Velasco, C., Bärfuss, K., Blechschmidt, A.-M., Block, K., Bougoudis, I., Bozem, H., Böckmann, C., Bracher, A., Bresson, H., Bretschneider, L., Buschmann, M., Chechin, D. G., Chylik, J., Dahlke, S., Deneke, H., Dethloff, K., Donth, T., Dorn, W., Dupuy, R., Ebell, K., Egerer, U., Engelmann, R., Eppers, O., Gerdes, R., Gierens, R., Gorodetskaya, I. V., Gottschalk, M., Griesche, H., Gryanik, V. M., Handorf, D., Harm-Altstädter, B., Hartmann, J., Hartmann, M., Heinold, B., Herber, A., Herrmann, H., Heygster, G., Höschel, I., Hofmann, Z., Hölemann, J., Hünerbein, A., Jafariserajehlou, S., Jäkel, E., Jacobi, C., Janout,

https://doi.org/10.5194/essd-2023-157
Preprint. Discussion started: 6 June 2023
© Author(s) 2023. CC BY 4.0 License.

M., Jansen, F., Jourdan, O., Jurányi, Z., Kalesse-Los, H., Kanzow, T., Käthner, R., Kliesch, L. L., Klingebiel, M., Knudsen, E. M., Kovács, T., Körtke, W., Krampe, D., Kretzschmar, J., Kreyling, D., Kulla, B., Kunkel, D., Lampert, A., Lauer, M., Lelli, L., von Lerber, A., Linke, O., Löhnert, U., Lonardi, M., Losa, S. N., Losch, M., Maahn, M., Mech, M., Mei, L., Mertes, S., Metzner, E., Mewes, D., Michaelis, J., Mioche, G., Moser, M., Nakoudi, K., Neggers, R., Neuber, R., Nomokonova, T., Oelker, J., Papakonstantinou-Presvelou, I., Pätzold, F., Pefanis, V., Pohl, C., van Pinxteren, M., Radovan, A., Rhein, M., Rex, M., Richter, A., Risse, N., Ritter, C., Rostosky, P., Rozanov, V. V., Donoso, E. R., Garfias, P. S., Salzmann, M., Schacht, J., Schäfer, M., Schneider, J., Schnierstein, N., Seifert, P., Seo, S., Siebert, H., Soppa, M. A., Spreen, G., Stachlewska, I. S., Stapf, J., Stratmann, F., Tegen, I., Viceto, C., Voigt, C., Vountas, M., Walbröl, A., Walter, M., Wehner, B., Wex, H., Willmes, S., Zanatta, M., and Zeppenfeld, S.: Atmospheric and Surface Processes, and Feedback Mechanisms Determining Arctic Amplification: A Review of First Results and Prospects of the (AC)3 Project, Bulletin of the American Meteorological Society, 104, E208 – E242, https://doi.org/10.1175/BAMS-D-21-0218.1, 2023.

Williams, C. R., Gage, K. S., Clark, W., and Kucera, P.: Monitoring the reflectivity calibration of a scanning radar using a profiling radar and a disdrometer, Journal of Atmospheric and Oceanic Technology, 22, 1004–1018, https://doi.org/https://doi.org/10.1175/JTECH1759.1, 2005.

Williams, C. R., Maahn, M., Hardin, J. C., and de Boer, G.: Clutter mitigation, multiple peaks, and high-order spectral moments in 35 GHz vertically pointing radar velocity spectra, Atmospheric Measurement Techniques, 11, 4963–4980, https://doi.org/10.5194/amt-11-4963-2018, 2018.

Yuter, S. E. and Houze Jr, R. A.: Three-dimensional kinematic and microphysical evolution of Florida cumulonimbus. Part II: Frequency distributions of vertical velocity, reflectivity, and differential reflectivity, Monthly weather review, 123, 1941–1963, https://doi.org/10.1175/1520-0493(1995)123<1941:TDKAME>2.0.CO;2, 1995.

Zängl, G., Reinert, D., Rípodas, P., and Baldauf, M.: The ICON (ICOsahedral Non-Hydrostatic) Modelling Framework of DWD and MPI-M: Description of the Non-Hydrostatic Dynamical Core, Quarterly Journal of the Royal Meteorological Society, 141, 563–579, https://doi.org/10.1002/qj.2378, 2015.

Zhao, C. and Garrett, T.: Ground-based remote sensing of precipitation in the Arctic, Journal of Geophysical Research: Atmospheres, 113, https://doi.org/10.1029/2007JD009222, 2008.

Chapter 5

Study 3: Assessing the role of turbulence in determining precipitation characteristics

This study is composed of a main manuscript, a supplement to the manuscript, and an additional analysis. The manuscript and supplement were submitted to a scientific journal on September 27th, 2023. Minor formatting changes were made to the manuscript and supplement for the inclusion in this dissertation. The additional analysis was not included in the submitted version. The manuscript starts at page 110, the supplement starts at page 126, while the additional analysis can be found in Section 5.1 at page 136. The details of the submitted manuscript are as follows:

Chellini, G., and S. Kneifel (2023). **Turbulence as a key driver of ice aggregation and riming in Arctic low-level mixed-phase clouds, revealed by long-term cloud radar observations**. Submitted to *Geophysical Research Letters*.

The final peer-reviewed article has been published under the Creative Commons Attribution 4.0 International Public License, and can be found at:

Chellini, G., and S. Kneifel (2024). **Turbulence as a key driver of ice aggregation and riming in Arctic low-level mixed-phase clouds, revealed by long-term cloud radar observations**. *Geophysical Research Letters*, `https://doi.org/10.1029/2023GL106599`.

Author contributions: GC planned and structured the article, with the supervision of SK. GC developed the EDR retrieval approach, combined and analyzed

data from all sources, and prepared the visualization of the results. Both authors contributed to the interpretation of the results. GC drafted the manuscript and reviewed it iteratively with SK. The additional analysis in Section 5.1 was developed independently by GC.

Turbulence as a key driver of ice aggregation and riming in Arctic low-level mixed-phase clouds, revealed by long-term cloud radar observations

Giovanni Chellini[1], and Stefan Kneifel[2]

[1]Institute for Geophysics and Meteorology, University of Cologne, Cologne, Germany
[2]Meteorological Institute, Ludwig-Maximilians-Universität in Munich, Munich, Germany

Key Points:

- Relation between turbulence and ice growth investigated based on long-term remote sensing dataset of Arctic low-level mixed-phase clouds
- Higher eddy dissipation rate (EDR) correlates with larger ice aggregates, and possibly higher degrees of fragmentation
- High EDR is an essential component needed for the formation of rimed particles

Corresponding author: Giovanni Chellini, g.chellini@uni-koeln.de

Abstract

Turbulence in clouds is known to enhance the probability of particles to collide. While this effect has been intensively studied for warm rain formation, a similar impact on ice growth processes is expected but a solid observational basis is still missing.

A statistical analysis of long-term cloud radar observations allows for the first time to quantify the impact of turbulence on ice aggregation and riming in Arctic low-level mixed-phase clouds.

Higher eddy dissipation rate regimes are directly associated with the presence of larger ice aggregates, together with signatures of increased ice particle concentration, likely caused by fragmentation. In temperature regimes more favorable to riming, turbulence dramatically enhances the particles' fall velocity, demonstrating markedly higher degrees of riming. Our findings thus reveal the key role of turbulence for the formation of precipitable ice, and highlight the need for an improved understanding of turbulence-hydrometeor interactions in cold clouds.

Plain Language Summary

Liquid and frozen precipitation mainly forms by collision and subsequent aggregation of small particles. Collisions between cloud particles, such as droplets and ice crystals, are thought to be increased by turbulence. While this effect has been intensively studied for liquid-only clouds, the impact of turbulence on ice-ice collisional growth (aggregation) and ice-liquid collisional growth (riming) is expected but has so far been poorly quantified. We study the effect of turbulence on aggregation and riming based on a long-term remote-sensing dataset of low-level clouds containing both ice and liquid particles, recorded at an Arctic site. Cloud radar observations are used to retrieve the dissipation rate of turbulent kinetic energy (i.e., the eddy dissipation rate; EDR), which is the relevant quantity driving increases in collision rates, and to characterize ice particle properties. We find evidence that higher EDR regimes enhance the aggregation of particles, and are associated with signatures of increased ice particle concentration, possibly caused by the production of particle fragments upon collision. In temperature regimes more favorable to riming, turbulence dramatically enhances the particles' fall velocity, denoting higher degrees of riming. Our findings thus highlight a key role of turbulence for the formation of precipitable ice.

1 Introduction

Precipitation formation is for the most part determined by hydrometeor collisional processes: in warm clouds, hydrometeors transition from cloud droplets into drizzle and raindrops via the collision-coalescence process, while in cold clouds precipitation mainly forms by aggregation, i.e., ice-ice collisions, and riming, i.e., collisions between ice particles and supercooled droplets (Pruppacher & Klett, 2012). The role of turbulence in the initiation of warm precipitation has been widely debated in the past century (e.g., Arenberg, 1939; East & Marshall, 1954), but a consensus has been reached in recent decades on the key role it plays (e.g., Shaw, 2003; Pumir & Wilkinson, 2016; Seifert & Onishi, 2016). Conversely, the role of turbulence in collisional ice-growth processes has received little attention. A limited number of authors have suggested, based on case studies, that turbulence might induce enhancements in ice collisional growth (e.g., Houze & Medina, 2005; Aikins et al., 2016), and that increases in ice-ice collision rates might further affect precipitation by substantially enhancing secondary ice processes, especially collisional fragmentation (Ramelli et al., 2021; Billault-Roux et al., 2023). Consequently, turbulence represents a poorly-understood pathway for the interaction between cloud dynamics and microphysics. Since most precipitation world-wide originates from the ice phase (Mülmenstädt et al., 2015; Heymsfield et

al., 2020), a deeper understanding and quantitative estimate of the impact of turbulence on ice microphysical process is likely to improve precipitation forecasts.

Theoretical fluid dynamics studies have shown dramatic increases in collision rates between particles suspended in a fluid with increasing turbulence (e.g., Pumir & Wilkinson, 2016). When particle inertia is negligible with respect to the fluid's inertia, particles act as tracers for the fluid motion, and turbulence-induced velocity gradients in the fluid increase collisions (Saffman & Turner, 1956). As particles grow, their inertia becomes comparable to that of the fluid and particles are subject to so-called inertial effects. Particles tend to cluster in regions of the flow with lower vorticity, and centrifugal forces generated by the eddies enhance relative velocities between particles, leading to large relative velocities even between particles of similar sizes (Squires & Eaton, 1991; Shaw et al., 1998; Voßkuhle et al., 2014). The relevance of these effects for increasing collisions between ice particles, as well as ice particles and supercooled droplets has been suggested by Naso et al. (2018) and Sheikh et al. (2022), among others.

To our knowledge, these theoretical considerations have been poorly supported by observations in atmospheric clouds. Based on case studies, a handful of authors have identified shear layers as regions of precipitation enhancement in orographic precipitation (Houze & Medina, 2005; Grazioli et al., 2015; Medina & Houze, 2015; Aikins et al., 2016; Ramelli et al., 2021; Gehring et al., 2022) and in warm conveyor belts (Gehring et al., 2020). Out of the mentioned studies, Houze and Medina (2005) first suggested that shear leads to the formation of overturning cells, and that subcellular motions might favour increasing differential settling velocities between hydrometeors, leading to enhanced aggregation and riming. Recently, Fitch and Garrett (2022b) reported that in Arctic low-level mixed-phase clouds graupel settling velocity and density increase with increasing turbulence.

Here, we present a new view on the subject of ice growth enhancement by turbulence, investigating the topic in low-level mixed-phase clouds (LLMPCs) at the Arctic site of Ny-Ålesund. Arctic LLMPCs are inherently turbulent, as the liquid layer typically located close to cloud top drives radiative cooling, which in turn produces buoyant overturning and turbulence throughout the cloud layer (e.g., Morrison et al., 2012). Ice is nucleated and grows in the liquid layer, first by vapor deposition, then via collisional processes, both by riming (Fitch & Garrett, 2022a; Maherndl et al., 2023), and by aggregation (Chellini et al., 2022). Due to the limited depth of LLMPCs, information on cloud-top temperature (CTT) allows us to constrain the ice habits that are nucleated (Myagkov et al., 2016; Bühl et al., 2016), which makes these clouds ideal natural laboratories to test the dependence of the turbulence-ice-growth interaction on ice habits. Furthermore, the wide spectrum of liquid water path (LWP) values typically observed, from a few tens up to 400 g m^{-2} (Gierens et al., 2020; Chellini et al., 2022) allows us to discriminate between scenarios with varying likelihood of riming. Our choice of investigating turbulence-microphysics interactions in Arctic LLMPCs is hence due to the wide spectrum of conditions that they provide. Therefore, we argue that the results here reported are likely to be applicable to other cloud types in other geographical areas as well.

2 Methods

We use the long-term dataset of ground-based remote-sensing observations presented in Chellini et al. (2023), which includes dual-wavelength and polarimetric Doppler cloud radar observations, as well as thermodynamic retrievals from a microwave radiometer. Millimeter-wavelength cloud radars have been widely used to study Arctic cloud properties and processes (e.g., Shupe et al., 2006; Zhao & Garrett, 2008; Kalesse et al., 2016; Griesche et al., 2021; Luke et al., 2021). Additionally, dual-wavelength and polarimetric observations respectively provide information on ice particle characteristic size and shape (e.g., Hogan et al., 2000; Bringi & Chandrasekar, 2001), and similar datasets have been used in past studies to investigate ice microphysical processes (e.g., Barrett et al., 2019; Dias Neto et al., 2019;

Trömel et al., 2021; Tetoni et al., 2022; von Terzi et al., 2022). Doppler observations further provide the unique opportunity to retrieve the eddy dissipation rate (EDR) (Rogers & Tripp, 1964; Bouniol et al., 2004; Borque et al., 2016), which is the key turbulence variable affecting hydrometeor collision rates (Vaillancourt & Yau, 2000; Pumir & Wilkinson, 2016).

The dataset was recorded at the AWIPEV observatory in Ny-Ålesund, located on the western coast of Spitsbergen at 79°N. It spans a 15-month period from 10 October 2021 until 31 December 2022, and only includes LLMPC events. The events were selected by requiring that ice and liquid phases, identified with the Cloudnet target classification (Illingworth et al., 2007), coexist for at least one hour, and cloud top remains below 2500 m. The two cornerstones of the dataset are a 94-GHz zenith-pointing single-polarization Doppler radar (hereafter referred to as W-band; Küchler et al. (2017)), and a 35-GHz scanning dual-polarization Doppler radar (hereafter Ka-band; Chellini et al. (2023)). The radar data have undergone quality control and post-processing, including attenuation corrections. Temperature profiles and LWP from a co-located microwave radiometer have been retrieved following the approaches by Crewell and Löhnert (2007) and Nomokonova et al. (2020). For further technical details on the dataset and the processing methods applied we refer the reader to Chellini et al. (2023).

We use equivalent radar reflectivity factor (hereafter reflectivity) Z_e and mean Doppler velocity (MDV) observed by the W-band in zenith, while polarimetric variables are taken from Ka-band observations at 30-40° elevation. Zenith reflectivities from the two systems are combined into the dual-wavelength ratio (DWR). The DWR is the ratio (in linear scale) between reflectivities observed at two separate frequencies, and is sensitive to the characteristic size of the ice particle population in the size range where hydrometeor backscattering is in the Rayleigh regime at the lower frequency, and non-Rayleigh at the higher frequency (Battaglia et al., 2020). For the used frequency combination (35-94 GHz), DWR is sensitive to mean particle sizes ranging from 0.5 to 5 mm approximately, and takes on increasing values up to approximately 10 dB, where it saturates and is no longer sensitive to further increases in size (e.g., Ori et al., 2020). As for polarimetric variables, we focus on differential reflectivity Z_{DR}, mostly sensitive to the aspect ratio, density, and size of asymmetrical particles (Schrom & Kumjian, 2016; Griffin et al., 2018), correlation coefficient ρ_{HV}, which decreases with increasing diversity in shape and orientation of particles (Andrić et al., 2013), and specific differential phase K_{DP}, related to the number concentration of small asymmetric ice particles (Bechini et al., 2013; Schrom et al., 2015). The EDR is retrieved via the variance of velocity time series, using a modified version of the approach by Borque et al. (2016). Further details are given in the Supplement.

3 Case study

Before we present and discuss the statistical analysis based on the long-term LLMPC dataset (section 4), we shortly illustrate the typical structure of LLMPCs occurring over Ny-Ålesund and introduce the most relevant observables in a case study (Fig. 1). We can identify three main periods based on turbulence characteristics: a first period from 3:00 until 5:00 UTC, when EDR is below 10^{-4} m^2 s^{-3} throughout the cloud layer, a second period between 5:00 and 11:00 UTC when EDR increases at cloud top, reaching values between 10^{-4} and 10^{-3} m^2 s^{-3}, and a third period after 11:00 UTC when EDR at cloud top is close to or higher than 10^{-3} m^2 s^{-3}, and high EDR values are found also below liquid base. The three periods are accompanied by varying microphysical fingerprints in the radar data.

The first two periods are characterized by similar CTTs close to -13° and LWP values mostly below 50 g m^{-2}. During the first period of low turbulence at cloud top, we find Z_{DR} values reaching up to 4 dB, consistent with the expected growth of dendritic particles within this temperature regime (e.g., Takahashi, 2014). As soon as turbulence at cloud top increases (ca. 5 UTC), Z_{DR} drops, and DWR below the liquid layer increases to values

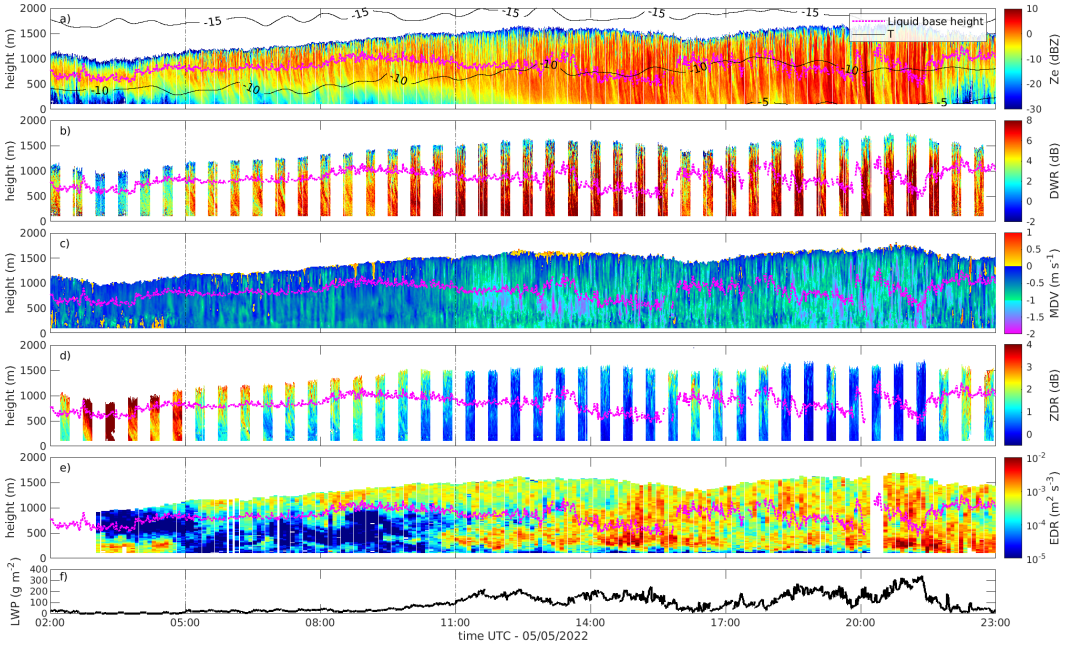

Figure 1. Case study of low-level mixed-phase cloud, detected on 5 May 2022. Panels respectively display: reflectivity from W-band radar with temperature contours overlayed (a), Ka-W dual-wavelength ratio (b), mean Doppler velocity from W-band radar, smoothed with a 2-min rolling average (c; negative values indicate targets moving towards the radar), differential reflectivity from Ka-band observations at 30° elevation (d), eddy dissipation rate (e), liquid water path (f). The dotted magenta line on panels a through e indicates liquid base height from a ceilometer, while the contours in panel a indicate temperature in °C retrieved from microwave radiometer data. Vertical dash-dotted lines indicate the three periods identified in the text.

between 4 and 7 dB. The increase in DWR together with the overall small change in MDV strongly suggests that the increasing turbulence fosters the formation of larger aggregates.

The third period with most intense turbulence seems to favor riming, likely alongside aggregation: DWR increases further up to 8-10 dB, accompanied by MDV exceeding, in some regions, values of 1.5 m s^{-1}, and much higher LWP values ranging between 100-350 g m^{-2}. The high MDV values are indicative of higher-density rimed particles (Mosimann, 1995; Kneifel & Moisseev, 2020), whose more spherical shape is consistent with Z_{DR} values being close to 0 dB. While the case study presented already establishes a potential connection between turbulence and collisional ice-growth processes in LLMPCs, the presence of such interaction can only be demonstrated via robust statistics based on a high number of events. Such analysis is presented in the next section.

4 Results and discussion

In this section we test the sensitivity of ice growth processes to varying turbulence conditions, discriminating the cases into various classes, based on ice habit (via CTT) and availability of liquid (via LWP). We build upon the results by Chellini et al. (2022), who observed that ice aggregation predominantly occurs in LLMPCs at Ny-Ålesund if the liquid layer of the cloud is at temperatures compatible with growth of plate-like particles, i.e., between -20 and -10°C. They attributed this to the rapid growth of dendritic particles,

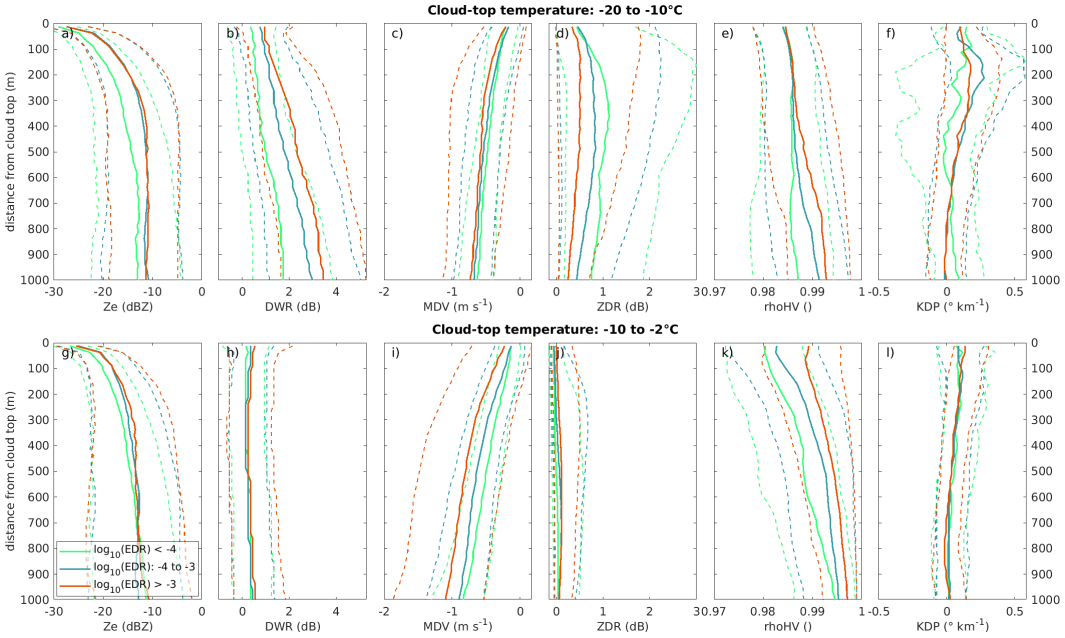

Figure 2. Contoured frequency by altitude diagram of several radar variables in eddy dissipation rate (EDR) classes, for profiles with cloud-top temperature between -20 and -10°C (a-f) and between -10 and -2°C (g-l). Solid lines indicate median values, dashed lines indicate lower and upper quartiles. Panels respectively display: reflectivity from W-band radar (a, g), Ka-W dual-wavelength ratio (b, h), mean Doppler velocity from W-band radar (c, i), differential reflectivity (d, j), correlation coefficient (e, k), specific differential phase (f, l). The y-axis indicates the distance from cloud top along the vertical direction. Profiles are classified based on the mean EDR across the topmost 500 m of the cloud layer. EDR values in the legend are reported in $m^2\ s^{-3}$, height bins are 25 m wide.

favored by saturation with respect to liquid; dendrites then aggregate efficiently due to their large cross sectional area and sticking efficiency (Pruppacher & Klett, 2012). Chellini et al. (2022) then reported a dramatic decrease in occurrence of ice aggregates when CTT is warmer than -10°C, hence the production of large, fast-falling particles in this temperature regime can be predominantly explained by riming. Therefore, we here classify all available profiles into either a *dendritic-growth regime* (CTT between -20 and -10°C), where both aggregation and riming can occur, or a *columnar regime* (CTT between -10 and -2°C), where predominantly riming can take place. In order to determine connections between microphysics and turbulence we classify profiles based on the mean EDR calculated across the layer between cloud top and 500 m below cloud top. The mean is computed in log-scale, as EDR is typically thought to be log-normally distributed (e.g., Siebert et al., 2006). The reasoning behind this approach is given in the Supplement, together with distributions of uppermost-500-m averaged EDR. All available profiles are classified into three EDR classes: EDR $< 10^{-4}\ m^2\ s^{-3}$, EDR between 10^{-4} and $10^{-3}\ m^2\ s^{-3}$, and EDR $> 10^{-3}\ m^2\ s^{-3}$. They were determined based on the quartiles of the distribution of uppermost 500 m averaged EDR throughout all events, which are: $10^{-4.2}$, $10^{-3.5}$, $10^{-2.9}\ m^2\ s^{-3}$.

4.1 Dependence of radar observables on EDR

The signatures obtained in the dendritic-growth regime in Fig. 2a-f confirm that the main ice-growth process in this temperature regime is aggregation. All median curves display values close to 0.6-0.7 m s^{-1}, compatible with low-density aggregates (Locatelli & Hobbs, 1974; Karrer et al., 2020). Increasing DWR with increasing EDR in Fig. 2b suggests that aggregation might be indeed enhanced by higher EDR. The three median DWR curves especially diverge in the top 500 m, with median values at 500 m below cloud top of 1.0, 1.8, and 2.4 dB. Z_{DR} in the low EDR class displays a vastly different behaviour compared to the intermediate and high EDR classes: it increases from cloud top until 300-400 m below cloud top, then decreases. This could be a signature of depositional growth. The absence of such signature in the two remaining EDR classes likely originates from onsetting aggregation already close to cloud top. Similar features were already observed when comparing the first and second period in the case study in Fig. 1. Hence, we argue that the combined decrease in Z_{DR} and increase in DWR with EDR and height are a clear indication of increasing aggregation with turbulence.

In the classical theory of aggregation, the process is considered one-dimensional, taking place along the vertical axis, and driven by sedimentation velocity differences (e.g., Field & Heymsfield, 2003; Westbrook et al., 2004). Turbulence can strongly enhance relative velocities both in the vertical and horizontal component and also lead to locally enhanced particle concentrations. Direct numerical simulations (DNS) by Sheikh et al. (2022) with 300-µm plate particles revealed that collision kernels display an approximate power law dependence on EDR with exponent 0.5. In the case of inertial particles, they attributed the collision rate increases to enhanced relative velocities generated by centrifugal forces. The lack of a clear peak in Z_{DR} in the intermediate and high EDR cases in Fig. 2d, compared to the low EDR, suggests that such an enhancement in collision rate might already be relevant close to cloud top. The enhanced K_{DP} between 100 and 300 m below cloud top might also be a consequence of an increase in collision rates, as it signals a higher number concentration of small particles. One possible explanation for this signature might be fragmentation of dendritic and stellar structures during particle collisions, which has been frequently suggested in literature (e.g., Rangno & Hobbs, 2001; Schwarzenboeck et al., 2009; von Terzi et al., 2022).

In the columnar regime, when CTT is higher than -10°C, aggregation is not dominant, as evident from DWR for the most part being below 1 dB in Fig. 2h. Hence, the main relevant ice-growth process is riming: MDV values in panel c are in fact compatible with small high-density ice particles (Locatelli & Hobbs, 1974; Barthazy & Schefold, 2006), and Z_{DR} is close to 0 dB, indicative of the presence of spherical particles. Reflectivity and MDV both display increasing median and quartile values with increasing EDR, while ρ_{HV} displays values reaching closer to unity as particles sediment, and moving from the lower EDR to the higher EDR class. All these signatures are compatible with increasing riming with EDR, however, it cannot be clearly inferred from Fig. 2g-l whether these fingerprints are generated by increased ice-liquid collision rates associated with increasing EDR, or by increased liquid production associated with conditions that favor high EDR. In the next section we disentangle the effects of increased liquid production and turbulence on the ice microphysics.

In Fig. 2l K_{DP} displays a similar behaviour in all EDR classes, with a maximum at cloud top close to 0.1 ° km^{-1}, then decreasing with height as particles sediment. Luke et al. (2021) reported the occurrence of secondary ice production in less than 10% of cases of MPCs in this temperature regime at the Arctic site of Utqiaġvik. Assuming a similar frequency of occurrence of secondary ice production at Ny-Ålesund, we can attribute most of the K_{DP} signal in Fig. 2l to primary ice production. The maximum at cloud top is likely associated with higher liquid water content (LWC) at cloud top (Mioche et al., 2017), as in Arctic MPCs ice nucleation is thought to originate from the liquid phase (Prenni et al., 2009; De Boer et al., 2011). Assuming that similar primary ice nucleation pathways are present

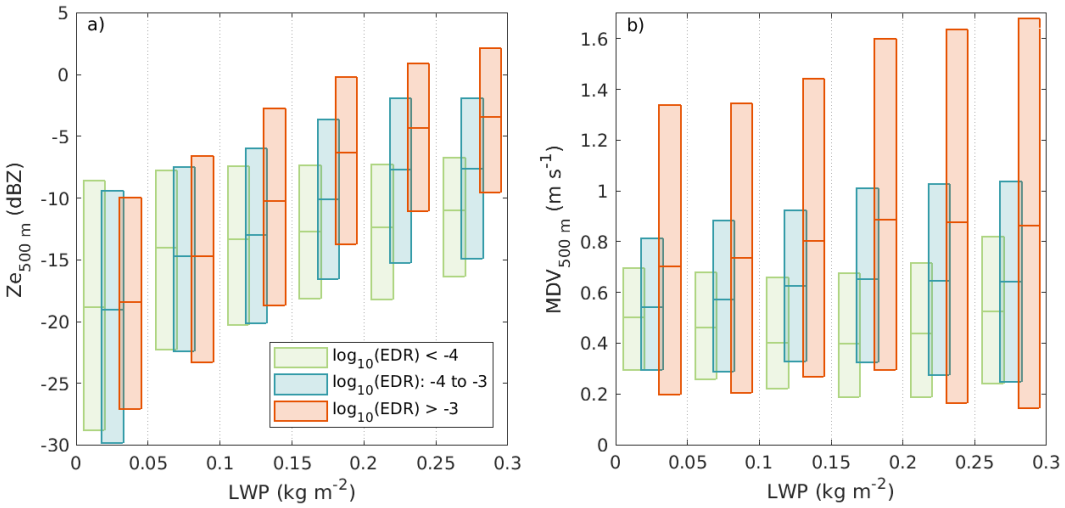

Figure 3. Quartiles of W-band reflectivity (a), and W-band mean Doppler velocity (b), measured at 500 m below cloud top, classified into liquid water path (LWP) and eddy dissipation rate (EDR) classes, for profiles with cloud-top temperature between -10 and -2°C. The edges of the LWP classes are indicated on the x-axis. Distributions belonging to the same LWP class, but different EDR classes are shifted with respect to each other to facilitate the interpretation of the plot. Profiles are classified based on the mean EDR across the topmost 500 m of the cloud layer. EDR values in the legend are reported in $m^2\ s^{-3}$.

above and below -10°C, the K_{DP} maxima between 100 and 300 m below cloud top in the dendritic regime in Fig. 2f can be indeed interpreted as generated by turbulence-induced secondary ice production. Therefore, increasing collision rates with turbulence might lead to higher number of fragments produced by collisions between plate-like particles. However, we do not have an explanation for the higher values of K_{DP} found in the intermediate EDR class compared to those in the high EDR class.

4.2 Combined impact of LWP and EDR on riming

In this section we aim at disentangling the contributions from turbulence and LWP, as in LLMPCs higher LWC has been reported in updrafts (Shupe, Kollias, Persson, & McFarquhar, 2008; Khain et al., 2022), and stronger updrafts might in turn be associated with higher EDR. In Figure 3 we display distributions of Z_e, and MDV, taken at 500 m below cloud top, classified based on LWP and uppermost-500-m averaged EDR, in the columnar regime. A similar figure for the dendritic regime can be found in the Supplement.

As already mentioned, in this temperature regime we can assume that riming is the dominant ice growth process. Z_e and MDV display an increase with EDR in all LWP classes with LWP > 100 g m^{-2}. The increase in MDV being accompanied by an increase in reflectivity indicates an enhancement in riming. Looking only at the lowest EDR class, median Z_e and MDV remain approximately constant throughout the whole range of LWP values investigated. Even in the higher LWP classes (LWP > 200 g m^{-2}), the values of Z_e and MDV shown in Fig. 3 suggest low degrees of riming when EDR $< 10^{-4}$ m^2 s^{-3}. We argue that this is a strong indication that turbulence is an essential component needed to obtain riming, at least in the shallow liquid layers subject of this study. In the two lowest LWP classes (i.e., LWP < 100 g m^{-2}), reflectivities are similar across all EDR classes, while MDV increases with EDR. This might in part be attributable to settling velocity

enhancement by turbulence, via a process known as preferential sweeping (Maxey, 1987; Aliseda et al., 2002; Li et al., 2021).

The riming intensification here reported might be attributed to higher EDR favoring the formation of larger droplets, via collision-coalescence enhancement; riming has been in fact shown to be sensitive to droplet size (Jensen & Harrington, 2015; Erfani & Mitchell, 2017). Erfani and Mitchell (2017) reported that for LWC of 0.05 g m^{-3} a doubling of the mass-median diameter of droplets from 8 to 16 µm quadruples the riming rate. In warm rain formation, the role of turbulence in favoring the formation of collision-coalescence initiators has been suggested. These are droplets sufficiently large to initiate precipitation formation, and are thought to be generated by cloud-top turbulence, which locally enhances collision-coalescence (Small & Chuang, 2008). Similarly, in MPCs turbulence might favor the initial formation of rimed crystals, which then collect droplets more and more efficiently as they rime, due to the dramatic dependence of collection efficiency on the particle's Reynolds number Re, which in turn increases with size (Wang & Ji, 2000).

In addition to a collision-coalescence enhancement, inertial effects have also been suggested to play a role in the enhancement of ice-liquid collision rates (Pinsky & Khain, 1998). Furthermore, we speculate that turbulence might favor collisions between ice crystals and droplets on the smaller side of the size distribution. Due to the small sizes and relatively low inertia of droplets, modifications of the flow field by the ice particle play a large role in riming. DNS studies have shown that if modifications of the flow by the collector are neglected, collision rates between ice crystals and droplets are only marginally increased under increasing EDR (Naso et al., 2018). In contrast, if the two-way interaction between the collector and the flow is taken into account, an increase in collision efficiency for small particles with EDR at constant collector Re has been suggested by Homann et al. (2016), although their study didn't look specifically at cloud microphysics applications.

5 Conclusions

In this study, we use state-of-the-art dual-frequency and polarimetric Doppler cloud radar observations of Arctic low-level mixed-phase clouds to evaluate the role of turbulence in the growth of precipitable ice particles. We perform a statistical analysis based on a large number of events, which highlights the key role that turbulence plays in cold precipitation formation. In particular, following previous studies, categorizing the events based on CTT allows us to discriminate between cases where both aggregation and riming are relevant growth processes (at CTT between -20 and -10°C, i.e., at dendritic-growth temperatures), and cases where only riming is relevant (at CTT warmer than -10°C, i.e., at columnar-growth temperatures). The main findings of this study are:

- At dendritic-growth temperatures higher EDR is associated with increasing size of ice particles. We argue that such an increase is attributable to increasing collision rates between ice particles, leading to larger aggregates. We suggest that, in this temperature regime, increasing collision rates with EDR might lead to increasing secondary ice production via fragmentation of dendritic structures, in addition to an enhancement in aggregation.
- At temperatures warmer than -10°C, turbulence appears to increase riming rates. Dramatic increases in MDV and reflectivity (up to 120% in MDV and 8 dB in Z_e) with increasing EDR and constant LWP are observed, suggesting that riming in shallow liquid layers, such as those observed in the LLMPCs here studied, is a fundamentally turbulent process. We discuss a number of possible processes that could lead to the observed increased riming rates, however the remote sensing observations here used don't allow us either to pinpoint or exclude specific processes. We deem that further work combining model experiments with remote-sensing observations is highly needed in this regard to explain the riming rate enhancement here reported.

We argue that turbulence is potentially a key component determining the characteristics of precipitation. The current study only highlighted this key role in shallow clouds characterized by low to intermediate EDR values, between 10^{-5} and 10^{-2} m^2 s^{-3}. Mid-latitude frontal systems display similar values (Chapman & Browning, 2001), while deep convective systems have been reported to produce EDR up to $10^{-0.5}$ m^2 s^{-3} (Feist et al., 2019). Therefore interactions between turbulence and ice growth might be at play in many cloud systems that produce precipitation at the mid-latitudes. The inclusion of turbulence-dependent collision kernels for collision-coalescence has been shown to produce large improvements in warm rain formation in models (e.g., Seifert et al., 2010). We thus argue that fully quantifying and parametrizing the impact of turbulence on snow and graupel growth is crucial to improve model performance. Further efforts are hence needed to reach an understanding of particle inertial effects in snow, as well as the processes leading to riming enhancement in turbulence.

6 Open Research

The remote-sensing data used in this study have been published in Chellini et al. (2023), and are available at: `doi.org/10.5281/zenodo.7803064`. The slow edge velocity, needed as input for the EDR retrieval, together with the EDR retrieval output have been published separately and are available at: `doi.org/10.5281/zenodo.8325221`.

Acknowledgments
The authors gratefully acknowledge the funding by the Deutsche Forschungsgemeinschaft (DFG, German Research Foundation) – project no. 268020496 – TRR 172, within the Transregional Collaborative Research Center "ArctiC Amplification: Climate Relevant Atmospheric and SurfaCe Processes, and Feedback Mechanisms $(AC)^3$".

The authors would like to express their gratitude to Paloma Borque and Rosa Gierens, for sharing code used in the EDR retrieval, and to Sabrina Schnitt, for providing detailed feedback on the manuscript. The authors would like to further acknowledge discussions with Eberhard Bodenschatz, Ulrich Löhnert, Maximilian Maahn, Dmitri Moisseev, Axel Seifert, Raymond Shaw, Christoph Siewert, and Miklós Szakáll, among others, whose constructive comments and criticism helped shape the analysis.

GC further acknowledges the support from the Graduate School of Geosciences (GSGS) of the University of Cologne, and the Integrated Research Training group (IRTG) of the $(AC)^3$ consortium.

References

Aikins, J., Friedrich, K., Geerts, B., & Pokharel, B. (2016). Role of a Cross-Barrier Jet and Turbulence on Winter Orographic Snowfall. *Monthly Weather Review*, *144*(9), 3277–3300. doi: 10.1175/MWR-D-16-0025.1

Aliseda, A., Cartellier, A., Hainaux, F., & Lasheras, J. C. (2002). Effect of preferential concentration on the settling velocity of heavy particles in homogeneous isotropic turbulence. *Journal of Fluid Mechanics*, *468*, 77–105. doi: 10.1017/S0022112002001593

Andrić, J., Kumjian, M. R., Zrnić, D. S., Straka, J. M., & Melnikov, V. M. (2013). Polarimetric signatures above the melting layer in winter storms: An observational and modeling study. *Journal of Applied Meteorology and Climatology*, *52*(3), 682–700. doi: 10.1175/JAMC-D-12-028.1

Arenberg, D. (1939). Turbulence as the major factor in the growth of cloud drops. *Bulletin of the American Meteorological Society*, *20*(10), 444–448.

Barrett, A. I., Westbrook, C. D., Nicol, J. C., & Stein, T. H. M. (2019). Rapid ice aggregation process revealed through triple-wavelength Doppler spectrum radar analysis. *Atmospheric Chemistry and Physics*, *19*(8), 5753–5769. doi: 10.5194/acp-19-5753-2019

Barthazy, E., & Schefold, R. (2006). Fall velocity of snowflakes of different riming degree and crystal types. *Atmospheric Research*, *82*(1-2), 391–398. doi: 10.1016/j.atmosres.2005.12.009

Battaglia, A., Tanelli, S., Tridon, F., Kneifel, S., Leinonen, J., & Kollias, P. (2020). Triple-Frequency Radar Retrievals. In V. Levizzani, C. Kidd, D. B. Kirschbaum, C. D. Kummerow, K. Nakamura, & F. J. Turk (Eds.), *Satellite Precipitation Measurement: volume 1* (pp. 211–229). Cham: Springer International Publishing. doi: 10.1007/978-3-030-24568-9_13

Bechini, R., Baldini, L., & Chandrasekar, V. (2013). Polarimetric radar observations in the ice region of precipitating clouds at C-band and X-band radar frequencies. *Journal of Applied Meteorology and Climatology*, *52*(5), 1147–1169. doi: 10.1175/JAMC-D-12-055.1

Billault-Roux, A.-C., Georgakaki, P., Gehring, J., Jaffeux, L., Schwarzenboeck, A., Coutris, P., ... Berne, A. (2023). Distinct secondary ice production processes observed in radar Doppler spectra: insights from a case study. *Atmospheric Chemistry & Physics Discussions*. doi: 10.5194/egusphere-2023-478

Borque, P., Luke, E., & Kollias, P. (2016). On the unified estimation of turbulence eddy dissipation rate using Doppler cloud radars and lidars. *Journal of Geophysical Research: Atmospheres*, *121*(10), 5972–5989. doi: 10.1002/2015JD024543

Bouniol, D., Illingworth, A., & Hogan, R. (2004). Deriving turbulent kinetic energy dissipation rate within clouds using ground based radar. In *Proceedings of ERAD* (Vol. 281).

Brewster, K. A., & Zrnić, D. S. (1986). Comparison of eddy dissipation rates from spatial spectra of Doppler velocities and Doppler spectrum widths. *Journal of Atmospheric and Oceanic Technology*, *3*(3), 440–452. doi: 10.1175/1520-0426(1986)003⟨0440:COEDRF⟩2.0.CO;2

Bringi, V. N., & Chandrasekar, V. (2001). *Polarimetric Doppler weather radar: principles and applications*. Cambridge University Press.

Bühl, J., Seifert, P., Myagkov, A., & Ansmann, A. (2016). Measuring ice-and liquid-water properties in mixed-phase cloud layers at the Leipzig Cloudnet station. *Atmospheric Chemistry and Physics*, *16*(16), 10609–10620. doi: 10.5194/acp-16-10609-2016

Chapman, D., & Browning, K. (2001). Measurements of dissipation rate in frontal zones. *Quarterly Journal of the Royal Meteorological Society*, *127*(576), 1939–1959. doi: 10.1002/qj.49712757605

Chellini, G., Gierens, R., Ebell, K., Kiszler, T., Krobot, P., Myagkov, A., ... Kneifel, S. (2023). Low-level mixed-phase clouds at the high Arctic site of Ny-Ålesund: A comprehensive long-term dataset of remote sensing observations. *Earth System Science Data Discussions*, *2023*, 1–33. doi: 10.5194/essd-2023-157

Chellini, G., Gierens, R., & Kneifel, S. (2022). Ice Aggregation in Low-Level Mixed-Phase Clouds at a High Arctic Site: Enhanced by Dendritic Growth and Absent Close to the Melting Level. *Journal of Geophysical Research: Atmospheres*, *127*(16), e2022JD036860. doi: 10.1029/2022JD036860

Crewell, S., & Löhnert, U. (2007). Accuracy of boundary layer temperature profiles retrieved with multifrequency multiangle microwave radiometry. *IEEE Transactions on Geoscience and Remote Sensing*, *45*(7), 2195–2201. doi: 10.1109/TGRS.2006.888434

De Boer, G., Morrison, H., Shupe, M., & Hildner, R. (2011). Evidence of liquid dependent ice nucleation in high-latitude stratiform clouds from surface remote sensors. *Geophysical Research Letters*, *38*(1). doi: 10.1029/2010GL046016

Dias Neto, J., Kneifel, S., Ori, D., Trömel, S., Handwerker, J., Bohn, B., ... Simmer, C. (2019). The TRIple-frequency and Polarimetric radar Experiment for improving process observations of winter precipitation. *Earth System Science Data*, *11*(2), 845–863. doi: 10.5194/essd-11-845-2019

East, T. W. R., & Marshall, J. (1954). Turbulence in clouds as a factor in precipitation. *Quarterly Journal of the Royal Meteorological Society*, *80*(343), 26–47. doi: 10.1002/qj.49708034305

Erfani, E., & Mitchell, D. L. (2017). Growth of ice particle mass and projected area

during riming. *Atmospheric Chemistry and Physics*, *17*(2), 1241–1257. doi: 10.5194/acp-17-1241-2017

Feist, M. M., Westbrook, C. D., Clark, P. A., Stein, T. H., Lean, H. W., & Stirling, A. J. (2019). Statistics of convective cloud turbulence from a comprehensive turbulence retrieval method for radar observations. *Quarterly Journal of the Royal Meteorological Society*, *145*(719), 727–744. doi: 10.1002/qj.3462

Field, P. R., & Heymsfield, A. J. (2003). Aggregation and scaling of ice crystal size distributions. *Journal of the Atmospheric Sciences*, *60*(3), 544–560. doi: 10.1175/1520-0469(2003)060⟨0544:AASOIC⟩2.0.CO;2

Fitch, K. E., & Garrett, T. J. (2022a). Graupel Precipitating From Thin Arctic Clouds With Liquid Water Paths Less Than 50 g m-2. *Geophysical Research Letters*, *49*(1), e2021GL094075. doi: 10.1029/2021GL094075

Fitch, K. E., & Garrett, T. J. (2022b). Measurement and Analysis of the Microphysical Properties of Arctic Precipitation Showing Frequent Occurrence of Riming. *Journal of Geophysical Research: Atmospheres*, *127*(7), e2021JD035980. doi: 10.1029/2021JD035980

Gehring, J., Oertel, A., Vignon, É., Jullien, N., Besic, N., & Berne, A. (2020). Microphysics and dynamics of snowfall associated with a warm conveyor belt over Korea. *Atmospheric Chemistry and Physics*, *20*(12), 7373–7392. doi: 10.5194/acp-20-7373-2020

Gehring, J., Vignon, É., Billault-Roux, A.-C., Ferrone, A., Protat, A., Alexander, S. P., & Berne, A. (2022). Orographic Flow Influence on Precipitation During an Atmospheric River Event at Davis, Antarctica. *Journal of Geophysical Research: Atmospheres*, *127*(2), e2021JD035210. doi: 10.1029/2021JD035210

Gierens, R., Kneifel, S., Shupe, M. D., Ebell, K., Maturilli, M., & Löhnert, U. (2020). Low-level mixed-phase clouds in a complex Arctic environment. *Atmospheric Chemistry and Physics*, *20*(6), 3459–3481. doi: 10.5194/acp-20-3459-2020

Grazioli, J., Lloyd, G., Panziera, L., Hoyle, C. R., Connolly, P. J., Henneberger, J., & Berne, A. (2015). Polarimetric radar and in situ observations of riming and snowfall microphysics during CLACE 2014. *Atmospheric Chemistry and Physics*, *15*(23), 13787–13802. doi: 10.5194/acp-15-13787-2015

Griesche, H. J., Ohneiser, K., Seifert, P., Radenz, M., Engelmann, R., & Ansmann, A. (2021). Contrasting ice formation in Arctic clouds: surface-coupled vs. surface-decoupled clouds. *Atmospheric Chemistry and Physics*, *21*(13), 10357–10374. doi: 10.5194/acp-21-10357-2021

Griesche, H. J., Seifert, P., Ansmann, A., Baars, H., Barrientos Velasco, C., Bühl, J., ... Macke, A. (2020). Application of the shipborne remote sensing supersite OCEANET for profiling of Arctic aerosols and clouds during Polarstern cruise PS106. *Atmospheric Measurement Techniques*, *13*(10), 5335–5358. doi: 10.5194/amt-13-5335-2020

Griffin, E. M., Schuur, T. J., & Ryzhkov, A. V. (2018). A polarimetric analysis of ice microphysical processes in snow, using quasi-vertical profiles. *Journal of Applied Meteorology and Climatology*, *57*(1), 31–50. doi: 10.1175/JAMC-D-17-0033.1

Heymsfield, A. J., Schmitt, C., Bansemer, A., Gettelman, A., Field, P. R., Liu, C., et al. (2020). Contributions of the liquid and ice phases to global surface precipitation: Observations and global climate modeling. *Journal of the Atmospheric Sciences*, *77*(8), 2629–2648. doi: 10.1175/JAS-D-19-0352.1

Hildebrand, P. H., & Sekhon, R. (1974). Objective Determination of the Noise Level in Doppler Spectra. *Journal of Applied Meteorology and Climatology*, *13*(7), 808–811. doi: 10.1175/1520-0450(1974)013⟨0808:ODOTNL⟩2.0.CO;2

Hogan, R. J., Illingworth, A. J., & Sauvageot, H. (2000). Measuring crystal size in cirrus using 35-and 94-GHz radars. *Journal of Atmospheric and Oceanic Technology*, *17*(1), 27–37. doi: 10.1175/1520-0426(2000)017⟨0027:MCSICU⟩2.0.CO;2

Homann, H., Guillot, T., Bec, J., Ormel, C., Ida, S., & Tanga, P. (2016). Effect of turbulence on collisions of dust particles with planetesimals in protoplanetary disks. *Astronomy & Astrophysics*, *589*, A129. doi: 10.1051/0004-6361/201527344

Houze, R. A., & Medina, S. (2005). Turbulence as a Mechanism for Orographic Precipitation

Enhancement. *Journal of the Atmospheric Sciences*, *62*(10), 3599–3623. doi: 10.1175/JAS3555.1

Illingworth, A., Hogan, R., O'connor, E., Bouniol, D., Brooks, M., Delanoë, J., ... others (2007). Cloudnet: Continuous evaluation of cloud profiles in seven operational models using ground-based observations. *Bulletin of the American Meteorological Society*, *88*(6), 883–898.

Jensen, A. A., & Harrington, J. Y. (2015). Modeling ice crystal aspect ratio evolution during riming: A single-particle growth model. *Journal of the Atmospheric Sciences*, *72*(7), 2569–2590. doi: 10.1175/JAS-D-14-0297.1

Kalesse, H., de Boer, G., Solomon, A., Oue, M., Ahlgrimm, M., Zhang, D., ... Protat, A. (2016). Understanding Rapid Changes in Phase Partitioning between Cloud Liquid and Ice in Stratiform Mixed-Phase Clouds: An Arctic Case Study. *Monthly Weather Review*, *144*(12), 4805–4826. doi: 10.1175/MWR-D-16-0155.1

Karrer, M., Seifert, A., Siewert, C., Ori, D., von Lerber, A., & Kneifel, S. (2020). Ice Particle Properties Inferred From Aggregation Modelling. *Journal of Advances in Modeling Earth Systems*, *12*(8), e2020MS002066. doi: 10.1029/2020MS002066

Khain, A., Pinsky, M., & Korolev, A. (2022). Combined Effect of the Wegener–Bergeron–Findeisen Mechanism and Large Eddies on Microphysics of Mixed-Phase Stratiform Clouds. *Journal of the Atmospheric Sciences*, *79*(2), 383–407. doi: 10.1175/JAS-D-20-0269.1

Kiszler, T., Ebell, K., & Schemann, V. (2023). A Performance Baseline for the Representation of Clouds and Humidity in Cloud-Resolving ICON-LEM Simulations in the Arctic. *Journal of Advances in Modeling Earth Systems*, *15*(5), e2022MS003299. doi: 10.1029/2022MS003299

Kneifel, S., & Moisseev, D. (2020). Long-Term Statistics of Riming in Nonconvective Clouds Derived from Ground-Based Doppler Cloud Radar Observations. *Journal of the Atmospheric Sciences*, *77*(10), 3495–3508. doi: 10.1175/JAS-D-20-0007.1

Kollias, P., Albrecht, B., Lhermitte, R., & Savtchenko, A. (2001). Radar observations of updrafts, downdrafts, and turbulence in fair-weather cumuli. *Journal of the Atmospheric Sciences*, *58*(13), 1750–1766. doi: 10.1175/1520-0469(2001)058⟨1750:ROOUDA⟩2.0.CO;2

Küchler, N., Kneifel, S., Löhnert, U., Kollias, P., Czekala, H., & Rose, T. (2017). A W-Band Radar–Radiometer System for Accurate and Continuous Monitoring of Clouds and Precipitation. *Journal of Atmospheric and Oceanic Technology*, *34*(11), 2375–2392. doi: 10.1175/JTECH-D-17-0019.1

Li, J., Abraham, A., Guala, M., & Hong, J. (2021). Evidence of preferential sweeping during snow settling in atmospheric turbulence. *Journal of Fluid Mechanics*, *928*, A8. doi: 10.1017/jfm.2021.816

Locatelli, J. D., & Hobbs, P. V. (1974). Fall speeds and masses of solid precipitation particles. *Journal of Geophysical Research*, *79*(15), 2185–2197. doi: 10.1029/JC079i015p02185

Luke, E. P., Yang, F., Kollias, P., Vogelmann, A. M., & Maahn, M. (2021). New insights into ice multiplication using remote-sensing observations of slightly supercooled mixed-phase clouds in the Arctic. *Proceedings of the National Academy of Sciences*, *118*(13). doi: 10.1073/pnas.2021387118

Maherndl, N., Moser, M., Lucke, J., Mech, M., Risse, N., Schirmacher, I., & Maahn, M. (2023). Quantifying riming from airborne data during HALO-$(AC)^3$. *EGUsphere*, *2023*, 1–32. doi: 10.5194/egusphere-2023-1118

Maxey, M. R. (1987). The gravitational settling of aerosol particles in homogeneous turbulence and random flow fields. *Journal of Fluid Mechanics*, *174*, 441–465. doi: 10.1017/S0022112087000193

Medina, S., & Houze, R. A. (2015). Small-scale precipitation elements in midlatitude cyclones crossing the California Sierra Nevada. *Monthly Weather Review*, *143*(7), 2842–2870. doi: 10.1175/MWR-D-14-00124.1

Mioche, G., Jourdan, O., Delanoë, J., Gourbeyre, C., Febvre, G., Dupuy, R., ... Gayet,

J.-F. (2017). Vertical distribution of microphysical properties of Arctic springtime low-level mixed-phase clouds over the Greenland and Norwegian seas. *Atmospheric Chemistry and Physics*, *17*(20), 12845–12869. doi: 10.5194/acp-17-12845-2017

Morrison, H., de Boer, G., Feingold, G., Harrington, J., Shupe, M. D., & Sulia, K. (2012). Resilience of persistent Arctic mixed-phase clouds. *Nature Geoscience*, *5*(1), 11–17. doi: 10.1038/ngeo1332

Mosimann, L. (1995). An improved method for determining the degree of snow crystal riming by vertical Doppler radar. *Atmospheric Research*, *37*(4), 305–323. doi: 10.1016/0169-8095(94)00050-N

Mülmenstädt, J., Sourdeval, O., Delanoë, J., & Quaas, J. (2015). Frequency of occurrence of rain from liquid-, mixed-, and ice-phase clouds derived from A-Train satellite retrievals. *Geophysical Research Letters*, *42*(15), 6502–6509. doi: 10.1002/2015GL064604

Myagkov, A., Seifert, P., Wandinger, U., Bühl, J., & Engelmann, R. (2016). Relationship between temperature and apparent shape of pristine ice crystals derived from polarimetric cloud radar observations during the ACCEPT campaign. *Atmospheric Measurement Techniques*, *9*(8), 3739–3754. doi: 10.5194/amt-9-3739-2016

Naso, A., Jucha, J., Lévêque, E., & Pumir, A. (2018). Collision rate of ice crystals with water droplets in turbulent flows. *Journal of Fluid Mechanics*, *845*, 615–641. doi: 10.1017/jfm.2018.238

Nomokonova, T., Ebell, K., Löhnert, U., Maturilli, M., & Ritter, C. (2020). The influence of water vapor anomalies on clouds and their radiative effect at Ny-Ålesund. *Atmospheric Chemistry and Physics*, *20*(8), 5157–5173. doi: 10.5194/acp-20-5157-2020

Ori, D., Schemann, V., Karrer, M., Dias Neto, J., von Terzi, L., Seifert, A., & Kneifel, S. (2020). Evaluation of ice particle growth in ICON using statistics of multi-frequency Doppler cloud radar observations. *Quarterly Journal of the Royal Meteorological Society*, *146*(733), 3830–3849. doi: 10.1002/qj.3875

O'Connor, E. J., Hogan, R. J., & Illingworth, A. J. (2005). Retrieving stratocumulus drizzle parameters using Doppler radar and lidar. *Journal of Applied Meteorology*, *44*(1), 14–27. doi: 10.1175/JAM-2181.1

Pinsky, M. B., & Khain, A. P. (1998). Some effects of cloud turbulence on water–ice and ice–ice collisions. *Atmospheric Research*, *47–48*, 69–86. doi: 10.1016/S0169-8095(98)00041-6

Pope, S. B. (2000). *Turbulent flows*. Cambridge University Press.

Prenni, A. J., Demott, P. J., Rogers, D. C., Kreidenweis, S. M., Mcfarquhar, G. M., Zhang, G., & Poellot, M. R. (2009). Ice nuclei characteristics from M-PACE and their relation to ice formation in clouds. *Tellus B: Chemical and Physical Meteorology*, *61*(2), 436–448. doi: 10.1111/j.1600-0889.2009.00415.x

Pruppacher, H. R., & Klett, J. D. (2012). *Microphysics of clouds and precipitation: Reprinted 1980*. Dordrecht: Springer. doi: 10.1007/978-94-009-9905-3

Pumir, A., & Wilkinson, M. (2016). Collisional Aggregation Due to Turbulence. *Annual Review of Condensed Matter Physics*, *7*(1), 141–170. doi: 10.1146/annurev-conmatphys-031115-011538

Ramelli, F., Henneberger, J., David, R. O., Lauber, A., Pasquier, J. T., Wieder, J., ... Lohmann, U. (2021). Influence of low-level blocking and turbulence on the microphysics of a mixed-phase cloud in an inner-Alpine valley. *Atmospheric Chemistry and Physics*, *21*(6), 5151–5172. doi: 10.5194/acp-21-5151-2021

Rangno, A. L., & Hobbs, P. V. (2001). Ice particles in stratiform clouds in the Arctic and possible mechanisms for the production of high ice concentrations. *Journal of Geophysical Research: Atmospheres*, *106*(D14), 15065–15075. doi: 10.1029/2000JD900286

Rogers, R., & Tripp, B. (1964). Some radar measurements of turbulence in snow. *Journal of Applied Meteorology and Climatology*, *3*(5), 603–610. doi: 10.1175/1520-0450(1964)003⟨0603:SRMOTI⟩2.0.CO;2

Saffman, P., & Turner, J. (1956). On the collision of drops in turbulent clouds. *Journal of Fluid Mechanics*, *1*(1), 16–30. doi: 10.1017/S0022112056000020

Schemann, V., & Ebell, K. (2020). Simulation of mixed-phase clouds with the ICON large-

eddy model in the complex Arctic environment around Ny-Ålesund. *Atmospheric Chemistry and Physics*, *20*(1), 475–485. doi: 10.5194/acp-20-475-2020

Schrom, R. S., & Kumjian, M. R. (2016). Connecting microphysical processes in Colorado winter storms with vertical profiles of radar observations. *Journal of Applied Meteorology and Climatology*, *55*(8), 1771–1787. doi: 10.1175/JAMC-D-15-0338.1

Schrom, R. S., Kumjian, M. R., & Lu, Y. (2015). Polarimetric radar signatures of dendritic growth zones within Colorado winter storms. *Journal of Applied Meteorology and Climatology*, *54*(12), 2365–2388. doi: 10.1175/JAMC-D-15-0004.1

Schwarzenboeck, A., Shcherbakov, V., Lefevre, R., Gayet, J. F., Pointin, Y., & Duroure, C. (2009). Indications for stellar-crystal fragmentation in Arctic clouds. *Atmospheric Research*, *92*(2), 220–228. doi: 10.1016/j.atmosres.2008.10.002

Seifert, A., Nuijens, L., & Stevens, B. (2010). Turbulence effects on warm-rain autoconversion in precipitating shallow convection. *Quarterly Journal of the Royal Meteorological Society*, *136*(652), 1753–1762. doi: 10.1002/qj.684

Seifert, A., & Onishi, R. (2016). Turbulence effects on warm-rain formation in precipitating shallow convection revisited. *Atmospheric Chemistry and Physics*, *16*(18), 12127–12141. doi: 10.5194/acp-16-12127-2016

Shaw, R. A. (2003). Particle-turbulence interactions in atmospheric clouds. *Annual Review of Fluid Mechanics*, *35*(1), 183–227. doi: 10.1146/annurev.fluid.35.101101.161125

Shaw, R. A., Reade, W. C., Collins, L. R., & Verlinde, J. (1998). Preferential concentration of cloud droplets by turbulence: Effects on the early evolution of cumulus cloud droplet spectra. *Journal of the Atmospheric Sciences*, *55*(11), 1965–1976. doi: 10.1175/1520-0469(1998)055⟨1965:PCOCDB⟩2.0.CO;2

Sheikh, M. Z., Gustavsson, K., Lévêque, E., Mehlig, B., Pumir, A., & Naso, A. (2022). Colliding Ice Crystals in Turbulent Clouds. *Journal of the Atmospheric Sciences*, *79*(9), 2205–2218. doi: 10.1175/JAS-D-21-0305.1

Shupe, M. D., Kollias, P., Persson, P. O. G., & McFarquhar, G. M. (2008). Vertical motions in Arctic mixed-phase stratiform clouds. *Journal of the Atmospheric Sciences*, *65*(4), 1304–1322. doi: 10.1175/2007JAS2479.1

Shupe, M. D., Kollias, P., Poellot, M., & Eloranta, E. (2008). On deriving vertical air motions from cloud radar Doppler spectra. *Journal of Atmospheric and Oceanic Technology*, *25*(4), 547–557. doi: 10.1175/2007JTECHA1007.1

Shupe, M. D., Matrosov, S. Y., & Uttal, T. (2006). Arctic Mixed-Phase Cloud Properties Derived from Surface-Based Sensors at SHEBA. *Journal of the Atmospheric Sciences*, *63*(2), 697–711. doi: 10.1175/JAS3659.1

Siebert, H., Lehmann, K., & Wendisch, M. (2006). Observations of small-scale turbulence and energy dissipation rates in the cloudy boundary layer. *Journal of the Atmospheric Sciences*, *63*(5), 1451–1466. doi: 10.1175/JAS3687.1

Small, J. D., & Chuang, P. Y. (2008). New observations of precipitation initiation in warm cumulus clouds. *Journal of the Atmospheric Sciences*, *65*(9), 2972–2982. doi: 10.1175/2008JAS2600.1

Squires, K. D., & Eaton, J. K. (1991). Preferential concentration of particles by turbulence. *Physics of Fluids A: Fluid Dynamics*, *3*(5), 1169–1178. doi: 10.1063/1.858045

Takahashi, T. (2014). Influence of liquid water content and temperature on the form and growth of branched planar snow crystals in a cloud. *Journal of the Atmospheric Sciences*, *71*(11), 4127–4142. doi: 10.1175/JAS-D-14-0043.1

Tetoni, E., Ewald, F., Hagen, M., Köcher, G., Zinner, T., & Groß, S. (2022). Retrievals of ice microphysical properties using dual-wavelength polarimetric radar observations during stratiform precipitation events. *Atmospheric Measurement Techniques*, *15*(13), 3969–3999. doi: 10.5194/amt-15-3969-2022

Trömel, S., Simmer, C., Blahak, U., Blanke, A., Doktorowski, S., Ewald, F., ... others (2021). Overview: Fusion of radar polarimetry and numerical atmospheric modelling towards an improved understanding of cloud and precipitation processes. *Atmospheric Chemistry and Physics*, *21*(23), 17291–17314. doi: 10.5194/acp-21-17291-2021

Vaillancourt, P. A., & Yau, M. (2000). Review of particle-turbulence interactions and

consequences for cloud physics. *Bulletin of the American Meteorological Society*, *81*(2), 285–298. doi: 10.1175/1520-0477(2000)081⟨0285:ROPIAC⟩2.3.CO;2

von Terzi, L., Dias Neto, J., Ori, D., Myagkov, A., & Kneifel, S. (2022). Ice microphysical processes in the dendritic growth layer: A statistical analysis combining multi-frequency and polarimetric Doppler cloud radar observations. *Atmospheric Chemistry and Physics*, *22*(17), 11795–11821. doi: 10.5194/acp-22-11795-2022

Voßkuhle, M., Pumir, A., Lévêque, E., & Wilkinson, M. (2014). Prevalence of the sling effect for enhancing collision rates in turbulent suspensions. *Journal of Fluid Mechanics*, *749*, 841–852. doi: 10.1017/jfm.2014.259

Wang, P. K., & Ji, W. (2000). Collision efficiencies of ice crystals at low–intermediate Reynolds numbers colliding with supercooled cloud droplets: A numerical study. *Journal of the Atmospheric Sciences*, *57*(8), 1001–1009. doi: 10.1175/1520-0469(2000)057⟨1001:CEOICA⟩2.0.CO;2

Westbrook, C., Ball, R., Field, P., & Heymsfield, A. (2004). Theory of growth by differential sedimentation, with application to snowflake formation. *Physical Review E*, *70*(2), 021403. doi: 10.1103/PhysRevE.70.021403

Zhao, C., & Garrett, T. (2008). Ground-based remote sensing of precipitation in the Arctic. *Journal of Geophysical Research: Atmospheres*, *113*(D14). doi: 10.1029/2007JD009222

Zhu, Z., Kollias, P., & Yang, F. (2023). Particle Inertia Effects on Radar Doppler Spectra Simulation. *Atmospheric Measurement Techniques*, *16*(15), 3727–3737. doi: 10.5194/amt-16-3727-2023

Supporting Information for "Turbulence as a key driver of ice aggregation and riming in Arctic low-level mixed-phase clouds, revealed by long-term cloud radar observations"

Giovanni Chellini[1], and Stefan Kneifel[2]

[1]Institute for Geophysics and Meteorology, University of Cologne, Cologne, Germany

[2]Meteorological Institute, Ludwig-Maximilians-Universität in Munich, Munich, Germany

Contents of this file

1. Text S1 to S3
2. Figures S1 to S3

Introduction

The present Supplement includes three sections: section S1 presents the approach used to retrieve the eddy dissipation rate (EDR) from cloud radar observations, section S2 presents statistics of retrieved EDR and motivates the EDR classification approach used in the analysis, section S3 presents statistics of the joint dependence of radar observables on EDR and liquid water path (LWP) at dendritic-growth temperatures, similar to the analysis reported in section 4.2.

S1: EDR retrieval

A variety of methods have been proposed to derive EDR estimates from cloud radar observations, with most of them focusing either on the Doppler spectrum width or on the variance of mean Doppler velocity (MDV) time series (Rogers & Tripp, 1964; Brewster & Zrnić, 1986; Kollias et al., 2001; Bouniol et al., 2004; Shupe et al., 2008; Borque et al., 2016; Griesche et al., 2020). Spectrum-width-based methods rely on the assumption that the microphysical contribution to spectrum width is negligible when compared to the turbulence-induced broadening of the Doppler spectrum (Rogers & Tripp, 1964; O'Connor et al., 2005; Borque et al., 2016), and is hence not suited for applications in precipitating clouds. We therefore use a velocity time series variance approach similar to that developed by Borque et al. (2016). Their approach consists in performing a fast Fourier transform (FFT) of MDV time series at a given range gate, and fitting a power law to the resulting spectrum with a fixed slope of -5/3 expected for vertical motions belonging to the inertial subrange (e.g., Pope, 2000). A linear fit to the FFT output (brought to log-log scale) is attempted in several frequency intervals $[f_{low}, f_{high}]$, and the EDR is computed for all frequency intervals whose fit has a slope within -5/3±1/3. Following this approach, the EDR is then computed as (Borque et al., 2016, eq. 2):

$$\mathrm{EDR} = \frac{2\pi}{V_h}\left(\frac{2}{3\alpha}\int_{f_{low}}^{f_{high}} S(f)df\right)^{3/2}\left(f_{low}^{-2/3} - f_{high}^{-2/3}\right)^{-3/2}, \tag{1}$$

where α is the Kolmogorov constant (here taken as 0.55), $S(f)$ is the MDV power spectrum (i.e., the FFT output), and V_h is the horizontal wind speed. Borque et al. (2016) then compute the final EDR value as the mean value across all valid frequency intervals. Compared to other MDV time series variance approaches, e.g., those by Bouniol et al. (2004) and Shupe et al. (2008), this approach has the advantage of computing the EDR only from the fraction of the MDV variance that is attributable to the inertial subrange, instead of the total MDV variance. A variant of this approach was validated against in-situ balloon-borne observations of EDR in Arctic LLMPCs

by Griesche et al. (2020), who found agreement within a factor of 3 between the in-situ and remote-sensing methods.

Here we apply some slight modifications to the retrieval approach by Borque et al. (2016), to make it more suited to our data and objective. Zhu, Kollias, and Yang (2023) recently analysed how cloud radar Doppler spectra are affected by inertial effects: they reported a lower degree of turbulence-induced broadening at the fast edge of Doppler spectra observed in rain, compared to the slow edge. This translates into a lower variance of MDV when inertial particles are present in the particle population, hence leading to a possible underestimation of the EDR. For this reason we apply the EDR retrieval to the slow edge velocity (SEV), instead of the MDV, as Zhu et al. (2023) found it not to be affected by inertial effects. We calculate the SEV as the velocity associated with the slowest Doppler bin above the peak noise level, belonging to a spectral cluster whose width is at least 5 Doppler bins. The choice of using the peak noise level as threshold was determined based on von Terzi, Dias Neto, Ori, Myagkov, and Kneifel (2022), who used a fixed threshold of 3 dB above the mean noise level: due to the varying Doppler resolution and Nyquist velocity, and hence spectral noise density, with range of the radars here used (see Table 2 in Chellini et al. (2023)), we determined that a threshold varying with noise characteristics is more suited, hence the choice of the peak noise level. Mean and peak noise level are determined based on the commonly used algorithm by Hildebrand and Sekhon (1974). Similarly to Griesche et al. (2020), the retrieval is performed in 5-minute intervals. Possible gaps in the data are allowed, for a maximum of 10% of the data points in each 5-minute time series, and are filled with a cubic spline interpolation. Several frequency intervals $[f_{low}, f_{high}]$ are attempted: the attempted values for the lower bound are $f_{low} = 10^{-4+0.1 \cdot n}$ Hz, while the attempted values for the higher bound are $f_{high} = 10^{0-0.1 \cdot m}$ Hz, with n and m non-negative integers. All $[f_{low}, f_{high}]$ combinations with $f_{high} \geq 5 \cdot f_{low}$ are attempted.

Horizontal wind speed information (V_h in Eq. 1) is here taken from Chellini et al. (2023) as well. They included horizontal wind fields from the ICOsahedral Non-hydrostatic Large Eddy Model (ICON-LEM) simulations by Schemann and Ebell (2020) and Kiszler, Ebell, and Schemann (2023).

S2: Vertical EDR distribution

In section 4 we classify profiles based on the mean value of $\log_{10}$(EDR) across the top 500 m of the cloud layer. Here, we justify this choice. Figure S1a displays quantiles of EDR as function of height, while Fig. S1b displays quantiles of the quantity:

$$\log_{10}(\mathrm{EDR}(z)) - \frac{1}{\mathrm{CTH} - z}\int_{z}^{\mathrm{CTH}} \log_{10}(\mathrm{EDR}(z'))dz', \tag{2}$$

where CTH stands for cloud-top height, and z indicates height from the ground. As such the value in the formula indicates the deviation between the EDR value retrieved at height z, and the mean EDR computed across the layer with base at height z and top at cloud top. The figure shows that the median deviation is approximately 0 from cloud top, until approximately 800 m below cloud top. Thus, in this height range the EDR is distributed symmetrically around the cloud-top-layer-averaged value. In the analysis in the main body of the paper we choose z = CTH - 500 m, because it falls within these values, while at the same time the spread around the cloud-top-layer-averaged value is contained. Looking at the 25th and 75th percentiles we can in fact deduce that, at this height, in 50% of the cases the deviation from the cloud-top-layer-averaged EDR value falls within half an order of magnitude (i.e ± 0.25 $\log_{10}(\mathrm{m}^2\ \mathrm{s}^{-3})$). Distributions of uppermost-500-m averaged EDR for all events are displayed in Fig. S2.

S3: Combined impact of LWP and EDR on riming and aggregation in the dendritic regime

Similarly to Fig. 3 in the main body of the article, in Fig. S3 we display distributions of DWR, Z_e, and MDV, taken at 500 m below cloud top, classified based on uppermost-500 m averaged EDR and LWP, in the dendritic regime. First, we focus on the two lowest LWP classes

(0 to 50 g m^{-2}, and 50 to 100 g m^{-2}), where we can expect riming to be minimal. In fact, in the two lowest LWP classes we find a marked dependence of DWR on EDR: the DWR quartiles increase by approximately 2 dB from the lowest to the highest EDR classes. This corroborates our conceptual interpretation of the vertical profiles shown in Fig. 2: EDR has a pronounced impact on aggregation, as revealed by strongly increasing DWR and Ze with EDR class, in contrast to the weak increase in median MDV. Looking at the entire LWP range in Fig. S3a, one finds DWR to be almost independent on LWP but to increase substantially with EDR class in any LWP bin. However, the steady increase of median MDV with LWP, from 0.4 m s^{-1} in the lowest LWP class to 0.7 m s^{-1} in the highest LWP class, indicates that riming might be still present also in the dendritic regime, and that while increasing EDR favors aggregation and riming, increasing LWP favors for the most part riming alone.

References

Borque, P., Luke, E., & Kollias, P. (2016). On the unified estimation of turbulence eddy dissipation rate using Doppler cloud radars and lidars. *Journal of Geophysical Research: Atmospheres*, *121*(10), 5972–5989. doi: 10.1002/2015JD024543

Bouniol, D., Illingworth, A., & Hogan, R. (2004). Deriving turbulent kinetic energy dissipation rate within clouds using ground based radar. In *Proceedings of ERAD* (Vol. 281).

Brewster, K. A., & Zrnić, D. S. (1986). Comparison of eddy dissipation rates from spatial spectra of Doppler velocities and Doppler spectrum widths. *Journal of Atmospheric and Oceanic Technology*, *3*(3), 440–452. doi: 10.1175/1520-0426(1986)003⟨0440:COEDRF⟩2.0.CO;2

Chellini, G., Gierens, R., Ebell, K., Kiszler, T., Krobot, P., Myagkov, A., ... Kneifel, S. (2023). Low-level mixed-phase clouds at the high Arctic site of Ny-Ålesund: A comprehensive long-term dataset of remote sensing observations. *Earth System Science Data Discussions*, *2023*, 1–33. doi: 10.5194/essd-2023-157

Griesche, H. J., Seifert, P., Ansmann, A., Baars, H., Barrientos Velasco, C., Bühl, J., ... Macke,

A. (2020). Application of the shipborne remote sensing supersite OCEANET for profiling of Arctic aerosols and clouds during Polarstern cruise PS106. *Atmospheric Measurement Techniques*, *13*(10), 5335–5358. doi: 10.5194/amt-13-5335-2020

Hildebrand, P. H., & Sekhon, R. (1974). Objective Determination of the Noise Level in Doppler Spectra. *Journal of Applied Meteorology and Climatology*, *13*(7), 808–811. doi: 10.1175/1520-0450(1974)013⟨0808:ODOTNL⟩2.0.CO;2

Kiszler, T., Ebell, K., & Schemann, V. (2023). A Performance Baseline for the Representation of Clouds and Humidity in Cloud-Resolving ICON-LEM Simulations in the Arctic. *Journal of Advances in Modeling Earth Systems*, *15*(5), e2022MS003299. doi: 10.1029/2022MS003299

Kollias, P., Albrecht, B., Lhermitte, R., & Savtchenko, A. (2001). Radar observations of updrafts, downdrafts, and turbulence in fair-weather cumuli. *Journal of the Atmospheric Sciences*, *58*(13), 1750–1766. doi: 10.1175/1520-0469(2001)058⟨1750:ROOUDA⟩2.0.CO;2

O'Connor, E. J., Hogan, R. J., & Illingworth, A. J. (2005). Retrieving stratocumulus drizzle parameters using Doppler radar and lidar. *Journal of Applied Meteorology*, *44*(1), 14–27. doi: 10.1175/JAM-2181.1

Pope, S. B. (2000). *Turbulent flows*. Cambridge University Press.

Rogers, R., & Tripp, B. (1964). Some radar measurements of turbulence in snow. *Journal of Applied Meteorology and Climatology*, *3*(5), 603–610. doi: 10.1175/1520-0450(1964)003⟨0603:SRMOTI⟩2.0.CO;2

Schemann, V., & Ebell, K. (2020). Simulation of mixed-phase clouds with the ICON large-eddy model in the complex Arctic environment around Ny-Ålesund. *Atmospheric Chemistry and Physics*, *20*(1), 475–485. doi: 10.5194/acp-20-475-2020

Shupe, M. D., Kollias, P., Poellot, M., & Eloranta, E. (2008). On deriving vertical air motions from cloud radar Doppler spectra. *Journal of Atmospheric and Oceanic Technology*, *25*(4), 547–557. doi: 10.1175/2007JTECHA1007.1

von Terzi, L., Dias Neto, J., Ori, D., Myagkov, A., & Kneifel, S. (2022). Ice microphysical processes in the dendritic growth layer: A statistical analysis combining multi-frequency and polarimetric Doppler cloud radar observations. *Atmospheric Chemistry and Physics*, *22*(17), 11795–11821. doi: 10.5194/acp-22-11795-2022

Zhu, Z., Kollias, P., & Yang, F. (2023). Particle Inertia Effects on Radar Doppler Spectra Simulation. *Atmospheric Measurement Techniques*, *16*(15), 3727–3737. doi: 10.5194/amt-16-3727-2023

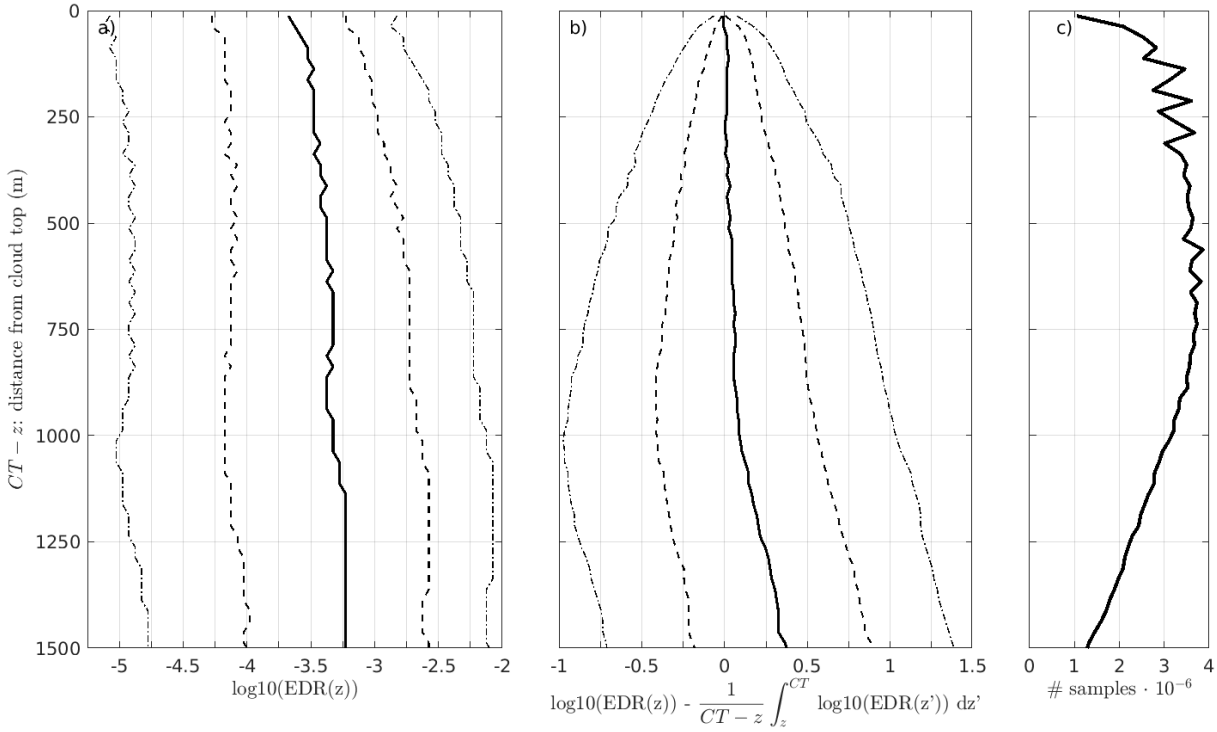

Figure S1. Contoured-frequency by altitude diagram of the logarithm of the eddy dissipation rate (EDR, expressed in $\log_{10}(\mathrm{m}^2\ \mathrm{s}^{-3})$; panel a) and of the difference between the logarithm of the eddy dissipation rate (EDR) at multiple heights and the average $\log_{10}$(EDR) computed between each height and cloud top (b). The curves represent the 0.1 and 0.9 (dot-dashed), 0.25 and 0.75 (dashed), and 0.5 (solid) quantiles. Panel c displays the number of samples available in each chosen height bin. Bins are 25 m wide.

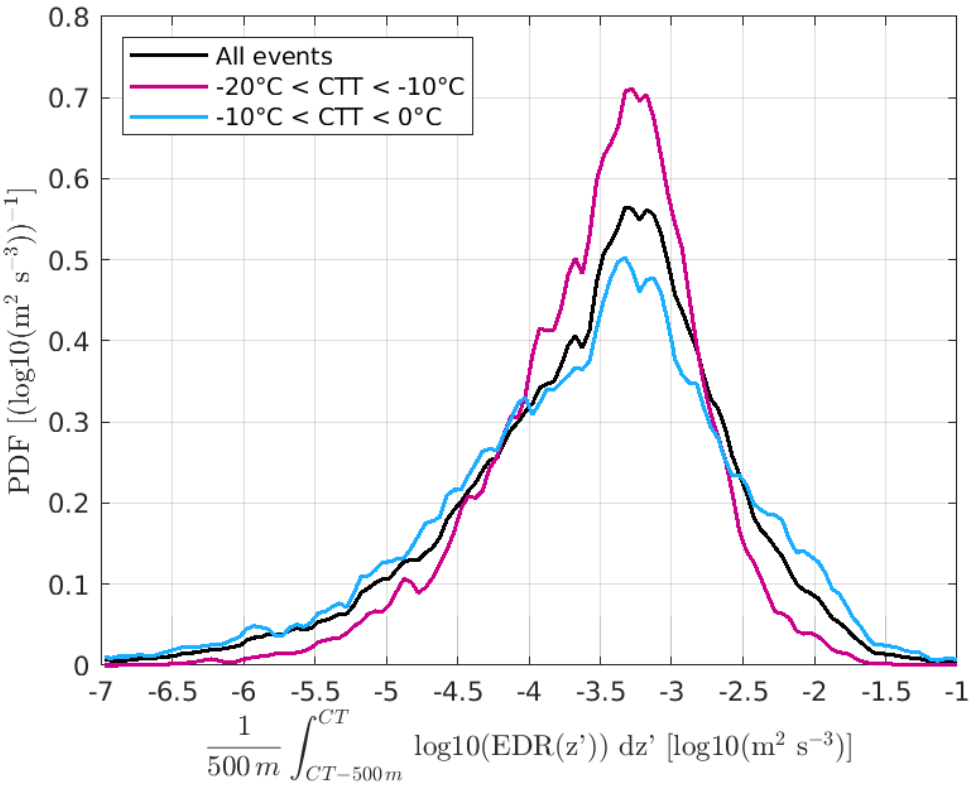

Figure S2. Probability density functions (PDF) for the average of the logarithm of the eddy dissipation rate (EDR) in the uppermost 500 m. PDFs are shown for all events, and for events with cloud-top temperature (CTT) between -20 and -10°C, and -10 and 0°C. Bins are 0.05 $\log_{10}(\mathrm{m}^2\ \mathrm{s}^{-3})$ wide.

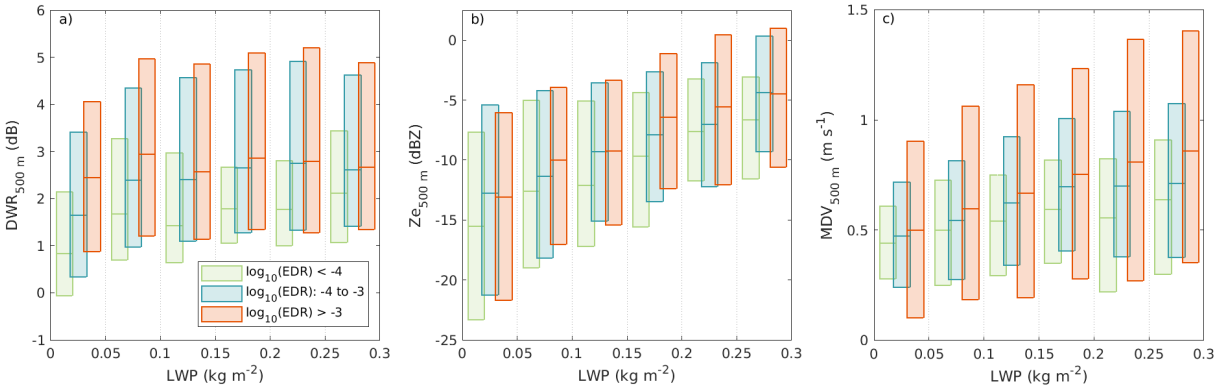

Figure S3. Quartiles of Ka-W dual-wavelength ratio (a), W-band reflectivity (b), and W-band mean Doppler velocity (c), measured at 500 m below cloud top, classified into liquid water path (LWP) and eddy dissipation rate (EDR) classes, for profiles with cloud-top temperature between -20 and -10°C. The edges of the LWP classes are indicated on the x-axis. Distributions belonging to the same LWP class, but different EDR classes are shifted with respect to each other to facilitate the interpretation of the plot. Profiles are classified based on the mean EDR across the topmost 500 m of the cloud layer. EDR values in the legend are reported in $m^2\ s^{-3}$.

5.1 A first look at the potential enhancement of ice particle fall velocity in turbulence

In addition to collision rates, turbulence is thought to enhance the velocities of settling particles. As illustrated in Section 2.2.3, the preferential sweeping process has been suggested to lead to particles oversampling descending regions of a turbulent flow, in turn leading to higher settling velocities. Additionally, a second process has been suggested to lead to the enhancement of settling velocities of asymmetrical particles, termed *differential settling*, and is induced by fluctuations in the canting angle of particle [e.g., Siewert et al., 2014, Gustavsson et al., 2017, 2021]. While preferential sweeping has been observed in snowfall by Li et al. [2021a] and Li et al. [2021c], observational evidence of differential settling is currently missing. Bréon and Dubrulle [2004] computed a root mean square tilt angle of approximately 3° for 1-mm plates sedimenting in a turbulent flow with EDR = 10^{-2} m^2 s^{-3}. This value is likely to only marginally affect fall velocities. At the same time, Zikmunda and Vali [1972] reported observing large orientation fluctuations for rimed column and needle particles, and limited fluctuations for plate-like particles, although they did not link these observations with turbulence estimates. They further reported rimed columns and needles falling with their major axes aligned vertically to have a velocity triple that of equivalent particles falling with their major axes aligned horizontally. In this section, the same data and methods used in **Study 3** will be employed to investigate whether, in addition to aggregation and riming enhancement, turbulence leads to an increase in settling velocities.

Fig. 5.1 displays contoured frequency by EDR diagrams of MDV, in the dendritic and columnar CTT regimes, and in varying DWR classes. The associated reflectivity distributions and number of samples are shown in Fig. 5.2. Only profiles corresponding to LWP < 50 g m^{-2} are included in the figure, in order to minimize possible contributions by increasing riming degree with EDR. The triple dependence on EDR, particle size (via DWR), and particle habit (via CTT) is introduced because the main parameter determining the intensity of the settling velocity enhancement in preferential sweeping, as well as the magnitude of orientation fluctuations, is the Stokes number St. St in turn depends on the particle relaxation time τ_p (see Eq. 2.7), which is a function of particle size, habit, and density [e.g., Aliseda et al., 2002, Gustavsson et al., 2021]. Figure 5.1 shows that, as EDR increases, median MDV remains constant until a certain threshold EDR value, then increases. The magnitude of the median MDV increase varies with DWR and CTT class. In the small columnar particle class (CTT between -10 and -2°C, DWR below 2 dB) MDV increases by 94.0% when comparing the median values at 10^{-5} and 10^{-2} m^2 s^{-3}. The corresponding values for dendritic particles are 22.4%, 12.1%, and 9.3%, respectively for the small (DWR below 2 dB), intermediate (DWR between

2 and 6 dB), and large (DWR between 6 and 10 dB) particle classes. While an increase in velocity is present in all classes, the magnitude is vastly larger for the columnar particles, compared to the dendritic particles. While in first instance this could be explained by the riming enhancement reported in **Study 3**, Fig. 5.2 paints a different picture: median reflectivity only increases by approximately 3 dB when comparing its minimum value at 10^{-5} m^2 s^{-3}, and its maximum at $10^{-2.5}$ m^2 s^{-3}. This modest increase in reflectivity is likely associated with an increase in particle density due to riming that can only marginally explain the dramatic increase in MDV [e.g., Kalesse et al., 2013]. Similar considerations apply to the dendritic particle classes, although riming cannot be excluded with a similar level of certainty due to the far lower increase in MDV.

For all particle classes the increase in median MDV occurs at specific EDR values: at 10^{-4} m^2 s^{-3} for the small column class, at $10^{-2.5}$ m^2 s^{-3} for the low-DWR dendritic class, and at 10^{-3} m^2 s^{-3} for the intermediate- and high-DWR dendritic classes. Assuming that the relaxation time τ_p doesn't significantly change within each particle class as EDR increases, the varying critical EDR that leads to enhancement in settling velocity can be explained as follows: as EDR increases, the Kolmogorov microscale τ_η decreases, leading to the Stokes number St increasing, and consequently to particles entering the $St \gtrsim 0.1$ regime where inertial effects start being relevant [Yang and Lei, 1998, Aliseda et al., 2002, Pumir and Wilkinson, 2016]. Therefore the different critical EDR values are only determined by τ_p. This interpretation of the results is tested in the next section, where a simple estimate of St in the various particle classes is attempted.

5.1.1 Stokes number estimate

In an attempt to validate the interpretation of Fig. 5.1 given in the previous section, the Stokes numbers associated with hypothetical particle populations that could produce the observed radar fingerprints are estimated in Fig. 5.3. For simplicity, inverse exponential size distributions are assumed, and the corresponding radar reflectivity, DWR, and velocity are forward simulated using the snowScatt database [Ori et al., 2021], in the case of pure dendrite and column aggregate particle populations. The widths of the size distributions were chosen to produce DWRs of 0.5, 4, and 8 dB. Such DWR values are compatible with the DWR classes chosen when classifying observations in Fig. 5.1. The Stokes number was computed for particles with sizes corresponding to the 0.25, 0.5, and 0.75 reflectivity-weighted quantiles (reflectivity at W-band in linear scale) of the particle population. Reflectivity-weighted quantiles were chosen for a more straightforward comparison with the MDV values reported in Fig. 5.1, as MDV is reflectivity

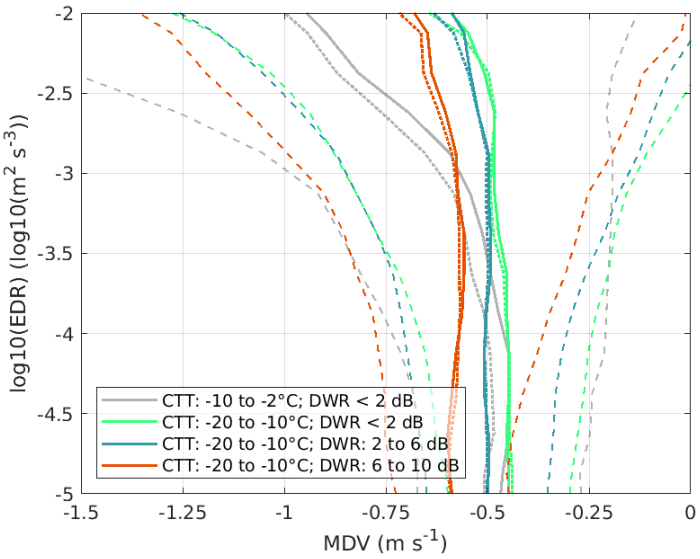

Figure 5.1: Contoured frequency by eddy dissipation rate (EDR) diagram of mean Doppler velocity (MDV) from the W-band cloud radar. Data are grouped based on cloud-top temperature (CTT), and dual wavelength ratio (DWR). Solid lines indicate median values, dotted lines indicate mean values, and dashed lines indicate the first and third quartiles. Please note that in contrast with the figures of **Study 3** where data are classified based on EDR averaged across the uppermost 500 m, in this figure the indicated EDR is not averaged in range. EDR bins are 0.25 $\log_{10}(\mathrm{m}^2\ \mathrm{s}^{-3})$ wide.

weighted. The particles' relaxation time was computed using the formula:

$$\tau_p = v_T g^{-1}, \tag{5.1}$$

which was introduced in Eq. 2.7. Terminal velocity v_T was also taken from snowScatt, which computes it using the approach by Böhm [1992]. The Stokes number can be then estimated as:

$$St = \tau_p \tau_\eta^{-1} = v_T g^{-1} \tau_\eta^{-1} = v_T g^{-1} \nu^{-1/2} \varepsilon^{1/2}. \tag{5.2}$$

This equation relies on the assumption that all particles are smaller than the Kolmogorov microscale η, which, in the case of snowflakes might not always be the case. In fact, at an EDR value of 10^{-3} m^2 s^{-3}, assuming $\nu = 1.5{\cdot}10^{-5}$ m^2 s^{-3}, the Kolmogorov microscale η takes on the value of 1.2 mm, which is smaller than a large fraction of the observed dendritic particles, especially those producing DWR > 2 dB. For this reason, following the approaches by Schmitt and Seuront [2008] and Xu and Bodenschatz [2008], a modified Stokes number is here used. In Eq. 5.2 τ_η is replaced with the time scale associated with eddies of the same size as the ice

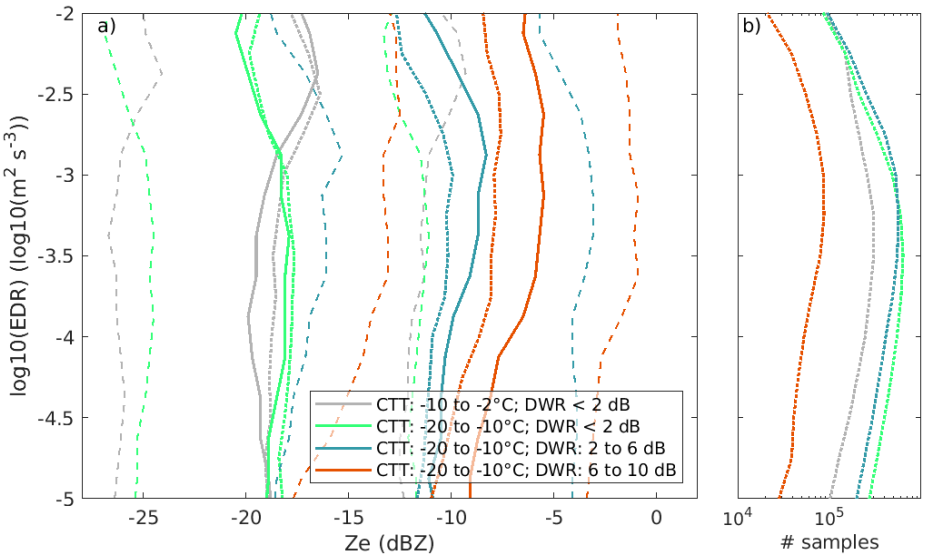

Figure 5.2: Same as in Fig. 5.1 but for reflectivity from the W-band cloud radar (panel a), and number of available samples in each EDR bin and particle class (b).

particle, if the particle is larger than η (i.e., $D_{max} > \eta$). The time scale τ_ℓ of an eddy with length scale ℓ in the inertial subrange can be obtained by dimensional analysis, by recalling that in the dissipation range statistical properties of the flow only depend on the EDR [Schmitt and Seuront, 2008, Xu and Bodenschatz, 2008]:

$$\tau_\ell = \ell^{2/3} \varepsilon^{-1/3}. \tag{5.3}$$

Therefore the modified Stokes number can be defined as:

$$St_{mod} = \begin{cases} St = \tau_p \tau_\eta^{-1} = v_T g^{-1} \tau_\eta = v_T g^{-1} \nu^{1/2} \varepsilon^{-1/2} & \text{if } D_{max} \leq \eta \\ \tau_p \tau_{D_{max}}^{-1} = v_T g^{-1} \tau_{D_{max}}^{-1} = v_T g^{-1} \varepsilon^{1/3} D_{max}^{-2/3} & \text{if } D_{max} > \eta, \end{cases} \tag{5.4}$$

where D_{max} is the size of the maximum dimension of the particle, and $\tau_{D_{max}}$ is the time scale associated with inertial-subrange eddies of length scale D_{max}, calculated following Eq. 5.3. Note that eddies with length scales comparable with the sizes of ice particles are likely in the dissipation range, not in the inertial subrange. Therefore the expression for τ_ℓ in Eq. 5.3 should be intended as a lower bound for their time scales. Consequently, the modified Stokes number St_{mod} defined in Eq. 5.4 should be intended as an upper bound for the actual Stokes number of the ice particle (when $D_{max} > \eta$).

The distributions of St and St_{mod} calculated respectively with equations 5.2 and 5.4 are shown in Figures 5.3 and 5.4, assuming $\nu = 1.5{\cdot}10^{-5}$ m^2 s^{-3}. The Stokes number St in Fig. 5.3 displays similar values for the intermediate and large

dendritic classes, together with the columnar class. This is in contradiction with the observational results in Fig. 5.1, where median MDV in the columnar class deviates from the low-turbulence median MDV value at 10^{-4} m^2 s^{-3}, while both dendritic classes start deviating at 10^{-3} m^2 s^{-3}. However, St for the columnar class rises above 0.1 approximately at 10^{-4} m^2 s^{-3}, which matches the lowest EDR value at which a deviation in MDV is observed in Fig. 5.1. A similar consideration applies to the small dendritic particle class, while it does not hold for the intermediate and large dendritic class.

A comparison between St in Fig. 5.3 and the modified Stokes number St_{mod} in Fig. 5.4 displays that particles in the columnar and small dendritic particle classes are, for the most part, always smaller than η in the investigated EDR range, as $St_{mod} = St$. This does not apply to the intermediate and large dendritic particle classes, whose St_{mod} deviates from St approximately at $10^{-3.5}$ and 10^{-4} m^2 s^{-3}. Starting at these EDR values, St_{mod} in fact increases with EDR at a lower rate compared to the columnar and small dendritic particle classes. This leads to the columnar particle class having much higher St_{mod} (by half an order of magnitude) than all dendritic particle classes when EDR is between 10^{-3} and 10^{-2} m^2 s^{-3}. This large difference in St_{mod} is indeed compatible with the much higher median MDV increase of the columnar particle class compared to the dendritic particle classes observed in Fig. 5.1 at EDR larger than 10^{-3} m^2 s^{-3}. Furthermore, the St values taken on by the columnar particle class at EDR larger than 10^{-3} m^2 s^{-3} are higher than 0.5, and reach values close to unity: it is at these St values that previous studies have reported preferential sweeping to enhance settling velocities the most [Yang and Lei, 1998, Aliseda et al., 2002].

In summary, the analysis reported in this section highlighted that enhancements in settling velocities with EDR are observed in LLMPCs at Ny-Ålesund. Riming is known to increase ice particle density and consequently increase its fall velocity, however it cannot fully explain the observed enhancements. Such enhancements are especially intense for particles nucleated at CTT warmer than -10°C, namely columnar particles. In the literature two main processes have been proposed to lead to settling velocity enhancement in turbulence: preferential sweeping and differential settling. Both these processes display a dependence on the Stokes number St, and as such the results here reported are inconclusive in terms of attributing the enhancement to any one specific process. It is likely that the two effects contribute together to the observed enhancement. Nevertheless, the far higher velocity enhancement observed for columns is compatible with these particles being characterized by higher St_{mod} than the other investigated particle classes, suggesting that particle inertial effects are indeed reasonable candidate processes to explain the observed enhancement.

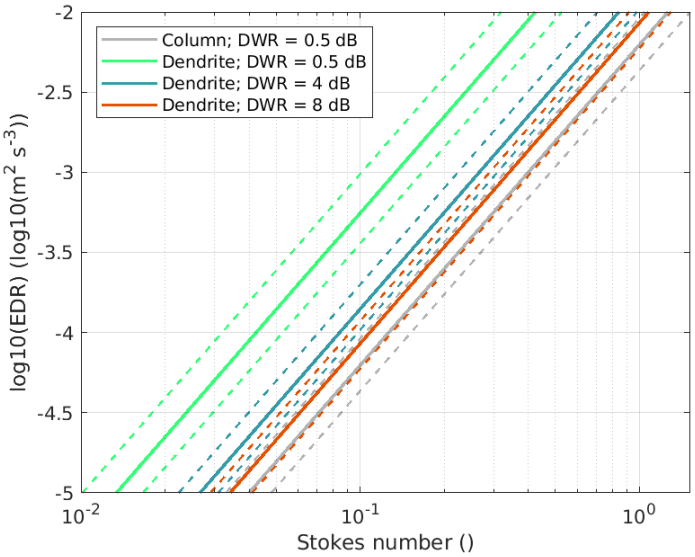

Figure 5.3: Stokes number St (Eq. 5.2) associated with the 0.5 (solid), 0.25 and 0.75 (dashed) reflectivity-weighted quantiles of an inverse exponential size distribution of dendrite and column aggregates, simulated with the snowScatt snowflake scattering database [Ori et al., 2021], at multiple values of eddy dissipation rate (EDR). Curves were computed for particle populations producing dual-wavelength ratios (DWRs) of 0.5, 4, and 8 dB.

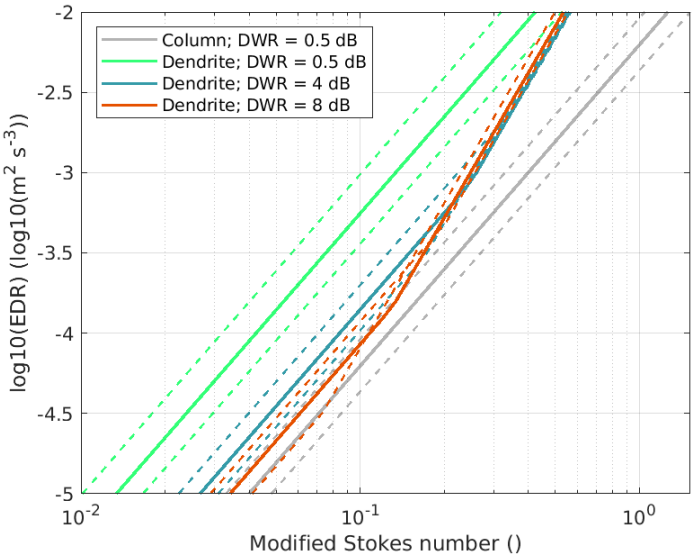

Figure 5.4: Same as Fig. 5.3 but for the modified Stokes number St_{mod} defined in Eq. 5.4.

Chapter 6

Conclusions

Low-level mixed-phase clouds (LLMPCs) cloak large portions of Earth's surface at high latitudes. Due to their extensive occurrence and long-lasting nature, they are highly relevant for the surface energy budget. However, weather and climate models are currently incapable of accurately representing them. This leads to large uncertainties in cloud radiative forcing and feedbacks in climate models. Out of the processes whose model representation needs to be improved, precipitation formation has been shown to be essential. In this thesis, the relevance and sensitivity of precipitation formation processes in LLMPCs was investigated, based on statistics of long-term ground-based remote sensing observations taken at the high Arctic site of Ny-Ålesund. The investigation relied on the interpretation of cloud radar observables, which contain valuable fingerprints of ice microphysical processes. Radar observables were further linked with thermodynamic information, as well as turbulence estimates, to establish the sensitivity of microphysical processes to varying thermodynamic and dynamic conditions. The statistics based on long-term remote-sensing observations allowed to derive robust signatures of microphysical processes. In this chapter, the results from **Study 1**, **Study 2**, and **Study 3** are summarized organically, and remaining knowledge gaps are identified. Finally, an outlook is given on future research directions stemming from the results here presented.

In the three studies it was found that precipitation characteristics in LLMPCs, together with the relevant processes, are dramatically sensitive to cloud-top temperature (CTT): the different ice habits nucleated lead to vastly different precipitation characteristics when comparing events with CTT between -20 and -10°C, with events with CTT between -10 and 0°C. Therefore the two regimes will be discussed separately. An overview of the main results is given in the diagram in Fig. 6.1.

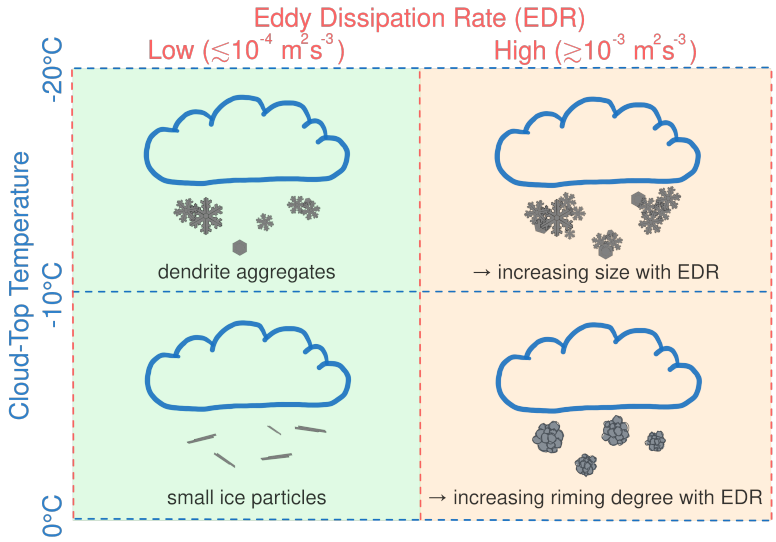

Figure 6.1: Diagram illustrating the main results of this dissertation. Graphical elements courtesy of Jan Kretzschmar.

6.1 Large aggregates at dendritic-growth temperatures

In **Study 1** it was shown that enhanced DWR signatures, signaling the presence of aggregates with sizes larger than 1 mm, occur predominantly in LLMPCs whose mixed-phase layer is, at least partly, at temperatures between -15 and -10°C. This feature is compatible with similar signatures observed at the mid-latitudes, and is typically attributed to enhanced aggregation due to mechanical entanglement of ice particles with dendritic branches, which preferentially grow in this temperature region [Dias Neto et al., 2019, Barrett et al., 2019, von Terzi et al., 2022]. The polarimetric observations presented in **Study 2** further confirmed such interpretation, as an enhancement of Z_{DR} and $sZ_{DR\,max}$, starting at -16°C, signaled the rapid growth of plate-like particles [Schrom and Kumjian, 2016, Griffin et al., 2018, von Terzi et al., 2022]. **Study 1** further found that the highest DWR values at the liquid base of the LLMPC are found in conjunction with temperatures of -13 to -14°C, in agreement with laboratory studies that reported the highest depositional growth rates at these temperatures [Takahashi et al., 1991, Takahashi, 2014, see also Fig. 2.2c]. While riming likely also plays a role, as shown in **Study 1**, these signatures together provided a strong indication that aggregation of dendritic particles is the leading ice-growth mechanism at these temperatures. Moreover, the relevance of aggregation in LLMPCs in this temperature region was further confirmed by the additional increase in DWR observed below the

liquid base, where riming cannot take place. One further element supporting this conclusion was the maximum in K_{DP} at -15°C observed in **Study 2**, related to the increase in number concentration of small asymmetric ice particles, and often observed at dendritic-growth temperatures in mid-latitude deep precipitating systems [Bechini et al., 2013, Schrom et al., 2015, Griffin et al., 2018, von Terzi et al., 2022]. Such maximum is possibly attributable to increases in secondary ice production by collisional fragmentation, due to the higher collisions and fragile structure of dendritic particles [e.g., Rangno and Hobbs, 2001, Schwarzenboeck et al., 2009, von Terzi et al., 2022, Pasquier et al., 2022].

In **Study 3** the role of turbulence in the production of large aggregates at dendritic-growth temperatures was investigated. Higher EDR was shown to be associated with increasing size of ice particles. It was argued that such an increase is attributable to increasing collision rates between ice particles, leading to larger aggregates. In this temperature regime, increasing collision rates with EDR might lead to increasing secondary ice production via fragmentation of dendritic structures, in addition to an enhancement in aggregation. While the dependence of the aggregation and collisional fragmentation processes on turbulence conditions have been suggested by a number studies [Houze and Medina, 2005, Grazioli et al., 2015, Medina and Houze, 2015, Aikins et al., 2016, Gehring et al., 2020, Ramelli et al., 2021, Gehring et al., 2022, Billault-Roux et al., 2023], **Study 3** is the first instance of the corresponding signatures being observed in robust long-term statistics.

In **Study 1** it was shown that high-DWR signals close to the melting level (-5 to 0°C) are absent in LLMPCs at Ny-Ålesund. Therefore, aggregation is minimal in these clouds at these temperatures. Typically, a second enhanced aggregation zone close to 0°C is observed in mid-latitude clouds [Fabry and Zawadzki, 1995, Dias Neto et al., 2019]; **Study 1** highlighted its presence in deeper cloud systems in Ny-Ålesund as well. This feature is usually attributed to the increased sticking efficiency of melting ice particles. Due to their shallow nature, LLMPCs span a limited temperature range, and ice particles nucleate and grow within this narrow temperature range. Particle populations sedimenting from colder temperatures, characterized by broader size distribution compared to those found in LLMPCs close to the melting level, might be necessary to trigger the enhanced aggregation typically observed. As such, further investigating the sensitivity of aggregation in this temperature regime to varying conditions bears the potential to substantially improve our understanding of aggregation in general, not only limited to LLMPCs.

6.2 Small particles and riming at columnar-growth temperatures

Study 1 and **Study 2** highlighted that at temperatures higher than -10°C LLMPCs at Ny-Ålesund typically produce smaller particles, characterized by DWR close to 0 dB, and fall velocities typical for small ice crystals with low degree of riming. **Study 2** in fact observed MDV and polarimetric signatures compatible with intermediate to high degrees of riming (as defined by e.g., Mosimann [1995]) in less than approximately 25% of cases.

This temperature regime is known for the growth of prolate particles, such as columns and needles [e.g., Bailey and Hallett, 2009, Myagkov et al., 2016], which can be easily detected via their enhanced LDR [Oue et al., 2015, Bühl et al., 2016, Li et al., 2021b]. In **Study 2**, signatures compatible with needle production were only observed in less than 25% of the cases at temperatures between -4 and 0°C, with frequency dramatically decreasing at colder temperatures. While these needle particles are known to produce aggregates, they did not seem to aggregate in LLMPCs at Ny-Ålesund, as DWR remained low.

In **Study 3** the dependence of riming on turbulence was investigated. At temperatures warmer than -10°C, turbulence appeared to increase riming rates. Dramatic increases in MDV and reflectivity with increasing EDR and constant LWP were observed, suggesting that riming in shallow liquid layers, such as those observed in the LLMPCs here studied, is a fundamentally turbulent process. A number of possible mechanisms that could lead to the observed increased riming rates was discussed, however the remote sensing observations here used didn't allow for the identification or exclusion of specific processes.

As discussed in Section 5.1, a dramatic enhancement in particle settling velocity was observed in this temperature regime under increasing turbulence. It was speculated that this velocity enhancement might be caused by turbulence, possibly via the processes of preferential sampling of the downwards regions of the eddies by ice particles, a phenomenon termed preferential sweeping, or by increases in fall velocities due to increased fluttering of aspherical particles, a phenomenon named differential settling. The extremely limited literature investigating these processes in snowfall, in particular the lack of explicit particle simulations with realistic particle and fluid assumptions, and laboratory studies resolving the dynamics of individual ice particles in turbulence, did not allow for the establishing of a conclusive link between the observed enhancement and specific processes.

6.3 Outlook

An improved picture of the relevant processes for precipitation formation in LLMPCs, together with their drivers, was achieved in this dissertation. Nevertheless, several outstanding questions remain. In the current section recommendations for future research are presented and discussed.

6.3.1 Aggregation at the melting level

In **Study 1** it was noted that major DWR increases attributable to aggregation are not observed close to the 0°C isotherm in LLMPCs at Ny-Ålesund. This has been extensively observed in previous studies for mid-latitude clouds [Chase et al., 2018, Dias Neto et al., 2019, Tridon et al., 2019, Ori et al., 2020], and in deeper cloud systems in Ny-Ålesund as well (see Appendix C in **Study 1**). In general, enhanced aggregation close to the melting level is thought to be caused by the thickening of a quasi-liquid layer on the snowflake surface, as discussed in Section 2.1.4. In **Study 1** it was hypothesized that particle populations nucleated at temperatures compatible with dendritic-growth, or colder, are needed to trigger the typically observed enhanced aggregation close to the melting level. Further investigating this hypothesis bears the potential to significantly improve our understanding of the aggregation process as a whole, and possibly precipitation forecasts. The sensitivity of the aggregation process to particle habits, size distributions, and degree of riming could in fact be tested using explicit Lagrangian particle models [e.g., Brdar and Seifert, 2018, Shima et al., 2020].

6.3.2 Aggregation and fragmentation enhancement by turbulence in other cloud types

Study 3 robustly demonstrated for the first time the dependence of ice aggregation, and possibly fragmentation, on turbulence. As discussed in the study, this effect is likely to be relevant for other cloud types in other geographical areas as well. The LLMPCs here investigated are characterized by low to intermediate EDR values, between 10^{-5} and 10^{-2} m^2 s^{-3}. Mid-latitude frontal systems, as well as cirrus clouds, display similar values [Gultepe and Starr, 1995, Chapman and Browning, 2001], while deep convective systems have been reported to produce EDR that can reach up to $10^{-0.5}$ m^2 s^{-3} [Feist et al., 2019]. The approach here adopted to retrieve the EDR could be applied to state-of-the-art datasets similar to that developed within **Study 2** to statistically assess the role of turbulence in the formation of large aggregates and the production of high ice number concentrations at other sites and in a wider spectrum of cloud types. Similar analyses could be performed based on the multi-frequency polarimetric Doppler cloud radar observations recorded during

the BAECC campaign in Hyytiälä, Finland [Petäjä et al., 2016], during AWARE in Western Antarctica [Lubin et al., 2020], and during TRIPEx and TRIPEx-pol in Jülich, Germany [Dias Neto et al., 2019, Dias Neto, 2021].

The enhancement in aggregation here reported might be especially relevant for the dendritic-growth zone (DGZ) in deep precipitating systems, as the maximum in depositional growth close to -15°C has been suggested to be linked with a large latent heat release, in turn generating buoyant overturning [Schrom and Kumjian, 2016, von Terzi et al., 2022]. The suggested higher TKE production is most likely associated with higher EDR, and hence it is possible that turbulence might increase collisions between dendritic particles, further favoring aggregation and possibly fragmentation.

Similarly, overturning motions have been suggested for the melting layer in deep precipitating systems [Szyrmer and Zawadzki, 1999]. Here, aggregation and break-up of melting ice particles are highly relevant for determining liquid precipitation characteristics [Stewart et al., 1984, Drummond et al., 1996, Barthazy et al., 1998, Heymsfield et al., 2015, Karrer et al., 2022]. Break-up and aggregation might be further enhanced by turbulence-induced collision rate increases.

6.3.3 Processes leading to riming enhancement by turbulence

In **Study 3** it was shown that increasing EDR is linked with enhanced riming of ice particles. The topic has received little attention in the literature, and while possible mechanisms that could lead to such enhancement were here discussed, it was impossible from the remote sensing perspective to pinpoint the exact processes. Theoretical and modeling work is highly needed in this regard, to explain the signatures reported in the study. Unfortunately, modeling frameworks capable of answering this question are currently missing. Direct numerical simulations (DNS) are in fact extremely computationally expensive, and past studies have focused on highly simplified scenarios, such as monodisperse size distributions, and one-way coupling between the particles and the flow, which doesn't allow for modifications of the flow by the particles [e.g., Naso et al., 2018]. Currently available Lagrangian ice particle models either do not include atmospheric dynamics [Brdar and Seifert, 2018], or do not resolve sub-scale turbulence, nor account for the inertia of particles [Shima et al., 2020]. Therefore, an assessment of the relevance of the mechanisms proposed in **Study 3** would need to rely on a number of different modeling approaches, each resolving different processes and scales.

Large-eddy simulations, such as the ICOsahedral Non-hydrostatic Large-Eddy Model (ICON-LEM; Zängl et al. [2015], Schemann and Ebell [2020], Kiszler et al. [2023]), could be used to assess whether the riming enhancement here reported could be explained by the formation of larger droplets due to increased collision-coalescence. In **Study 3** it was discussed that higher EDR might be associated

with an increase in collision-coalescence, which leads to larger droplets, which in turn are collected by ice crystals more efficiently. In the Seifert and Beheng [2006] two-moment microphysical scheme, used in ICON-LEM, the collection efficiency of liquid droplets by ice crystals $\widetilde{E}_{coll}(m_i)$ (introduced in Sec. 2.1.4, Eq. 2.11) has a dependence on droplet size (see Eq. 64-66 in Seifert and Beheng [2006]). Therefore the inclusion of the turbulent collision-coalescence parametrization by Seifert et al. [2010] could potentially lead to an increase in riming under increasing turbulence, due to the presence of larger droplets in the simulations.

A further process that was identified as a candidate mechanism to explain the riming enhancement is an increase in collision efficiency for small droplets under increasing EDR. Small droplets that would otherwise follow the flow around the ice particle might in fact collide with the collector ice particle in higher EDR regimes. Such interaction between modifications of the flow by an individual ice crystal, turbulence, and droplet dynamics could be evaluated with a DNS setup similar to that used by Homann et al. [2016].

Finally, the relevance and role of inertial effects would be drastically more challenging to quantify. While some effects can be evaluated purely analytically [Pinsky and Khain, 1998], the high degree of complexity of this problem is likely to require explicit particle and flow simulations, and vast advancements in computational techniques will be essential.

6.3.4 Settling velocity enhancement in turbulence

In Section 5.1 a first assessment of ice particle settling velocity enhancement by turbulence was proposed. While the analysis shown was not fully conclusive, it provided an indication that, under specific conditions, turbulence might lead to a dramatic increase in particle settling velocity, up to 94%. Two mechanisms that could explain this increase are differential settling, and preferential sweeping. While observational evidence of differential settling is extremely limited, preferential sweeping was recently observed in snowfall via particle image velocimetry by Li et al. [2021a] and Li et al. [2021c]. Further investigations are highly needed in this regard to assess whether these processes are relevant for clouds and precipitation. Cloud micro- and macrophysical properties in model simulations have been in fact shown to be highly sensitive to ice particle fall velocity parametrizations [Mitchell et al., 2008, Lin and Colle, 2009, Avramov and Harrington, 2010, Reitter et al., 2011, Adams-Selin et al., 2013, Zhao et al., 2017]. For instance, faster fall velocities reduce the occurrence and ice water content (IWC) of high-level clouds in climate simulations [Zhao et al., 2017], and the inclusion of faster falling ice habits in NWP simulations of Arctic LLMPCs has been shown to reduce the IWC and increase the LWC [Avramov and Harrington, 2010]. Therefore, the possible dependence of ice particle fall velocity on turbulence could potentially affect cloud

lifetime, total hydrometeor mass, and, in the case of MPCs, the phase partitioning. If such dependence is confirmed, its omission in models would be introducing a systematic negative bias in ice particle fall velocity in a number of fairly to highly turbulent cold cloud types, such as LLMPCs, cirrus clouds, altocumuli and certain altostrati, as well as deeper precipitating systems. Furthermore, both preferential sweeping and differential settling could potentially further increase the collision rates between particles, leading to further enhancements of aggregation by turbulence. In the case of preferential sweeping, collisions would be facilitated by the higher particle concentration in the downward regions of eddies [Li et al., 2021a]; conversely, differential settling would introduce a greater variance in fall velocities, even resulting in identical particles having largely different fall velocities if they are oriented differently [Siewert et al., 2014].

On the one hand, the possible enhancement of ice particle fall velocity in turbulence should be further investigated via modeling or observational approaches capable of resolving the dynamics of individual particles, in order to determine the relevant processes. On the other hand, the relevance and implications of such processes for clouds and precipitation should be investigated using long-term observational datasets. The analysis presented in Section 5.1 highlighted that long-term cloud radar observations, constrained with temperature information, provide an ideal framework to study the interaction between turbulence and ice particle fall velocities under different ice habits. The main uncertainty encountered in Section 5.1 was the likely contribution of riming to the observed fall velocity enhancement. Therefore, repeating a similar analysis for turbulent ice-only clouds, such as cirrus clouds, would allow to more easily isolate the possible signature of fall velocity enhancement by turbulence.

6.3.5 Model implementation and validation

Especially relevant for the $(AC)^3$ project is the implementation of the results here presented in models. In particular, daily ICON-LEM simulations are currently being ran semi-operationally in the area surrounding Ny-Ålesund [Kiszler et al., 2023]. Some of the results reported in this dissertation could be implemented in existing models, including ICON-LEM. Similarly to the work done by Karrer et al. [2021], part of the results concerning ice aggregation could be easily integrated in ICON-LEM. Karrer et al. [2021] implemented a modified sticking efficiency function $E_{stick}(T)$ (introduced in Sec. 2.1.4, Eq. 2.9), to account for the increased sticking efficiency of plate-like particles nucleated at temperatures between -20 and -10°C, and obtained an improved agreement with observations. Similarly, the enhancement of aggregation in the DGZ here reported in LLMPCs, together with its absence close to the melting level, could be implemented by introducing a separate sticking efficiency function $E_{stick}(T)$ used for low-level clouds only, and characterized by a

maximum at approximately -15°C, increased values between -20 and -10°C, and lower values at warmer temperatures.

In contrast, the enhancement of aggregation with turbulence could not be implemented in models as easily. As discussed in **Study 3**, the underlying processes have not been largely studied. While evidence for an increase in collision rates between ice crystals was here presented, large efforts are still needed to reach a quantitative representation and parametrization of such collision rate increase. The inclusion of turbulence-dependent collision kernels for collision-coalescence has been shown to produce large improvements in warm rain formation in models [e.g., Seifert et al., 2010], and the development of similar parametrizations for ice aggregation bears the same potential.

As mentioned in Section 6.3.3, the ICON-LEM could be further used to assess whether the riming enhancement here reported could be explained by the formation of larger droplets due to increased collision-coalescence. The other processes that could lead to a riming enhancement hypothesized in **Study 3** would be more challenging to implement, as our understanding is currently very poor.

The state-of-the-art dataset developed within **Study 2** provides an ideal framework to validate model representation of LLMPCs, and ice microphysical processes in particular. As demonstrated in **Study 2** and **Study 3**, the dataset in fact contains observational fingerprints of a number of microphysical processes, including aggregation, riming, sedimentation, and the occurrence of specific ice habits. Moreover, the high number of events included allows for robust model-observation comparisons based on statistics. Comparisons based on a single or a low number of cases studies may be challenging to interpret due to the large case-by-case variability, which makes process inference difficult. Such large variability can be filtered out in the statistics, facilitating the identification of model-inherent biases [e.g., Reitter et al., 2011, Karrer et al., 2021]. As such, statistics of observed radar variables can be compared with similar statistics of radar variables forward-simulated based on model output, to identify deficiencies and strengths of the representation of specific processes in model setups.

Bibliography

The current bibliography includes all references cited in Chapters 1, 2, and 6, as well as Section 5.1. The references cited in **Study 1**, **Study 2**, and **Study 3** are listed therein.

C. Acquistapace, U. Löhnert, M. Maahn, and P. Kollias. A new criterion to improve operational drizzle detection with ground-based remote sensing. *Journal of Atmospheric and Oceanic Technology*, 36(5):781–801, 2019. doi:10.1175/JTECH-D-18-0158.1.

R. D. Adams-Selin, S. C. van den Heever, and R. H. Johnson. Impact of Graupel Parameterization Schemes on Idealized Bow Echo Simulations. *Monthly Weather Review*, 141(4):1241 – 1262, 2013. doi:10.1175/MWR-D-12-00064.1.

J. Aikins, K. Friedrich, B. Geerts, and B. Pokharel. Role of a Cross-Barrier Jet and Turbulence on Winter Orographic Snowfall. *Monthly Weather Review*, 144 (9):3277–3300, 2016. doi:10.1175/MWR-D-16-0025.1.

A. Aliseda, A. Cartellier, F. Hainaux, and J. C. Lasheras. Effect of preferential concentration on the settling velocity of heavy particles in homogeneous isotropic turbulence. *Journal of Fluid Mechanics*, 468:77–105, 2002. doi:10.1017/S0022112002001593.

C. Andronache. *Mixed-phase Clouds: Observations and Modeling*. Elsevier, 2017. doi:10.1016/B978-0-12-810549-8.00001-5.

A. Ansmann, M. Tesche, P. Seifert, D. Althausen, R. Engelmann, J. Fruntke, U. Wandinger, I. Mattis, and D. Müller. Evolution of the ice phase in tropical altocumulus: SAMUM lidar observations over Cape Verde. *Journal of Geophysical Research: Atmospheres*, 114(D17), 2009. doi:10.1029/2008JD011659.

A. Avramov and J. Y. Harrington. Influence of parameterized ice habit on simulated mixed phase Arctic clouds. *Journal of Geophysical Research: Atmospheres*, 115 (D3), 2010. doi:10.1029/2009JD012108.

M. P. Bailey and J. Hallett. A comprehensive habit diagram for atmospheric ice crystals: Confirmation from the laboratory, AIRS II, and other field studies. *Journal of the Atmospheric Sciences*, 66(9):2888–2899, 2009. doi:10.1175/2009JAS2883.1.

A. I. Barrett, R. J. Hogan, and R. M. Forbes. Why are mixed-phase altocumulus clouds poorly predicted by large-scale models? Part 2. Vertical resolution sensitivity and parameterization. *Journal of Geophysical Research: Atmospheres*, 122 (18):9927–9944, 2017. doi:10.1002/2016JD026322.

A. I. Barrett, C. D. Westbrook, J. C. Nicol, and T. H. M. Stein. Rapid ice aggregation process revealed through triple-wavelength Doppler spectrum radar analysis. *Atmospheric Chemistry and Physics*, 19(8):5753–5769, 2019. doi:10.5194/acp-19-5753-2019.

P. A. Barrett, A. Blyth, P. R. Brown, and S. J. Abel. The structure of turbulence and mixed-phase cloud microphysics in a highly supercooled altocumulus cloud. *Atmospheric Chemistry and Physics*, 20(4):1921–1939, 2020. doi:10.5194/acp-20-1921-2020.

E. Barthazy, W. Henrich, and A. Waldvogel. Size distribution of hydrometeors through the melting layer. *Atmospheric Research*, 47-48:193–208, 1998. doi:10.1016/S0169-8095(98)00065-9.

A. Battaglia, S. Tanelli, F. Tridon, S. Kneifel, J. Leinonen, and P. Kollias. Triple-Frequency Radar Retrievals. In V. Levizzani, C. Kidd, D. B. Kirschbaum, C. D. Kummerow, K. Nakamura, and F. J. Turk, editors, *Satellite Precipitation Measurement: volume 1*, pages 211–229. Springer International Publishing, Cham, 2020. doi:10.1007/978-3-030-24568-9_13.

J. Bec, L. Biferale, M. Cencini, A. Lanotte, S. Musacchio, and F. Toschi. Heavy particle concentration in turbulence at dissipative and inertial scales. *Physical Review Letters*, 98(8):084502, 2007. doi:10.1103/PhysRevLett.98.084502.

R. Bechini, L. Baldini, and V. Chandrasekar. Polarimetric radar observations in the ice region of precipitating clouds at C-band and X-band radar frequencies. *Journal of Applied Meteorology and Climatology*, 52(5):1147–1169, 2013. doi:10.1175/JAMC-D-12-055.1.

T. Bergeron. On the physics of clouds and precipitation. *Proc. 5th Assembly UGGI, Lisbon, Portugal, 1935*, pages 156–180, 1935.

G. Bertens, G. Bagheri, H. Xu, E. Bodenschatz, and J. Moláček. In situ cloud particle tracking experiment. *Review of Scientific Instruments*, 92(12):125105, 2021. doi:10.1063/5.0065806.

G. P. Bewley, E.-W. Saw, and E. Bodenschatz. Observation of the sling effect. *New Journal of Physics*, 15(8):083051, 2013. doi:10.1088/1367-2630/15/8/083051.

A.-C. Billault-Roux, P. Georgakaki, J. Gehring, L. Jaffeux, A. Schwarzenboeck, P. Coutris, A. Nenes, and A. Berne. Distinct secondary ice production processes observed in radar Doppler spectra: insights from a case study. *Atmospheric Chemistry and Physics*, 23(17):10207–10234, 2023. doi:10.5194/acp-23-10207-2023.

A. Bodas-Salcedo, K. D. Williams, M. A. Ringer, I. Beau, J. N. Cole, J.-L. Dufresne, T. Koshiro, B. Stevens, Z. Wang, and T. Yokohata. Origins of the solar radiation biases over the Southern Ocean in CFMIP2 models. *Journal of Climate*, 27(1): 41–56, 2014. doi:10.1175/JCLI-D-13-00169.1.

A. Bodas-Salcedo, P. G. Hill, K. Furtado, K. D. Williams, P. R. Field, J. C. Manners, P. Hyder, and S. Kato. Large Contribution of Supercooled Liquid Clouds to the Solar Radiation Budget of the Southern Ocean. *Journal of Climate*, 29(11):4213–4228, 2016. doi:10.1175/JCLI-D-15-0564.1.

J. P. Böhm. A general hydrodynamic theory for mixed-phase microphysics. Part I: Drag and fall speed of hydrometeors. *Atmospheric research*, 27(4):253–274, 1992. doi:10.1016/0169-8095(92)90035-9.

C. F. Bohren and D. R. Huffman. *Absorption and scattering of light by small particles*. John Wiley & Sons, Ltd, 1998. doi:10.1002/9783527618156.

P. Borque, E. Luke, and P. Kollias. On the unified estimation of turbulence eddy dissipation rate using Doppler cloud radars and lidars. *Journal of Geophysical Research: Atmospheres*, 121(10):5972–5989, 2016. doi:10.1002/2015JD024543.

D. Bouniol, A. Illingworth, and R. Hogan. Deriving turbulent kinetic energy dissipation rate within clouds using ground based radar. In *Proceedings of ERAD*, pages 281–285. Copernicus GmbH, 2004. URL `https://www.copernicus.org/erad/2004/online/ERAD04_P_281.pdf`.

S. Brdar and A. Seifert. McSnow: A Monte-Carlo particle model for riming and aggregation of ice particles in a multidimensional microphysical phase space. *Journal of Advances in Modeling Earth Systems*, 10(1):187–206, 2018. doi:10.1002/2017MS001167.

F.-M. Bréon and B. Dubrulle. Horizontally oriented plates in clouds. *Journal of the Atmospheric Sciences*, 61(23):2888–2898, 2004. doi:10.1175/JAS-3309.1.

B. Brümmer. Roll and Cell Convection in Wintertime Arctic Cold-Air Outbreaks. *Journal of the Atmospheric Sciences*, 56(15):2613 – 2636, 1999. doi:10.1175/1520-0469(1999)056<2613:RACCIW>2.0.CO;2.

J. Bühl, P. Seifert, A. Myagkov, and A. Ansmann. Measuring ice-and liquid-water properties in mixed-phase cloud layers at the Leipzig Cloudnet station. *Atmospheric Chemistry and Physics*, 16(16):10609–10620, 2016. doi:10.5194/acp-16-10609-2016.

D. Chapman and K. Browning. Measurements of dissipation rate in frontal zones. *Quarterly Journal of the Royal Meteorological Society*, 127(576):1939–1959, 2001. doi:10.1002/qj.49712757605.

R. J. Chase, J. A. Finlon, P. Borque, G. M. McFarquhar, S. W. Nesbitt, S. Tanelli, O. O. Sy, S. L. Durden, and M. R. Poellot. Evaluation of triple-frequency radar retrieval of snowfall properties using coincident airborne in situ observations during OLYMPEX. *Geophysical Research Letters*, 45(11):5752–5760, 2018. doi:10.1029/2018GL077997.

G. Chellini, R. Gierens, and S. Kneifel. Ice Aggregation in Low-Level Mixed-Phase Clouds at a High Arctic Site: Enhanced by Dendritic Growth and Absent Close to the Melting Level. *Journal of Geophysical Research: Atmospheres*, 127(16): e2022JD036860, 2022. doi:10.1029/2022JD036860.

G. Chellini, R. Gierens, K. Ebell, T. Kiszler, P. Krobot, A. Myagkov, V. Schemann, and S. Kneifel. Low-level mixed-phase clouds at the high Arctic site of Ny-Ålesund: A comprehensive long-term dataset of remote sensing observations. *Earth System Science Data Discussions*, 2023:1–33, 2023. doi:10.5194/essd-2023-157.

T. Choularton, D. Griggs, B. Humood, and J. Latham. Laboratory studies of riming, and its relation to ice splinter production. *Quarterly Journal of the Royal Meteorological Society*, 106(448):367–374, 1980. doi:10.1002/qj.49710644809.

R. J. Clausius. *Die mechanische Wärmetheorie: Die mechanische Behandlung der Electricität*, volume 2. Vieweg, 1879.

J. Cohen, X. Zhang, J. Francis, T. Jung, R. Kwok, J. Overland, T. Ballinger, U. Bhatt, H. Chen, D. Coumou, et al. Divergent consensuses on Arctic amplification influence on midlatitude severe winter weather. *Nature Climate Change*, 10(1):20–29, 2020. doi:10.1038/s41558-019-0662-y.

P. Connolly, C. Emersic, and P. Field. A laboratory investigation into the aggregation efficiency of small ice crystals. *Atmospheric Chemistry and Physics*, 12(4): 2055–2076, 2012. doi:10.5194/acp-12-2055-2012.

P. J. Connolly, C. P. R. Saunders, M. W. Gallagher, K. N. Bower, M. J. Flynn, T. W. Choularton, J. Whiteway, and R. P. Lawson. Aircraft observations of the influence of electric fields on the aggregation of ice crystals. *Quarterly Journal of the Royal Meteorological Society*, 131(608):1695–1712, 2005. doi:10.1256/qj.03.217.

W. A. Cooper. *Ice Initiation in Natural Clouds*, pages 29–32. American Meteorological Society, Boston, MA, 1986. doi:10.1007/978-1-935704-17-1_4.

W. R. Cotton, G. J. Tripoli, R. M. Rauber, and E. A. Mulvihill. Numerical Simulation of the Effects of Varying Ice Crystal Nucleation Rates and Aggregation Processes on Orographic Snowfall. *Journal of Applied Meteorology and Climatology*, 25(11):1658 – 1680, 1986. doi:10.1175/1520-0450(1986)025<1658:NSOTEO>2.0.CO;2.

I. Crawford, K. Bower, T. Choularton, C. Dearden, J. Crosier, C. Westbrook, G. Capes, H. Coe, P. Connolly, J. Dorsey, et al. Ice formation and development in aged, wintertime cumulus over the UK: observations and modelling. *Atmospheric Chemistry and Physics*, 12(11):4963–4985, 2012. doi:10.5194/acp-12-4963-2012.

S. Crewell and U. Löhnert. Accuracy of boundary layer temperature profiles retrieved with multifrequency multiangle microwave radiometry. *IEEE Transactions on Geoscience and Remote Sensing*, 45(7):2195–2201, 2007. doi:10.1109/TGRS.2006.888434.

T. W. Cronin and E. Tziperman. Low clouds suppress Arctic air formation and amplify high-latitude continental winter warming. *Proceedings of the National Academy of Sciences*, 112(37):11490–11495, 2015. doi:10.1073/pnas.1510937112.

J. Crosier, K. Bower, T. Choularton, C. D. Westbrook, P. Connolly, Z. Cui, I. Crawford, G. Capes, H. Coe, J. Dorsey, et al. Observations of ice multiplication in a weakly convective cell embedded in supercooled mid-level stratus. *Atmospheric Chemistry and Physics*, 11(1):257–273, 2011. doi:10.5194/acp-11-257-2011.

J. A. Curry, J. L. Schramm, W. B. Rossow, and D. Randall. Overview of Arctic cloud and radiation characteristics. *Journal of Climate*, 9(8):1731–1764, 1996. doi:10.1175/1520-0442(1996)009<1731:OOACAR>2.0.CO;2.

S. Dahlke and M. Maturilli. Contribution of Atmospheric Advection to the Amplified Winter Warming in the Arctic North Atlantic Region. *Advances in Meteorology*, 2017. doi:10.1155/2017/4928620.

G. De Boer, H. Morrison, M. Shupe, and R. Hildner. Evidence of liquid dependent ice nucleation in high-latitude stratiform clouds from surface remote sensors. *Geophysical Research Letters*, 38(1), 2011. doi:10.1029/2010GL046016.

J. W. Deardorff. On the distribution of mean radiative cooling at the top of a stratocumulus-capped mixed layer. *Quarterly Journal of the Royal Meteorological Society*, 107(451):191–202, 1981. doi:10.1002/qj.49710745112.

P. J. DeMott, A. J. Prenni, G. R. McMeeking, R. C. Sullivan, M. D. Petters, Y. Tobo, M. Niemand, O. Möhler, J. R. Snider, Z. Wang, et al. Integrating laboratory and field data to quantify the immersion freezing ice nucleation activity of mineral dust particles. *Atmospheric Chemistry and Physics*, 15(1): 393–409, 2015. doi:10.5194/acp-15-393-2015.

R. Dhariwal and A. D. Bragg. Small-scale dynamics of settling, bidisperse particles in turbulence. *Journal of Fluid Mechanics*, 839:594–620, 2018. doi:10.1017/jfm.2018.24.

J. Dias Neto. *Investigating aggregation in ice and snow clouds using novel combination of triple-frequency cloud radars and radar Doppler spectra*. PhD thesis, Universität zu Köln, Cologne, 2021. URL `https://kups.ub.uni-koeln.de/53405/`.

J. Dias Neto, S. Kneifel, D. Ori, S. Trömel, J. Handwerker, B. Bohn, N. Hermes, K. Mühlbauer, M. Lenefer, and C. Simmer. The TRIple-frequency and Polarimetric radar Experiment for improving process observations of winter precipitation. *Earth System Science Data*, 11(2):845–863, 2019. doi:10.5194/essd-11-845-2019.

X. Dong and G. G. Mace. Arctic stratus cloud properties and radiative forcing derived from ground-based data collected at Barrow, Alaska. *Journal of Climate*, 16(3):445–461, 2003. doi:10.1175/1520-0442(2003)016<0445:ASCPAR>2.0.CO;2.

R. J. Doviak and D. S. Zrnić. *Doppler radar and weather observations*. Academic Press, Inc., first edition, 1984.

F. J. Drummond, R. R. Rogers, S. A. Cohn, W. L. Ecklund, D. A. Carter, and J. S. Wilson. A New Look at the Melting Layer. *Journal of Atmospheric Sciences*, 53 (5):759 – 769, 1996. doi:10.1175/1520-0469(1996)053<0759:ANLATM>2.0.CO;2.

K. Ebell, T. Nomokonova, M. Maturilli, and C. Ritter. Radiative Effect of Clouds at Ny-Ålesund, Svalbard, as Inferred from Ground-Based Remote Sensing Observations. *Journal of Applied Meteorology and Climatology*, 59(1):3–22, 2020. doi:10.1175/JAMC-D-19-0080.1.

G. K. Eirund, U. Lohmann, and A. Possner. Cloud ice processes enhance spatial scales of organization in Arctic stratocumulus. *Geophysical Research Letters*, 46 (23):14109–14117, 2019. doi:10.1029/2019GL084959.

F. Fabry. *Radar Meteorology: Principles and Practice*. Cambridge University Press, 2015. doi:10.1017/CBO9781107707405.

F. Fabry and I. Zawadzki. Long-term radar observations of the melting layer of precipitation and their interpretation. *Journal of Atmospheric Sciences*, 52(7): 838–851, 1995. doi:10.1175/1520-0469(1995)052<0838:LTROOT>2.0.CO;2.

G. Falkovich and A. Pumir. Sling effect in collisions of water droplets in turbulent clouds. *Journal of the Atmospheric Sciences*, 64(12):4497–4505, 2007. doi:10.1175/2007JAS2371.1.

G. Falkovich, A. Fouxon, and M. G. Stepanov. Acceleration of rain initiation by cloud turbulence. *Nature*, 419(6903):151–154, 2002. doi:10.1038/nature00983.

M. Fang, B. A. Albrecht, V. P. Ghate, and P. Kollias. Turbulence in continental stratocumulus, Part II: Eddy dissipation rates and large-eddy coherent structures. *Boundary-layer meteorology*, 150:361–380, 2014. doi:10.1007/s10546-013-9872-4.

M. M. Feist, C. D. Westbrook, P. A. Clark, T. H. Stein, H. W. Lean, and A. J. Stirling. Statistics of convective cloud turbulence from a comprehensive turbulence retrieval method for radar observations. *Quarterly Journal of the Royal Meteorological Society*, 145(719):727–744, 2019. doi:10.1002/qj.3462.

A. Fick. Ueber Diffusion. *Annalen der Physik*, 170(1):59–86, 1855. doi:10.1002/andp.18551700105.

Z. Findeisen. Die kolloidmeteorologischen Vorgänge bei der Niederschlagsbildung. *Meteorologische Zeitschrift*, 55:121–133, 1938.

R. P. Fleishauer, V. E. Larson, and T. H. V. Haar. Observed Microphysical Structure of Midlevel, Mixed-Phase Clouds. *Journal of the Atmospheric Sciences*, 59(11): 1779–1804, 2002. doi:10.1175/1520-0469(2002)059<1779:OMSOMM>2.0.CO;2.

N. H. Fletcher. *The physics of rainclouds*. Cambridge University Press, 1962a.

N. H. Fletcher. Surface structure of water and ice. *Philosophical Magazine*, 7(74): 255–269, 1962b. doi:10.1080/14786436208211860.

A. Frisch and S. Clifford. A study of convection capped by a stable layer using Doppler radar and acoustic echo sounders. *Journal of Atmospheric Sciences*, 31 (6):1622–1628, 1974. doi:10.1175/1520-0469(1974)031<1622:ASOCCB>2.0.CO;2.

K. Furtado and P. Field. The Role of Ice Microphysics Parametrizations in Determining the Prevalence of Supercooled Liquid Water in High-Resolution Simulations of a Southern Ocean Midlatitude Cyclone. *Journal of the Atmospheric Sciences*, 74(6):2001 – 2021, 2017. doi:10.1175/JAS-D-16-0165.1.

K. Furtado, P. R. Field, I. A. Boutle, C. J. Morcrette, and J. M. Wilkinson. A Physically Based Subgrid Parameterization for the Production and Maintenance of Mixed-Phase Clouds in a General Circulation Model. *Journal of the Atmospheric Sciences*, 73(1):279 – 291, 2016. doi:10.1175/JAS-D-15-0021.1.

J. Gehring, A. Oertel, É. Vignon, N. Jullien, N. Besic, and A. Berne. Microphysics and dynamics of snowfall associated with a warm conveyor belt over Korea. *Atmospheric Chemistry and Physics*, 20(12):7373–7392, 2020. doi:10.5194/acp-20-7373-2020.

J. Gehring, É. Vignon, A.-C. Billault-Roux, A. Ferrone, A. Protat, S. P. Alexander, and A. Berne. Orographic Flow Influence on Precipitation During an Atmospheric River Event at Davis, Antarctica. *Journal of Geophysical Research: Atmospheres*, 127(2):e2021JD035210, 2022. doi:10.1029/2021JD035210.

P. Georgakaki, G. Sotiropoulou, É. Vignon, A.-C. Billault-Roux, A. Berne, and A. Nenes. Secondary ice production processes in wintertime alpine mixed-phase clouds. *Atmospheric Chemistry and Physics*, 22(3):1965–1988, 2022. doi:10.5194/acp-22-1965-2022.

R. Gierens. *Observations of Arctic low-level mixed-phase clouds at Ny-Ålesund: Characterization and insights gained by high-resolution Doppler radar*. PhD thesis, Universität zu Köln, Köln, 2021. URL `https://kups.ub.uni-koeln.de/53900/`.

H. Goosse, J. E. Kay, K. C. Armour, A. Bodas-Salcedo, H. Chepfer, D. Docquier, A. Jonko, P. J. Kushner, O. Lecomte, F. Massonnet, H.-S. Park, et al. Quantifying climate feedbacks in polar regions. *Nature Communications*, 9(1):1919, 2018. doi:10.1038/s41467-018-04173-0.

J. Grazioli, G. Lloyd, L. Panziera, C. R. Hoyle, P. J. Connolly, J. Henneberger, and A. Berne. Polarimetric radar and in situ observations of riming and snowfall microphysics during CLACE 2014. *Atmospheric Chemistry and Physics*, 15(23): 13787–13802, 2015. doi:10.5194/acp-15-13787-2015.

E. M. Griffin, T. J. Schuur, and A. V. Ryzhkov. A polarimetric analysis of ice microphysical processes in snow, using quasi-vertical profiles. *Journal of Applied Meteorology and Climatology*, 57(1):31–50, 2018. doi:10.1175/JAMC-D-17-0033.1.

P. Grzegorczyk, S. Yadav, F. Zanger, A. Theis, S. K. Mitra, S. Borrmann, and M. Szakáll. Fragmentation of ice particles: laboratory experiments on graupel–graupel and graupel–snowflake collisions. *Atmospheric Chemistry and Physics*, 23(20):13505–13521, 2023. doi:10.5194/acp-23-13505-2023.

I. Gultepe and D. O. Starr. Dynamical structure and turbulence in cirrus clouds: Aircraft observations during FIRE. *Journal of Atmospheric Sciences*, 52(23): 4159–4182, 1995. doi:10.1175/1520-0469(1995)052<4159:DSATIC>2.0.CO;2.

K. Gustavsson, J. Jucha, A. Naso, E. Lévêque, A. Pumir, and B. Mehlig. Statistical model for the orientation of nonspherical particles settling in turbulence. *Physical Review Letters*, 119(25):254501, 2017. doi:10.1103/PhysRevLett.119.254501.

K. Gustavsson, M. Sheikh, A. Naso, A. Pumir, and B. Mehlig. Effect of particle inertia on the alignment of small ice crystals in turbulent clouds. *Journal of the Atmospheric Sciences*, 78(8):2573–2587, 2021. doi:10.1175/JAS-D-20-0221.1.

J. Hallett and S. Mossop. Production of secondary ice particles during the riming process. *Nature*, 249(5452):26–28, 1974. doi:10.1038/249026a0.

L. Hande, C. Engler, C. Hoose, and I. Tegen. Seasonal variability of Saharan desert dust and ice nucleating particles over Europe. *Atmospheric Chemistry and Physics*, 15(8):4389–4397, 2015. doi:10.5194/acp-15-4389-2015.

L. B. Hande and C. Hoose. Partitioning the primary ice formation modes in large eddy simulations of mixed-phase clouds. *Atmospheric Chemistry and Physics*, 17 (22):14105–14118, 2017. doi:10.5194/acp-17-14105-2017.

J. Y. Harrington and P. Q. Olsson. On the potential influence of ice nuclei on surface-forced marine stratocumulus cloud dynamics. *Journal of Geophysical Research: Atmospheres*, 106(D21):27473–27484, 2001. doi:10.1029/2000JD000236.

J. Henneberger, J. P. Fugal, O. Stetzer, and U. Lohmann. HOLIMO II: a digital holographic instrument for ground-based in situ observations of microphysical properties of mixed-phase clouds. *Atmospheric Measurement Techniques*, 6(11): 2975–2987, 2013. doi:10.5194/amt-6-2975-2013.

A. Heymsfield and P. Willis. Cloud conditions favoring secondary ice particle production in tropical maritime convection. *Journal of the Atmospheric Sciences*, 71(12):4500–4526, 2014. doi:10.1175/JAS-D-14-0093.1.

A. J. Heymsfield and S. Mossop. Temperature dependence of secondary ice crystal production during soft hail growth by riming. *Quarterly Journal of the Royal Meteorological Society*, 110(465):765–770, 1984. doi:10.1002/qj.49711046512.

A. J. Heymsfield, A. Bansemer, M. R. Poellot, and N. Wood. Observations of Ice Microphysics through the Melting Layer. *Journal of the Atmospheric Sciences*, 72(8):2902 – 2928, 2015. doi:10.1175/JAS-D-14-0363.1.

R. J. Hogan and C. D. Westbrook. Equation for the microwave backscatter cross section of aggregate snowflakes using the self-similar Rayleigh–Gans approximation. *Journal of the Atmospheric Sciences*, 71(9):3292–3301, 2014. doi:10.1175/JAS-D-13-0347.1.

R. J. Hogan, A. J. Illingworth, and H. Sauvageot. Measuring crystal size in cirrus using 35- and 94-GHz radars. *Journal of Atmospheric and Oceanic Technology*, 17(1):27–37, 2000. doi:10.1175/1520-0426(2000)017<0027:MCSICU>2.0.CO;2.

H. Homann, T. Guillot, J. Bec, C. Ormel, S. Ida, and P. Tanga. Effect of turbulence on collisions of dust particles with planetesimals in protoplanetary disks. *Astronomy & Astrophysics*, 589:A129, 2016. doi:10.1051/0004-6361/201527344.

R. A. Houze and S. Medina. Turbulence as a Mechanism for Orographic Precipitation Enhancement. *Journal of the Atmospheric Sciences*, 62(10):3599–3623, 2005. doi:10.1175/JAS3555.1.

Y. Hu, S. Rodier, K.-m. Xu, W. Sun, J. Huang, B. Lin, P. Zhai, and D. Josset. Occurrence, liquid water content, and fraction of supercooled water clouds from combined CALIOP/IIR/MODIS measurements. *Journal of Geophysical Research: Atmospheres*, 115(D4), 2010. doi:10.1029/2009JD012384.

Y. Huang, S. T. Siems, M. J. Manton, A. Protat, and J. Delanoë. A study on the low-altitude clouds over the Southern Ocean using the DARDAR-MASK. *Journal of Geophysical Research: Atmospheres*, 117(D18), 2012. doi:10.1029/2012JD017800.

P. D. Huck, C. Bateson, R. Volk, A. Cartellier, M. Bourgoin, and A. Aliseda. The role of collective effects on settling velocity enhancement for inertial particles in turbulence. *Journal of Fluid Mechanics*, 846:1059–1075, 2018. doi:10.1017/jfm.2018.272.

P. Hyder, J. M. Edwards, R. P. Allan, H. T. Hewitt, T. J. Bracegirdle, J. M. Gregory, R. A. Wood, A. J. Meijers, J. Mulcahy, P. Field, et al. Critical Southern Ocean climate model biases traced to atmospheric model cloud errors. *Nature Communications*, 9(1):3625, 2018. doi:10.1038/s41467-018-05634-2.

A. Illingworth, R. Hogan, E. O'Connor, D. Bouniol, M. Brooks, J. Delanoë, D. Donovan, J. Eastment, N. Gaussiat, J. Goddard, et al. Cloudnet: Continuous evaluation of cloud profiles in seven operational models using ground-based observations. *Bulletin of the American Meteorological Society*, 88(6):883–898, 2007. doi:10.1175/BAMS-88-6-883.

J. D. Jackson. *Classical electrodynamics*. Wiley, 1975.

W. Ji and P. K. Wang. Ventilation Coefficients for Falling Ice Crystals in the Atmosphere at Low–Intermediate Reynolds Numbers. *Journal of the Atmospheric Sciences*, 56(6):829 – 836, 1999. doi:10.1175/1520-0469(1999)056<0829:VCFFIC>2.0.CO;2.

J. E. Jiusto and H. Weickmann. Types of snowfall. *Bulletin of the American Meteorological Society*, 54(11):1148–1162, 1973. doi:10.1175/1520-0477(1973)054<1148:TOS>2.0.CO;2.

H. Kalesse, P. Kollias, and W. Szyrmer. On using the relationship between Doppler velocity and radar reflectivity to identify microphysical processes in midlatitudinal ice clouds. *Journal of Geophysical Research: Atmospheres*, 118(21):12–168, 2013. doi:10.1002/2013JD020386.

T. Kanitz, P. Seifert, A. Ansmann, R. Engelmann, D. Althausen, C. Casiccia, and E. Rohwer. Contrasting the impact of aerosols at northern and southern midlatitudes on heterogeneous ice formation. *Geophysical Research Letters*, 38 (17), 2011. doi:10.1029/2011GL048532.

Z. A. Kanji, L. A. Ladino, H. Wex, Y. Boose, M. Burkert-Kohn, D. J. Cziczo, and M. Krämer. Overview of ice nucleating particles. *Meteorological Monographs*, 58: 1–1, 2017. doi:10.1175/AMSMONOGRAPHS-D-16-0006.1.

M. Karrer, A. Seifert, C. Siewert, D. Ori, A. von Lerber, and S. Kneifel. Ice Particle Properties Inferred From Aggregation Modelling. *Journal of Advances in Modeling Earth Systems*, 12(8):e2020MS002066, 2020. doi:10.1029/2020MS002066.

M. Karrer, A. Seifert, D. Ori, and S. Kneifel. Improving the representation of aggregation in a two-moment microphysical scheme with statistics of multi-frequency Doppler radar observations. *Atmospheric Chemistry and Physics*, 21 (22):17133–17166, 2021. doi:10.5194/acp-21-17133-2021.

M. Karrer, J. Dias Neto, L. von Terzi, and S. Kneifel. Melting Behavior of Rimed and Unrimed Snowflakes Investigated With Statistics of Triple-Frequency Doppler Radar Observations. *Journal of Geophysical Research: Atmospheres*, 127(9): e2021JD035907, 2022. doi:10.1029/2021JD035907.

A. Khain, K. Beheng, A. Heymsfield, A. Korolev, S. Krichak, Z. Levin, M. Pinsky, V. Phillips, T. Prabhakaran, A. Teller, et al. Representation of microphysical processes in cloud-resolving models: Spectral (bin) microphysics versus bulk parameterization. *Reviews of Geophysics*, 53(2):247–322, 2015. doi:10.1002/2014RG000468.

M. D. King, S. Platnick, W. P. Menzel, S. A. Ackerman, and P. A. Hubanks. Spatial and temporal distribution of clouds observed by MODIS onboard the Terra and Aqua satellites. *IEEE Transactions on Geoscience and Remote Sensing*, 51(7): 3826–3852, 2013. doi:10.1109/TGRS.2012.2227333.

T. Kiszler, K. Ebell, and V. Schemann. A Performance Baseline for the Representation of Clouds and Humidity in Cloud-Resolving ICON-LEM Simulations in the Arctic. *Journal of Advances in Modeling Earth Systems*, 15(5):e2022MS003299, 2023. doi:10.1029/2022MS003299.

S. Kneifel and D. Moisseev. Long-Term Statistics of Riming in Nonconvective Clouds Derived from Ground-Based Doppler Cloud Radar Observations. *Journal of the Atmospheric Sciences*, 77(10):3495–3508, 2020. doi:10.1175/JAS-D-20-0007.1.

S. Kneifel, A. Lerber, J. Tiira, D. Moisseev, P. Kollias, and J. Leinonen. Observed relations between snowfall microphysics and triple-frequency radar measurements. *Journal of Geophysical Research: Atmospheres*, 120(12):6034–6055, 2015. doi:10.1002/2015JD023156.

S. Kneifel, P. Kollias, A. Battaglia, J. Leinonen, M. Maahn, H. Kalesse, and F. Tridon. First observations of triple-frequency radar Doppler spectra in snowfall: Interpretation and applications. *Geophysical Research Letters*, 43(5):2225–2233, 2016. doi:10.1002/2015GL067618.

P. Kollias, B. Albrecht, R. Lhermitte, and A. Savtchenko. Radar observations of updrafts, downdrafts, and turbulence in fair-weather cumuli. *Journal of the Atmospheric Sciences*, 58(13):1750–1766, 2001. doi:10.1175/1520-0469(2001)058<1750:ROOUDA>2.0.CO;2.

P. Kollias, B. Albrecht, and F. Marks Jr. Why Mie? Accurate observations of vertical air velocities and raindrops using a cloud radar. *Bulletin of the American Meteorological Society*, 83(10):1471–1484, 2002. doi:10.1175/BAMS-83-10-1471.

P. Kollias, E. Clothiaux, M. Miller, B. Albrecht, G. Stephens, and T. Ackerman. Millimeter-wavelength radars: New frontier in atmospheric cloud and precipitation research. *Bulletin of the American Meteorological Society*, 88(10):1608–1624, 2007. doi:10.1175/BAMS-88-10-1608.

P. Kollias, J. Rémillard, E. Luke, and W. Szyrmer. Cloud radar Doppler spectra in drizzling stratiform clouds: 1. Forward modeling and remote sensing applications. *Journal of Geophysical Research: Atmospheres*, 116(D13), 2011. doi:10.1029/2010JD015237.

A. N. Kolmogorov. Dissipation of energy in the locally isotropic turbulence. In *Doklady Akademii Nauk SSSR*, volume 32, pages 19–21, 1941a.

A. N. Kolmogorov. The local structure of turbulence in incompressible viscous fluid for very large reynolds numbers. In *Doklady Akademii Nauk SSSR*, volume 30, pages 301–305, 1941b.

A. Korolev and T. Leisner. Review of experimental studies of secondary ice production. *Atmospheric Chemistry and Physics*, 20(20):11767–11797, 2020. doi:10.5194/acp-20-11767-2020.

A. Korolev, M. P. Bailey, J. Hallett, and G. A. Isaac. Laboratory and in situ observation of deposition growth of frozen drops. *Journal of Applied Meteorology and Climatology*, 43(4):612–622, 2004. doi:10.1175/1520-0450(2004)043<0612:LAISOO>2.0.CO;2.

A. Korolev, G. McFarquhar, P. R. Field, C. Franklin, P. Lawson, Z. Wang, E. Williams, S. J. Abel, D. Axisa, S. Borrmann, et al. Mixed-phase clouds: Progress and challenges. *Meteorological Monographs*, 58:5–1, 2017. doi:10.1175/AMSMONOGRAPHS-D-17-0001.1.

A. Korolev, I. Heckman, M. Wolde, A. S. Ackerman, A. M. Fridlind, L. A. Ladino, R. P. Lawson, J. Milbrandt, and E. Williams. A new look at the environmental conditions favorable to secondary ice production. *Atmospheric Chemistry and Physics*, 20(3):1391–1429, 2020. doi:10.5194/acp-20-1391-2020.

J. Kretzschmar, J. Stapf, D. Klocke, M. Wendisch, and J. Quaas. Employing airborne radiation and cloud microphysics observations to improve cloud representation in ICON at kilometer-scale resolution in the Arctic. *Atmospheric Chemistry and Physics*, 20(21):13145–13165, 2020. doi:10.5194/acp-20-13145-2020.

N. Küchler, S. Kneifel, U. Löhnert, P. Kollias, H. Czekala, and T. Rose. A W-Band Radar–Radiometer System for Accurate and Continuous Monitoring of Clouds and Precipitation. *Journal of Atmospheric and Oceanic Technology*, 34(11): 2375–2392, 2017. doi:10.1175/JTECH-D-17-0019.1.

M. R. Kumjian. Weather Radars. In C. Andronache, editor, *Remote Sensing of Clouds and Precipitation*, pages 15–63. Springer International Publishing, Cham, 2018. doi:10.1007/978-3-319-72583-3_2.

M. Labitt. Coordinated radar and aircraft observations of turbulence. Technical report, Massachusetts Institute of Technology Lincoln Laboratory, 1981. URL `https://apps.dtic.mil/sti/citations/ADA114708`.

D. Lamb and J. Verlinde. *Physics and Chemistry of Clouds*. Cambridge University Press, 2011. doi:10.1017/CBO9780511976377.

S. Lasher-Trapp, D. C. Leon, P. J. DeMott, C. M. Villanueva-Birriel, A. V. Johnson, D. H. Moser, C. S. Tully, and W. Wu. A multisensor investigation of rime splintering in tropical maritime cumuli. *Journal of the Atmospheric Sciences*, 73 (6):2547–2564, 2016. doi:10.1175/JAS-D-15-0285.1.

J. Latham and C. Saunders. The electrostatic forces on charged ice crystals separated by small distances in an electric field. *Quarterly Journal of the Royal Meteorological Society*, 96(408):266–272, 1970. doi:10.1002/qj.49709640809.

A. Lauber, A. Kiselev, T. Pander, P. Handmann, and T. Leisner. Secondary ice formation during freezing of levitated droplets. *Journal of the Atmospheric Sciences*, 75(8):2815–2826, 2018. doi:10.1175/JAS-D-18-0052.1.

P. Lawson, C. Gurganus, S. Woods, and R. Bruintjes. Aircraft observations of cumulus microphysics ranging from the tropics to midlatitudes: Implications for a "new" secondary ice process. *Journal of the Atmospheric Sciences*, 74(9): 2899–2920, 2017. doi:10.1175/JAS-D-17-0033.1.

R. P. Lawson and A. Gettelman. Impact of Antarctic mixed-phase clouds on climate. *Proceedings of the National Academy of Sciences*, 111(51):18156–18161, 2014. doi:10.1073/pnas.1418197111.

K. Lehmann, H. Siebert, M. Wendisch, and R. A. Shaw. Evidence for inertial droplet clustering in weakly turbulent clouds. *Tellus B: Chemical and Physical Meteorology*, 59(1):57–65, 2007. doi:10.1111/j.1600-0889.2006.00229.x.

C. Li, K. Lim, T. Berk, A. Abraham, M. Heisel, M. Guala, F. Coletti, and J. Hong. Settling and clustering of snow particles in atmospheric turbulence. *Journal of Fluid Mechanics*, 912:A49, 2021a. doi:10.1017/jfm.2020.1153.

H. Li, O. Möhler, T. Petäjä, and D. Moisseev. Two-year statistics of columnar-ice production in stratiform clouds over Hyytiälä, Finland: environmental conditions and the relevance to secondary ice production. *Atmospheric Chemistry and Physics*, 21(19):14671–14686, 2021b. doi:10.5194/acp-21-14671-2021.

J. Li, A. Abraham, M. Guala, and J. Hong. Evidence of preferential sweeping during snow settling in atmospheric turbulence. *Journal of Fluid Mechanics*, 928: A8, 2021c. doi:10.1017/jfm.2021.816.

L. Liao, R. Meneghini, T. Iguchi, and A. Detwiler. Use of dual-wavelength radar for snow parameter estimates. *Journal of Atmospheric and Oceanic Technology*, 22(10):1494–1506, 2005. doi:10.1175/JTECH1808.1.

Y. Lin and B. A. Colle. The 4–5 December 2001 IMPROVE-2 Event: Observed Microphysics and Comparisons with the Weather Research and Forecasting Model. *Monthly Weather Review*, 137(4):1372 – 1392, 2009. doi:10.1175/2008MWR2653.1.

Y.-L. Lin, R. D. Farley, and H. D. Orville. Bulk parameterization of the snow field in a cloud model. *Journal of Applied Meteorology and Climatology*, 22(6): 1065–1092, 1983. doi:10.1175/1520-0450(1983)022<1065:BPOTSF>2.0.CO;2.

C. Listowski, J. Delanoë, A. Kirchgaessner, T. Lachlan-Cope, and J. King. Antarctic clouds, supercooled liquid water and mixed phase, investigated with DARDAR: Geographical and seasonal variations. *Atmospheric Chemistry and Physics*, 19 (10):6771–6808, 2019. doi:10.5194/acp-19-6771-2019.

J. D. Locatelli and P. V. Hobbs. Fall speeds and masses of solid precipitation particles. *Journal of Geophysical Research*, 79(15):2185–2197, 1974. doi:10.1029/JC079i015p02185.

U. Lohmann, F. Lüönd, and F. Mahrt. *An Introduction to Clouds: From the Microscale to Climate*. Cambridge University Press, 2016. doi:10.1017/CBO9781139087513.

Y. Lu, E. E. Clothiaux, K. Aydin, G. Botta, and J. Verlinde. Modeling variability in dendritic ice crystal backscattering cross sections at millimeter wavelengths using a modified Rayleigh–Gans theory. *Journal of Quantitative Spectroscopy and Radiative Transfer*, 131:95–104, 2013. doi:10.1016/j.jqsrt.2013.05.008.

Y. Lu, K. Aydin, E. E. Clothiaux, and J. Verlinde. Retrieving cloud ice water content using millimeter-and centimeter-wavelength radar polarimetric observables. *Journal of Applied Meteorology and Climatology*, 54(3):596–604, 2015. doi:10.1175/JAMC-D-14-0169.1.

D. Lubin, D. Zhang, I. Silber, R. C. Scott, P. Kalogeras, A. Battaglia, D. H. Bromwich, M. Cadeddu, E. Eloranta, A. Fridlind, et al. AWARE: The atmospheric radiation measurement (ARM) west Antarctic radiation experiment. *Bulletin of the American Meteorological Society*, 101(7):E1069–E1091, 2020. doi:10.1175/BAMS-D-18-0278.1.

E. P. Luke and P. Kollias. Separating Cloud and Drizzle Radar Moments during Precipitation Onset Using Doppler Spectra. *Journal of Atmospheric and Oceanic Technology*, 30(8):1656 – 1671, 2013. doi:10.1175/JTECH-D-11-00195.1.

E. P. Luke, F. Yang, P. Kollias, A. M. Vogelmann, and M. Maahn. New insights into ice multiplication using remote-sensing observations of slightly supercooled

mixed-phase clouds in the Arctic. *Proceedings of the National Academy of Sciences*, 118(13), 2021. doi:10.1073/pnas.2021387118.

M. Maahn and P. Kollias. Improved Micro Rain Radar snow measurements using Doppler spectra post-processing. *Atmospheric Measurement Techniques*, 5(11): 2661–2673, 2012. doi:10.5194/amt-5-2661-2012.

M. Maahn, C. Burgard, S. Crewell, I. V. Gorodetskaya, S. Kneifel, S. Lhermitte, K. Van Tricht, and N. P. van Lipzig. How does the spaceborne radar blind zone affect derived surface snowfall statistics in polar regions? *Journal of Geophysical Research: Atmospheres*, 119(24):13–604, 2014. doi:10.1002/2014JD022079.

M. Maahn, D. Moisseev, I. Steinke, N. Maherndl, and M. D. Shupe. Introducing the Video In Situ Snowfall Sensor (VISSS). *Atmospheric Measurement Techniques*, 17(2):899–919, 2024. doi:10.5194/amt-17-899-2024.

A. V. Matus and T. S. L'Ecuyer. The role of cloud phase in Earth's radiation budget. *Journal of Geophysical Research: Atmospheres*, 122(5):2559–2578, 2017. doi:10.1002/2016JD025951.

M. R. Maxey. The gravitational settling of aerosol particles in homogeneous turbulence and random flow fields. *Journal of Fluid Mechanics*, 174:441–465, 1987. doi:10.1017/S0022112087000193.

M. R. Maxey and J. J. Riley. Equation of motion for a small rigid sphere in a nonuniform flow. *The Physics of Fluids*, 26(4):883–889, 1983. doi:10.1063/1.864230.

D. T. McCoy, D. L. Hartmann, M. D. Zelinka, P. Ceppi, and D. P. Grosvenor. Mixed-phase cloud physics and Southern Ocean cloud feedback in climate models. *Journal of Geophysical Research: Atmospheres*, 120(18):9539–9554, 2015. doi:10.1002/2015JD023603.

G. M. McFarquhar, C. S. Bretherton, R. Marchand, A. Protat, P. J. DeMott, S. P. Alexander, G. C. Roberts, C. H. Twohy, D. Toohey, S. Siems, et al. Observations of clouds, aerosols, precipitation, and surface radiation over the Southern Ocean: An overview of CAPRICORN, MARCUS, MICRE, and SOCRATES. *Bulletin of the American Meteorological Society*, 102(4):E894–E928, 2021. doi:10.1175/BAMS-D-20-0132.1.

S. Medina and R. A. Houze. Small-scale precipitation elements in midlatitude cyclones crossing the California Sierra Nevada. *Monthly Weather Review*, 143(7): 2842–2870, 2015. doi:10.1175/MWR-D-14-00124.1.

N. B. Miller, M. D. Shupe, C. J. Cox, V. P. Walden, D. D. Turner, and K. Steffen. Cloud Radiative Forcing at Summit, Greenland. *Journal of Climate*, 28(15): 6267–6280, 2015. doi:10.1175/JCLI-D-15-0076.1.

G. Mioche, O. Jourdan, M. Ceccaldi, and J. Delanoë. Variability of mixed-phase clouds in the Arctic with a focus on the Svalbard region: A study based on spaceborne active remote sensing. *Atmospheric Chemistry and Physics*, 15(5): 2445–2461, 2015. doi:10.5194/acp-15-2445-2015.

D. L. Mitchell. Evolution of snow-size spectra in cyclonic storms. Part I: Snow growth by vapor deposition and aggregation. *Journal of Atmospheric Sciences*, 45 (22):3431–3451, 1988. doi:10.1175/1520-0469(1988)045<3431:EOSSSI>2.0.CO;2.

D. L. Mitchell, P. Rasch, D. Ivanova, G. McFarquhar, and T. Nousiainen. Impact of small ice crystal assumptions on ice sedimentation rates in cirrus clouds and GCM simulations. *Geophysical Research Letters*, 35(9):L09806, 2008. doi:10.1029/2008GL033552.

M. Momenifar, R. Dhariwal, and A. D. Bragg. Influence of Reynolds number on the motion of settling, bidisperse inertial particles in turbulence. *Physical Review Fluids*, 4(5):054301, 2019. doi:10.1103/PhysRevFluids.4.054301.

R. Monchaux and A. Dejoan. Settling velocity and preferential concentration of heavy particles under two-way coupling effects in homogeneous turbulence. *Physical Review Fluids*, 2:104302, 2017. doi:10.1103/PhysRevFluids.2.104302.

A. E. Morrison, S. T. Siems, and M. J. Manton. A Three-Year Climatology of Cloud-Top Phase over the Southern Ocean and North Pacific. *Journal of Climate*, 24(9):2405–2418, 2011. doi:10.1175/2010JCLI3842.1.

H. Morrison, G. de Boer, G. Feingold, J. Harrington, M. D. Shupe, and K. Sulia. Resilience of persistent Arctic mixed-phase clouds. *Nature Geoscience*, 5(1): 11–17, 2012. doi:10.1038/ngeo1332.

H. Morrison, M. van Lier-Walqui, A. M. Fridlind, W. W. Grabowski, J. Y. Harrington, C. Hoose, A. Korolev, M. R. Kumjian, J. A. Milbrandt, H. Pawlowska, et al. Confronting the Challenge of Modeling Cloud and Precipitation Microphysics. *Journal of Advances in Modeling Earth Systems*, 12(8):e2019MS001689, 2020. doi:10.1029/2019MS001689.

L. Mosimann. An improved method for determining the degree of snow crystal riming by vertical Doppler radar. *Atmospheric Research*, 37(4):305–323, 1995. doi:10.1016/0169-8095(94)00050-N.

S. Mossop. Production of secondary ice particles during the growth of graupel by riming. *Quarterly Journal of the Royal Meteorological Society*, 102(431):45–57, 1976. doi:10.1002/qj.49710243104.

S. Mossop. The influence of drop size distribution on the production of secondary ice particles during graupel growth. *Quarterly Journal of the Royal Meteorological Society*, 104(440):323–330, 1978. doi:10.1002/qj.49710444007.

O. F. Mossotti. *Discussione analitica sull'influenza che l'azione di un mezzo dielettrico ha sulla distribuzione dell'elettricità alla superficie di più corpi elettrici disseminati in esso*, volume 24. Società italiana delle scienze, 1846.

A. Muhlbauer, I. L. McCoy, and R. Wood. Climatology of stratocumulus cloud morphologies: microphysical properties and radiative effects. *Atmospheric Chemistry and Physics*, 14(13):6695–6716, 2014. doi:10.5194/acp-14-6695-2014.

J. Mülmenstädt, O. Sourdeval, J. Delanoë, and J. Quaas. Frequency of occurrence of rain from liquid-, mixed-, and ice-phase clouds derived from A-Train satellite retrievals. *Geophysical Research Letters*, 42(15):6502–6509, 2015. doi:10.1002/2015GL064604.

D. M. Murphy and T. Koop. Review of the vapour pressures of ice and supercooled water for atmospheric applications. *Quarterly Journal of the Royal Meteorological Society*, 131(608):1539–1565, 2005. doi:10.1256/qj.04.94.

A. Myagkov, P. Seifert, U. Wandinger, J. Bühl, and R. Engelmann. Relationship between temperature and apparent shape of pristine ice crystals derived from polarimetric cloud radar observations during the ACCEPT campaign. *Atmospheric Measurement Techniques*, 9(8):3739–3754, 2016. doi:10.5194/amt-9-3739-2016.

A. Naso, J. Jucha, E. Lévêque, and A. Pumir. Collision rate of ice crystals with water droplets in turbulent flows. *Journal of Fluid Mechanics*, 845:615–641, 2018. doi:10.1017/jfm.2018.238.

C. M. Naud, A. D. D. Genio, and M. Bauer. Observational Constraints on the Cloud Thermodynamic Phase in Midlatitude Storms. *Journal of Climate*, 19 (20):5273–5288, 2006. doi:10.1175/JCLI3919.1.

A. Nemes, T. Dasari, J. Hong, M. Guala, and F. Coletti. Snowflakes in the atmospheric surface layer: observation of particle–turbulence dynamics. *Journal of Fluid Mechanics*, 814:592–613, 2017. doi:10.1017/jfm.2017.13.

T. Nomokonova, K. Ebell, U. Löhnert, M. Maturilli, and C. Ritter. The influence of water vapor anomalies on clouds and their radiative effect at Ny-Ålesund.

Atmospheric Chemistry and Physics, 20(8):5157–5173, 2020. doi:10.5194/acp-20-5157-2020.

R. Onishi and A. Seifert. Reynolds-number dependence of turbulence enhancement on collision growth. *Atmospheric Chemistry and Physics*, 16(19):12441–12455, 2016. doi:10.5194/acp-16-12441-2016.

D. Ori, V. Schemann, M. Karrer, J. Dias Neto, L. von Terzi, A. Seifert, and S. Kneifel. Evaluation of ice particle growth in ICON using statistics of multi-frequency Doppler cloud radar observations. *Quarterly Journal of the Royal Meteorological Society*, 146(733):3830–3849, 2020. doi:10.1002/qj.3875.

D. Ori, L. von Terzi, M. Karrer, and S. Kneifel. snowScatt 1.0: Consistent model of microphysical and scattering properties of rimed and unrimed snowflakes based on the selfsimilar Rayleigh-Gans Approximation. *Geoscientific Model Development*, 14(3):1511–1531, 2021. doi:10.5194/gmd-14-1511-2021.

M. Oue, M. R. Kumjian, Y. Lu, J. Verlinde, K. Aydin, and E. E. Clothiaux. Linear Depolarization Ratios of Columnar Ice Crystals in a Deep Precipitating System over the Arctic Observed by Zenith-Pointing Ka-Band Doppler Radar. *Journal of Applied Meteorology and Climatology*, 54(5):1060–1068, 2015. doi:10.1175/JAMC-D-15-0012.1.

E. J. O'Connor, R. J. Hogan, and A. J. Illingworth. Retrieving stratocumulus drizzle parameters using doppler radar and lidar. *Journal of Applied Meteorology*, 44(1):14–27, 2005. doi:10.1175/JAM-2181.1.

J. T. Pasquier, J. Henneberger, F. Ramelli, A. Lauber, R. O. David, J. Wieder, T. Carlsen, R. Gierens, M. Maturilli, and U. Lohmann. Conditions favorable for secondary ice production in Arctic mixed-phase clouds. *Atmospheric Chemistry and Physics*, 22(23):15579–15601, 2022. doi:10.5194/acp-22-15579-2022.

T. Petäjä, E. J. O'Connor, D. Moisseev, V. A. Sinclair, A. J. Manninen, R. Väänänen, A. von Lerber, J. A. Thornton, K. Nicoll, W. Petersen, et al. BAECC: A field campaign to elucidate the impact of biogenic aerosols on clouds and climate. *Bulletin of the American Meteorological Society*, 97(10):1909–1928, 2016. doi:10.1175/BAMS-D-14-00199.1.

A. J. Petersen, L. Baker, and F. Coletti. Experimental study of inertial particles clustering and settling in homogeneous turbulence. *Journal of Fluid Mechanics*, 864:925–970, 2019. doi:10.1017/jfm.2019.31.

V. T. Phillips, S. Patade, J. Gutierrez, and A. Bansemer. Secondary ice production by fragmentation of freezing drops: Formulation and theory. *Journal of the Atmospheric Sciences*, 75(9):3031–3070, 2018. doi:10.1175/JAS-D-17-0190.1.

M. B. Pinsky and A. P. Khain. Some effects of cloud turbulence on water–ice and ice–ice collisions. *Atmospheric Research*, 47–48:69–86, 1998. doi:10.1016/S0169-8095(98)00041-6.

F. Pithan and T. Mauritsen. Arctic amplification dominated by temperature feedbacks in contemporary climate models. *Nature Geoscience*, 7(3):181–184, 2014. doi:10.1038/ngeo2071.

R. L. Pitter, H. R. Pruppacher, and A. E. Hamielec. A Numerical Study of the Effect of Forced Convection on Mass Transport from a Thin Oblate Spheroid of Ice in Air. *Journal of Atmospheric Sciences*, 31(4):1058 – 1066, 1974. doi:10.1175/1520-0469(1974)031<1058:ANSOTE>2.0.CO;2.

S. B. Pope. *Turbulent Flows*. Cambridge University Press, 2000. doi:10.1017/CBO9780511840531.

D. C. Powell and C. Elderkin. An investigation of the application of Taylor's hypothesis to atmospheric boundary layer turbulence. *Journal of Atmospheric Sciences*, 31 (4):990–1002, 1974. doi:10.1175/1520-0469(1974)031<0990:AIOTAO>2.0.CO;2.

A. J. Prenni, P. J. Demott, D. C. Rogers, S. M. Kreidenweis, G. M. Mcfarquhar, G. Zhang, and M. R. Poellot. Ice nuclei characteristics from M-PACE and their relation to ice formation in clouds. *Tellus B: Chemical and Physical Meteorology*, 61(2):436–448, 2009. doi:10.1111/j.1600-0889.2009.00415.x.

U. Proske, S. Ferrachat, D. Neubauer, M. Staab, and U. Lohmann. Assessing the potential for simplification in global climate model cloud microphysics. *Atmospheric Chemistry and Physics*, 22(7):4737–4762, 2022. doi:10.5194/acp-22-4737-2022.

H. R. Pruppacher and J. D. Klett. *Microphysics of Clouds and Precipitation: Reprinted 1980*. Springer, Dordrecht, 2012. doi:10.1007/978-94-009-9905-3.

A. Pumir and M. Wilkinson. Collisional Aggregation Due to Turbulence. *Annual Review of Condensed Matter Physics*, 7(1):141–170, 2016. doi:10.1146/annurev-conmatphys-031115-011538.

F. Ramelli, J. Henneberger, R. O. David, A. Lauber, J. T. Pasquier, J. Wieder, J. Bühl, P. Seifert, R. Engelmann, M. Hervo, et al. Influence of low-level blocking and turbulence on the microphysics of a mixed-phase cloud in an

inner-Alpine valley. *Atmospheric Chemistry and Physics*, 21(6):5151–5172, 2021. doi:10.5194/acp-21-5151-2021.

A. L. Rangno. Fragmentation of freezing drops in shallow maritime frontal clouds. *Journal of the Atmospheric Sciences*, 65(4):1455–1466, 2008. doi:10.1175/2007JAS2295.1.

A. L. Rangno and P. V. Hobbs. Ice particles in stratiform clouds in the Arctic and possible mechanisms for the production of high ice concentrations. *Journal of Geophysical Research: Atmospheres*, 106(D14):15065–15075, 2001. doi:10.1029/2000JD900286.

R. M. Rauber and L. O. Grant. The Characteristics and Distribution of Cloud Water over the Mountains of Northern Colorado during Wintertime Storms. Part II: Spatial Distribution and Microphysical Characteristics. *Journal of Climate and Applied Meteorology*, 25(4):489–504, 1986. doi:10.1175/1520-0450(1986)025<0489:TCADOC>2.0.CO;2.

R. M. Rauber and A. Tokay. An explanation for the existence of supercooled water at the top of cold clouds. *Journal of Atmospheric Sciences*, 48(8):1005–1023, 1991. doi:10.1175/1520-0469(1991)048<1005:AEFTEO>2.0.CO;2.

S. Ravichandran and R. Govindarajan. Caustics and clustering in the vicinity of a vortex. *Physics of Fluids*, 27(3), 2015. doi:10.1063/1.4916583.

S. Reitter, K. Fröhlich, A. Seifert, S. Crewell, and M. Mech. Evaluation of ice and snow content in the global numerical weather prediction model GME with CloudSat. *Geoscientific Model Development*, 4(3):579–589, 2011. doi:10.5194/gmd-4-579-2011.

L. F. Richardson. *Weather prediction by numerical process*. Cambridge University Press, 1922.

R. Rogers and B. Tripp. Some radar measurements of turbulence in snow. *Journal of Applied Meteorology and Climatology*, 3(5):603–610, 1964. doi:10.1175/1520-0450(1964)003<0603:SRMOTI>2.0.CO;2.

P. Saffman and J. Turner. On the collision of drops in turbulent clouds. *Journal of Fluid Mechanics*, 1(1):16–30, 1956. doi:10.1017/S0022112056000020.

C. P. R. Saunders and N. M. A. Wahab. The Influence of Electric Fields on the Aggregation of Ice Crystals. *Journal of the Meteorological Society of Japan. Ser. II*, 53(2):121–126, 1975. doi:10.2151/jmsj1965.53.2_121.

E. W. Saw, R. A. Shaw, S. Ayyalasomayajula, P. Y. Chuang, and A. Gylfason. Inertial clustering of particles in high-Reynolds-number turbulence. *Physical Review Letters*, 100(21):214501, 2008. doi:10.1103/PhysRevLett.100.214501.

E.-W. Saw, G. P. Bewley, E. Bodenschatz, S. Sankar Ray, and J. Bec. Extreme fluctuations of the relative velocities between droplets in turbulent airflow. *Physics of Fluids*, 26(11), 2014. doi:10.1063/1.4900848.

V. Schemann and K. Ebell. Simulation of mixed-phase clouds with the ICON large-eddy model in the complex Arctic environment around Ny-Ålesund. *Atmospheric Chemistry and Physics*, 20(1):475–485, 2020. doi:10.5194/acp-20-475-2020.

I. Schirmacher, P. Kollias, K. Lamer, M. Mech, L. Pfitzenmaier, M. Wendisch, and S. Crewell. Assessing Arctic low-level clouds and precipitation from above – a radar perspective. *Atmospheric Measurement Techniques*, 16(17):4081–4100, 2023. doi:10.5194/amt-16-4081-2023.

F. G. Schmitt and L. Seuront. Intermittent turbulence and copepod dynamics: Increase in encounter rates through preferential concentration. *Journal of Marine Systems*, 70(3):263–272, 2008. doi:10.1016/j.jmarsys.2007.01.008.

R. S. Schrom and M. R. Kumjian. Connecting microphysical processes in Colorado winter storms with vertical profiles of radar observations. *Journal of Applied Meteorology and Climatology*, 55(8):1771–1787, 2016. doi:10.1175/JAMC-D-15-0338.1.

R. S. Schrom, M. R. Kumjian, and Y. Lu. Polarimetric radar signatures of dendritic growth zones within Colorado winter storms. *Journal of Applied Meteorology and Climatology*, 54(12):2365–2388, 2015. doi:10.1175/JAMC-D-15-0004.1.

A. Schwarzenboeck, V. Shcherbakov, R. Lefevre, J. F. Gayet, Y. Pointin, and C. Duroure. Indications for stellar-crystal fragmentation in Arctic clouds. *Atmospheric Research*, 92(2):220–228, 2009. doi:10.1016/j.atmosres.2008.10.002.

A. Seifert and K. D. Beheng. A two-moment cloud microphysics parameterization for mixed-phase clouds. Part 1: Model description. *Meteorology and Atmospheric Physics*, 92(1-2):45–66, 2006. doi:10.1007/s00703-005-0112-4.

A. Seifert, L. Nuijens, and B. Stevens. Turbulence effects on warm-rain autoconversion in precipitating shallow convection. *Quarterly Journal of the Royal Meteorological Society*, 136(652):1753–1762, 2010. doi:10.1002/qj.684.

M. Z. Sheikh, K. Gustavsson, E. Lévêque, B. Mehlig, A. Pumir, and A. Naso. Colliding Ice Crystals in Turbulent Clouds. *Journal of the Atmospheric Sciences*, 79(9):2205–2218, 2022. doi:10.1175/JAS-D-21-0305.1.

S. Shima, Y. Sato, A. Hashimoto, and R. Misumi. Predicting the morphology of ice particles in deep convection using the super-droplet method: development and evaluation of SCALE-SDM 0.2.5-2.2.0, -2.2.1, and -2.2.2. *Geoscientific Model Development*, 13(9):4107–4157, 2020. doi:10.5194/gmd-13-4107-2020.

M. D. Shupe and J. M. Intrieri. Cloud radiative forcing of the Arctic surface: The influence of cloud properties, surface albedo, and solar zenith angle. *Journal of Climate*, 17(3):616–628, 2004. doi:10.1175/1520-0442(2004)017<0616:CRFOTA>2.0.CO;2.

M. D. Shupe, P. Kollias, P. O. G. Persson, and G. M. McFarquhar. Vertical motions in Arctic mixed-phase stratiform clouds. *Journal of Atmospheric Sciences*, 65(4): 1304–1322, 2008a. doi:10.1175/2007JAS2479.1.

M. D. Shupe, P. Kollias, M. Poellot, and E. Eloranta. On deriving vertical air motions from cloud radar Doppler spectra. *Journal of Atmospheric and Oceanic Technology*, 25(4):547–557, 2008b. doi:10.1175/2007JTECHA1007.1.

C. Siewert, R. P. J. Kunnen, and W. Schröder. Collision rates of small ellipsoids settling in turbulence. *Journal of Fluid Mechanics*, 758:686–701, 2014. doi:10.1017/jfm.2014.554.

L. F. Simpfendoerfer, J. Verlinde, J. Y. Harrington, M. D. Shupe, Y.-S. Chen, E. E. Clothiaux, and J.-C. Golaz. Formation of Arctic stratocumuli through atmospheric radiative cooling. *Journal of Geophysical Research: Atmospheres*, 124(16):9644–9664, 2019. doi:10.1029/2018JD030189.

B. Slater and A. Michaelides. Surface premelting of water ice. *Nature Reviews Chemistry*, 3(3):172–188, 2019. doi:10.1038/s41570-019-0080-8.

D. M. Smith, J. A. Screen, C. Deser, J. Cohen, J. C. Fyfe, J. García-Serrano, T. Jung, V. Kattsov, D. Matei, R. Msadek, et al. The Polar Amplification Model Intercomparison Project (PAMIP) contribution to CMIP6: investigating the causes and consequences of polar amplification. *Geoscientific Model Development*, 12(3):1139–1164, 2019. doi:10.5194/gmd-12-1139-2019.

K. D. Squires and J. K. Eaton. Preferential concentration of particles by turbulence. *Physics of Fluids A: Fluid Dynamics*, 3(5):1169–1178, 1991. doi:10.1063/1.858045.

K. R. Sreenivasan. On the universality of the Kolmogorov constant. *Physics of Fluids*, 7(11):2778–2784, 1995. doi:10.1063/1.868656.

R. C. Srivastava and D. Atlas. Effect of finite radar pulse volume on turbulence measurements. *Journal of Applied Meteorology and Climatology*, 13(4):472–480, 1974. doi:10.1175/1520-0450(1974)013<0472:EOFRPV>2.0.CO;2.

R. E. Stewart, J. D. Marwitz, J. C. Pace, and R. E. Carbone. Characteristics through the Melting Layer of Stratiform Clouds. *Journal of Atmospheric Sciences*, 41(22): 3227 – 3237, 1984. doi:10.1175/1520-0469(1984)041<3227:CTTMLO>2.0.CO;2.

J. L. Stith, L. M. Avallone, A. Bansemer, B. Basarab, S. W. Dorsi, B. Fuchs, R. P. Lawson, D. C. Rogers, S. Rutledge, and D. W. Toohey. Ice particles in the upper anvil regions of midlatitude continental thunderstorms: the case for frozen-drop aggregates. *Atmospheric Chemistry and Physics*, 14(4):1973–1985, 2014. doi:10.5194/acp-14-1973-2014.

T. Storelvmo, I. Tan, and A. V. Korolev. Cloud Phase Changes Induced by CO2 Warming—a Powerful yet Poorly Constrained Cloud-Climate Feedback. *Current Climate Change Reports*, 1(4):288–296, 2015. doi:10.1007/s40641-015-0026-2.

J. Stout, S. Arya, and E. Genikhovich. The effect of nonlinear drag on the motion and settling velocity of heavy particles. *Journal of Atmospheric Sciences*, 52(22): 3836–3848, 1995. doi:10.1175/1520-0469(1995)052<3836:TEONDO>2.0.CO;2.

C. J. Stubenrauch, W. B. Rossow, S. Kinne, S. Ackerman, G. Cesana, H. Chepfer, L. Di Girolamo, B. Getzewich, A. Guignard, A. Heidinger, et al. Assessment of global cloud datasets from satellites: Project and database initiated by the GEWEX radiation panel. *Bulletin of the American Meteorological Society*, 94(7): 1031–1049, 2013. doi:10.1175/BAMS-D-12-00117.1.

R. B. Stull. *An introduction to boundary layer meteorology*. Springer, 1988. doi:10.1007/978-94-009-3027-8.

Z. Sun and K. P. Shine. Parameterization of ice cloud radiative properties and its application to the potential climatic importance of mixed-phase clouds. *Journal of Climate*, 8(7):1874–1888, 1995. doi:10.1175/1520-0442(1995)008<1874:POICRP>2.0.CO;2.

W. Szyrmer and I. Zawadzki. Modeling of the melting layer. Part I: Dynamics and microphysics. *Journal of the Atmospheric Sciences*, 56(20):3573–3592, 1999. doi:10.1175/1520-0469(1999)056<3573:MOTMLP>2.0.CO;2.

T. Takahashi. High ice crystal production in winter cumuli over the Japan Sea. *Geophysical Research Letters*, 20(6):451–454, 1993. doi:10.1029/93GL00613.

T. Takahashi. Influence of liquid water content and temperature on the form and growth of branched planar snow crystals in a cloud. *Journal of the Atmospheric Sciences*, 71(11):4127–4142, 2014. doi:10.1175/JAS-D-14-0043.1.

T. Takahashi, T. Endoh, G. Wakahama, and N. Fukuta. Vapor diffusional growth of free-falling snow crystals between -3 and -23°c. *Journal of the Meteorological Society of Japan. Ser. II*, 69(1):15–30, 1991. doi:10.2151/jmsj1965.69.1_15.

T. Takahashi, Y. Nagao, and Y. Kushiyama. Possible high ice particle production during graupel–graupel collisions. *Journal of the Atmospheric Sciences*, 52(24): 4523–4527, 1995. doi:10.1175/1520-0469(1995)052<4523:PHIPPD>2.0.CO;2.

I. Tan and T. Storelvmo. Evidence of strong contributions from mixed-phase clouds to Arctic climate change. *Geophysical Research Letters*, 46(5):2894–2902, 2019. doi:10.1029/2018GL081871.

I. Tan, T. Storelvmo, and M. D. Zelinka. Observational constraints on mixed-phase clouds imply higher climate sensitivity. *Science*, 352(6282):224–227, 2016. doi:10.1126/science.aad5300.

G. I. Taylor. The spectrum of turbulence. *Proceedings of the Royal Society of London. Series A-Mathematical and Physical Sciences*, 164(919):476–490, 1938. doi:10.1098/rspa.1938.0032.

H. Tennekes and J. L. Lumley. *A first course in turbulence*. MIT press, Cambridge, Massachusetts, and London, England, 1972.

J. Tom and A. D. Bragg. Multiscale preferential sweeping of particles settling in turbulence. *Journal of Fluid Mechanics*, 871:244–270, 2019. doi:10.1017/jfm.2019.337.

F. Tridon, A. Battaglia, R. J. Chase, F. J. Turk, J. Leinonen, S. Kneifel, K. Mroz, J. Finlon, A. Bansemer, S. Tanelli, et al. The microphysics of stratiform precipitation during OLYMPEX: Compatibility between triple-frequency radar and airborne in situ observations. *Journal of Geophysical Research: Atmospheres*, 124(15):8764–8792, 2019. doi:10.1029/2018JD029858.

É. Vignon, S. P. Alexander, P. J. DeMott, G. Sotiropoulou, F. Gerber, T. C. J. Hill, R. Marchand, A. Nenes, and A. Berne. Challenging and Improving the Simulation of Mid-Level Mixed-Phase Clouds Over the High-Latitude Southern Ocean. *Journal of Geophysical Research: Atmospheres*, 126(7):e2020JD033490, 2021. doi:10.1029/2020JD033490.

L. von Terzi, J. Dias Neto, D. Ori, A. Myagkov, and S. Kneifel. Ice microphysical processes in the dendritic growth layer: A statistical analysis combining multi-frequency and polarimetric Doppler cloud radar observations. *Atmospheric Chemistry and Physics*, 22(17):11795–11821, 2022. doi:10.5194/acp-22-11795-2022.

M. Voßkuhle, A. Pumir, E. Lévêque, and M. Wilkinson. Prevalence of the sling effect for enhancing collision rates in turbulent suspensions. *Journal of Fluid Mechanics*, 749:841–852, 2014. doi:10.1017/jfm.2014.259.

M. Voßkuhle, A. Pumir, E. Lévêque, and M. Wilkinson. Collision rate for suspensions at large Stokes numbers–comparing Navier–Stokes and synthetic turbulence. *Journal of Turbulence*, 16(1):15–25, 2015. doi:10.1080/14685248.2014.948628.

F. Waitz, M. Schnaiter, T. Leisner, and E. Järvinen. In situ observation of riming in mixed-phase clouds using the PHIPS probe. *Atmospheric Chemistry and Physics*, 22(11):7087–7103, 2022. doi:10.5194/acp-22-7087-2022.

J. M. Wallace and P. V. Hobbs. *Atmospheric Science (Second Edition)*. Academic Press, San Diego, second edition, 2006. doi:10.1016/C2009-0-00034-8.

L.-P. Wang and M. R. Maxey. Settling velocity and concentration distribution of heavy particles in homogeneous isotropic turbulence. *Journal of Fluid Mechanics*, 256:27–68, 1993. doi:10.1017/S0022112093002708.

P. K. Wang and W. Ji. Collision efficiencies of ice crystals at low–intermediate Reynolds numbers colliding with supercooled cloud droplets: A numerical study. *Journal of the Atmospheric Sciences*, 57(8):1001–1009, 2000. doi:10.1175/1520-0469(2000)057<1001:CEOICA>2.0.CO;2.

A. Wegener. *Thermodynamik der atmosphäre*. J.A. Barth, 1911.

M. Wendisch, A. Macke, A. Ehrlich, C. Lüpkes, M. Mech, D. Chechin, K. Dethloff, C. B. Velasco, H. Bozem, M. Brückner, H.-C. Clemen, et al. The Arctic Cloud Puzzle: Using ACLOUD/PASCAL Multiplatform Observations to Unravel the Role of Clouds and Aerosol Particles in Arctic Amplification. *Bulletin of the American Meteorological Society*, 100(5):841–871, 2019. doi:10.1175/BAMS-D-18-0072.1.

M. Wendisch, M. Brückner, S. Crewell, A. Ehrlich, J. Notholt, C. Lüpkes, A. Macke, J. P. Burrows, A. Rinke, J. Quaas, M. Maturilli, et al. Atmospheric and Surface Processes, and Feedback Mechanisms Determining Arctic Amplification: A Review of First Results and Prospects of the (AC)3 Project. *Bulletin of the American Meteorological Society*, 104(1):E208 – E242, 2023. doi:10.1175/BAMS-D-21-0218.1.

C. D. Westbrook and A. J. Illingworth. Evidence that ice forms primarily in supercooled liquid clouds at temperatures > –27°C. *Geophysical Research Letters*, 38(14), 2011. doi:10.1029/2011GL048021.

C. D. Westbrook, R. C. Ball, and P. R. Field. Radar scattering by aggregate snowflakes. *Quarterly Journal of the Royal Meteorological Society*, 132(616): 897–914, 2006. doi:10.1256/qj.05.82.

C. D. Westbrook, R. J. Hogan, and A. J. Illingworth. The capacitance of pristine ice crystals and aggregate snowflakes. *Journal of the Atmospheric Sciences*, 65 (1):206–219, 2008. doi:10.1175/2007JAS2315.1.

S. Wildeman, S. Sterl, C. Sun, and D. Lohse. Fast dynamics of water droplets freezing from the outside in. *Physical Review Letters*, 118(8):084101, 2017. doi:10.1103/PhysRevLett.118.084101.

E. J. Woittiez, H. J. Jonker, and L. M. Portela. On the combined effects of turbulence and gravity on droplet collisions in clouds: a numerical study. *Journal of the Atmospheric Sciences*, 66(7):1926–1943, 2009. doi:10.1175/2005JAS2669.1.

H. Xu and E. Bodenschatz. Motion of inertial particles with size larger than Kolmogorov scale in turbulent flows. *Physica D: Nonlinear Phenomena*, 237(14): 2095–2100, 2008. doi:10.1016/j.physd.2008.04.022.

C. Yang and U. Lei. The role of the turbulent scales in the settling velocity of heavy particles in homogeneous isotropic turbulence. *Journal of Fluid Mechanics*, 371:179–205, 1998. doi:10.1017/S0022112098002328.

G. Zängl, D. Reinert, P. Rípodas, and M. Baldauf. The ICON (ICOsahedral Non-hydrostatic) modelling framework of DWD and MPI-M: Description of the non-hydrostatic dynamical core. *Quarterly Journal of the Royal Meteorological Society*, 141(687):563–579, 2015. doi:10.1002/qj.2378.

M. D. Zelinka, D. A. Randall, M. J. Webb, and S. A. Klein. Clearing clouds of uncertainty. *Nature Climate Change*, 7(10):674–678, 2017. doi:10.1038/nclimate3402.

X. Zhao, Y. Lin, Y. Peng, B. Wang, H. Morrison, and A. Gettelman. A single ice approach using varying ice particle properties in global climate model microphysics. *Journal of Advances in Modeling Earth Systems*, 9(5):2138–2157, 2017. doi:10.1002/2017MS000952.

J. Zikmunda and G. Vali. Fall patterns and fall velocities of rimed ice crystals. *Journal of Atmospheric Sciences*, 29(7):1334–1347, 1972. doi:10.1175/1520-0469(1972)029<1334:FPAFVO>2.0.CO;2.

P. Zuidema, B. Baker, Y. Han, J. Intrieri, J. Key, P. Lawson, S. Matrosov, M. Shupe, R. Stone, and T. Uttal. An Arctic springtime mixed-phase cloudy boundary layer observed during SHEBA. *Journal of the Atmospheric Sciences*, 62(1):160–176, 2005. doi:10.1175/JAS-3368.1.

List of Symbols

A non-coherent power, introduced in Section 3 of **Study 2**.

$\mathcal{A}$ particle cross-sectional area perpendicular to the direction of gravity.

a size of a particle; in the case of a spherical particle defined as the sphere's radius, and in the case of an ice crystal defined as half the maximum span across the basal crystal face.

α aspect ratio of an ice crystal, defined as the ratio between the maximum span across the basal crystal face, and the span of the crystal along the direction perpendicular to the basal face.

α_K Kolmogorov constant, introduced in Eq. 2.15.

$\mathbf{B}$ coherency matrix, introduced in Section 3 of **Study 2**.

b_A exponent of area-size relation for ice particles, see e.g., Karrer et al. [2020].

B_{hh} first diagonal component of the coherency matrix $\mathbf{B}$, introduced in Section 3 of **Study 2**.

$\widetilde{B}_{hh}$ first diagonal component of the coherency matrix $\mathbf{B}$, after noise identification and removal, introduced in Section 3 of **Study 2**.

$\dot{B}_{hv}$ off-diagonal component of the coherency matrix $\mathbf{B}$, introduced in Section 3 of **Study 2**.

b_m exponent of mass-size relation for ice particles, see e.g., Karrer et al. [2020].

B_{vv} second diagonal component of the coherency matrix $\mathbf{B}$, introduced in Section 3 of **Study 2**.

$\widetilde{B}_{vv}$ second diagonal component of the coherency matrix $\mathbf{B}$, after noise identification and removal, introduced in Section 3 of **Study 2**.

$\mathbf{C}$ fully coherent component of the coherency matrix $\mathbf{B}$, introduced in Section 3 of **Study 2**.

C ice particle capacitance, introduced in Section 2.1.2.

$\mathcal{C}$ radial distribution function, introduced in Eq. 2.20.

c speed of light.

C_D particle drag coefficient, discussed in Section 2.1.3.

D diameter.

$\mathbf{D}$ diagonalized coherency matrix, introduced in Section 3 of **Study 2**.

D_2 correlation dimension of a particle population, see Section 4.2.2 in Pumir and Wilkinson [2016], and references therein.

D_a radar antenna diameter.

D_{cc} first diagonal component of the diagonalized coherency matrix $\mathbf{D}$, including coherent and non-coherent contributions, introduced in Section 3 of **Study 2**.

D_{max} particle maximum dimension.

D'_v diffusivity of water vapor in air.

D_{xx} second diagonal component of the diagonalized coherency matrix $\mathbf{D}$, including solely non-coherent contributions, introduced in Section 3 of **Study 2**.

δ backscatter differential phase, introduced in Section 2.3.3.

Δr distance between the centers of two particles.

Δt averaging time interval used in a number of EDR retrieval approaches introduced in Section 2.3.6.

δt radar integration time.

E kinetic energy of air, per unit mass.

$\mathbf{E}$ electric field in vector form.

E_{coll} collection efficiency, introduced in Section 2.1.4.

$\widetilde{E}_{coll}$ collection efficiency averaged across a droplet population, introduced in Section 2.1.4.

E_h horizontal component of the electric field received by the radar.

E_{stick} sticking efficiency, introduced in Section 2.1.4.

E_v vertical component of the electric field received by the radar.

ε turbulent kinetic energy dissipation rate, or eddy dissipation rate, introduced in Section 2.2.2.

ϵ_W complex relative permittivity of liquid water, not to be confused with the dielectric constant $|K_W|^2$; see Section 2.3.1.

η Kolmogorov length scale, introduced in Eq. 2.16a.

f frequency.

F_{drag} drag force acting on a particle.

F_{grav} gravitational force acting on a particle.

$f_{low,\,high}$ frequency integration extremes used in the EDR retrieval approach by Borque et al. [2016], introduced in Section 2.3.6.

$\mathbf{g}$ gravitational acceleration in vector form.

g gravitational acceleration, scalar.

$\mathbf{I}$ unity matrix, defined as having diagonal elements equal to 1, and off-diagonal elements equal to 0.

K_0 constant parameter in Eq. 2.23.

$k_{0,\,1,\,2}$ wavenumber integration extremes $k_{0,\,1,\,2} = 2\pi\ell_{0,\,1,\,2}^{-1}$, introduced in Section 2.3.6.

K_{agg} aggregation kernel, introduced in Section 2.1.4.

$\mathrm{K_{DP}}$ specific differential phase shift, introduced in Section 2.3.3.

$k_{low,\,high}$ wavenumber integration extremes used in the EDR retrieval approach by Borque et al. [2016], introduced in Section 2.3.6.

k'_T heat conductivity of air.

$|K_W|^2$ dielectric constant of liquid water, not to be confused with the complex relative permittivity ϵ_W; see Section 2.3.1.

κ wavenumber, for the purpose of this thesis defined as $\kappa = 2\pi\lambda^{-1}$, where λ is the wavelength.

ℓ length scale of a turbulent eddy.

$\ell_{0,\,1,\,2}$ length scales associated with the integration extremes $k_{0,\,1,\,2} = 2\pi\ell_{0,\,1,\,2}^{-1}$, introduced in Section 2.3.6.

ℓ_{DI} demarcation size between eddies belonging to the inertial subrange, and to the dissipation range, introduced in Section 2.2.2.

ℓ_{EI} demarcation size between eddies belonging to the energy containing range, and to the universal equilibrium range, introduced in Section 2.2.2.

l_s latent heat of sublimation of water per unit mass.

λ wavelength.

M_n n-th moment of the Doppler spectrum; definitions given in Section 2.3.4.

m_p particle mass.

M_w molecular weight of water.

$n(m,t)$ mass distribution of an ice particle population at time t, introduced in Section 2.1.4.

n' particle number concentration.

$N(\sigma_{b,\lambda})$ distribution of the backscattering cross section across a particle population, introduced in Section 2.3.1.

n_{air} index of refraction of air.

$\mathcal{N}_{S-T}$ number of collisions per unit time and unit volume, between particles suspended in a turbulent flow, as derived by Saffman and Turner [1956]; introduced in Eq. 2.19.

n_t complex index of refraction of the substance constituting a radar target.

n_W complex index of refraction of liquid water.

ν kinematic viscosity of air.

p air pressure.

P_r power of the signal received by the radar.

P_t power of the signal transmitted by the radar.

ϕ phase.

Φ_{DP} differential phase shift, introduced in Section 2.3.3.

ϕ_{HH} phase of the received radar signal at horizontal polarization, introduced in Section 2.3.3.

ϕ_{VV} phase of the received radar signal at vertical polarization, introduced in Section 2.3.3.

$\mathcal{R}$ collision rate for one particle affected by inertial effects, given in Eq. 2.24.

$\overline{R}$ universal gas constant.

R distance between radar target and the instrument, same as range r in absence of range folding; introduced in Section 4.4 of **Study 2**.

r radar target range.

$\mathcal{R}_{adv}$ collision rate for one particle due to advective effects, introduced in Eq. 2.20.

Re_λ Taylor-microscale Reynolds number, see e.g., Section 3.2 in Tennekes and Lumley [1972].

Re_p particle Reynolds number.

$R_{max,\,min}$ maximum or minimum range of a given chirp sequence; introduced in Section 4.4 of **Study 2**.

$\mathcal{R}_{sling}$ collision rate for one particle due to the sling effect alone, introduced in Eq. 2.23.

$\mathcal{R}_{S-T}$ collision rate for one particle due to the Saffman-Turner mechanism alone [Saffman and Turner, 1956], introduced in Eq. 2.21.

R_{unamb} maximum unambiguous range; introduced in Section 4.4 of **Study 2**.

ρ_a air density.

ρ_{HV} copolar correlation coefficient, introduced in Section 2.3.3.

ρ_p particle density.

S output of the FFT of a velocity time series, introduced in Section 2.3.6.

S_0 constant parameter in Eq. 2.23.

s_i vapor supersaturation with respect to ice.

St Stokes number, introduced in Eq. 2.18.

St_{mod} modified Stokes number, introduced in Eq. 5.4.

$s(v_D)$ spectral reflectivity in linear scale normalized with respect to Doppler-bin width.

$\mathrm{sZ_{DR}}$ spectral differential reflectivity, introduced in Section 3 of **Study 2**.

$\mathrm{sZ_{DR\,max}}$ maximum spectral differential reflectivity, introduced in Section 3 of **Study 2**.

sZ_e spectral equivalent radar reflectivity factor.

$\sigma_{b,\lambda}$ backscattering cross section of a radar target, introduced in Section 2.3.1.

σ_D Doppler spectrum width, introduced in Eq. 2.37.

$\sigma_{\overline{v}}^2$ variance of a MDV time series, introduced in Section 2.3.6.

T temperature.

$T(0,r)$ transmissivity of the atmosphere along the path between the radar and the target located at range r.

T_∞ temperature at a large distance from the studied particle.

θ radar half-power beamwidth.

ϑ duration of the pulse transmitted by the radar.

θ_v virtual potential temperature.

$\tau_{D_{max}}$ time scale of an eddy of length scale coinciding with the maximum dimension of an ice particle D_{max}; introduced in Section 5.1.1.

τ_η Kolmogorov time scale, introduced in Eq. 2.16b.

τ_ℓ time scale of an eddy of length scale ℓ; in the case of an eddy in the inertial subrange, the relation between τ_ℓ and ℓ is given in Eq. 5.3.

τ_p particle relaxation time, introduced in Section 2.1.3.

$\mathbf{u}$ air velocity, vector form.

u air velocity, modulus.

u_η Kolmogorov velocity scale, introduced in Eq. 2.16c.

$u_{x,y,z}$ air velocity along the x, y, or z direction.

$\mathbf{v}$ velocity of a particle, vector form.

v velocity of a particle, modulus.

v_D Doppler velocity of a radar target, introduced in Eq. 2.35.

v_{mD} mean Doppler velocity, introduced in Eq. 2.36.

v_T particle terminal velocity, introduced in Section 2.1.3.

$v_{x,y,z}$ velocity of a particle along the x, y, or z direction.

$\mathbf{x}^p(t)$ position of a particle at time t, in vector form.

$\dot{\mathbf{x}}^p(t)$ velocity of a particle at time t, in vector form; same as $\mathbf{v}$.

$\ddot{\mathbf{x}}^p(t)$ acceleration of a particle at time t, in vector form.

$\mathrm{Z_{DR}}$ differential reflectivity, introduced in Section 2.3.3.

$\mathrm{Z_e}$ equivalent radar reflectivity factor, introduced in Eq. 2.27.

$\mathrm{Z_{e\,H}}$ equivalent radar reflectivity factor at horizontal polarization.

$\mathrm{Z_{e\,V}}$ equivalent radar reflectivity factor at vertical polarization.

Acknowledgments

This PhD dissertation was carried out within and funded by the Transregional Collaborative Research Center TRR 172 "ArctiC Amplification: Climate Relevant Atmospheric and SurfaCe Processes, and Feedback Mechanisms $(AC)^3$", funded by the Deutsche Forschungsgemeinschaft (DFG, German Research Foundation). The Integrated Research Training Group (IRTG) of the $(AC)^3$ consortium, and the Graduate School of Geosciences (GSGS) of the University of Cologne provided training, support, and travel funds. A special thank you goes to the coordinators of the IRTG and GSGS, Christa and Karin, for their support, and for genuinely caring about the students.

I am extremely grateful to my supervisors, Stefan, Uli, and Max, for giving me invaluable feedback and guidance throughout these three years. An enormous thank you goes especially to Stefan, whose passionate mentorship, continuous encouragement, and contagious curiosity have had a tremendous impact on my work and beyond.

A big thank you goes to the colleagues of the Institute for Geophysics and Meteorology of the University of Cologne, who make this institute a truly welcoming and stimulating place on a daily basis. Special thanks go to Bernhard, Davide, Kerstin, Leonie, Lukas, Markus, Pavel, Rosa, Sabrina, Tracy, and Vera, who helped me at various points with feedback, discussions, or support. A big thank you also goes to Dagmar, for helping me countless times with navigating the maze that is university bureaucracy.

Outside the University of Cologne, I would like to thank Alexander for spending several hours explaining me the intricacies of radar operation, physical principles, and processing. Speaking of radar operation, I would also like to thank the staff of the AWIPEV station, especially Fieke, Guillaume, and Wilfried, for assisting me with instrument problems on numerous occasions. This thesis would have not been possible without Christoph and Marion, who shared the microwave radiometer and ceilometer data they collected at AWIPEV, and without the Cloudnet team, whose target classification product was a central element of my approach. I would like to further express my gratitude to the many scientists who during conferences, workshops, meetings, and research visits gave me feedback; it would be impossible to name them all. And a final thank you goes to the colleagues of the $(AC)^3$ project for their goodwill and comradery.

Erklärung zur Dissertation
gemäß der Promotionsordnung vom 12. März 2020

Hiermit versichere ich an Eides statt, dass ich die vorliegende Dissertation selbstständig und ohne die Benutzung anderer als der angegebenen Hilfsmittel und Literatur angefertigt habe. Alle Stellen, die wörtlich oder sinngemäß aus veröffentlichten und nicht veröffentlichten Werken dem Wortlaut oder dem Sinn nach entnommen wurden, sind als solche kenntlich gemacht. Ich versichere an Eides statt, dass diese Dissertation noch keiner anderen Fakultät oder Universität zur Prüfung vorgelegen hat; dass sie - abgesehen von unten angegebenen Teilpublikationen und eingebundenen Artikeln und Manuskripten - noch nicht veröffentlicht worden ist sowie, dass ich eine Veröffentlichung der Dissertation vor Abschluss der Promotion nicht ohne Genehmigung des Promotionsausschusses vornehmen werde. Die Bestimmungen dieser Ordnung sind mir bekannt. Darüber hinaus erkläre ich hiermit, dass ich die Ordnung zur Sicherung guter wissenschaftlicher Praxis und zum Umgang mit wissenschaftlichem Fehlverhalten der Universität zu Köln gelesen und sie bei der Durchführung der Dissertation zugrundeliegenden Arbeiten und der schriftlich verfassten Dissertation beachtet habe und verpflichte mich hiermit, die dort genannten Vorgaben bei allen wissenschaftlichen Tätigkeiten zu beachten und umzusetzen. Ich versichere, dass die eingereichte elektronische Fassung der eingereichten Druckfassung vollständig entspricht.

Teilpublikationen:

Chellini, G., R. Gierens, and S. Kneifel (2022). **Ice aggregation in low-level mixed-phase clouds at a high Arctic site: Enhanced by dendritic growth and absent close to the melting level.** *Journal of Geophysical Research: Atmospheres*, 127, e2022JD036860, https://doi.org/10.1029/2022JD036860.

Chellini, G., R. Gierens, K. Ebell, T. Kiszler, P. Krobot, A. Myagkov, V. Schemann, and S. Kneifel (2023). **Low-level mixed-phase clouds at the high Arctic site of Ny-Ålesund: A comprehensive long-term dataset of remote sensing observations.** *Earth System Science Data Discussions [preprint]*, https://doi.org/10.5194/essd-2023-157, in review.

Chellini, G., and S. Kneifel (2023). **Turbulence as a key driver of ice aggregation and riming in Arctic low-level mixed-phase clouds, revealed by long-term cloud radar observations.** Submitted to *Geophysical Research Letters*.

Köln, 10. Oktober 2023
Giovanni Chellini